

Combined Channel Sounding and Direction Finding Studies of HF Radio  
Propagation Effects Observed Over High Latitude Communication Paths

By

Clive Andrew Jackson

Thesis submitted to the Faculty of Science, University of Leicester for the degree of  
Doctor of Philosophy

Department of Engineering,

University of Leicester.

March 2003

UMI Number: U496591

All rights reserved

INFORMATION TO ALL USERS

The quality of this reproduction is dependent upon the quality of the copy submitted.

In the unlikely event that the author did not send a complete manuscript and there are missing pages, these will be noted. Also, if material had to be removed, a note will indicate the deletion.



UMI U496591

Published by ProQuest LLC 2013. Copyright in the Dissertation held by the Author.  
Microform Edition © ProQuest LLC.

All rights reserved. This work is protected against  
unauthorized copying under Title 17, United States Code.



ProQuest LLC  
789 East Eisenhower Parkway  
P.O. Box 1346  
Ann Arbor, MI 48106-1346

# Combined Channel Sounding and Direction Finding Studies of HF Radio Propagation Effects Observed Over High Latitude Communication Paths

Clive Andrew Jackson

## Abstract

The high latitude ionosphere is a dynamic region that is subject to a variety of disturbed conditions affecting oblique propagation of HF radio signals. Multipath and off great circle propagation resulting from rough ionospheric reflecting surfaces introduce time dispersion, while movements in the ionosphere impose Doppler dispersion. These effects, when combined, result in very complex signal characteristics, which cause degradation to the performance of communication systems if the delay or Doppler dispersion exceeds system dependent bounds.

Results are presented based around measurements of signals, produced by the Doppler And Multipath SOunding Network, recorded using a six channel spaced array receiving system, during a 10 day campaign at Kiruna in March 1998. In addition to delay and Doppler processing, the directions of arrival (DOA) of the signal components were estimated using a super resolution direction finding algorithm.

Most signals were narrow in delay and Doppler, however a significant statistical spread in their DOA was observed. Statistics on the occurrence and characteristics of the remaining signals revealed that trends in DOA are often associated with complex delay and Doppler propagation. A number of cases had Doppler spread exceeding a specified Doppler boundary of operation, while none exceeded the delay spread boundary.

Case studies revealed detailed propagation effects. Of particular interest is the often observed East → West trend in DOA with Doppler offset. This is attributed to scattering from irregularities embedded in turbulent bulk convection flows. E-region modes with good spectral and geographic distribution of signal energy are often observed in otherwise complex cases.

Spatial filtering, using two or three element arrays was investigated and found to be effective at reducing large Doppler spreads to lower values more amenable to high data rate communication systems. Fast solver spatial filtering methods were found to be very robust, effective and a lot quicker.

**Mum**

Maureen Mary Jackson (nee' Salvage)

1935 – 2002

## Acknowledgements

Firstly I would like to acknowledge the love and support of my Mum and Dad who have enthusiastically encouraged me throughout my academic career and provided me with a firm foundation to build my life on. Mum was always very proud of my achievements and was looking forward to having a Doctor for her son. To my eternal grief Mum died from ovarian cancer before I was able to finish so I have dedicated this thesis to her. Since then Dad has continued to provide support and encouragement and I in turn enthusiastically thank him.

I should acknowledge the rest of my family, particularly Jane and her cats Genghis and Sensi who are just great. My friends from university, badminton, sailing and work deserve much admiration too, not only for their good taste but also for their patience.

I would like to thank AMS Radar Systems Division for their patience and allowing me time off from work in order to complete this thesis.

On the academic side thanks go to:

QinetiQ (formerly the UK Defence Evaluation and Research Agency), the Canadian Communications Research Centre, the Norwegian Defence Research Establishment, the Swedish Institute of Space Physics and the Swedish Defence Research Establishment for their help in the use of the DAMSON transmissions.

The Swedish Institute of Space Physics in Kiruna for hosting the receiving system.

Professor P.S. Cannon of QinetiQ (and the University of Bath) for providing the financial support to do this work.

Finally my supervisor, Dr. E.M. Warrington of the Radio Systems Laboratory, for allowing me the opportunity of working at the University of Leicester.

<b>1.</b>	<b>INTRODUCTION</b>	<b>1-1</b>
1.1	<b>The Ionosphere</b>	<b>1-1</b>
1.1.1	Morphology of the ionosphere	1-2
1.2	<b>Solar terrestrial relations</b>	<b>1-3</b>
1.3	<b>Ionospheric radiowave propagation</b>	<b>1-4</b>
1.1.1	Applied magnetic field	1-6
1.1.2	Collisions	1-7
1.1.3	Applied magnetic field and collisions	1-8
1.4	<b>Vertical and oblique propagation</b>	<b>1-8</b>
1.4.1	The 'secant law'	1-9
1.1.2	Breit and Tuve's theorem	1-9
1.1.3	Martyn's (equivalent path) theorem	1-9
1.1.4	Curved Earth	1-9
1.1.5	Oblique ray paths	1-10
1.5	<b>Radio probing of the ionosphere</b>	<b>1-11</b>
1.6	<b>Off great circle path propagation</b>	<b>1-13</b>
1.7	<b>Communications system performance</b>	<b>1-13</b>
1.8	<b>Channel sounding</b>	<b>1-14</b>
<b>2.</b>	<b>REVIEW OF CHANNEL SOUNDING AND DIRECTION FINDING STUDIES</b>	<b>2-1</b>
2.1	<b>Channel sounding</b>	<b>2-1</b>
2.1.1	The Naval Research Laboratory's (NRL) HF channel probe	2-1
1.1.2	The DAMSON project	2-3
1.2	<b>Direction finding</b>	<b>2-7</b>
1.2.1	Experimental direction finding studies	2-8
1.3	<b>DAMSON DF</b>	<b>2-11</b>

<b>3.</b>	<b>EXPERIMENTAL ARRANGEMENT</b>	<b>3-1</b>
<b>3.1</b>	<b>The RSL multi-channel HF-DF system</b>	<b>3-1</b>
3.1.1	The system scheduler	3-3
<b>3.2</b>	<b>DAMSON schedule and signal format</b>	<b>3-4</b>
3.2.1	Signal format	3-5
<b>3.3</b>	<b>Post processing</b>	<b>3-6</b>
3.3.1	Calibration	3-6
3.3.2	Time of flight corrections	3-7
1.1.3	DAMSON signal processing	3-7
<b>1.4</b>	<b>First pass data selection.</b>	<b>3-9</b>
<b>1.5</b>	<b>Direction finding of received signals.</b>	<b>3-10</b>
1.5.1	Antenna sensitivity patterns and sidelobes.	3-10
1.5.2	DD-DF calculation	3-11
<b>1.6</b>	<b>Visualisation</b>	<b>3-11</b>
<b>1.7</b>	<b>Data analysis</b>	<b>3-12</b>
1.7.1	Thresholding	3-12
1.7.2	Region finding, clustering and parameter extraction	3-13
<b>1.8</b>	<b>Interferer signals from ~165° azimuth.</b>	<b>3-16</b>
<b>4.</b>	<b>SURVEY OF CAMPAIGN DATA</b>	<b>4-1</b>
<b>4.1</b>	<b>First pass data analysis</b>	<b>4-2</b>
<b>4.2</b>	<b>Time delay spreads</b>	<b>4-3</b>
1.1.1	Signal to Noise ratio considerations	4-4
<b>1.3</b>	<b>Doppler spreads</b>	<b>4-5</b>
1.3.1	Signal to Noise ratio considerations	4-6
<b>1.4</b>	<b>Summary</b>	<b>4-7</b>
<b>1.5</b>	<b>Occurrence statistics of both narrow delay and Doppler spreads</b>	<b>4-8</b>
1.1.1	Summary	4-10
<b>1.6</b>	<b>Occurrence statistics of time delay spreads</b>	<b>4-12</b>

<b>1.7</b>	<b>Occurrence statistics of large Doppler spreads</b>	<b>4-13</b>
<b>1.8</b>	<b>Concluding remarks</b>	<b>4-15</b>
<b>5.</b>	<b>PROPAGATION ANALYSIS</b>	<b>5-1</b>
<b>5.1</b>	<b>Time delay spreads</b>	<b>5-1</b>
1.1.1	Svalbard – Kiruna, 13:00UT → 23:59UT, 23 <sup>rd</sup> March 1998 (Day 82)	5-1
1.1.1	Harstad – Kiruna, 13:00UT → 23:59UT, 23 <sup>rd</sup> March 1998 (Day 82)	5-4
<b>1.2</b>	<b>Large Doppler spreads</b>	<b>5-6</b>
1.2.1	Direction of arrival considerations	5-6
1.2.2	Doppler offset as a function of azimuth	5-7
1.1.3	E-region ~GCP modes	5-12
1.1.4	Doppler spreading observed over both paths.	5-12
<b>1.3</b>	<b>Concluding remarks</b>	<b>5-13</b>
<b>6.</b>	<b>SPATIAL FILTERING</b>	<b>6-1</b>
<b>6.1</b>	<b>Selection of cases for investigation.</b>	<b>6-1</b>
<b>6.2</b>	<b>Signal processing for spatial filtering.</b>	<b>6-2</b>
6.2.1	Two element arrays (constant amplitude, variable phase summation)	6-2
1.1.2	Two element arrays (variable amplitude, variable phase summation)	6-3
1.1.3	Three element array (constant amplitude, varying phases)	6-3
<b>1.3</b>	<b>Analysis - Two element arrays</b>	<b>6-4</b>
1.1.1	Case studies and examples	6-4
1.1.2	Statistical treatment	6-7
1.1.3	SNR considerations.	6-11
<b>1.4</b>	<b>Analysis - Three element arrays</b>	<b>6-11</b>
<b>1.5</b>	<b>Analysis – Fast solver method</b>	<b>6-12</b>
<b>1.6</b>	<b>Concluding remarks</b>	<b>6-14</b>
<b>7.</b>	<b>CONCLUSIONS AND SUGGESTIONS FOR FURTHER WORK</b>	<b>7-1</b>
<b>7.1</b>	<b>Statistical survey</b>	<b>7-1</b>
<b>7.2</b>	<b>Detailed case studies</b>	<b>7-2</b>

<b>7.3</b>	<b>Spatial filtering</b>	<b>7-3</b>
<b>1.4</b>	<b>Further Work</b>	<b>7-5</b>
<b>8.</b>	<b>REFERENCES</b>	<b>8-1</b>
<b>8.1</b>	<b>World Wide Web references.</b>	<b>8-13</b>

# 1. Introduction

This thesis is concerned with point-to-point digital communications via the high latitude narrowband High Frequency (HF) ionospheric radio channel. In such a system, data is digitally modulated onto HF radio carrier waves, which are propagated from a transmitter on or near the surface of the Earth, via the ionosphere, to a receiver, also on or near the surface of the Earth, where they are demodulated and the data recovered.

For a perfect channel there will be no distortion of the signal and the data recovered at the receiver will be a perfect copy of that sent by the transmitter. However, the HF channel is known to suffer time varying environmental noise, multipath propagation and Doppler effects, all of which contribute to signal distortion and consequent errors in the received data.

The aim of the work presented in this thesis is to gain an understanding of some of the physical propagation processes that have an influence on the performance of HF data communication systems operating at high latitudes and to investigate ways of mitigating their impact. Of particular interest is the directional structure of incoming signals at a receive site after propagation via the ionosphere.

In order to achieve the best performance from a communication system it is necessary to understand the characteristics of the channel it is attempting to use.

## 1.1 The Ionosphere

The ionosphere can be defined as that part of the upper atmosphere where sufficient ionisation exists to affect the propagation of radio waves. This occurs in a region that extends in altitude from approximately 50km to greater than 1000km. The term 'ionosphere' is usually used to distinguish the ionised part of the upper atmosphere from the background neutral gas. The ionosphere is vertically differentiated and characterised by its electron density versus altitude. A typical profile is illustrated in Figure 1.1.

The different layers of the ionosphere are specified alphabetically:

D. – extends from approximately 60km to 90km in altitude, the D-region is produced by Lyman  $\alpha$  and hard X-rays from the Sun.

E. – extends from approximately 90km to 140km in altitude, the E-region is produced by solar soft X-rays. Under certain conditions a layer, known as sporadic E (Es) develops which can have an electron density exceeding that of the normal E-region by more than 4 times.

F. - the peak electron density is usually found in the F-region at an altitude of approximately 140 km or above. The F-region, which can be subdivided into the F1 and F2 layers during the summer daytime, is produced by Solar Extreme Ultraviolet (EUV) radiation.

The ionised nature of the ionosphere means that electromagnetic waves can interact with it. In particular the ionosphere provides a refractive medium for electromagnetic waves, which under certain conditions give rise to total internal reflection. Importantly, for communications purposes, these conditions are often met for radio waves in the HF band (3MHz - 30MHz).

#### *1.1.1 Morphology of the ionosphere*

The structure of the ionosphere varies in a complicated fashion both temporally and spatially. For the most part these variations can be accounted for by the amount of ionising solar radiation incident upon it and electron recombination rates.

Large diurnal variations in solar illumination occur through the day and lead to changes in the structure of the electron density profile, such as those illustrated in Figure 1.2(a), where the electron density increases rapidly after sunrise, reaches a peak in the afternoon and decreases slowly after sunset. There is also a seasonal variation in structure illustrated in Figure 1.2(b). Surprisingly the peak electron densities occur in the winter months in these profiles. This is due to an increase in the amount of atomic oxygen in the atmosphere in winter allowing more ions to be produced, while at the same time the lower temperatures retard one of the ion-electron recombination processes.

The 11 year sunspot cycle has an effect on electron density distribution, the increased solar activity associated with high sunspot numbers leads to increases in the peak electron density, as illustrated in Figure 1.3, which shows marked increases with sunspot number.

There is significant geographical variation in ionospheric structure too, much of this is related to other solar phenomena and the interaction of the Earth's magnetic field with the interplanetary magnetic field.

## 1.2 Solar terrestrial relations

The ionosphere is generated by the action of solar radiation and particles on the upper atmosphere and is thus sensitive to changes in this solar flux. However, the ionosphere is also affected by the interaction of the Sun and Earth's magnetic fields in the solar wind plasma (see *Davies* [1990]).

The solar wind is formed as open solar magnetic field lines expand away from the Sun and allow coronal plasma to escape and flow into interplanetary space. This solar wind plasma in turn interacts with the Sun's magnetic field and carries it into the interplanetary medium, where it is then denoted the Interplanetary Magnetic Field (IMF).

This solar wind flows around the Earth's magnetic field to produce the 'geomagnetic cavity', which has a structure illustrated in Figure 1.4.

At low latitudes the Earth's magnetic field is closed and approximates a dipole field inclined at  $12^\circ$  to the Earth's axis of rotation. At higher latitudes, however, the geomagnetic field interacts with the IMF and is swept back to form the magnetotail. The magnetosphere formed in this way has structure. In the low latitudes the closed geomagnetic field lines are swept around with the Earth and contain the region known as the plasmasphere. At higher latitudes the field lines are swept back into the centre of the magnetotail, called the plasma sheet, these field lines correspond to field lines in the auroral oval. The auroral oval is the region where precipitation of magnetospheric particles causes ionisation of the atmosphere in addition to that from the solar flux, producing visible structures called 'Aurora'. The aurora are confined to this auroral oval, which has been statistically specified by observation of photographic data (*Feldstein & Starkov* [1967]) for different levels of geomagnetic activity. The orientation of this oval zone is fixed with respect to the Sun, the Earth rotates beneath it, Figure 1.5. At high latitudes the open geomagnetic field lines reconnect with the IMF, these field lines map back onto the Earth in a region known as the 'Polar Cap'.

Magnetospheric electric fields, produced by magnetospheric convection, map into the polar cap where they drive plasma convection across the polar cap dependent on the orientation of the IMF ( $B_x$ ,  $B_y$ ,  $B_z$ )

Figure 1.6 gives some examples of these convection flows (*Lockwood [1993]*). These convection flows can extend into the mid latitude sunlit ionosphere and convect highly ionised plasma back into the low electron density polar cap. At the altitudes where electron recombination rates are low these regions of enhanced ionisation can persist for several hours and drift for large distances across the polar cap.

Field aligned irregularities may be produced in the presence of the steep electron density gradients perpendicular to the magnetic field in regions such as the edges of electron density enhancements or by precipitation within the auroral oval. These irregularity structures may be carried in the convection flows over large distances.

The mid latitude trough is a depletion of the electron density in the F-region found equator-wards of the auroral oval during night time hours. The pole-ward wall of the trough is formed by enhancement of ionospheric plasma density by the electron precipitation in the auroral oval, the equator-ward wall is the boundary between the trough and the mid latitude ionosphere (*Davies [1990]*).

### 1.3 Ionospheric radiowave propagation

A theory of ionospheric radiowave propagation was devised by Appleton in the 1920's. The equation for the calculation of the complex refractive index,  $n = (\mu - i\chi)$ , of the ionosphere is known as the Appleton or Appleton-Hartree equation, Equation 1.1. This has been generalised to include the effect of heavy ions and the electron collision frequency (*Davies [1990]*).

$$n^2 = (\mu - i\chi)^2 = 1 - \frac{X}{1 - iZ - \frac{Y_r^2}{2(1 - X - iZ)} \pm \sqrt{\frac{Y_r^4}{4(1 - X - iZ)^2} + Y_L^2}}$$

Equation 1.1

Where  $X = Ne^2/\epsilon_0 m \omega^2$

$N$  = electron density

$e$  = charge on an electron

$\epsilon_0$  = permittivity of free space

$m$  = mass of an electron

$\omega$  = radio wave angular frequency

$$Y_T = eB_T/m\omega$$

$B_T$  = transverse magnetic field (normal to wavefront normal – in the plane of the wavefront)

$$Y_L = eB_L/m\omega$$

$B_L$  = longitudinal magnetic field (parallel to wavefront normal)

$$Z = \nu/\omega$$

$\nu$  = electron collision frequency

When collisions are considered negligible ( $Z \approx 0$ ) and the magnetic field is considered negligible ( $Y \ll 1$ ) Equation 1.1 reduces to

$$\mu^2 = 1 - X = 1 - \left( \frac{f_N}{f} \right)^2 = 1 - k \frac{N}{f^2}$$

Equation 1.2

Where  $f$  = radio wave frequency

$$f_N = \frac{1}{2\pi} \sqrt{\frac{Ne^2}{\epsilon_0 m}}, \text{ the 'plasma frequency' (Hz)}$$

Equation 1.3

The value  $\mu$  represents the real part of the refractive index. Since  $\mu$  is real,  $\mu^2$  must be greater than 0. In Equation 1.2 it is also indicated that  $\mu^2$  is less than 1. This results in  $\mu$  having a value between 0 and 1.

Further examination of Equation 1.2 reveals that the refractive index decreases with increasing electron density and/or decreasing radiowave frequency.

Snell's law describes ray behaviour in a refractive layer:

$$\mu \sin \phi = \mu_0 \sin \phi_0$$

Equation 1.4

In this case  $\mu$  represents the refractive index of an ionospheric layer and  $\phi$  the angle between the wave normal in the layer and the perpendicular to the base of the layer.  $\phi_0$  and  $\mu_0=1$  are the values at the base of the layer.

For reflection to occur  $\phi_r$  must equal  $90^\circ$  hence:

$$\mu_r = \sin \phi_0$$

Equation 1.5

In the case of vertical propagation in a horizontally stratified ionosphere  $\phi_0 = 0^\circ$  which results in  $\mu_r = 0$ . Referring to Equation 1.2 leads to the conclusion that reflection can only occur if the ionospheric layer in question has a plasma frequency  $f_N$  greater than or equal to the wave frequency  $f$ . If the wave frequency,  $f$ , is greater than the maximum plasma frequency of the ionosphere then the ray will not reflect at all but will pass through. This frequency is referred to as the 'critical frequency',  $f_c$ .

### 1.3.1 Applied magnetic field

If the case where an external magnetic field is applied, but collisions are still negligible, is considered, equation 1.1 may be written,

$$\mu^2 = 1 - \frac{2X(1-X)}{2(1-X) - Y_T^2 \pm \sqrt{Y_T^4 + 4(1-X)^2 Y_L^2}}$$

Equation 1.6

After substituting  $\mu = 0$ , for vertical incidence reflections, there are three solutions to this equation,

The positive solution gives

$$X = 1 \quad \text{'ordinary wave'} \quad \text{Equation 1.6a}$$

The negative solution gives

$$X = 1 - Y \quad \text{When } Y < 1, \text{ for the first 'extraordinary wave'} \quad \text{Equation 1.6b}$$

$$X = 1 + Y \quad \text{When } Y > 1, \text{ for the second 'extraordinary wave'} \quad \text{Equation 1.6c}$$

Equation 1.6a represents the ordinary wave. This is so named since it is reflected at the same height as the zero magnetic field case. The negative solutions represent the extraordinary wave. In general the ordinary and extraordinary waves have different polarisation and reflect at different heights. Under certain conditions, however, energy from the ordinary wave may couple into the extraordinary wave. This can occur at high latitudes for near vertical incidence propagation since the Earth's magnetic field lines run nearly parallel to the wave direction. In this case the composite signal is called the z-wave.

### 1.3.2 Collisions

If the effect of collisions between the free electrons and neutral gas molecules, in the absence of a magnetic field, is considered. Equation 1.1 may be written,

$$n^2 = (\mu - i\chi)^2 = 1 - \frac{X}{1 - iZ}$$

Equation 1.7

In this case the refractive index,  $n$ , is complex.

Energy in the propagating wave is transferred into kinetic energy of the free electrons, which in turn transfer some of this kinetic energy to the neutral gas molecules via collisions. The propagating wave is attenuated and the neutral gas is thus heated.

The absorption coefficient for this case is given by the imaginary part of the propagation function,

$$\begin{aligned}\kappa &= \frac{\omega}{c} \chi \\ &= \frac{\omega}{c} \left( \frac{-XZ}{2\mu(1+Z^2)} \right) \\ &= \frac{e^2}{2\epsilon_0 mc} \cdot \frac{Nv}{\mu(\omega^2 + \mu^2)}\end{aligned}$$

Equation 1.8

It is clear that at the reflection condition ( $\mu \rightarrow 0$ ) there will be strong absorption. This mechanism is known as deviative absorption.

In the lower ionosphere, such as the D-region, although  $\mu > 0$  and there is no reflection condition,  $Nv$  is large and absorption does occur here, this type of absorption is termed 'non-deviative' absorption. The density of the D-region varies with time of day hence absorption is usually strongest close to local noon and weakest at night.

In the higher ionospheric layers  $v^2 \ll \omega^2$  and the absorption is inversely proportional to the wave frequency squared.

### 1.3.3 Applied magnetic field and collisions

If the case where collisions in a medium with an applied magnetic field is considered, the (non-deviative) absorption coefficient for the extraordinary wave is greater than that for the ordinary wave.

## 1.4 Vertical and oblique propagation

The ability of the ionosphere to reflect radio waves is used to allow communications over large distances of the Earth's surface and in particular over the horizon or 'Beyond the Line of Sight' (BLOS). This requires radio waves to propagate obliquely through the ionosphere. A full discussion of oblique propagation is available in standard texts, such as *Davies* [1990], the main points are highlighted below.

#### 1.4.1 The 'secant law'

This relates the frequencies and paths of two waves, one reflecting normally, the other obliquely from the same true height. Figure 1.7 represents this graphically, for a flat Earth model, in two dimensions.

In the case of the oblique wave, if it is at incidence ( $\phi_0 > 0^\circ$ ) to a plane ionosphere, in which the electron density increases with altitude to cause total internal reflection, then the wave will return to Earth. If both collisions and an imposed magnetic field are neglected then the Appleton formula and Snell's Law combine to give a relationship between the frequency,  $f_o$ , of the oblique wave reflected at a given real height and the frequency,  $f_v$ , of a normally incident wave reflected at the same real height.

$$f_o = f_v \sec \phi_0$$

Equation 1.9

$f_v$  is known as the 'equivalent vertical frequency' corresponding to  $f_o$ . This represents the ability of the ionosphere to reflect much higher frequencies obliquely than it can vertically.

#### 1.4.2 Breit and Tuve's theorem

This states that the time taken for a wave to traverse the curved path TBR, Figure 1.7, in the ionosphere is the same as for that wave to traverse the equivalent or virtual triangular path TAR in free space.

#### 1.4.3 Martyn's (equivalent path) theorem

This states that the virtual heights of reflection for two waves with equivalent frequencies propagating vertically ( $f_v$ ) and obliquely ( $f_o$ ) in a flat ionosphere will be equal.

#### 1.4.4 Curved Earth

The curvature of the surface of the Earth is important for ground ranges greater than approx. 500km (Davies [1990]). If a thin ionosphere is assumed (the thickness of the ionosphere is negligible compared to the altitude) then the curvature of the Earth leads to an effective shortening of the distance between transmitter and receiver (i.e. the chord

through the Earth) and the effective height of the ionosphere is increased by the distance BC, illustrated in Figure 1.8. This thin layer approximation is reasonable in the case of propagation via Sporadic E.

If the thickness of the ionosphere is significant compared to the altitude then the curvature of the layer must also be considered. This leads to a revision of the secant law:

$$f_o = f_v \sec \phi_r$$

Equation 1.10

where  $\phi_r$  is illustrated in Figure 1.9.

$f_v$ , the equivalent vertical frequency, depends on the true reflection height and hence the electron density profile. A good approximation to this formula is to replace  $\sec \phi_r$  with  $k \cdot \sec \phi_0$  where  $k$  falls between 1.0 to 1.2 and can be calculated from model ionospheres.

The maximum useable frequency (MUF) for a path is defined as the frequency above which rays are no longer reflected by an ionospheric layer, but penetrate and do not return to the ground. This MUF can be related to the critical frequency for vertical propagation by replacing  $f_v$  with  $f_c$  in Equation 1.10

$$MUF = f_c k \sec \phi_0 = M f_c$$

Equation 1.11

The factor  $M$  in Equation 1.11 is known as the MUF or ‘obliquity’ factor.

#### 1.4.5 Oblique ray paths

A radio wave travelling between a transmitter and a receiver may follow a path involving several ionospheric reflections, which may or may not also involve intermediate ground reflections. Some examples of this behaviour are illustrated in Figure 1.10. There is a common nomenclature used to describe these paths, which is also illustrated in the figure.

In addition a signal may travel by more than one path to the same receiver as illustrated in Figure 1.11. Since movements in the ionosphere at the different reflection points can introduce Doppler shifts and spreads to the signal, the signal components will arrive at

the receiver with different delay and Doppler properties. In general there will not be a constant phase relationship between the components and the amplitude of the signal at the receiver will also vary with time or 'fade'.

The ionosphere cannot be considered as a smooth reflector and a single mode is transmitted via a scattering region as opposed to a point, which introduces 'in-mode' fading on the received signal, Figure 1.12. The fading of these composite ionospheric reflections can be modelled as the sum of the contributions from a steady, specular, component and a diffracted component.

## **1.5 Radio probing of the ionosphere**

The most widely used instrument for probing the ionosphere is the swept frequency ionosonde. This is essentially a vertical, high frequency, pulsed radar used to measure the virtual height of the ionospheric layers. It operates by transmitting short pulses of radio energy vertically into the ionosphere where, providing the carrier frequency does not exceed the vertical critical frequency ( $f_c$ ), they are reflected back towards the ground by the various layers. The time delay between transmission of the pulses and their echo returns gives an indication of the virtual height of each layer. A record of the virtual height versus frequency, called an ionogram, is obtained if the carrier frequency is varied over time. Various trade-offs must be made in the design of ionosondes, if the sounding frequency is varied slowly then a good echo signal-to-noise ratio may be achieved by integrating the returning pulses, however, the ability of the ionogram to represent short term variation in the ionosphere is compromised. Short term variability may be monitored using shorter sweep duration but at the cost of echo signal-to-noise level.

An alternative to the pulse sounder design, described above, is the chirp sounder. This employs linear frequency modulated pulses and uses frequency analysis to resolve the pulse flight times and hence the layer virtual heights. Such sounders are usually much lower power than pulse sounders, however, with a relatively slow sweep rate a chirp sounder will require a much longer time to cover the HF band than a pulse sounder. Other alternatives include the use of digital pulse compression waveforms and digital signal processing techniques.

Oblique ionograms are obtained when the transmitter and receiver are separated, provided that good synchronisation between the sites is maintained (usually through the use of satellite time signals). These traces represent the state of the ionosphere at the path reflection points rather than directly overhead. Such an arrangement can be useful if the state of the ionosphere above an inaccessible region (such as the sea) is required. Clearly the form of the oblique ionograms will be different compared to vertical soundings. In particular the time of flight will depend on the path length as well as layer height while the maximum frequency of a layer is now the oblique frequency, not the vertical critical frequency. Examination of these traces can lead to an understanding of the mode structure and propagation frequency limits of a particular path, which may be useful if operating a communications link over the path.

The simplest ionosondes record only the time delays of the returning echo's, however, more complex designs record other properties of the returns such as pulse amplitude, polarisation, phase, Doppler shift and even direction of arrival (DOA). An example vertical ionogram collected at Svalbard ionosonde is presented in Figure 1.13. Three distinct traces are evident, the E-layer reflections at about 120km altitude have a critical frequency around 3.5MHz while the F-layer reflections have been split into the ordinary (o) and extraordinary (x) waves having critical frequencies of around 5.5MHz and 6MHz respectively. Note that in addition to the derived virtual height traces, the returning pulse amplitude is represented by the colour scale.

Ionosondes are useful tools both for ionospheric research and monitoring. Research ionosondes can be installed in specified locations and their operational modes controlled directly by a researcher to provide data tailored to their experiment. Monitoring ionosondes on the other hand are used to automatically record the properties of the ionosphere over long periods of time. The important parameters from ionograms recorded over a world wide distribution of ionosondes is collected by the 'World Data Centre for Solar Terrestrial Physics' at the Rutherford Appleton Laboratory and made available over the internet (see References)

## **1.6 Off great circle path propagation**

In the presence of significant horizontal electron density gradients (tilts) such as are encountered in the high latitude ionosphere (for example the walls of the mid latitude trough or the edges of regions of enhanced ionisation) ray paths are unlikely to follow great circle paths (GCP). Electron density gradients perpendicular to the path or high electron density features to the side of a path will lead to non GCP routes between transmitter and receiver and the direction of arrival (DOA) of signals approaching the receiver will be different to the true bearing of the transmitter, Figure 1.14. Gradients parallel to the path will cause the elevation of the incoming wave to be different to the non-tilted case, see Figure 1.15.

Radio waves may be scattered by field aligned irregularities within the ionosphere. These can occur as described in section 1.2. The scatter propagation is due to Bragg scattering from the irregularities, this is strongest when the incident radiation is perpendicular to the irregularities. At high latitudes, where the magnetic field is nearly vertically inclined, the ray must already be refracted almost as far as reaching reflection. The distance between transmitter to irregularity and irregularity to receiver must therefore be equal so that the ray is refracted by equal amounts on its upward and downward journeys. Off GCP propagation can occur if irregularity regions are off to the side of the GCP, although scattering from irregularities is generally aspect sensitive and decreases as the angle of incidence moves away from perpendicularity.

If the irregularities are much larger than the wavelength of the propagating waves then the effect would be that of a rough ionosphere as described in Section 1.4.5 and Figure 1.12.

Ground side-scatter may also lead to off GCP propagation in multi-hop paths, where signal energy is incident at the receiver after scattering from irregularities on the Earth's surface. In some cases it is possible to receive signal energy scattered from directions behind the receiver with respect to the transmitter.

## **1.7 Communications system performance**

The performance of an HF communication system, over a given path, is to a large extent dependent on the selection of the transmitted waveform as well as more fundamental

parameters such as frequency, transmitter power and antenna gain. It is important to use the appropriate waveform for the propagation path and conditions. In particular it should be noted that data modems operate well under conditions of low Doppler spread and low delay spread. Their performances degrade significantly when these spreads exceed certain, modem dependent, levels.

*ITU-R Rec. F-1487* outlines a method for the testing of HF modems using ionospheric channel simulators. *Cannon et al.* [2002], provides more details on the characteristics of the channel models used in ionospheric simulators. This is based on the work of *Arthur and Maundrell* [1997], *Angling et al.* [1997] and *Angling and Davies* [1999], who measured the responses to multipath and Doppler spread of Mil-Std-188-110A modems, operating at various data rates using HF channel simulators. Figure 1.16 and Figure 1.17 are modem performance surfaces for a Mil-Std-188-110A modem operating at 1200bps and 300bps respectively. These are based on data supplied by M.J. Angling at QinetiQ, Malvern. The 300bps modem is considered to be relatively robust while the 1200bps modem sacrifices robustness for speed. For each value of Doppler and multipath spread, the surface represents the signal-to-noise ratio (SNR) required for the modem to perform with a nominal Bit Error Rate (BER) of  $1 \times 10^{-3}$ . The low SNR at values of Doppler spread below 7Hz and multipath spread below 7ms in Figure 1.16, indicate that the Mil-Std 1200bps modem works well in this region. In other words, in this region only a relatively low SNR (~5dB) is required to achieve a BER within the required range. Above these values of Doppler and multipath spread the SNR required rapidly increases until the surface reaches a plateau (arbitrarily set at 60dB) that indicates that the required BER range cannot be achieved, and that further increasing the SNR cannot reduce the BER of the modem. These boundaries in the performance of a given modem have been termed the 'breaking points'. In Figure 1.16, representing the Mil-Std-188-110A 1200bps modem, these breaking points are clearly seen at around 7ms multipath delay spread and 7Hz Doppler spread, while in Figure 1.17, representing the 300bps modem, the breaking points are around 7ms delay spread and 25Hz Doppler spread.

## **1.8 Channel sounding**

The same radio signal may arrive at a receiver with a number of different times of flight. This can be due to the signal travelling via multiple modes (e.g. 1E, 1F, 2F etc.) as

described in Figure 1.11; the signal may also travel via off great circle propagation paths, thus introducing further delays. Since the nature of the ionosphere varies geographically and temporally, in general, its behaviour at the reflection points for the various paths will be different. In particular, considerable Doppler shifting and/or spreading will occur if the ionosphere at a given reflection point is disturbed. Thus for a transmitter – receiver channel, the resulting characteristics at the receiver may be complicated by the signal being multi-moded and each separate mode subject to different delay and Doppler dispersion. For a communications system, operating over such a channel can be challenging.

The amount of frequency and time dispersion over a channel can be described by the ‘Channel Scattering function’; it describes the way in which signal energy is redistributed in delay and Doppler as a result of propagation via the (ionospheric) medium. This scattering function can be represented as a three dimensional surface having x- and y- axes with units of delay and frequency respectively, and a height (z-axis) with units of power. This representation is commonly known as a ‘scattergram’ or a ‘delay-Doppler surface’.

An approximation to the scattering function may be derived from pulse response functions measured with a channel probe. Each pulse response consists of a series of complex samples,  $s_i = 1..n$ , separated by time increment  $t$ . A series of pulse responses are repeatedly measured with a period of  $T$  between the start of each measurement. The scattering function estimate is arrived at by computing the set of discrete Fourier transforms of each of the sequence of samples,  $s_i$ , with time intervals  $T$ .

By providing delay and Doppler spread parameters, along with knowledge of the signal to noise ratio, the channel scattering function is a useful diagnostic for evaluating the state of a given channel and hence its performance potential for communication purposes.

The signals used in the investigations described in this thesis are generated by two of the transmitters in the Doppler And Multipath SOunding Network (DAMSON) operated by the Radio Science and Propagation Group, QinetiQ, Malvern. This network has been established to allow the characterisation of a number of high latitude communication paths, in terms of delay and Doppler, in support of the development of applications

requiring high data rate communications. Transmitters are located at Isfjord Radio Station on Svalbard and at Harstad in Norway while receivers are located at Tuentangen in Norway and Kiruna in Sweden. As illustrated in Figure 1.18 these provide for a range of path lengths between 192km and 2019km with orientations both tangential and parallel to the auroral oval. Of the two paths studied in this thesis, one is the long trans-auroral path from Svalbard – Kiruna and the other the short sub-auroral path running tangential to the oval from Harstad – Kiruna. While the DAMSON network uses a number of waveforms, the most suitable for the purposes of estimating scattering functions is denoted the Delay-Doppler (DD) waveform. A typical scattergram derived from processing of a received DD signal is plotted in the coloured centre panel of Figure 1.19. The x- and y- axes have units of time and frequency respectively while the z-axis is represented by a colour code where the value is normalised to 0dB relative to the peak over the surface. In this example the received signal energy does appear to be clustered into three distinct regional components on the scattergram where each component has different delay and Doppler offsets and spreads. Clearly the signal energy has been propagated via multiple paths with different Doppler properties at the reflection points. Due to the large delay of the third component it seems likely that there has been off great circle propagation too but the reflection points cannot be inferred because the spatial distribution of the incoming signal components is unknown.

The investigations described in this thesis use data, recorded from a multi-channel HF receiver system connected to a wide aperture antenna array, to measure the direction of arrival of narrow band pulsed channel sounding signals propagated over high latitude paths. The delay and Doppler characteristics of the high latitude paths were found by processing the signals received on each antenna to provide an approximation to the channel scattering function. A direction finding algorithm was then used to determine the directional characteristics of each of the signal components.

This thesis is intended to show that the integration of direction finding information alongside traditional DAMSON processing will provide useful diagnostic information towards the analysis of HF propagation at high latitudes.

Also, given the disturbed dynamic nature of the high latitude ionosphere and the sometimes localised nature of ionospheric features, the spatial distribution of signal energy and the relationship to its delay-Doppler characteristics is of particular interest.

With this information it may be possible to explain some features, already observed in previously collected DAMSON data sets.

This will lead to a better understanding of propagation of HF radio signals at high latitudes and may provide options for improved signal processing in high data rate applications.

Chapter 3 of this thesis contains details of the disposition of the transmitters and the receiver system used for the data capture, along with a detailed description of the delay-Doppler signal format and some of the signal and image processing techniques used to calculate the channel scattering function, determine the directional characteristics of each of the signal components and characterise the propagation. Included in Chapter 2 are a description of the objectives of the DAMSON project and a review of some of the findings to date. A section of Chapter 2 will be dedicated to a review of some direction of arrival studies conducted over various high latitude paths in recent years.

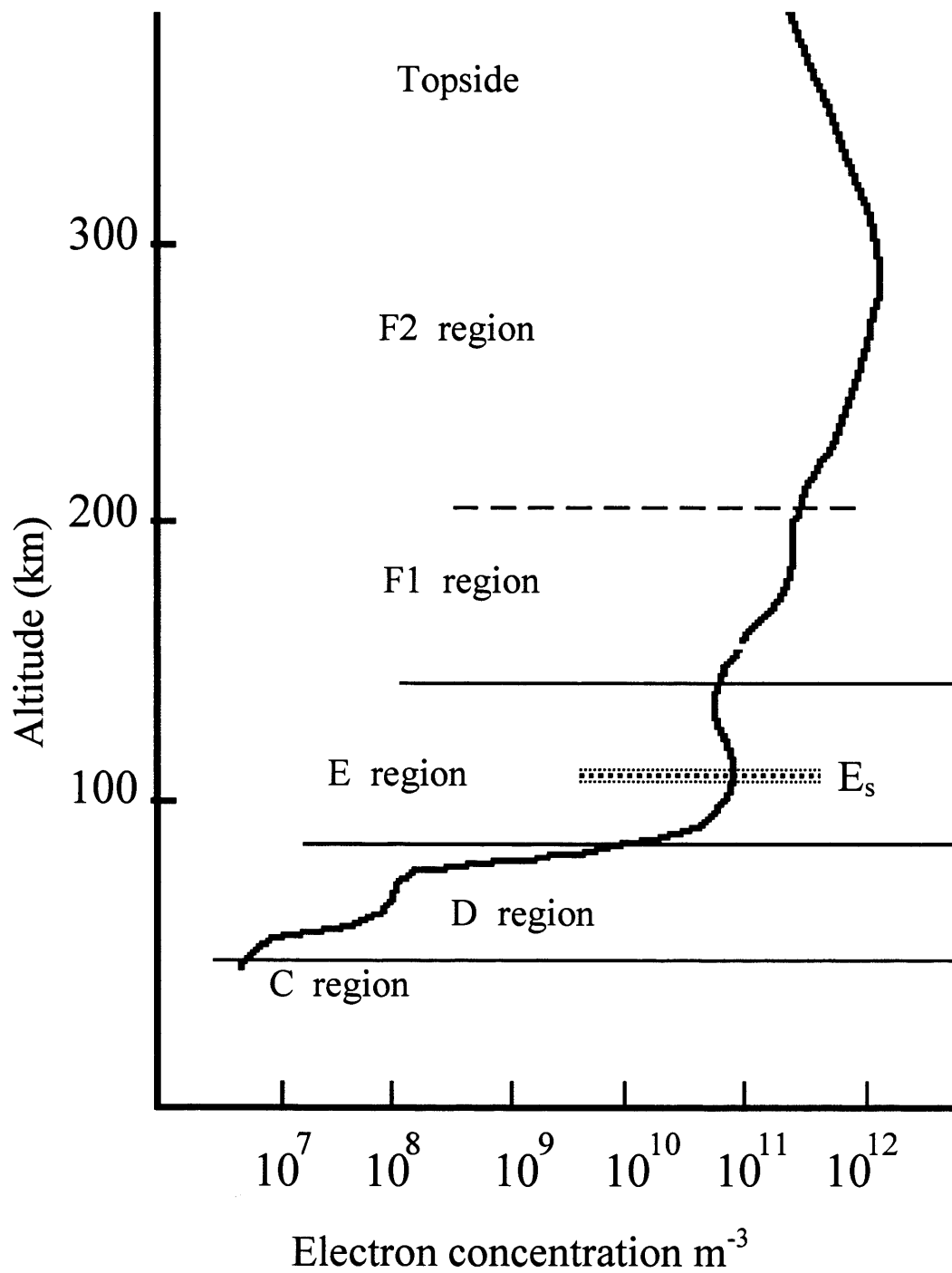


Figure 1.1 Detail of a summer daytime ionospheric electron density profile

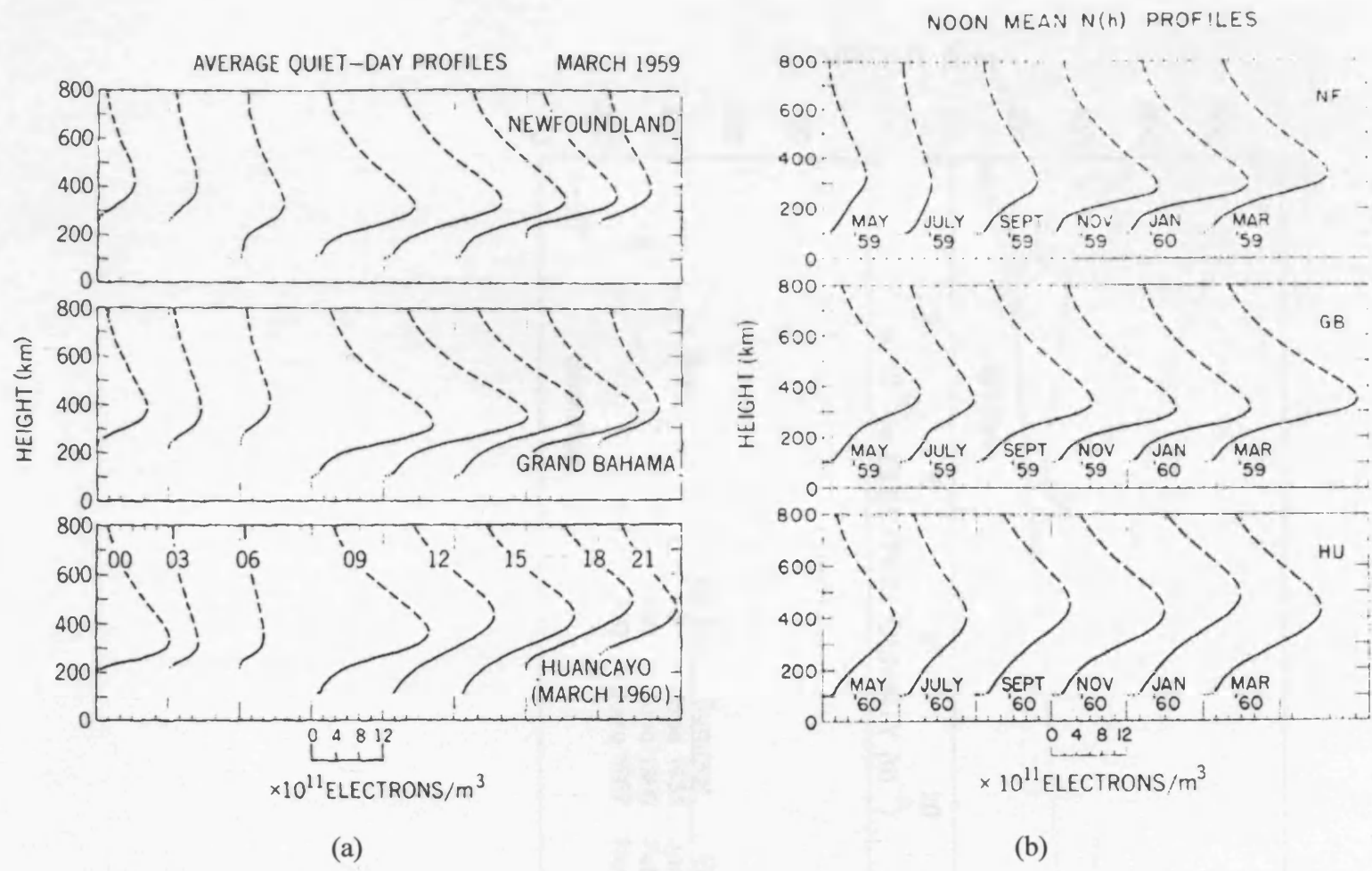


Figure 1.2 (a) Diurnal and (b) Seasonal variation in ionospheric electron density. *Davies* [1990].

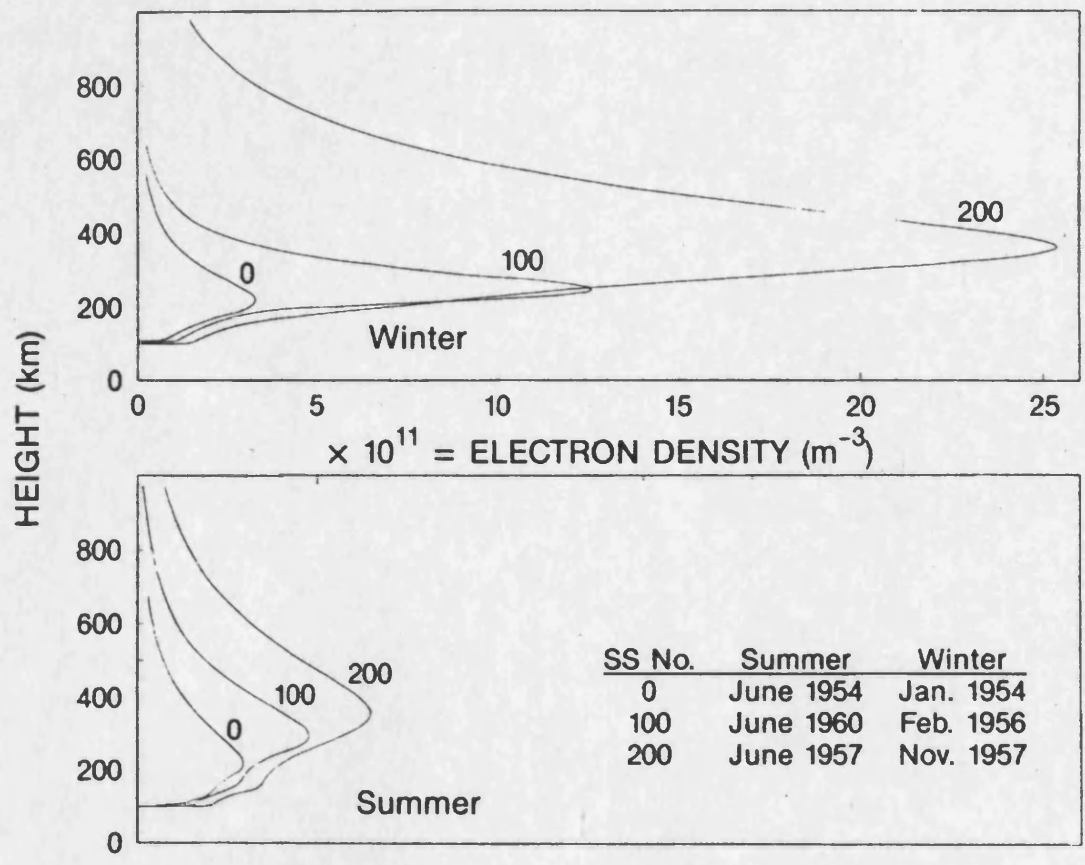


Figure 1.3 (a) Typical electron density profiles, during summer and winter, at sunspot numbers 0, 100 and 200 (after *Wright* [1962]).

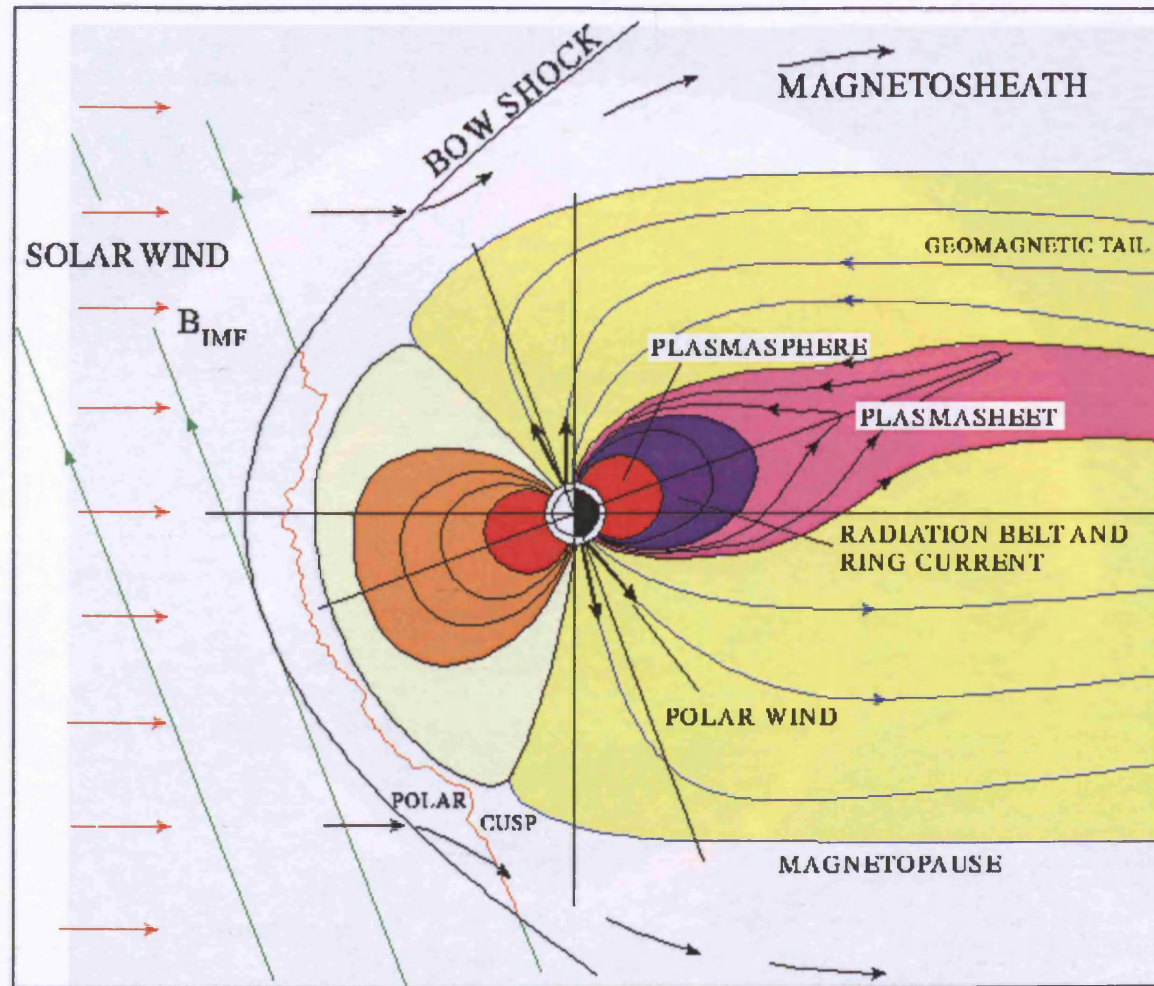


Figure 1.4 (a) Image of the Auroral Oval taken from space shows the magnetosphere (taken by the Spock-Sun Auroral Imager) (b) Schematic of the Magnetosphere - Courtesy L. Frank, the University of Iowa, and NASA.

Figure 1.4 Magnetosphere formed by interaction between the Earth's magnetic field and the IMF (Courtesy of RSPPG web site, see references).

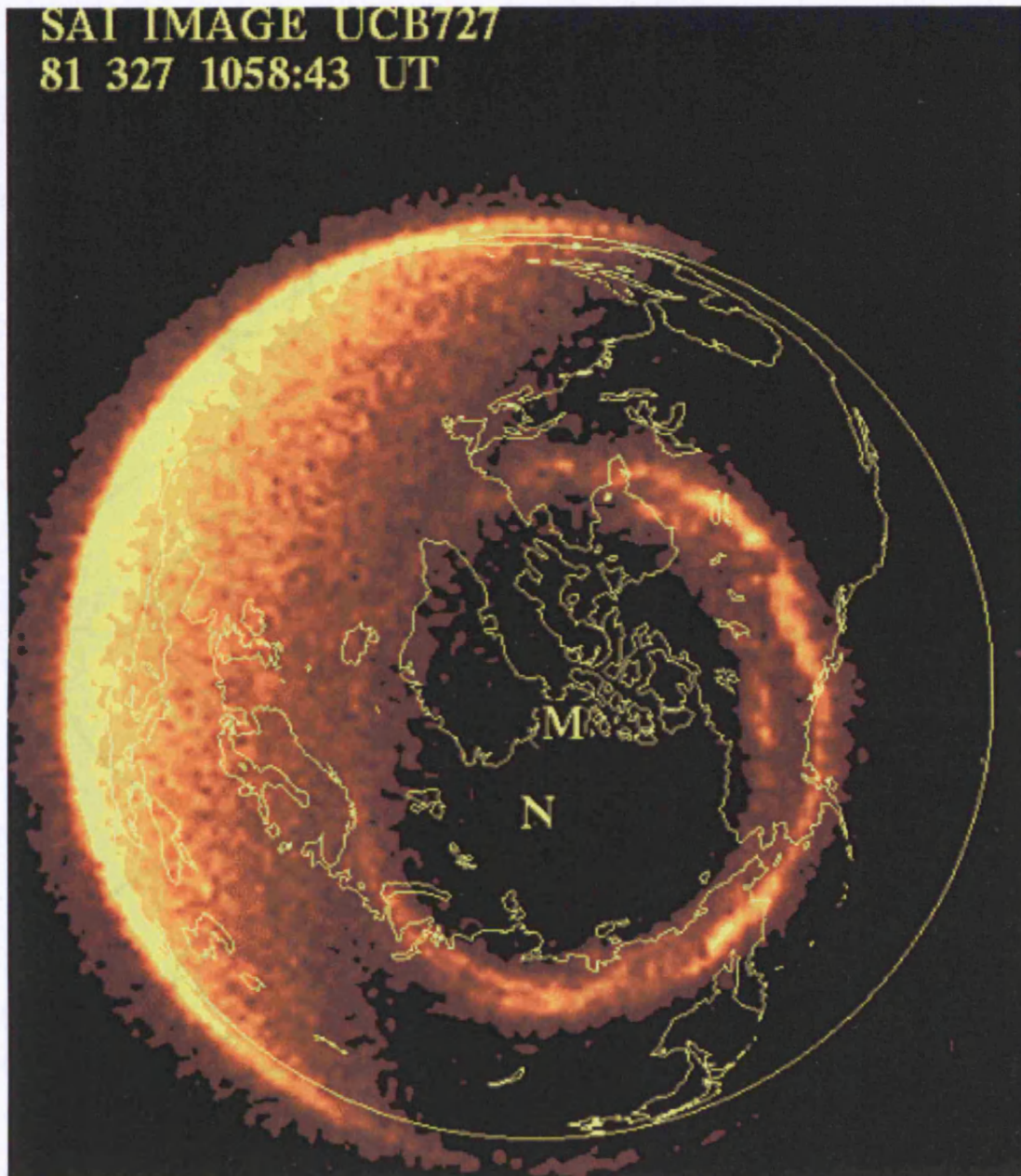


Figure 1.5 UV image of the Auroral Oval taken from space above the North Pole – “Image taken by the Spin-Scan Auroral Imaging instrument on board Dynamics Explorer – 1. Courtesy L. Frank, the University of Iowa, and NASA.”

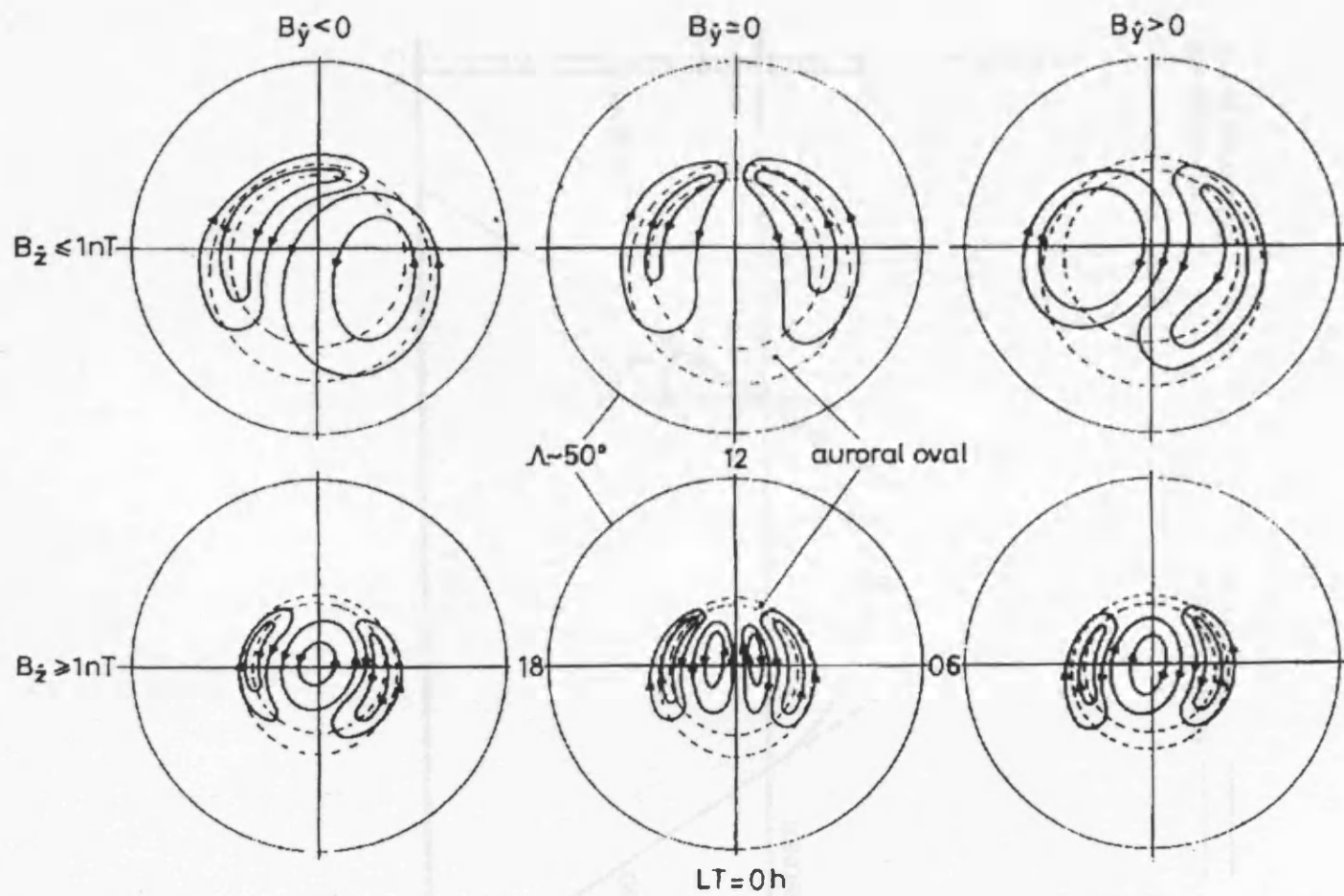


Figure 1.6 Model of the cross polar cap convection flow, Lockwood [1993]

T = TRANSMITTER  
R = RECEIVER

REAL PATH ———  
VIRTUAL PATH - - - - -

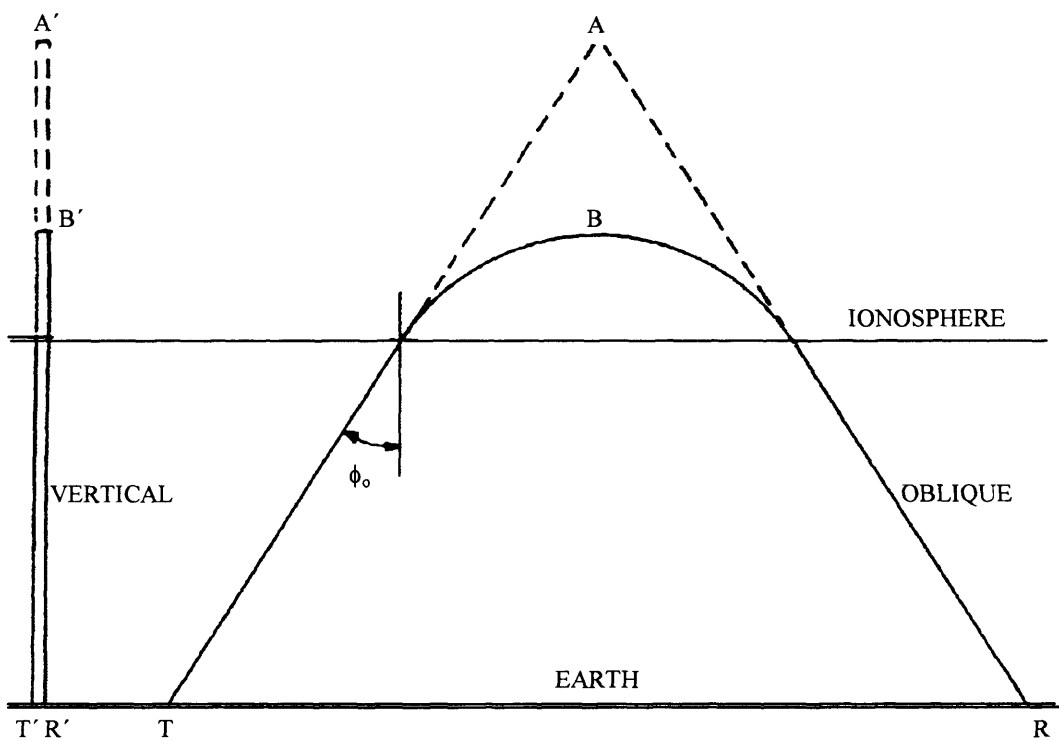


Figure 1.7 Equivalent waves reflected obliquely and vertically at the same height and the same virtual heights. Plane Earth and ionosphere. *Davies* [1990]

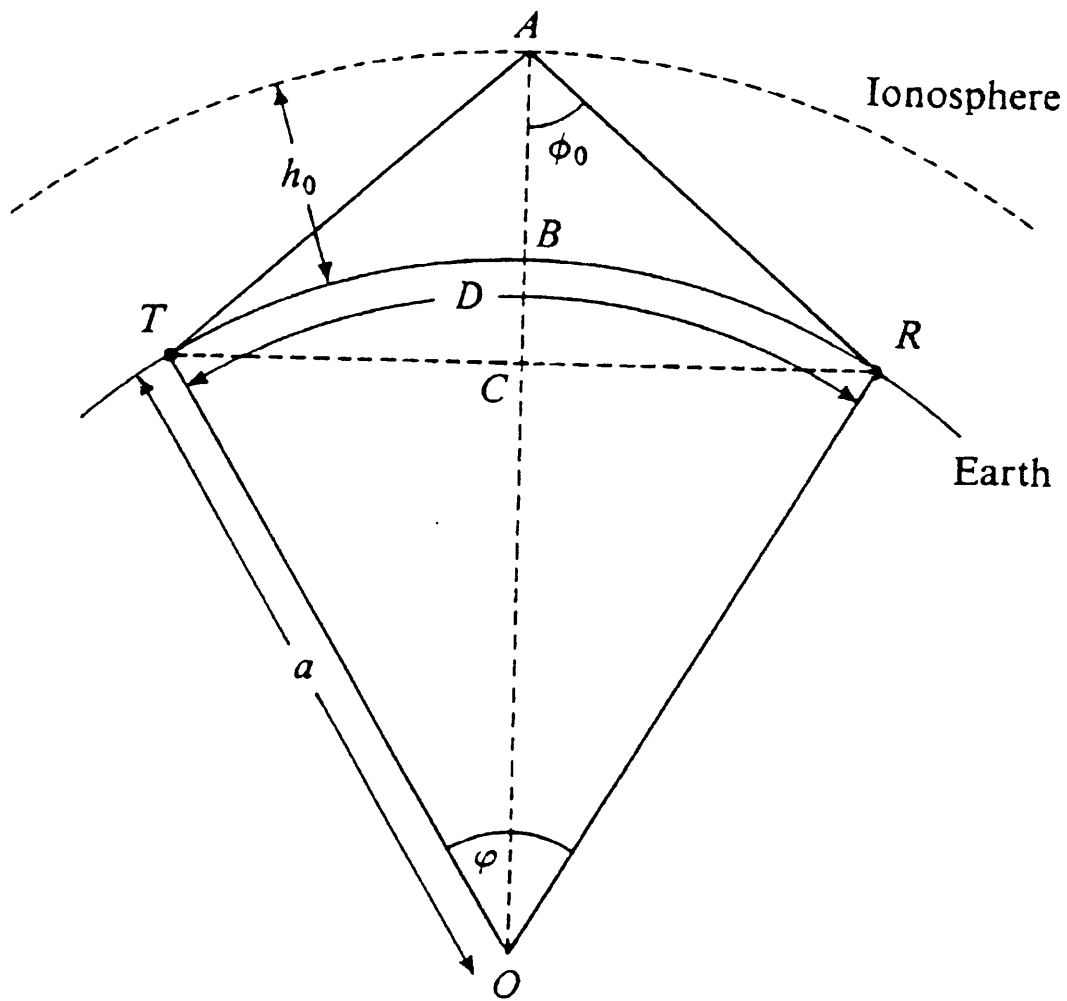


Figure 1.8 Reflection geometry for a thin curved ionosphere. *Davies* [1990]

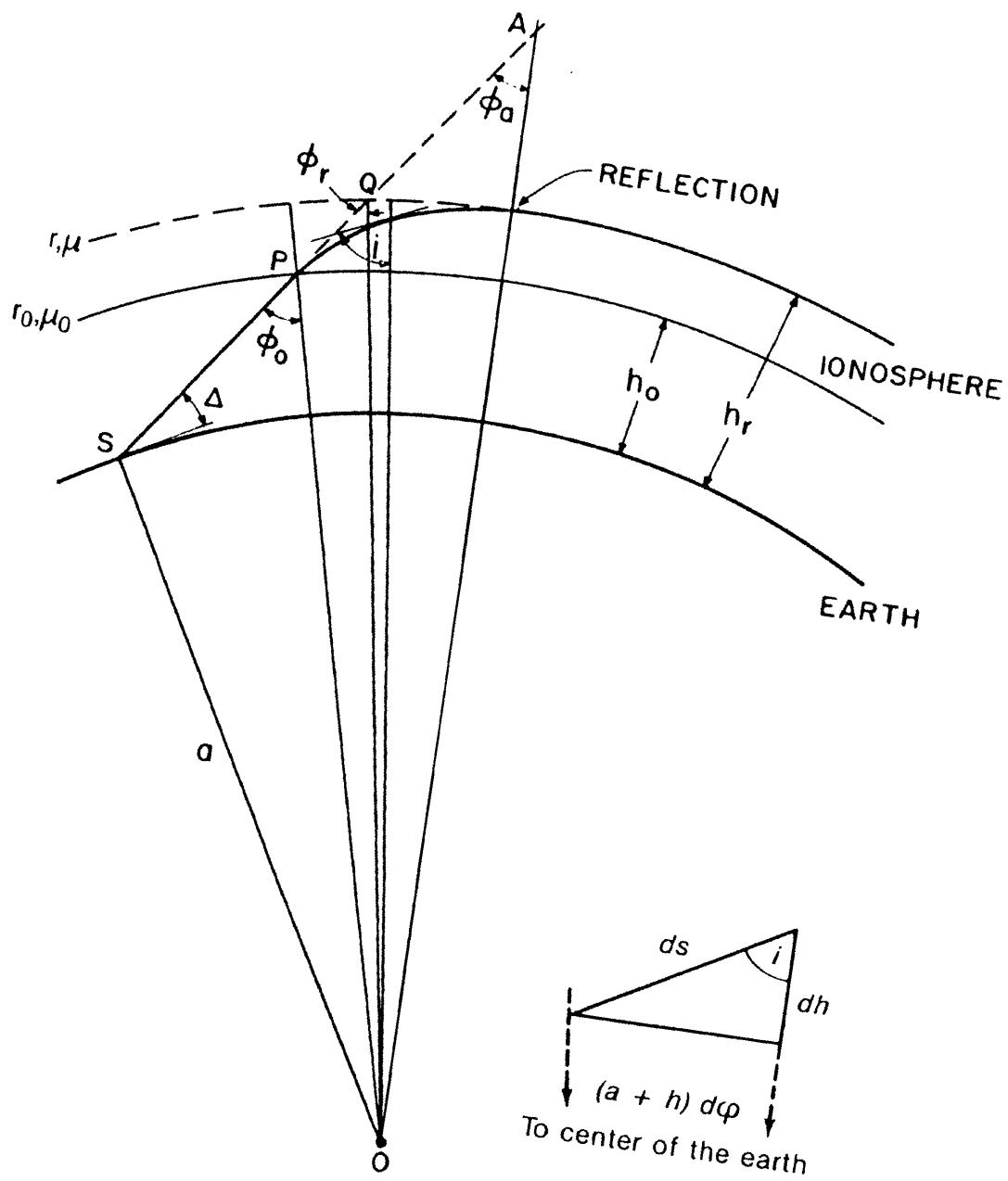


Figure 1.9 Ray reflection in a thick curved ionosphere. Davies [1990]

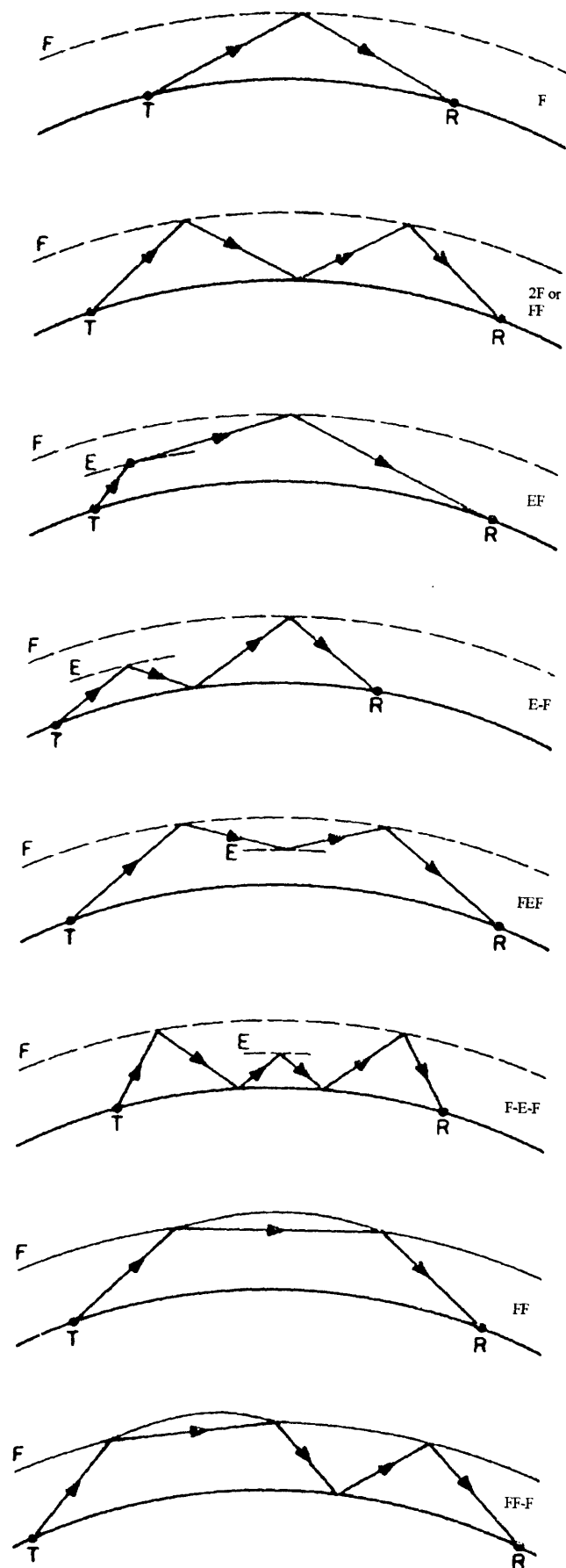


Figure 1.10 Oblique ray paths. *Davies* [1990]

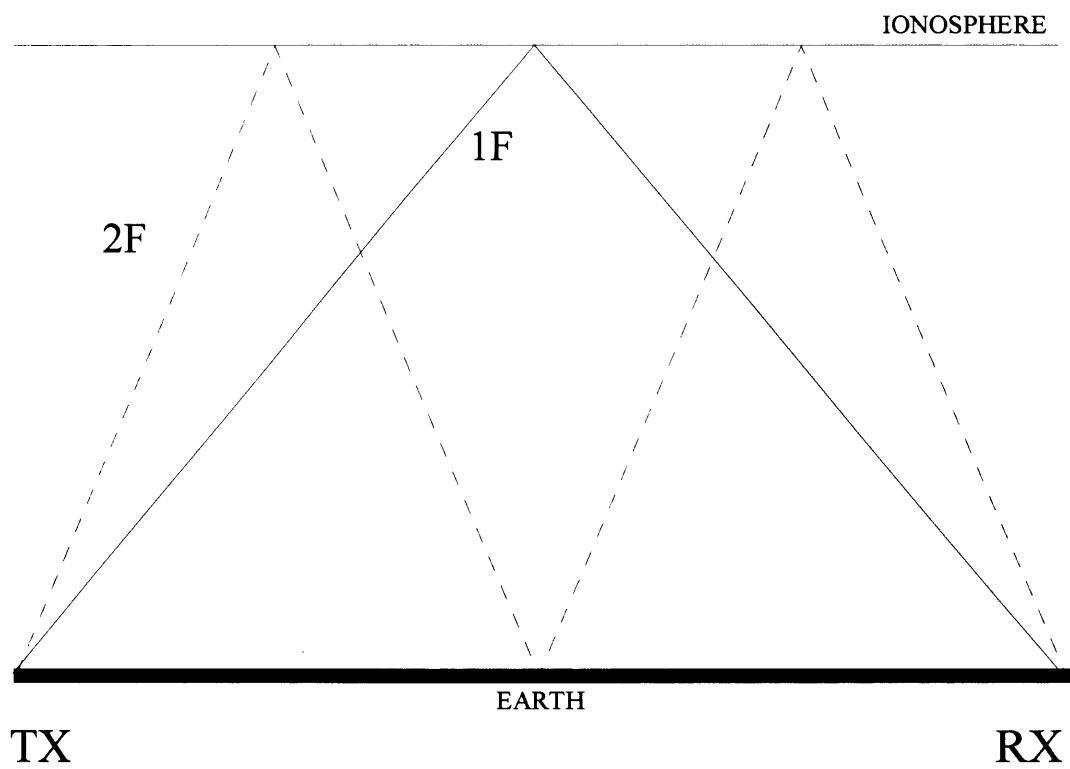


Figure 1.11 Propagation via more than one mode.

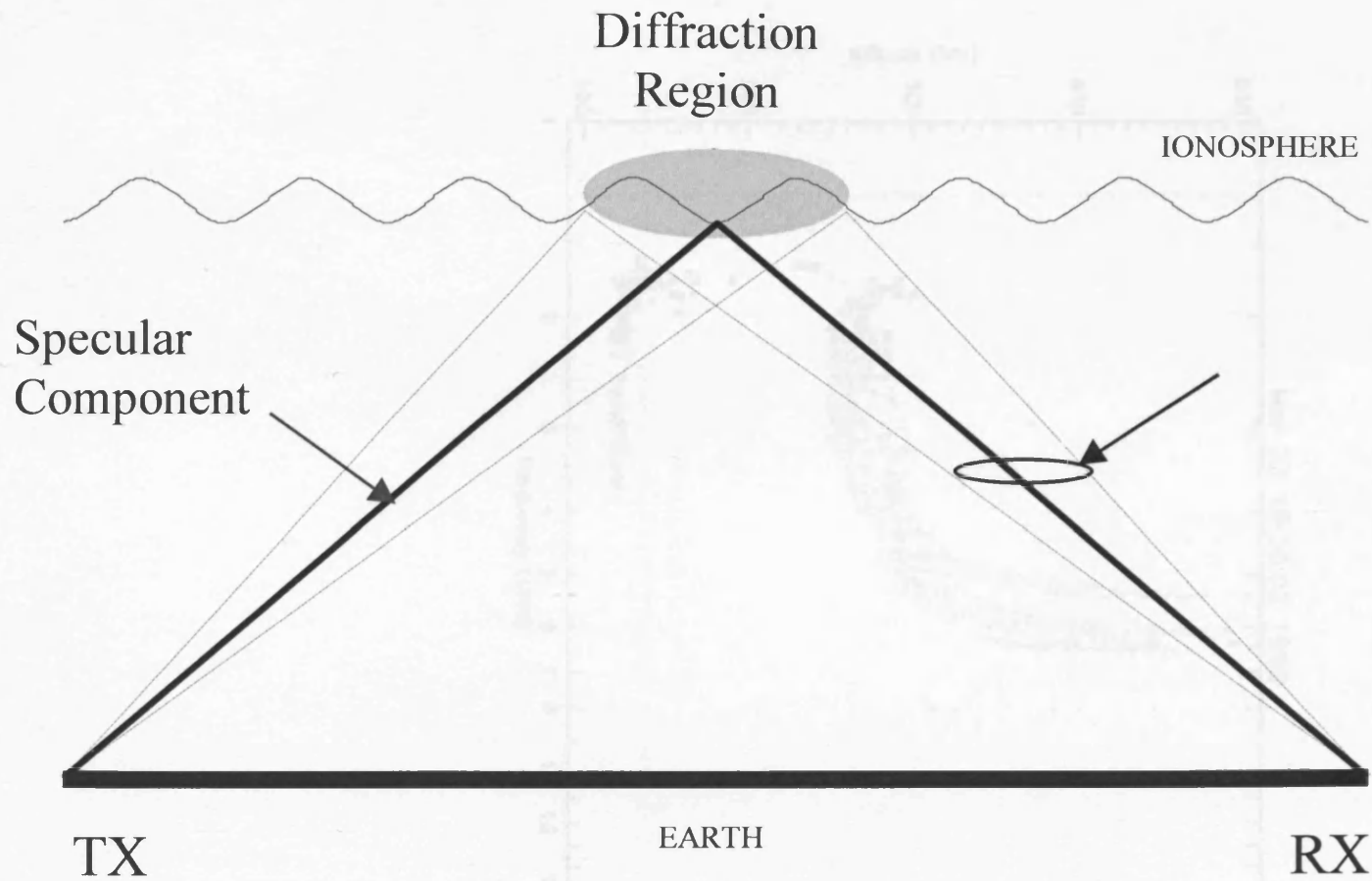


Figure 1.12 In mode fading due to a scattering region

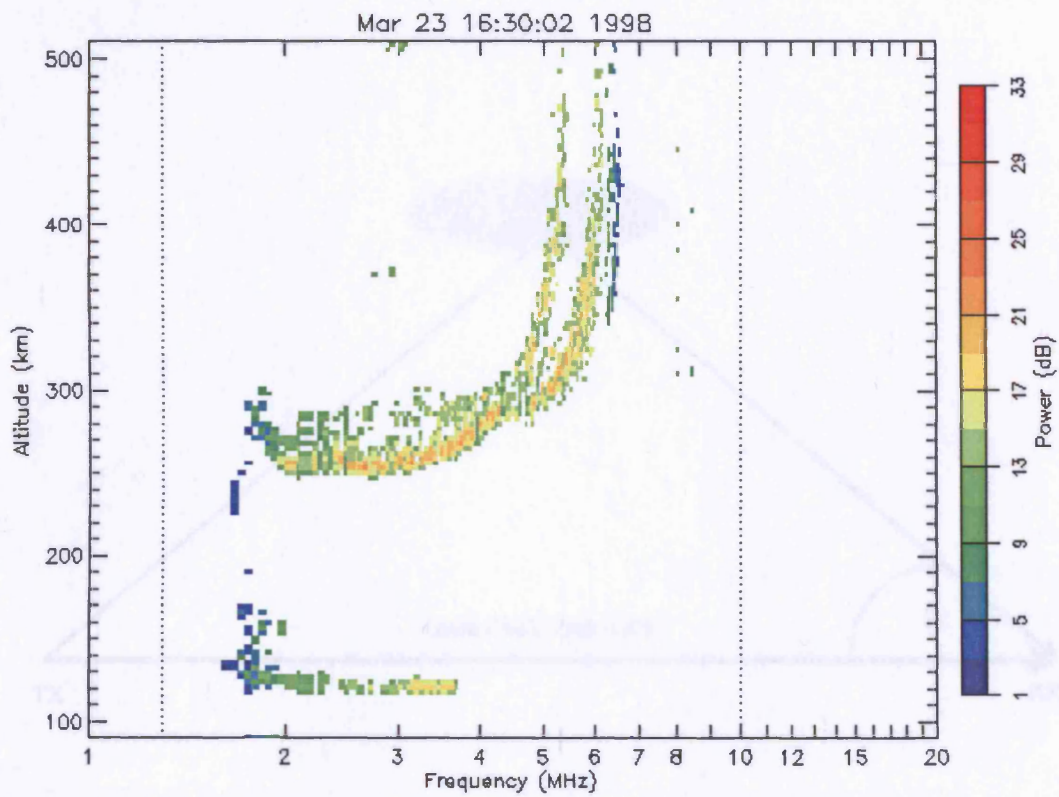


Figure 1.13 Example ionogram collected by Svalbard ionosonde. Note that in addition to the derived virtual height traces, the returning pulse amplitude is represented by the colour scale (Courtesy of RSPPG web site, see references).

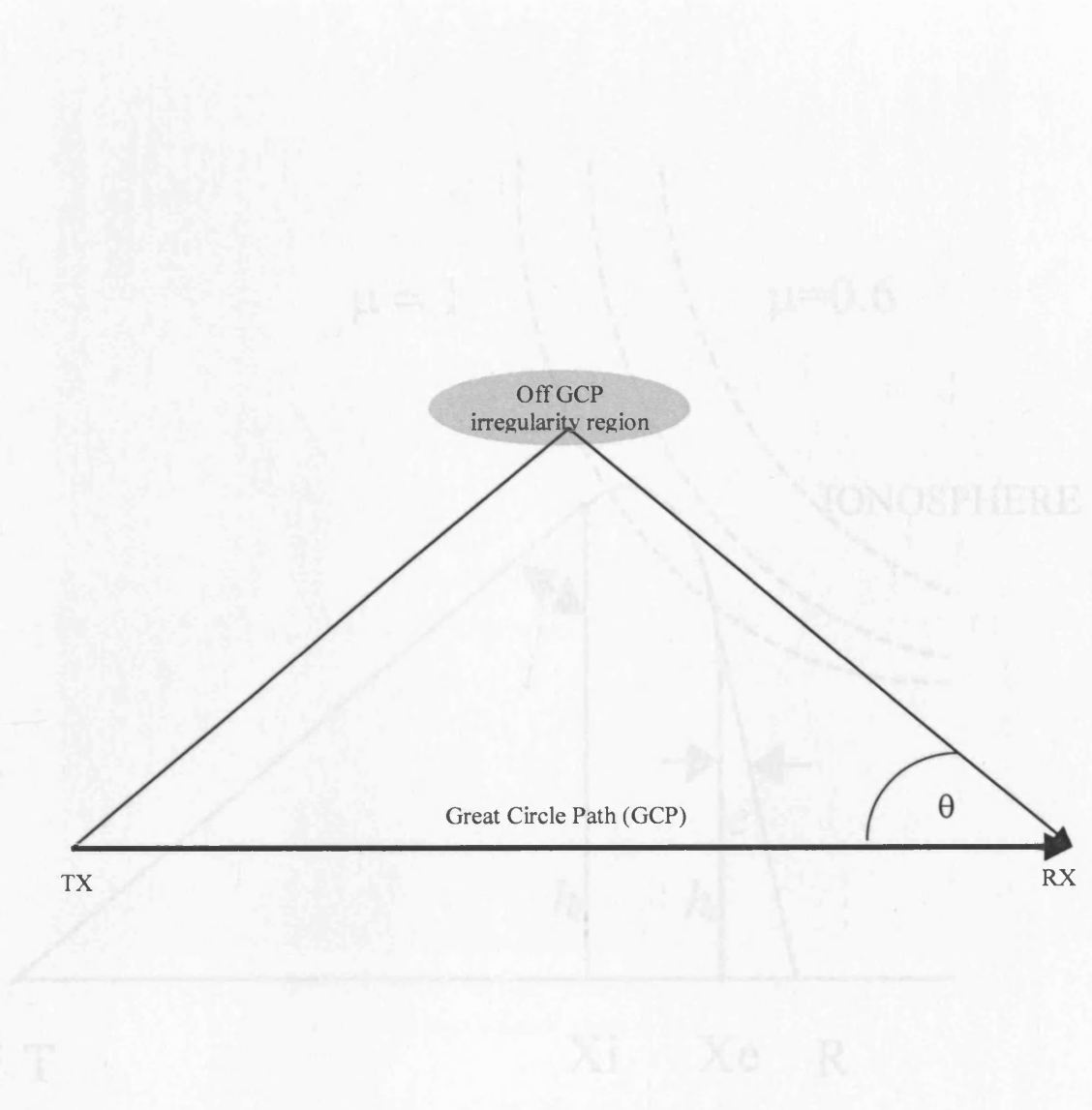


Figure 1.15 The effect of ionospheric gradients on a ray path, the angle of incidence,  $i$ , is different to the angle of exit,  $e$ , and the heights of entry,  $h_e$ , and exit,  $h_x$ , are different (from an original by Davies [1990])

Figure 1.14 Off Great Circle propagation via an irregularity region.

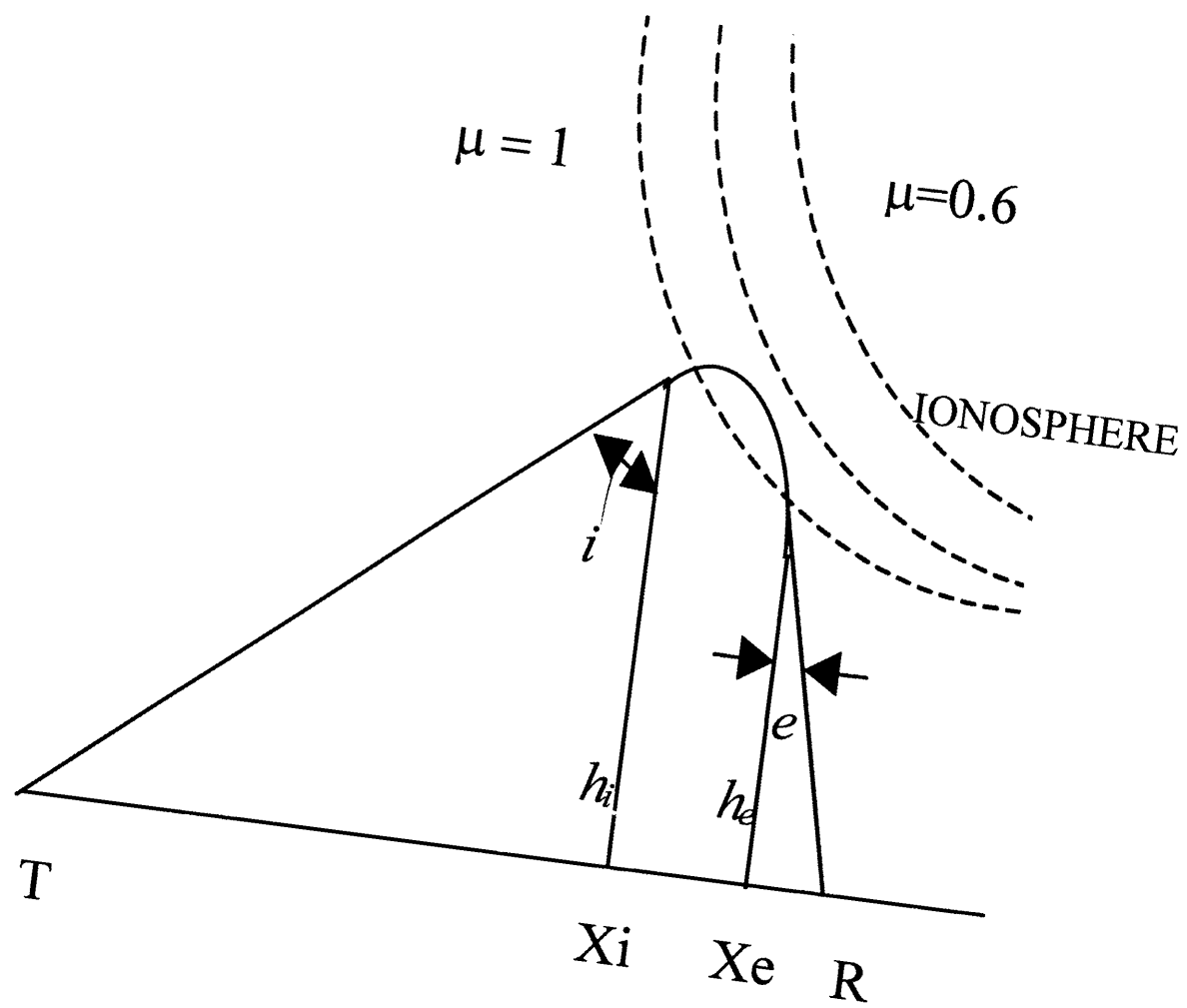


Figure 1.15 The effect of ionospheric gradients on a ray path, the angle of incidence,  $i$ , is different to the angle of exit,  $e$ , and the heights of entry,  $h_i$ , and exit,  $h_e$ , are different (from an original by *Davies* [1990])

SNR (dB) required for BER =  $10^{-3}$

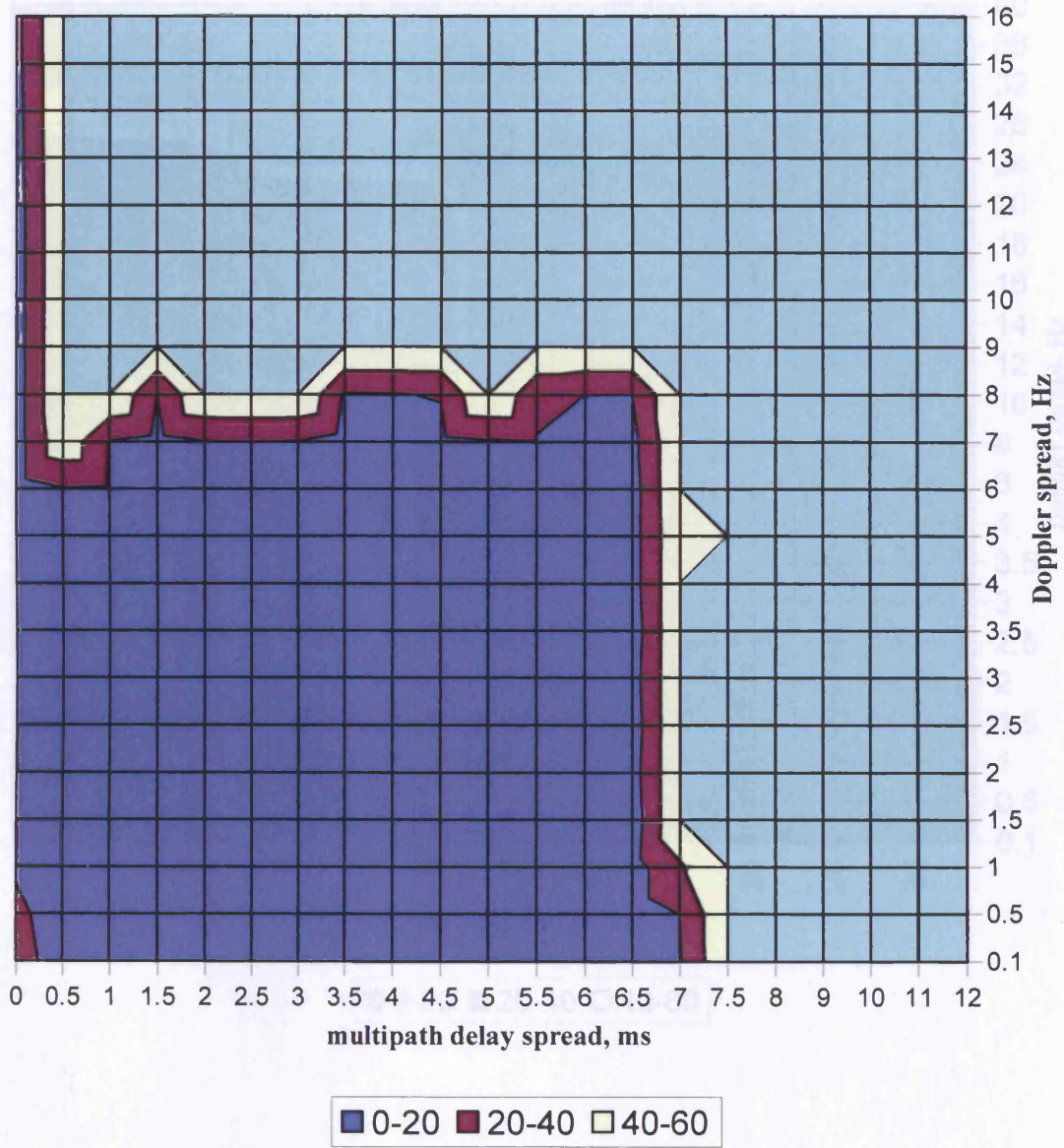
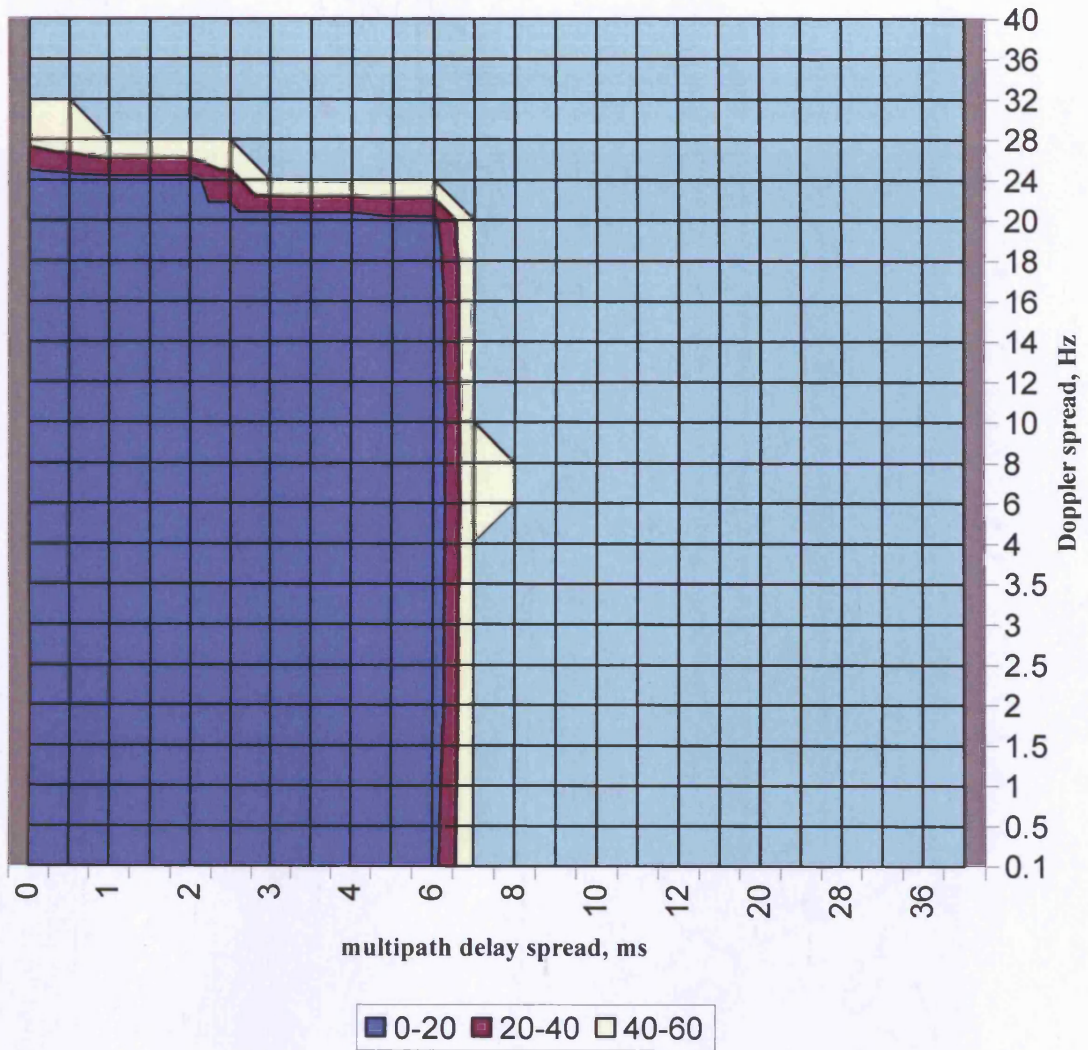


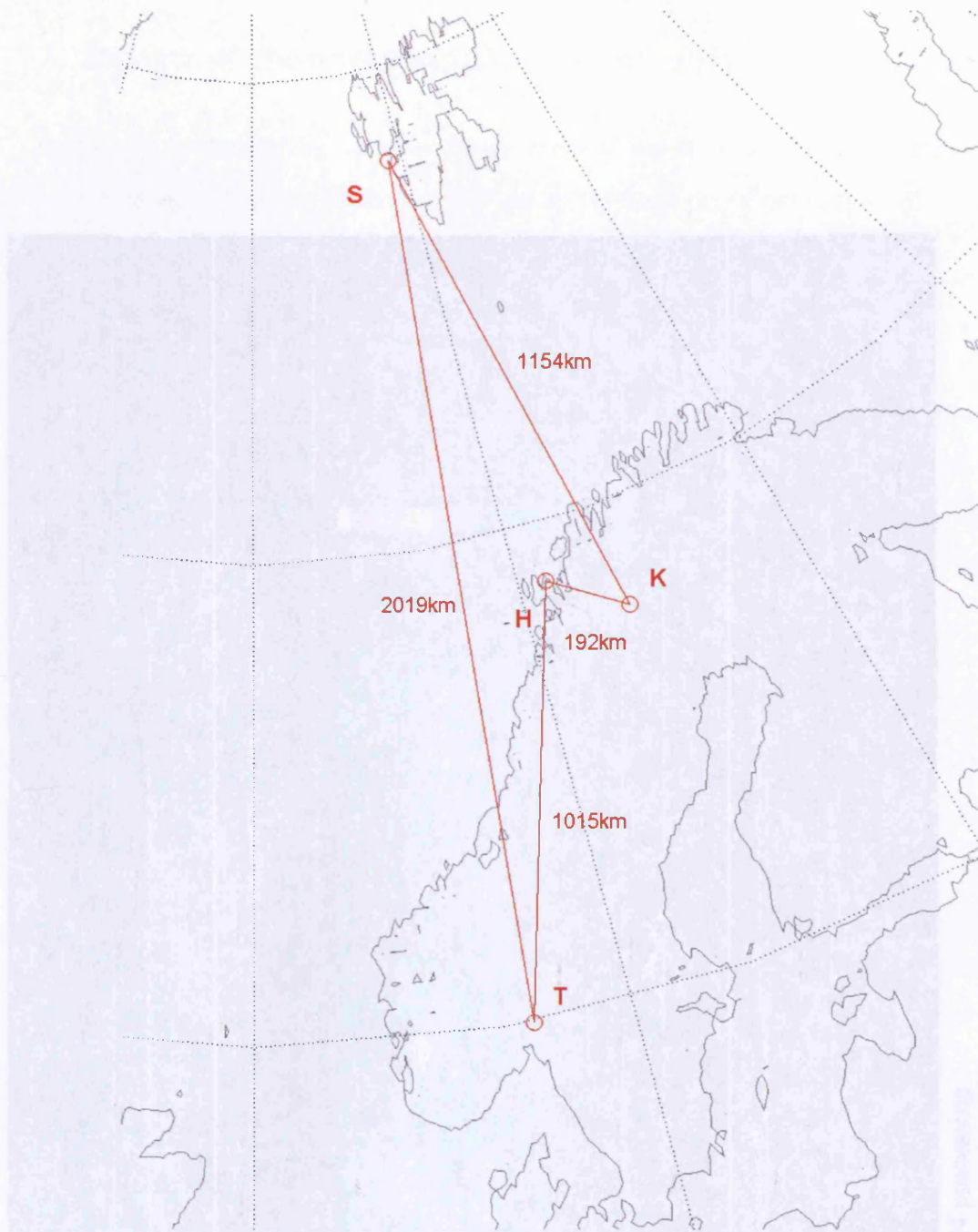
Figure 1.16 Mil-Std-188-110A 1200bps performance surface

SNR (dB) required for BER= 10<sup>-3</sup>



Station	Lat/Long	Altitude	Frequency
Transmitter (Tx)	38° 01' N	12° 47' E	300 Hz
Receiver (Rx)	38° 45' N	16° 30' E	300 Hz
Receiver (Rx)	67° 52' N	28° 15' E	300 Hz
Receiver (Rx)	59° 38' N	11° 55' E	300 Hz

Figure 1.17 Mil-Std-188-110A 300bps performance surface



Location	Identifier	Latitude	Longitude
Svalbard (Tx)	S	78°03' N	13°47' E
Harstad (Tx)	H	68°48' N	16°30' E
Kiruna (Rx)	K	67°52' N	20°15' E
Tuentangen (Rx)	T	59°58' N	11°05' E

Figure 1.18 Map showing the positions of the transmitters and receivers in the DAMSON network and the great circle ground length of each path

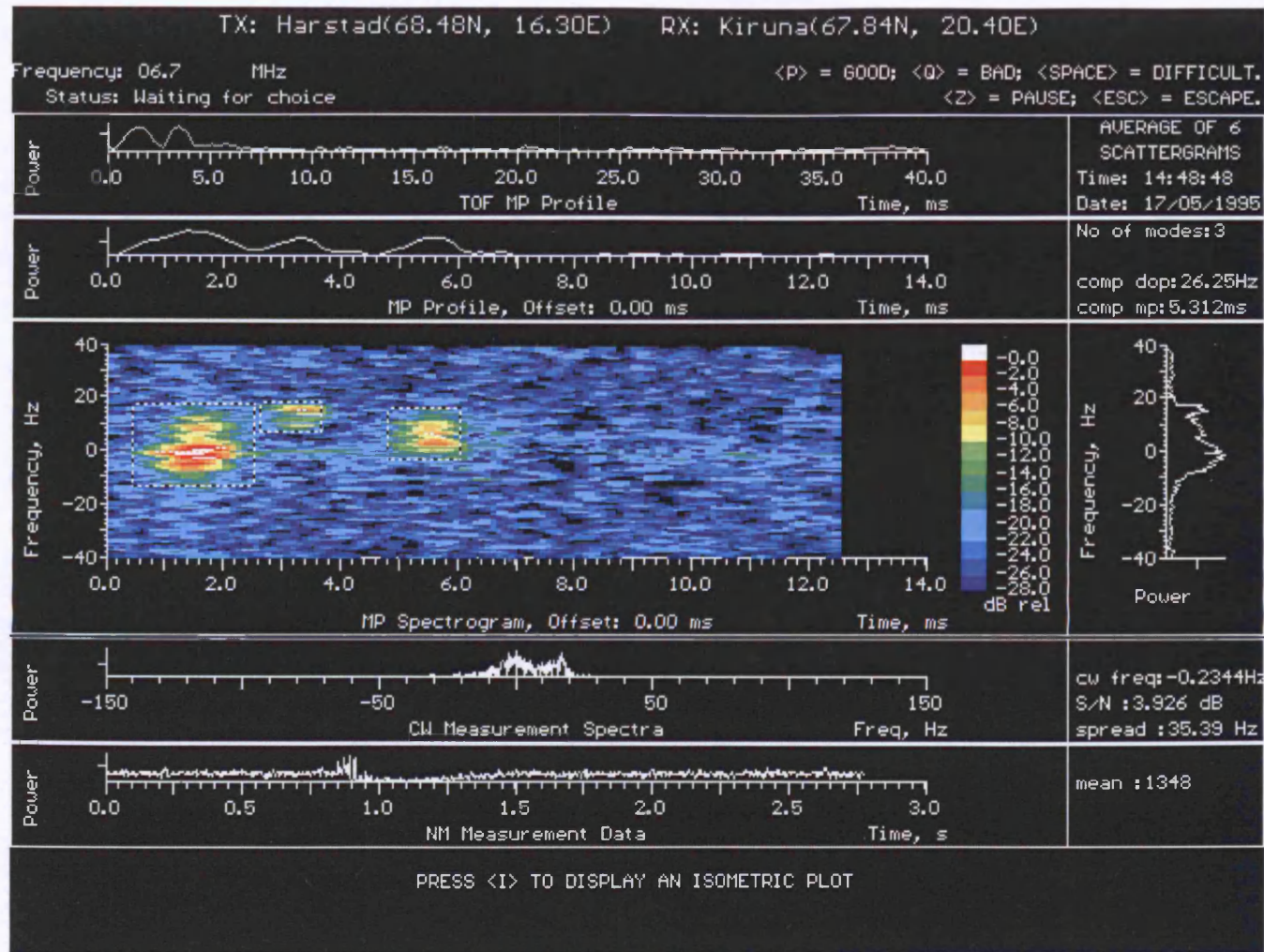


Figure 1.19 Typical results of DAMSON processing

## 2. Review of channel sounding and direction finding studies

Since the investigations in this thesis are concerned with the combined channel sounding and direction finding of HF radio propagation effects observed over high latitude communication paths, each topic is separately reviewed below.

### 2.1 Channel sounding

As described in Chapter 1, a channel sounding system provides the opportunity to determine the channel scattering function, which is a useful diagnostic of the state of a communications channel. Several channel sounding systems have been used to probe the ionosphere, the following discussion highlights two of these systems with an emphasis on the findings over high latitude paths.

#### 2.1.1 *The Naval Research Laboratory's (NRL) HF channel probe*

The NRL HF channel probe is a bistatic, wideband, coherent sounder for measuring the complex pulse response of an ionospheric channel on a number of different frequencies in the HF band. It uses a long bi-phase modulated Pseudo Noise (PN) sequence to modulate a transmitted HF carrier frequency. After detection at a receiving site the signal is cross correlated with a series of delayed replicas of the transmitted sequence, this results in an output signal equivalent to a short pulse sounder. The probe is able to operate at several signal bandwidths between 31.25kHz and 1MHz. The transmitter and receiver are scheduled to synchronously step through a frequency band of interest. Sample rates are selectable and can accommodate a Doppler spread of up to  $\pm 30$ Hz. The channel probe can also be operated as a conventional sounder in order to measure the general condition of the ionosphere.

*Wagner et al.* [1988 and 1989] made measurements, using this system, between October 1985 and July 1986 on a 2300km transauroral path between a transmitter at Frobisher Bay, Canadian Northwest Territories and a receiver site near Rome, New York. They compared these with data collected over mid-latitude paths. During quiet magnetic conditions, when the one-hop path midpoint was to the south of the furthest extent of the auroral oval, the channel behaviour was similar to a mid-latitude path with single specular reflections having narrow Doppler spread, see Figure 2.1(a). At other times,

however, the channel also showed specular multipath behaviour with comparable SNR but broader Doppler spread. At night, when the path midpoint was within the auroral oval, low SNR returns were observed with large Doppler spreads, up to  $\sim 10\text{Hz}$ , consistent with propagation via scattering regions, see Figure 2.1(b). The delay dependent Doppler shifts in the two earliest signal groups of Figure 2.1(b) were attributed to motion of the signal scatterers transverse to the great circle path between transmitter and receiver. Asymmetries in this delay-Doppler characteristic could be explained as reflections from a tilted, drifting irregularity region, however, neither the orientation of the tilt nor the drift direction could be inferred from these measurements.

In 1988 Wagner and his co-workers measured scattering functions on a short high latitude path for a variety of HF channel conditions varying from benign to highly disturbed. The incidence of a large transient fluctuation in the terrestrial magnetic field was highlighted. Figure 2.2 illustrates the ionospheric conditions 2 hours before the magnetic disturbance. At this time there was little Doppler spread but appreciable delay spread. The measurements illustrated in Figure 2.3 represent the ionospheric conditions soon after the magnetic disturbance, they reveal a diffuse scattering function characterised by delay spread of the order 1.5ms and Doppler spread of the order 15Hz. The implications are that the irregularities responsible for the scattered returns are both spatially extensive and drifting at high speed after the magnetic disturbance compared to previously. A selection of these measurements, chosen to illustrate the variability of the auroral radio channel, and their conclusions were presented in *Wagner et al.* [1989 and 1991].

Results from a campaign involving channel probe observations of propagation conditions along a 1294km transauroral path between Sondrestrom, Greenland and Keflavik, Iceland over the period from 13th March to 2nd April, 1992 are described in *Wagner et al.* [1995]. Received signals for this path fell into three groups (1) strong, specularly reflected ionospheric returns characteristic of a daytime ionospheric channel during magnetically quiet conditions; (2) strong specular multipath signals reflected from horizontal gradients of electron density associated with large irregular patches of enhanced electron density and encountered regularly at night; and (3) weak scatter returns from embedded field aligned irregularities, also at night. The multipath and scatter returns both exhibited large delay and Doppler spreads, however, the scatter

returns were usually observed at delays exceeding those expected for one-hop propagation. A simple irregularity drift model produced delay and Doppler shift curves that were consistent with those observed for the scatter component of the received signal, see Figure 2.4, and supports a hypothesis of irregularity drift parallel to the GCP with a velocity of around 1200m/s.

In these studies using the NRL HF channel probe, two different working definitions of a 'channel spread factor' were used. The first definition is the simple product of the delay and Doppler spread factors, where the individual spread factors are defined as twice the standard deviation ( $2\sigma$ ) of the parameter spread about its mean value. The second definition, which may be more representative of channel spread, is defined by the area on the delay-Doppler plane beneath a given fraction (0.75 in *Wagner et al.* [1991]) of the power in the scattering function. In most cases these two definitions provide comparable results.

Although the combined data sets of the campaigns described by Wagner and his co-workers are extensive, it was observed that additional measurements in other seasons and other phases of the solar cycle would be necessary to provide a more comprehensive set.

### 2.1.2 *The DAMSON project*

DAMSON (Doppler and Multipath SOunding Network) has been developed by QinetiQ (formerly the UK Defence Evaluation and Research Agency (DERA)) in collaboration with the Canadian Communications Research Centre, the Norwegian Defence Research Establishment, the Swedish Institute of Space Physics and the Swedish Defence Research Establishment. It is an oblique channel sounding system designed to characterise the disturbed narrow band (3kHz) HF channel by measuring its scattering function. The approach used to measure the scattering function is similar to that of *Wagner et al.* [1988], however the real time nature of the DAMSON processing makes it unique in the frequency range.

The objective of the DAMSON project is to statistically quantify Doppler spreads, Doppler shifts, multipath delay and signal strengths for a number of high latitude paths. In addition, however, the information obtained will be used to assess the effects of high latitude propagation conditions on current and future HF data modem waveforms and

used to specify HF simulator characteristics for more representative testing of communications systems and modems. It may also be possible to incorporate the knowledge base acquired through the experiment into propagation prediction codes.

A summary of the important features of the system are given below while a detailed description can be found in *Davies et al.* [1992] and *Davies and Cannon* [1993].

The system hardware is based on commercially available equipment (such as Personal Computers, DSP interface cards and HF transmitters and receivers). Global Positioning System (GPS) receivers provide accurate system timing to within  $\sim 10\mu\text{s}$  and allow absolute time of flight measurements to be made. Figure 2.5 illustrates the transmitter and receiver equipment configurations.

A variety of pulse compression waveforms are used to measure time of flight, time dispersion, frequency dispersion, signal strength and signal to noise ratio over point to point communications paths. These waveforms are flexibly scheduled for transmission at different times and on a range of frequencies in the HF band between 2MHz and 22MHz. The waveform designed for measuring the scattering function has been denoted the delay-Doppler (DD) waveform, it provides for measurements of multipath spread up to 12.5ms and Doppler spread up to  $\pm 40\text{Hz}$  with a resolution of 0.63Hz.

The majority of DAMSON measurements have been made on high latitude paths between four sites in Scandinavia (*Cannon et al.* [2000]). Transmitters are located at Isfjord Radio Station on Svalbard and at Harstad in Norway while receivers are located at Tuentangen in Norway and Kiruna in Sweden. As illustrated in Figure 1.18 these provide for a range of path lengths between 192km and 2019km with orientations both tangential and parallel to the auroral oval. This system was operated almost continuously between 1995 and 1999 and provided a very large data set of high latitude HF channel characterisations.

Early analysis concentrated on the long Svalbard – Tuentangen path (*Cannon et al.* [1995] and *Angling et al.* [1995(1)]). Example scattergrams were seen to have large Doppler and delay spreads, Figure 2.6. These were identified with propagation due to scattering from drifting irregularities as per *Wagner et al.* [1988] and *Wagner et al.* [1995]. Time sequences were produced which showed marked diurnal variations in Doppler spread, with the maximum spread occurring at night, and a correlation with the

Q activity index. It was also found that, for sounding frequencies up to approximately 15MHz, Doppler spread decreased with sounding frequency rather than increasing as predicted by the Doppler equation, this is illustrated in the upper panels of Figure 2.7. The effect was attributed to a change from 1-hop to multi-hop propagation over the path such that one of the multi-hop control points fell within the disturbed auroral ionosphere, the lower panel of Figure 2.7 illustrates the path geometry.

Estimations of the relative stability of the channel over all paths were made and presented in *Willink and Landry [1997]* and *Willink [1997]*. These involved the definition of an *exceedance* function, which was a measure of the continuous amount time, in minutes, a particular parameter (SNR, Doppler spread or delay spread) remained within certain bounds in the measured data. Plots of *exceedance* functions are presented in Figure 2.8. It was found that SNR varied much more rapidly than the other parameters and would probably be the limiting factor in choosing a time between channel probes for a communications network. While all paths varied more rapidly during the night and had reduced *exceedance* at higher frequencies, the Harstad – Kiruna path was the most variable of all. In *Willink [1997]* and *Willink et al. [1999]* the need for robust waveforms was recognised. Values of the SNR and spread parameters beyond which a non-robust waveform will typically fail were used to estimate the proportion of the time a robust waveform would be required. It was concluded that in order to maintain 95% availability over these paths, the robust waveform should be designed to handle multipath spreads up to 12ms and Doppler spreads in excess of 40Hz.

In work described in *Angling et al. [1997]* and *Angling and Davies [1999]*, estimations of the availability of high data rate HF modems such as Mil-Std-188-110A 300bps and 1200bps, were made. These were arrived at by comparing data collected over all the DAMSON paths with modem performance results similar to those described in section 1.7 and illustrated in Figure 1.16 and Figure 1.17. It was found that, as expected, the Mil-Std-188-110A 300bps modem had the highest availability, however, over the period of the experiment the overall throughput (i.e. the modem availability multiplied by the data rate) of both the Mil-Std-188-110A 300bps and Mil-Std-188-110A 1200bps modems are very similar. The implication is that this throughput could be maximised if the system were able to adaptively vary the data rate in real time in response to the varying channel conditions.

After making the observation that it is less common for both large delay and Doppler spreads to occur simultaneously than for them to occur separately, see Figure 2.9, *Otnes and Jodalen* [2001] proposed a solution whereby a system can choose from a pool of waveforms at each data rate. The basic waveform in a pool is one of the currently standardised waveforms such as Mil-Std-188-110A. The other waveforms in the pool are designed to have either improved tolerance to delay spreading or improved tolerance to Doppler spreading (but not both at the same time). This is achieved by changing the length and repeat frequency of the regularly inserted channel probe sequences in the waveform. The system must then estimate the delay and Doppler channel conditions and select the best waveform for these conditions. DAMSON data from both the Harstad – Kiruna path and the Svalbard – Tuentangen path were used to analyse the increase in availability using such schemes. The increase in availability was found to be generally small, with the Harstad – Kiruna path demonstrating better improvements at both data rates than the Svalbard – Tuentangen path. The improvements were generally better at night than during the day. It was observed that increasing the number of available waveforms in a pool from 1 to 3 resulted in some improvements, however it was found that there was little to be gained by increasing the number of waveforms further up towards  $\infty$ . Similar work, examining the effect on availability of improved waveform tolerance to low SNR, is presented in *Otnes* [2001(1)&(2)]. It was concluded that when the availability is low, there is generally more to gain from improving the SNR tolerance than from improving the delay spread or Doppler spread tolerance.

Recently DAMSON has been upgraded to 12kHz bandwidth with new DSP boards and software. Complex uniform Barker-25 is used as the pulse compression code (*Jodalen et al.* [2000]). This system has been operating simultaneously over the Harstad – Kiruna path and a shorter (90km) Harstad – Abisko path, both of which can be considered NVIS (Near Vertical Incidence Skywave) paths. Comparison of the channel parameters over both paths reveals that the channels are very similar, as indicated in Figure 2.10. The lower panel of Figure 2.10 reveals that at times around geomagnetic midnight there exists a strong auroral E-layer giving good availability of signals but with low SNR. Another experiment utilising the new 12kHz bandwidth DAMSON over the path Harstad – Tuentangen is described in *Smith et al.* [2001]. Simultaneous measurements are made at different non-contiguous frequencies in order to aid the design of effective

multi-carrier modems and simulators. Unfortunately the 12kHz data set was prone to strong interference for long periods of the day so analysis was concentrated on a limited set of 3kHz bandwidth measurements and the reaction of the channel to sunrise. Scattering functions for two simultaneous measurements at frequencies separated by 219kHz are presented in Figure 2.11. It was found that the Doppler spreads measured at different carrier frequencies over approximately 0.5MHz were well correlated. Further investigations, however, are required to determine whether this result is applicable to other forms of ionospheric disturbance.

## 2.2 Direction finding

Direction finding (DF) systems are used to determine the Direction of Arrival (DOA) of incoming signals, they generally employ arrays of antennas where measurements of the phase and amplitude of the incoming signals are made at each antenna.

When an array is illuminated by an incoming wavefront from a particular direction, there is a characteristic phase relationship between the signals received at each antenna. If a combination of phases are added to the signals received at each antenna in such a way that when the resulting signals are combined they are in phase, then the array will be particularly sensitive to signals arriving from this direction. It can be said that a sensitivity 'beam' has been steered in that direction. The width of this beam depends largely on the dimensions and geometry of the array. Most common HF arrays are classed as 'Wide Aperture Direction Finders' (WADF), see *British Standard 204* [1960], and extend over a distance comparable to or greater than one wavelength. This is important when attempting to resolve the direction of arrival of more than one signal. If the signals are arriving from directions within one beam width of each other then they cannot be resolved.

Super-directivity has been defined (*IEEE standard* [1969]) as 'The directivity of an antenna when its value exceeds the value which could be expected from the antenna on the basis of its dimensions and the excitation that would have yielded in-phase addition in the direction of maximum radiation intensity'. This can also apply to antenna arrays where the processing of the signals at each antenna makes it possible to resolve multiple closely spaced signal DOA, even when the physical dimensions of the array appear to be insufficient, by using super-directivity or super resolution techniques.

The resolution of multiple signal DOAs has been an active area of research in HF DF for a number of years, *Gething* [1991] provides a good survey of some of this work as does *Johnson and Miner* [1986]. In recent years, the development of high speed digital signal processing has allowed the design and implementation of operational real time super resolution direction finding (SRDF) systems. One particularly successful implementation, employing the 'classic' SRDF algorithm called MUSIC, is described in *Tarran* [1997]

Limitations in the performance of MUSIC at HF, however, has lead to a lot of work being carried out investigating alternative super resolution direction finding algorithms. A number of papers, by authors including *Strangeways*, *Zatman*, *Featherstone* and *Warrington*, are included in the references section at the end of this thesis. In particular the Iterative Null Steering (INS) algorithm, which is based on the IMP (*Brandwood* [1994]) and DOSE (*Zatman et al.* [1993]) algorithms, performs well at resolving multiple DOA without *a priori* knowledge of the number of expected DOA and has been found to be particularly robust when used at HF. On a typical wide aperture DF array INS is capable of resolving multiple directions of arrival and provides the DOA (to within  $\sim 1^\circ$ ) of at least the strongest two (primary and secondary) incoming signals.

The detailed operation and performance of the INS algorithm is not discussed here. An in depth description of the algorithm and performance comparisons of INS with MUSIC, have been carried out by *Warrington* [1995(2)].

### 2.2.1 *Experimental direction finding studies*

A number of experimental direction finding studies have been carried out by members of the Radio Systems Laboratory at the University of Leicester. The following is a brief review of some of these studies. The purpose of the experiments is to attempt to gain an understanding of ionospheric radiowave propagation in terms of its effect on the spatial distribution of signals arriving at the receiver and the physical processes which occur to cause these distributions.

In November 1990 DF investigations (described in *Jones and Warrington* [1992] and *Warrington and Jones* [1993]) over high latitude paths in Northern Canada were carried out including long transauroral paths and two short paths (one contained entirely within the polar cap). Two types of DF instrument were used, a wide aperture goniometric

system and an interferometric system, neither of which employ super resolution techniques. On geomagnetically quiet days the measured directions of arrival were close to the GCP direction of the transmitter, however, on more active days large deviations from the GCP direction were observed. On the mid-latitude short path these deviations were always seen to the North of the path while for the polar cap path, large swings in the bearing ( $>\pm 50^\circ$ ) were seen and the direction of change of the bearing was reversed in the afternoon compared to the morning, this is illustrated in Figure 2.12. It is suggested that these large bearing errors are the result of reflections from large blobs of over-dense plasma convecting across the polar cap. The reversal in the direction of the swings on the polar path are accounted for by the rotation of the earth under the convection flows changing the orientation of the path with respect to the flow patterns, also illustrated in Figure 2.12. This topic was revisited in detail by *Warrington et al.* [1997(2)].

A series of experiments was carried out in 1991 and 1992 where the direction of arrival of oblique chirp sounder signals was measured (*Warrington et al.* [1992 and 1993]) for two long transauroral paths. Deviations from the GCP direction in the measured bearing up to  $\sim 20^\circ$  were found to be associated with a spread nose extension in the oblique ionogram traces at propagation above the conventional MUF, see Figure 2.13, with the largest deviations occurring at the highest operating frequency. It was concluded that these effects were produced by reflection from ionospheric tilts and gradients, which produce a propagation path longer than the direct GCP. The bearing deviations throughout the experiment were consistent with such tilts being present in the auroral zone region through which the signals propagated.

In 1994, measurements of the amplitude and phase of ionospherically propagated HF radio signals, transmitted from a number of European broadcast transmitters, were received over an array of spaced antennas in the UK. These measurements were used to estimate the directions of arrival of the radio signals through the use of two separate super resolution direction finding algorithms, MUSIC (*Schmidt* [1986]) and the iterative null steering (INS) algorithm. The details of these experiments are described in *Warrington* [1995(1)] and a detailed description of both the INS and MUSIC algorithms is included in *Warrington et al.* [1995(2)]. It was concluded that the iterative null steering algorithm was significantly better at resolving the various propagation modes than MUSIC particularly in the cases when the number of modes is unknown and/or for

short signal analysis periods, Figure 2.14. A similar study, using a modified null steering algorithm resulting in smoother time history traces, is related in *Moyle and Warrington* [1997].

Observations of signals propagated over two paths which lie tangential to, and equatorward of, the auroral oval indicate that propagation occurs at times outside those predicted by computer based, long term, HF prediction models. Direction of arrival measurements on these signals, collected between December 1993 and March 1994, were made using a goniometric DF system. These measurements, described, amongst others, in *Warrington et al.* [1996] and *Rogers et al.* [1997], show large off GCP bearings at the times when the models predict no propagation and GCP bearings during the predicted propagation times, Figure 2.15. These off GCP signals are thought to have reflected from electron density gradients associated with the mid latitude trough, whose existence, extent and intensity is dependent on several factors including the time of day, the condition of the IMF and geomagnetic activity. Bearing swings were also noticed at dawn and dusk, this was associated with the conventional models of the ionosphere, which indicate that the electron density is always greatest to the south of the path at these times. Prediction models often employ numerical maps of the ionosphere based on vertical soundings and it is assumed that the signals are propagated via great circle paths between the transmitter and receiver. It was suggested that prediction models could be modified to incorporate this information and hence provide improved prediction.

A ray tracing simulation to investigate this off great circle propagation in the presence of the mid-latitude trough was carried out by *Stocker et al.* [2000]. In this investigation two propagation mechanisms were studied. It was found that results obtained from non-specular sea scatter at locations to the south of the trough appeared to give a better agreement with the experimental observations than reflections from the trough wall itself, Figure 2.16.

It is clear from the results of the experimental studies that significant off great circle propagation can occur over high latitude paths. Furthermore these large bearing deviations can be the result of a variety of physical propagation processes including reflection and scattering from convecting blobs across the polar cap, auroral tilts, the walls of the mid latitude trough, day/night terminator effects and non specular sea

scatter. Although an understanding of these physical processes was gained, the effect of the processes on a potential communications link was not addressed.

### **2.3 DAMSON DF**

The combination of a channel sounder and a DF system is a powerful tool in the analysis of HF propagation and its effect on the received signal. The spatial distribution of signal energy and the relationship to its delay-Doppler characteristics is of particular interest. The following describes some of the work to date on DF measurements associated with DAMSON soundings of the ionosphere.

In 1995 direction of arrival estimates of the components of DAMSON pulse compression sounder signals transmitted from Svalbard, were calculated from measurements made on a multi-channel receiver system in southern England (*Warrington* [1996(1) and 1997]) using the iterative null steering SRDF algorithm. Some large Doppler spreads were observed along with a variation in the bearing with Doppler frequency. Although the midpoint of this long path should be well south of the furthest extent of the auroral oval, these bearing trends were attributed to reflections from drifting ionospheric irregularities. Figure 2.17 is an example of this behaviour, at a sounding frequency of 14.4MHz, with an accompanying schematic illustrating the geometry leading to the Doppler spreading. The sense of the Doppler shifts are in agreement with supporting evidence, obtained from CUTLASS HF backscatter radar measurements made at the same time, indicating the presence of drifting irregularities at similar latitudes to the path midpoint. The magnitude of the Doppler shifts, however, are larger than anticipated from the CUTLASS measurements of flow velocity.

Similar investigations were carried out on data collected in 1996 at Alert in the Canadian North West Territories (*Warrington and Jackson* [1997]), with largely similar conclusions. Spreads in bearing up to  $\sim 35^\circ$  were observed on these measurements and a change in the angular spread of incoming signals was also seen when propagation changed from 2- to 1-hop as the transmission frequencies increased.

Frequency	Mean	Standard deviation
2.8 MHz	64.7°	26.4°
4.0 MHz	67.7°	34.7°
4.7 MHz	67.0°	32.7°
6.8 MHz	74.7°	1.1°
9.0 MHz	69.8°	2.2°
11.2 MHz	71.2°	0.1°

Table 2.1 Variation of the mean and standard deviation of the angular power distribution with sounding frequency. 01:46 UT, 22 January 1996

These two sets of measurements are re-visited in detail in *Warrington* [1998].

Some results from the DAMSON DF measurement campaign conducted in March 1998, over two paths between Svalbard – Kiruna and Harstad – Kiruna using a six channel receiving system are presented in *Warrington et al.* [2000(1)]. Continuing investigations into this data set are the subject of Chapters 4 and 5 of this thesis.

Most recently it has been suggested that it may be possible to combine received signals in simple two or three element receiving arrays in such a way as to steer beams or nulls in the array directional sensitivity pattern to enhance selected signal components or remove others, in order to improve the spread characteristics of the signal presented to a communications modem. Investigations into this, using the existing DAMSON DF data set collected at Kiruna, are the subject of Chapter 6 of this thesis and two published papers (*Warrington et al.* [2000(2) and 2001]).

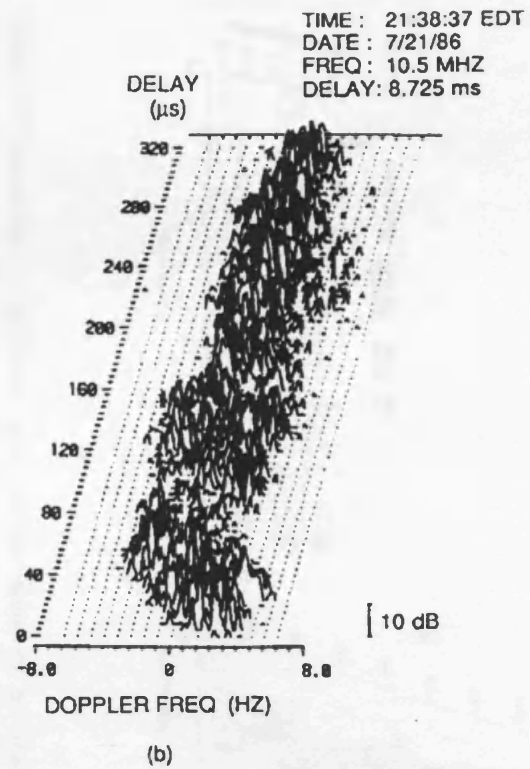
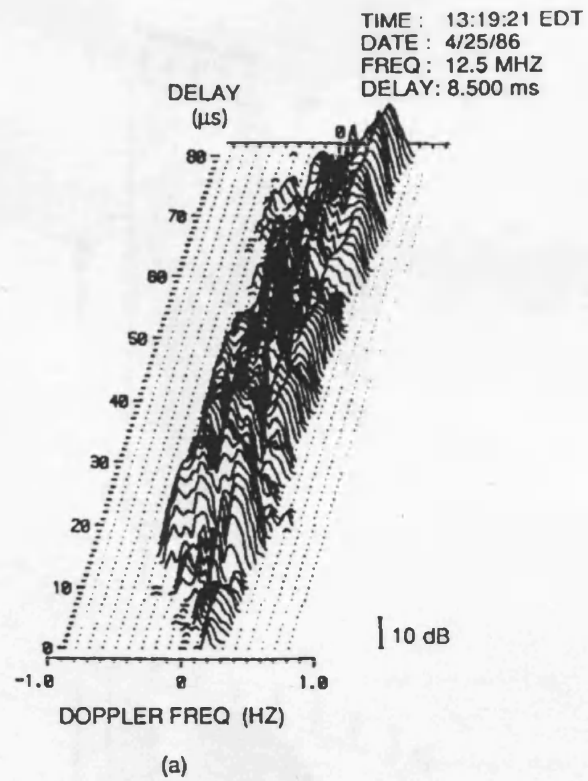


Figure 2.1 Scattering function diagrams for a long transauroral channel. (a) midday 1F2 mode during quiet magnetic conditions; (b) nighttime 1F2 return during moderately disturbed conditions. *Wagner et al.* [1989].

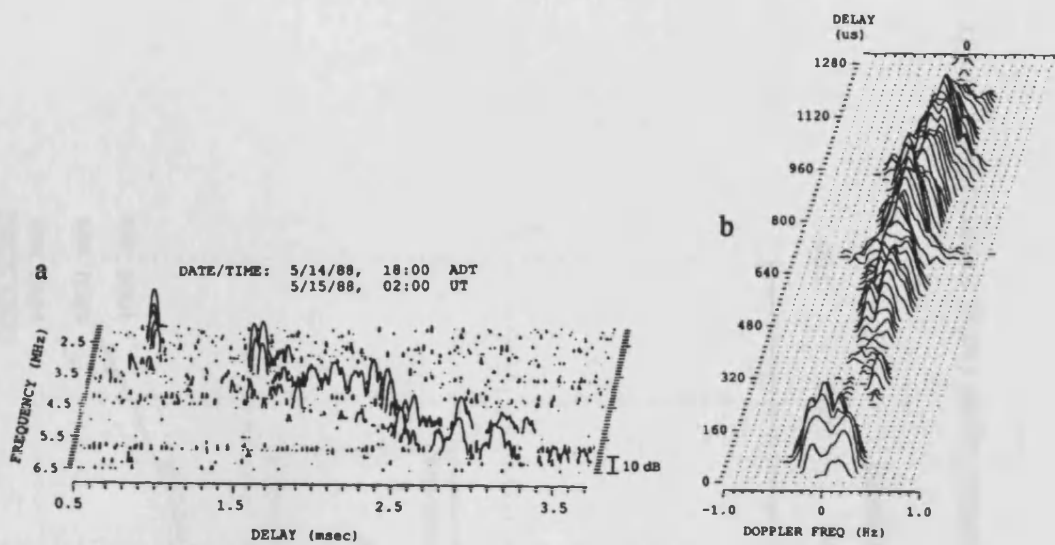


Figure 2.2 Ionospheric conditions prior to the onset of an isolated magnetic disturbance. (a) Ionogram; (b) scattering function measured at 5.3MHz. *Wagner et al.* [1991]

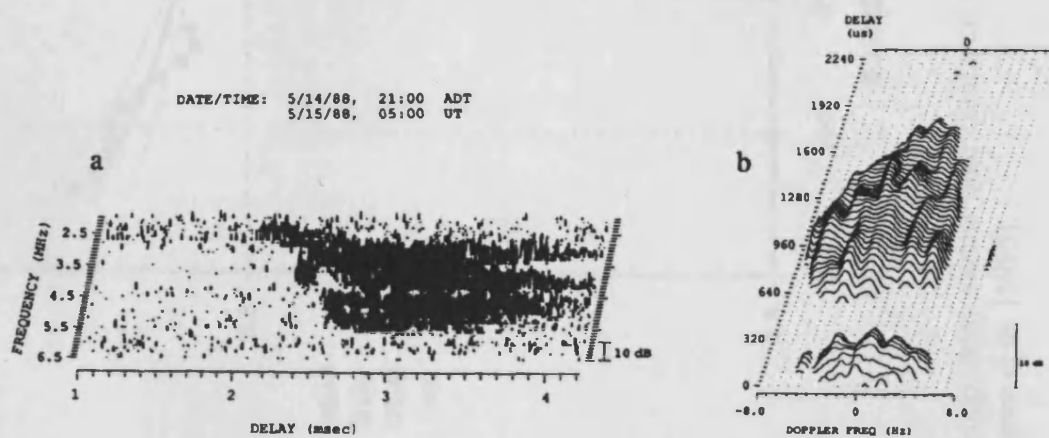


Figure 2.3 Ionospheric conditions soon after the peak of the isolated magnetic disturbance. (a) Ionogram; (b) scattering function measured at 3.8MHz. *Wagner et al.* [1991]

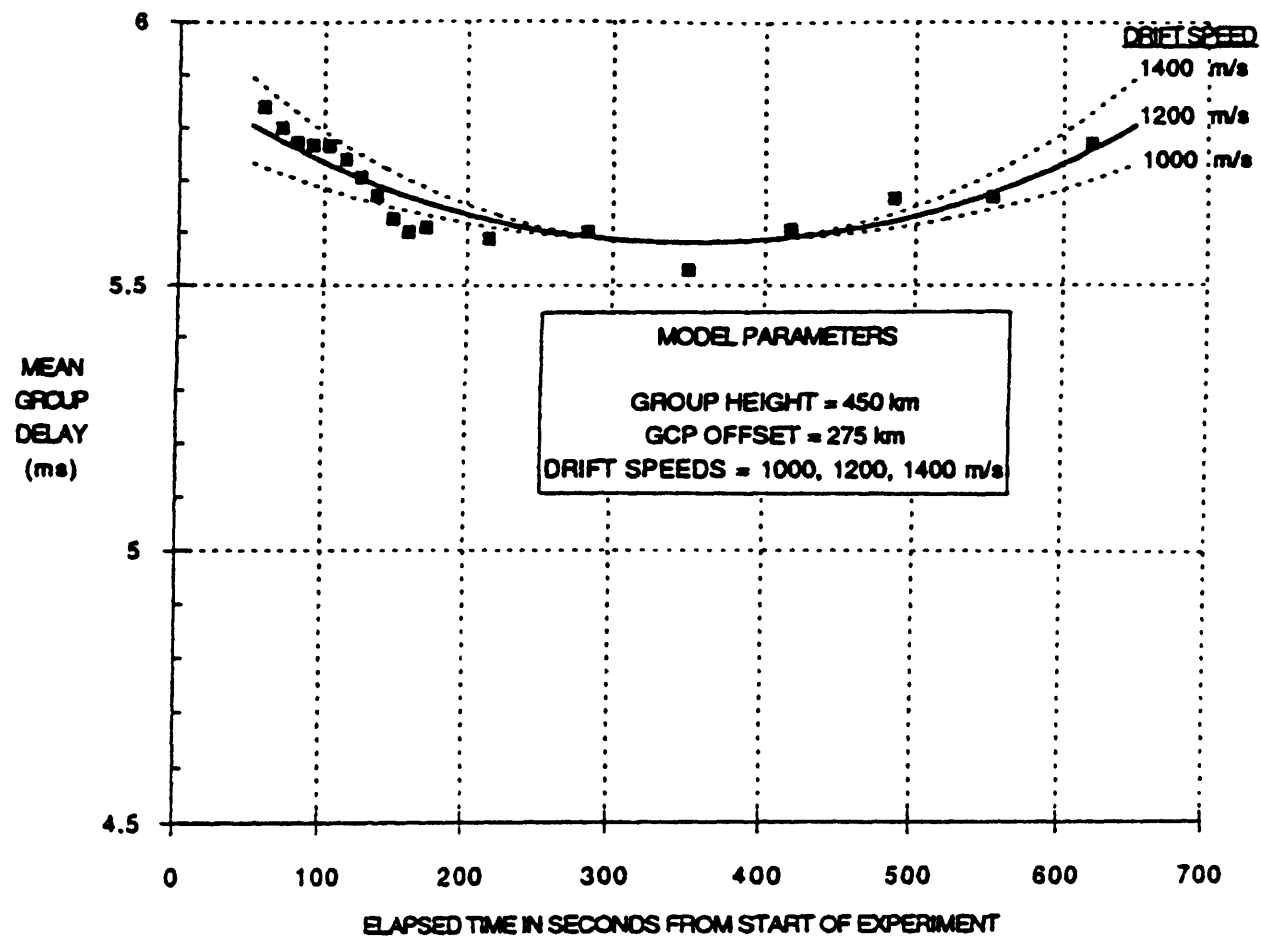
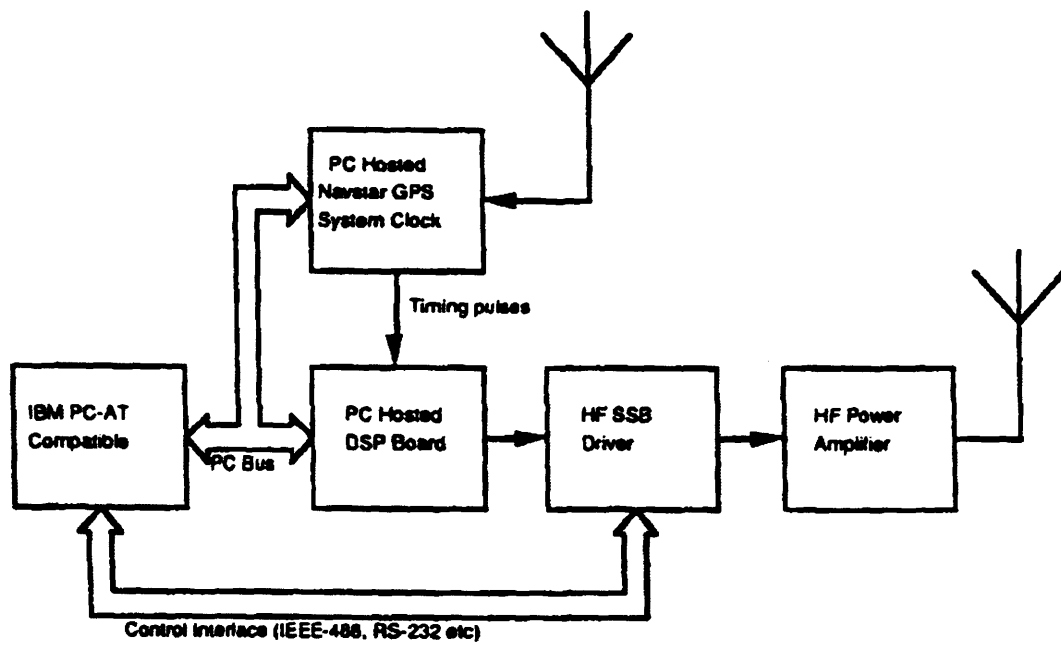
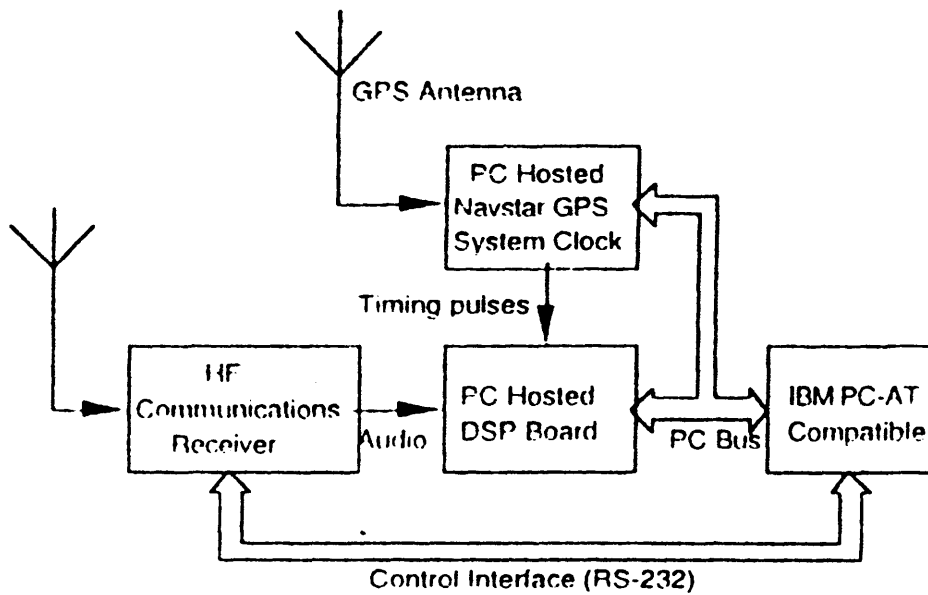


Figure 2.4 Modelled group delay versus time compared with observed mean delay of the scatter signal (solid squares) for 7.7MHz NRL HF channel soundings. *Wagner et al.* [1995].



(a)



(b)

Figure 2.5 Configuration of DAMSON (a) Transmit and (b) Receive Sub-systems. Davies and Cannon [1993].

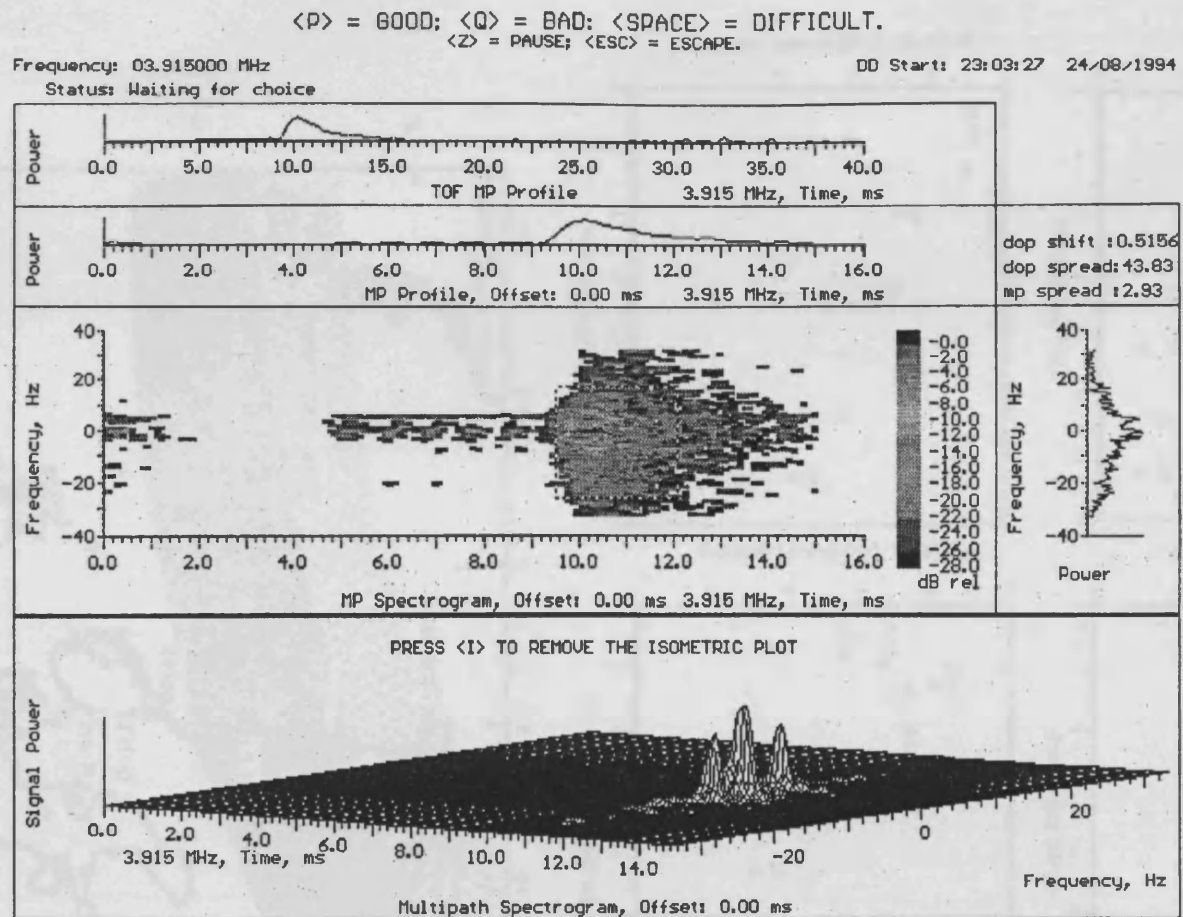


Figure 2.6 Example DAMSON scattergram having large delay and Doppler spread. Svalbard – Tuentangen. Cannon et al. [1995].

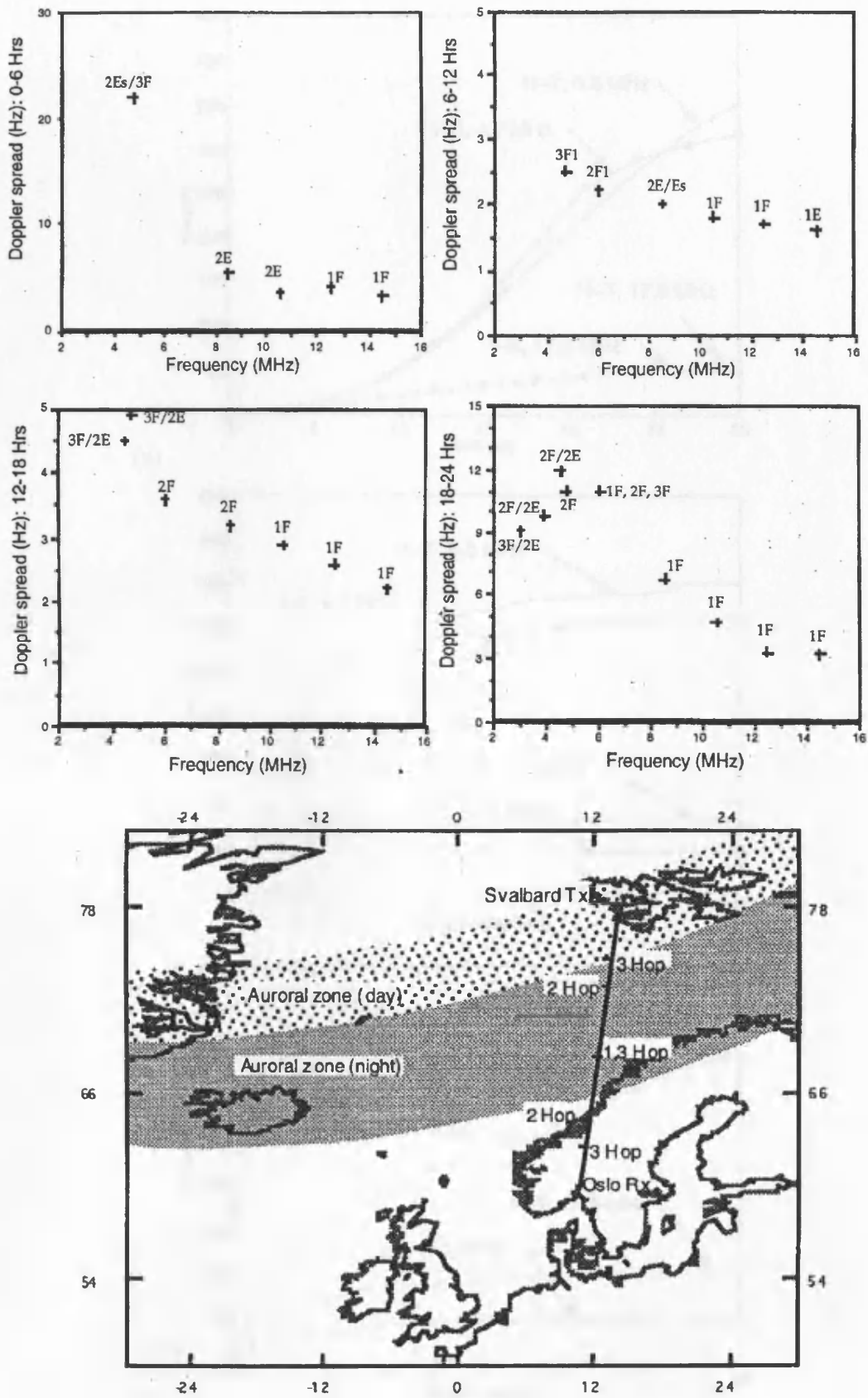


Figure 2.7 Upper panels - Doppler spread vs. Frequency for each quarter of the day with the most likely mode labelled. Lower panel - Path geometry and approximate positions of day and night auroral oval zone ( $k_p=2$ ). Cannon *et al.* [1995]

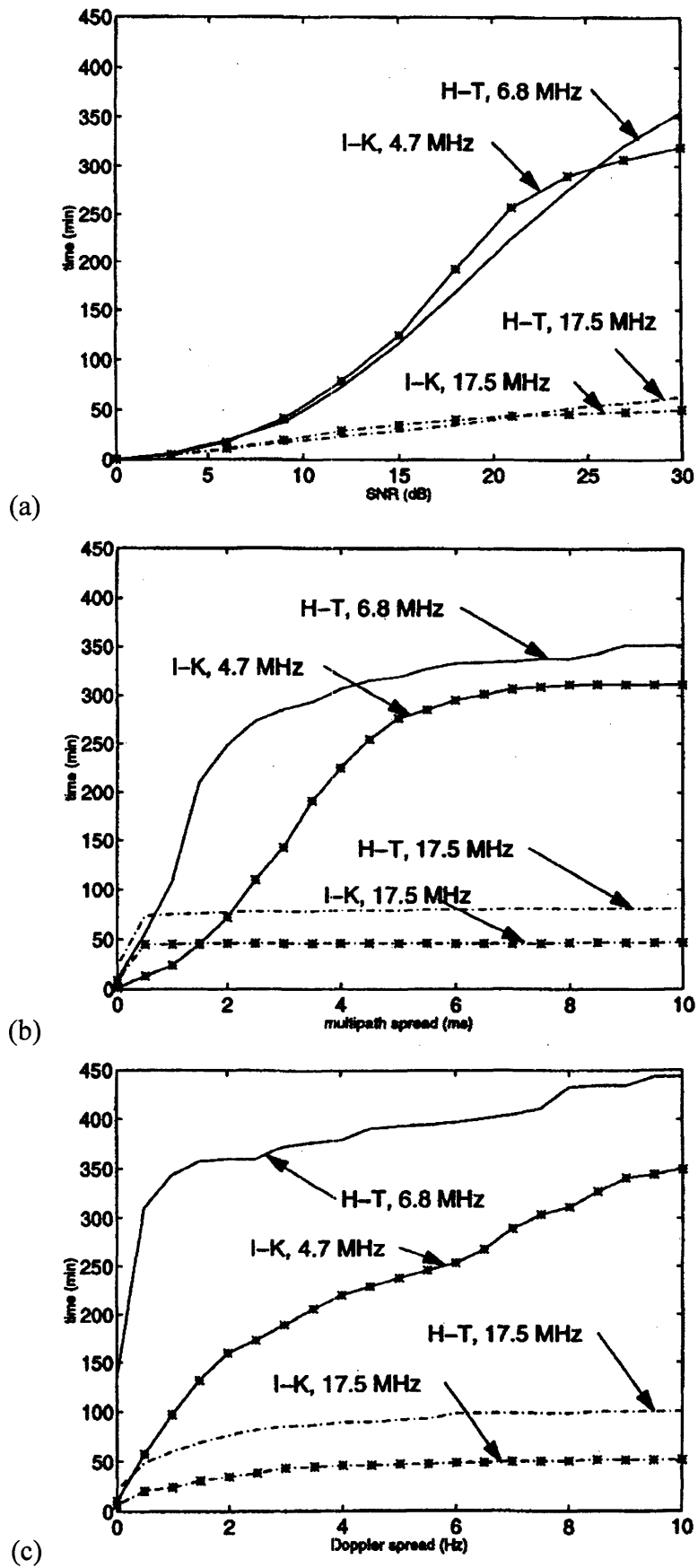


Figure 2.8 Exceedance functions for (a) SNR (b) multipath spread (c) Doppler spread, *Willink* [1997].

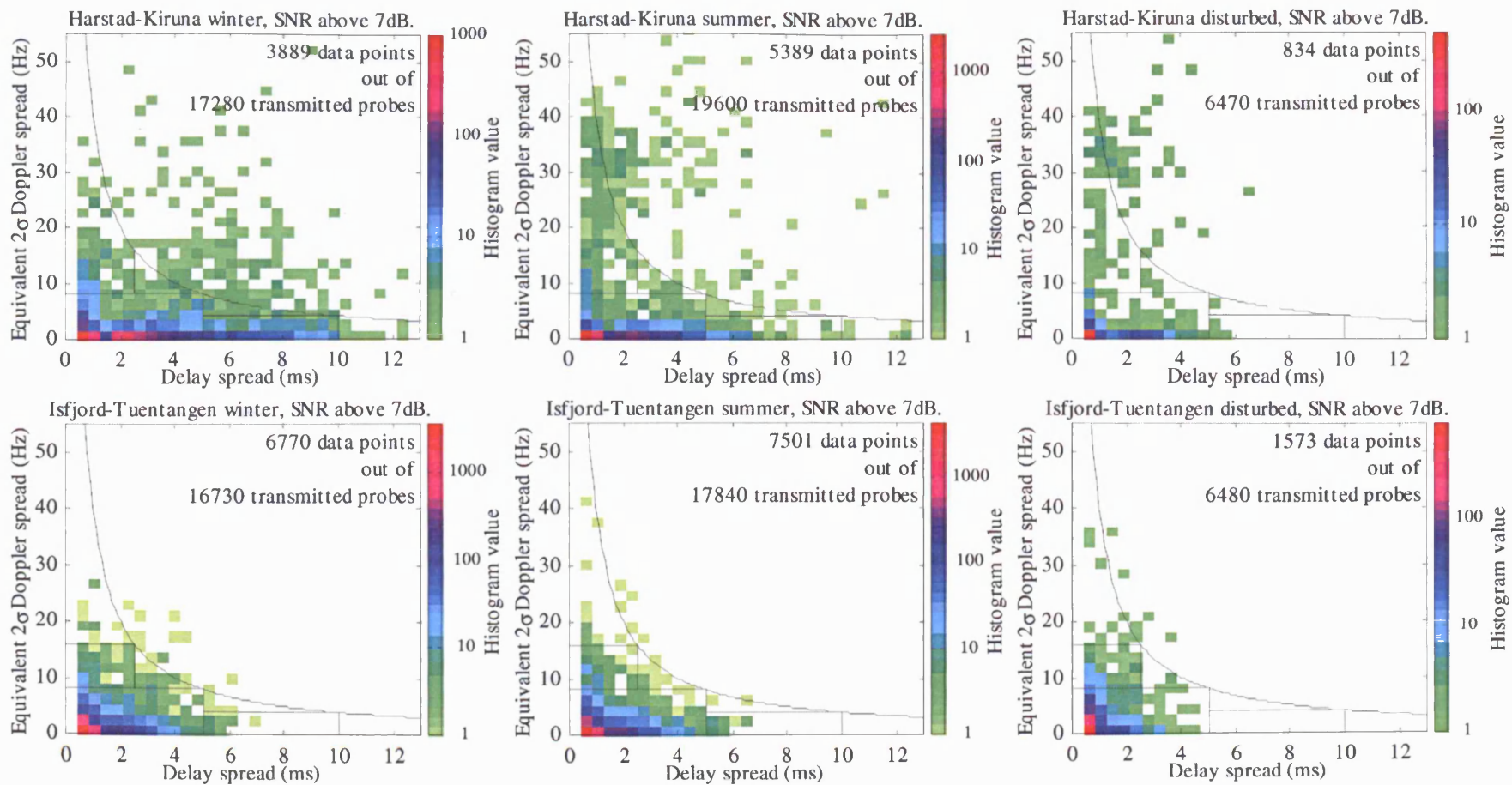


Figure 2.9 Two dimensional histograms showing the simultaneous distribution of multipath and Doppler spread (all 10 DAMSON frequencies are included). The rectangles illustrate the availability of the three alternative 1200bps waveforms. *Otnes and Jodalen [2001]*.

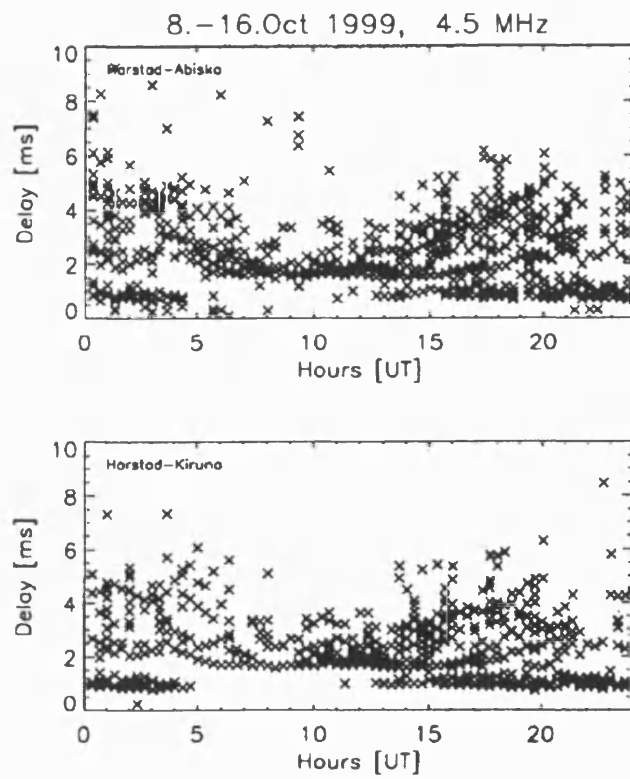
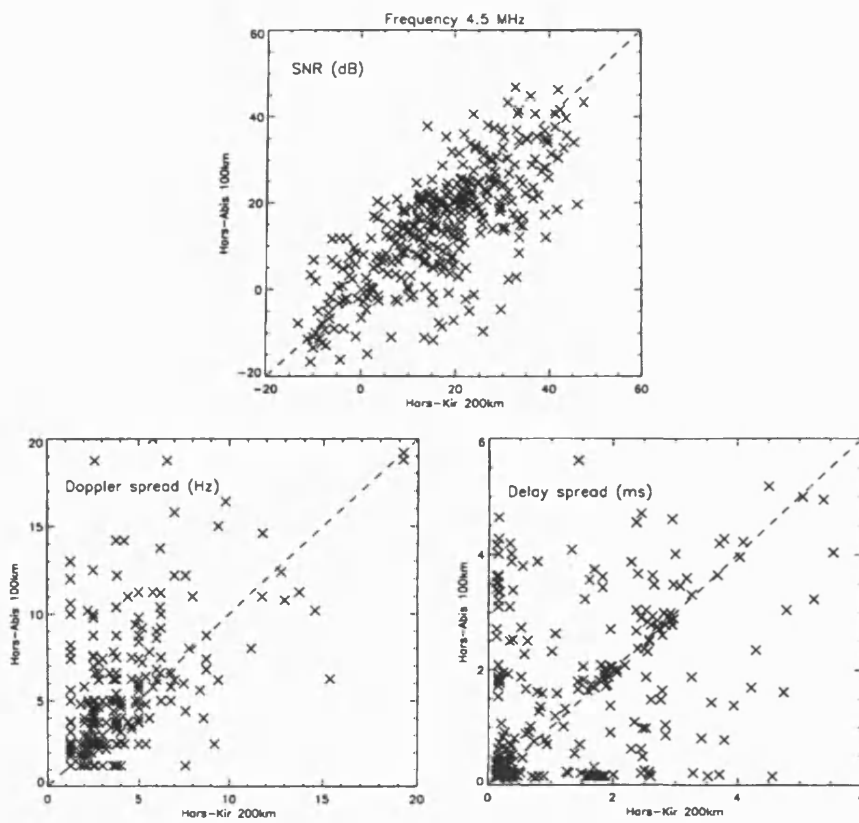


Figure 2.10 Simultaneous measurements over the Harstad – Abisko and Harstad – Kiruna paths at 4.5MHz. *Jodalen et al. [2000]*.

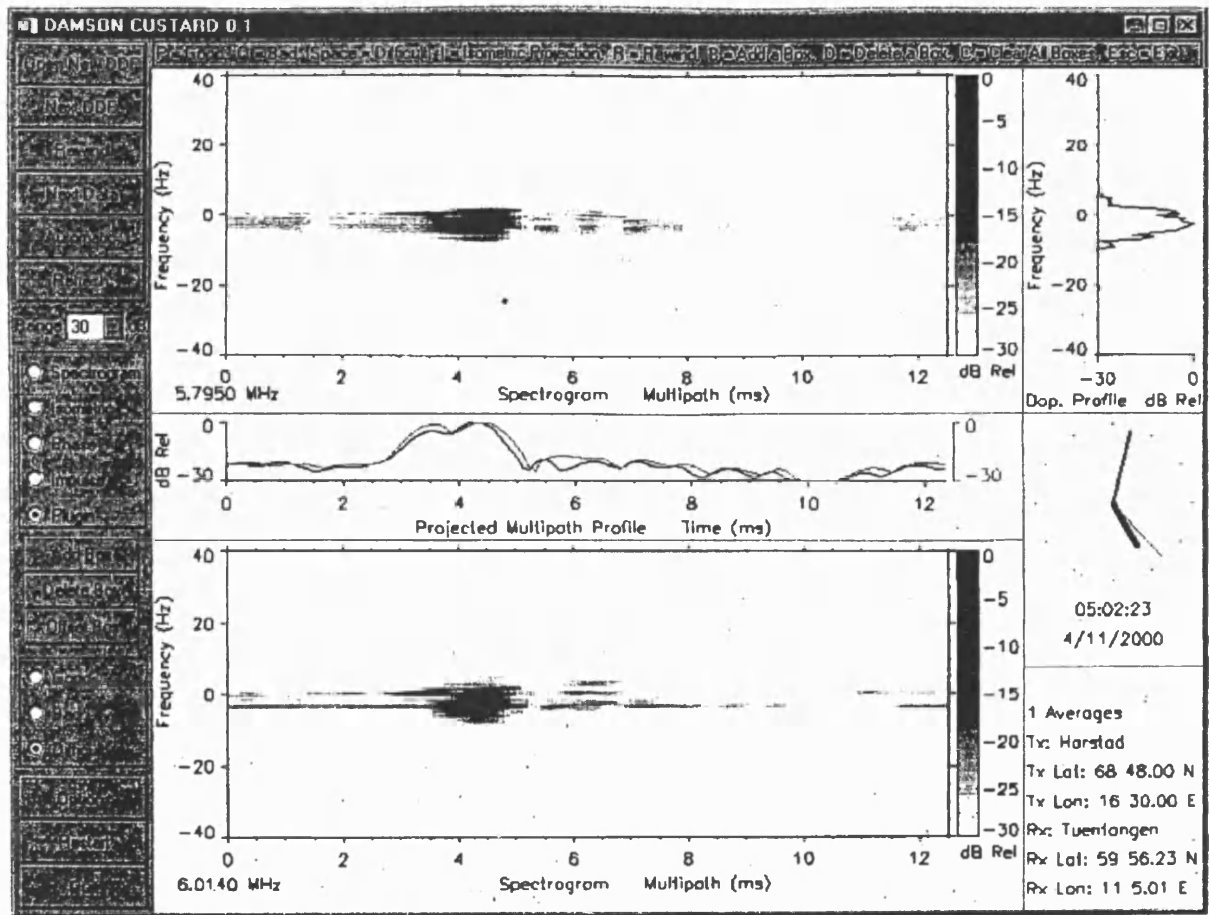


Figure 2.11 Scattering functions for two simultaneous 3kHz measurements at frequencies separated by 219kHz. *Smith et al.* [2001].

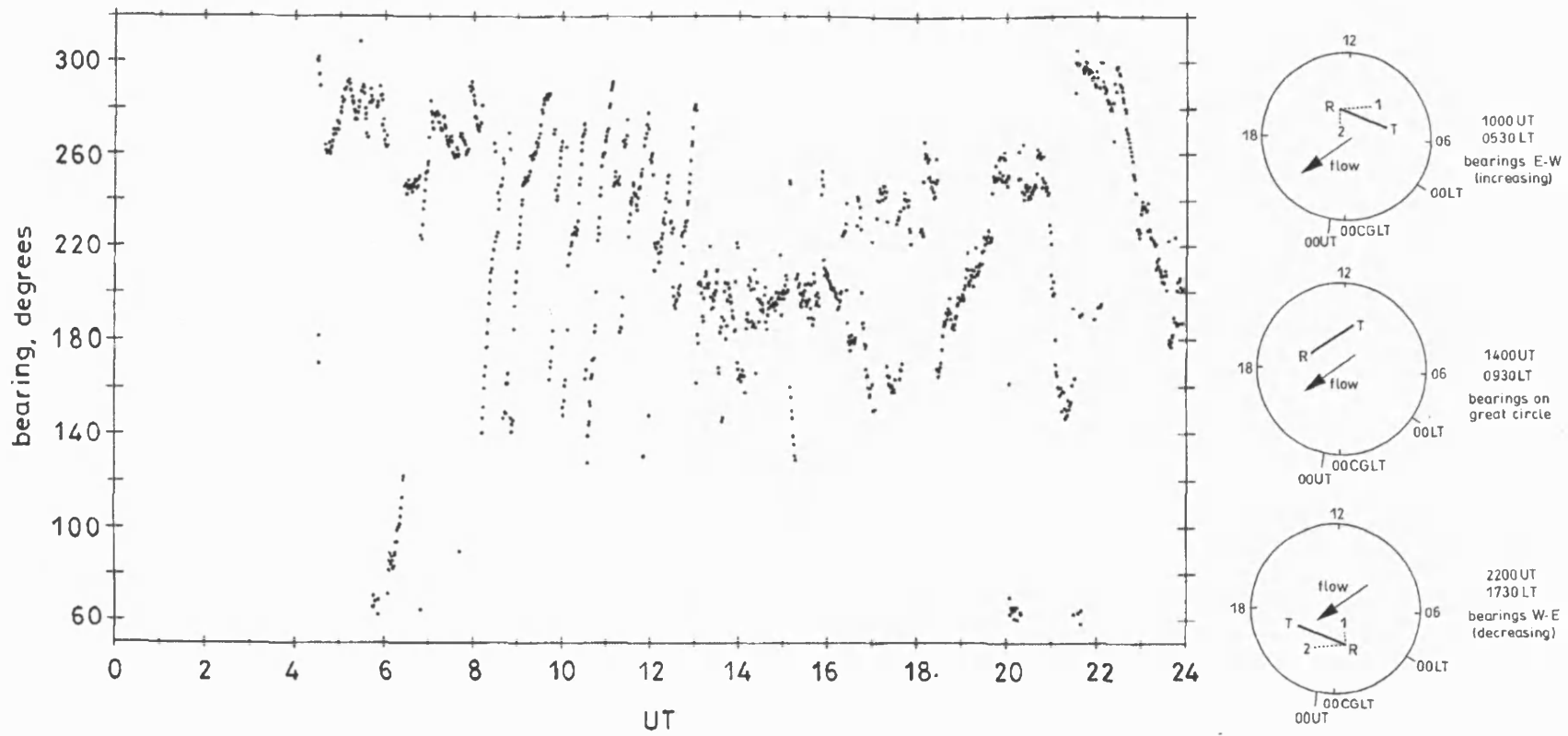


Figure 2.12 Examples of very large, rapid bearing swings over a short polar cap path, 18th November 1990, *Warrington et al.* [1997(2)], the swing direction reversal in the afternoon is explained in the right hand panel.

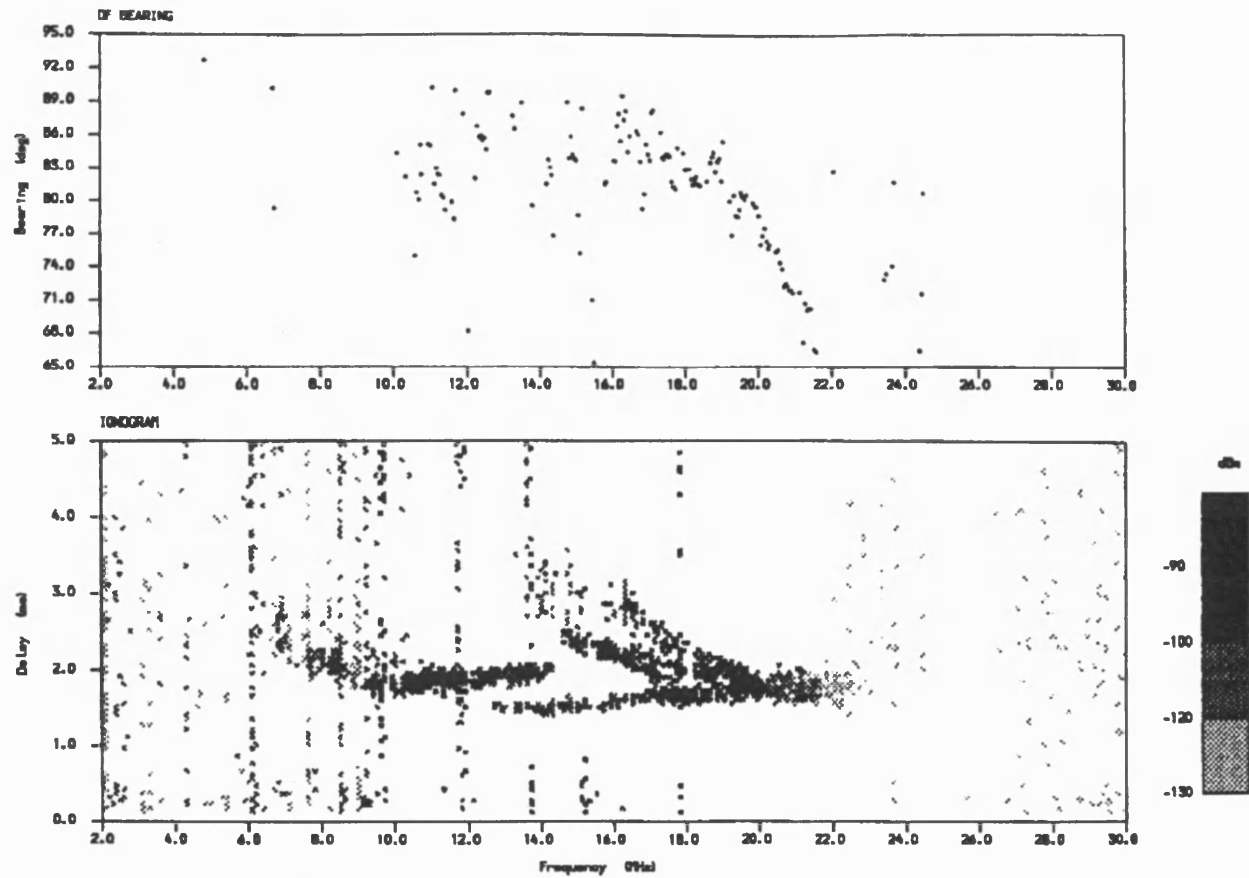
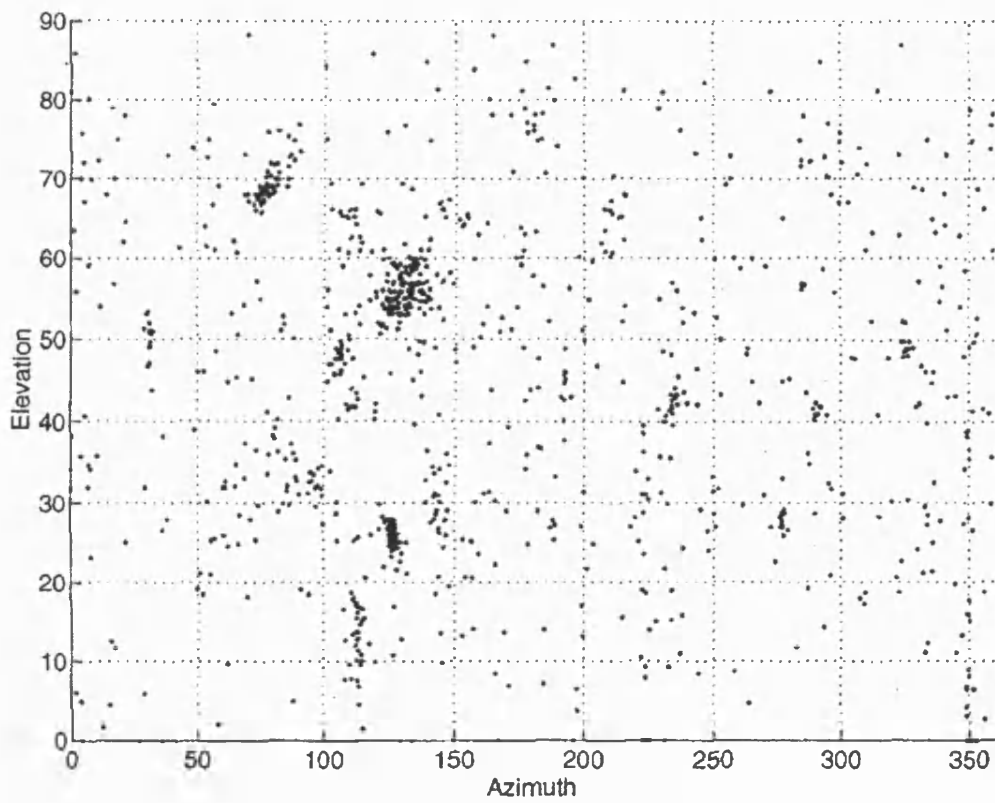
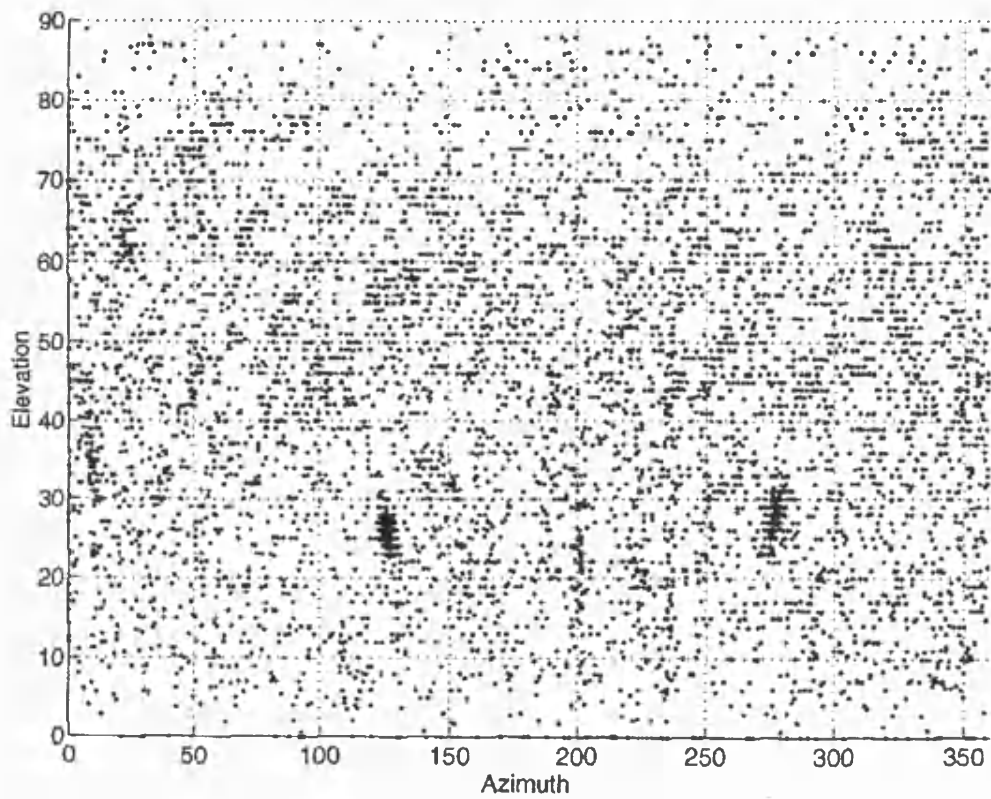


Figure 2.13 Oblique ionogram and associated bearing measurements for a long trans-auroral path, *Warrington et al.* [1993]. Note the bearing deviations associated with the ionogram spread nose extension.

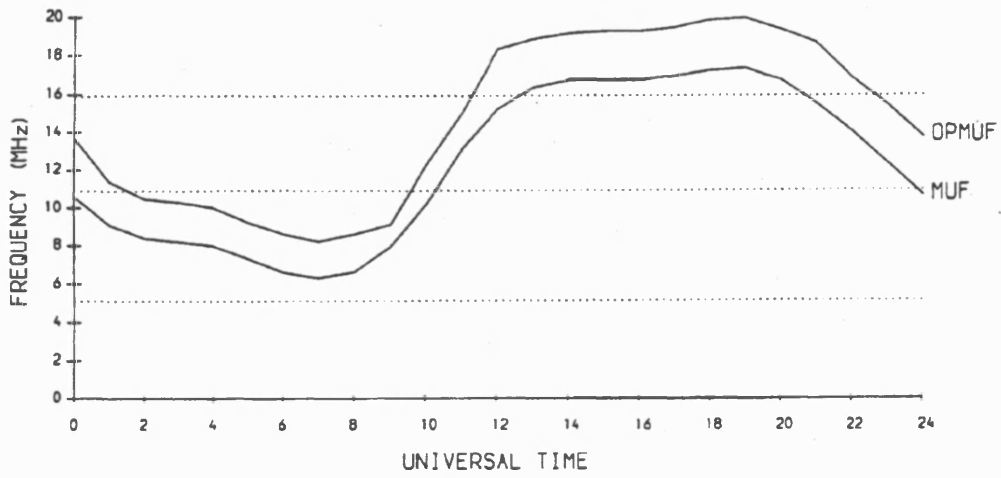


(a)

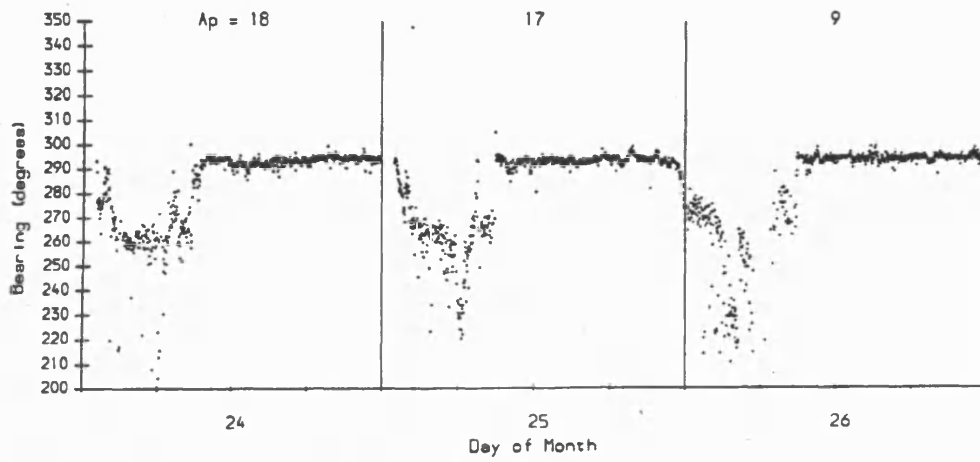


(b)

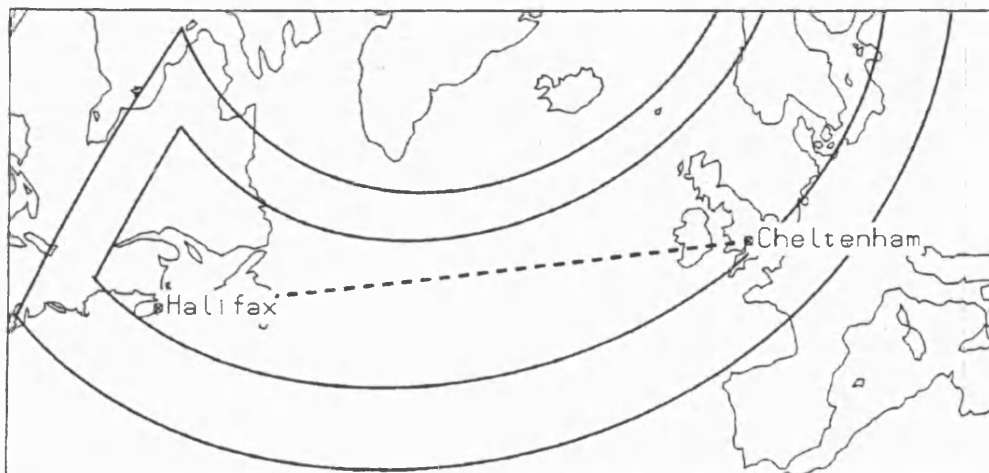
Figure 2.14 Scatter plots of DOA determinations with 1 second integration time using (a) INS and (b) MUSIC *Warrington* [1995(2)]



(a) Model predictions of MUF and OPMUF (Modified MUF)



(b) DOAs of 10.945 MHz soundings, note night time deviations to the south



(c) Path in relation to the mid-latitude trough at low geomagnetic activity, 00UT

Figure 2.15 Halifax-Cheltenham March 1994, *Warrington et al.* [1996]

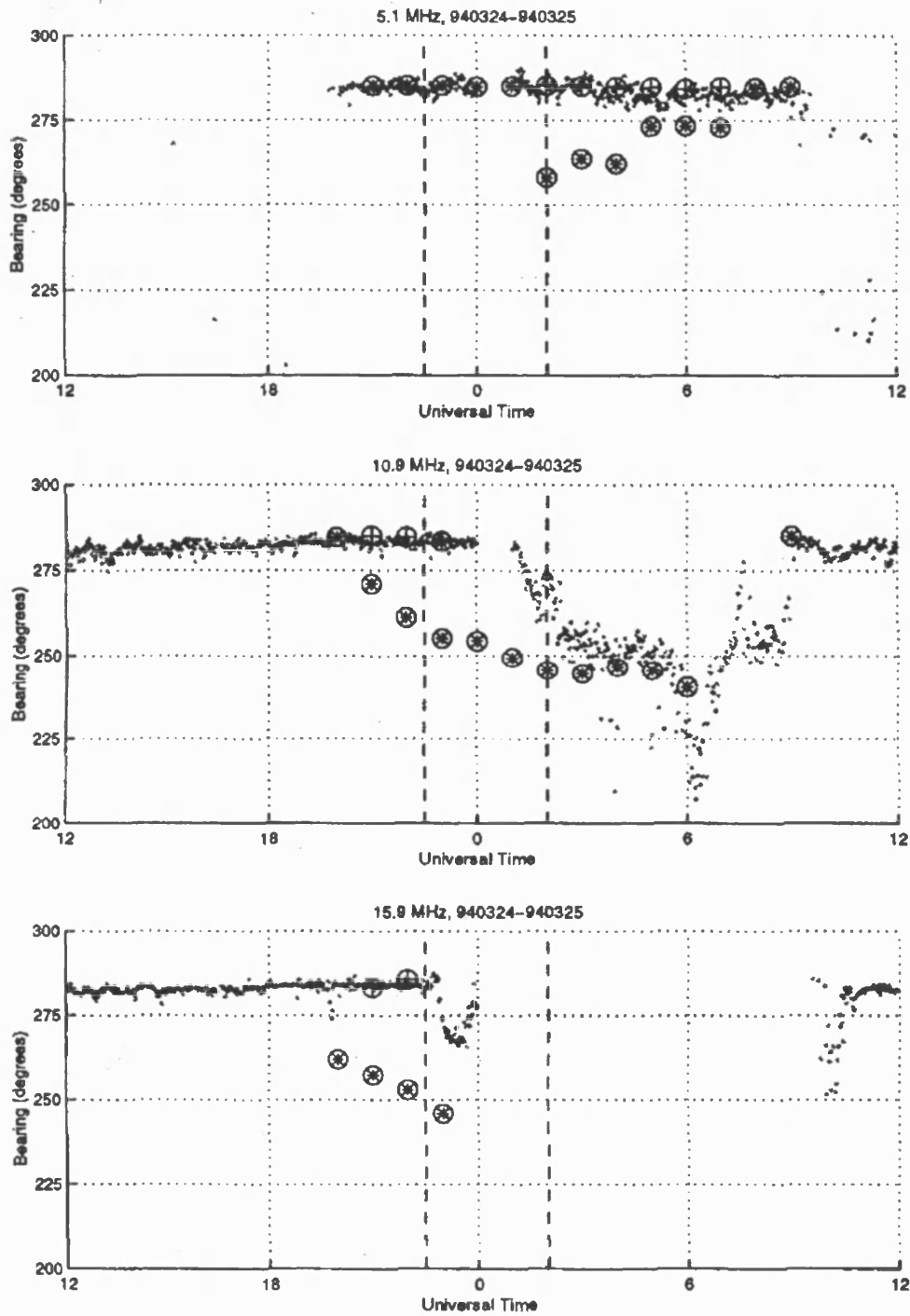
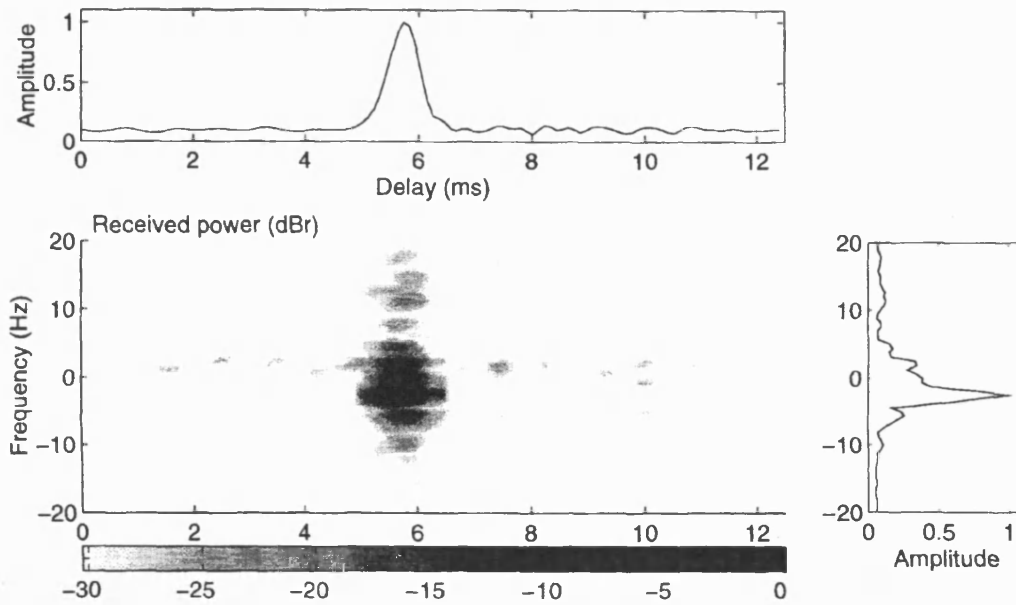
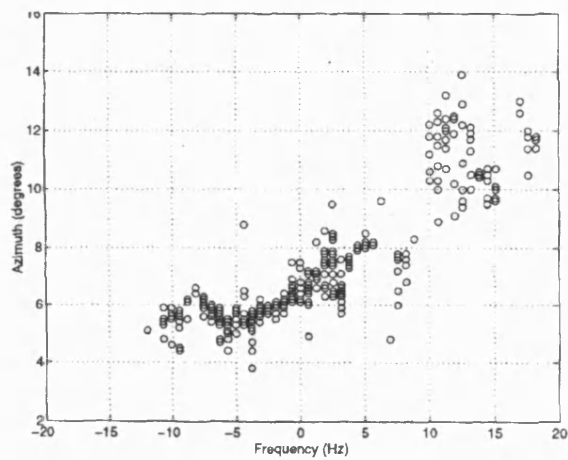


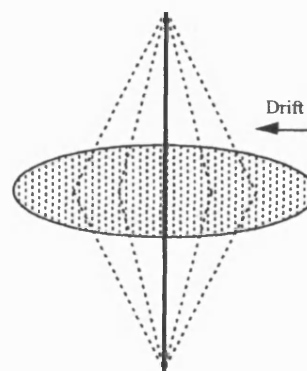
Figure 2.16 Observed and simulated bearings as a function of time between 12UT on 24<sup>th</sup> March 1994 and 12UT on 25<sup>th</sup> March 1994. Experimental data are given by the light grey trace. The values obtained from the ray tracing simulation are given by the symbols  $\otimes$  and  $\oplus$ . *Stocker et al.* [2000]



(a)



(b)



(c)

Figure 2.17 14.4MHz signal over the Svalbard – Cricklade path. (a) Delay-Doppler plot. (b) Variation of azimuth with Doppler frequency. (c) Schematic diagram of propagation via moving scattering regions where the drift direction is East-West. Warrington [1996(1)]

### **3. Experimental arrangement**

Described below are the details of the experimental arrangements, including (a) the location of the receive and transmit sites of interest, (b) the collection of the DAMSON signals using the RSL multi-channel DF system, (c) the processing to produce delay-Doppler (DD) plots from the stored signals, (d) the direction finding to produce the DD-DF information and (e) the subsequent data processing referred to in the analysis chapters.

The analysis in this thesis is based around data collected during an experimental campaign at a receiving site in Kiruna (67.84°N, 20.40°E), northern Sweden. The site was shared with a co-located DAMSON receiver system, which was operational throughout the campaign. The signals of interest were generated by the DAMSON transmitters in Isfjord (78.06°N, 13.63°E), on the Svalbard archipelago, and Harstad (68.48°N, 16.30°E) in Norway. Figure 1.18 is a map with the locations of the transmitter and receiver sites marked. The great circle ground tracks and lengths are also marked. The campaign was conducted over the period between 18<sup>th</sup> to 30<sup>th</sup> March 1998.

#### **3.1 The RSL multi-channel HF-DF system**

The data was collected using the Radio Systems Laboratories multi-channel HF receiving system, developed in Leicester by this student. Typically a multi-channel system such as this employs a spaced antenna array, each element of which is connected to a separate, good quality, HF communications receiver. The output of these receivers is sampled simultaneously and stored, using a computer, for subsequent processing and analysis. In order to achieve acceptable performance from the Super Resolution Direction Finding (SRDF) algorithm it is necessary to have reliable amplitude and phase matching through the receivers. This matching is achieved by calibration of the system at appropriate intervals, dependent on the native phase-amplitude stability of the receivers. Subsequent correction of the collected data is based on the results of the calibration analysis.

Figure 3.1 is a diagrammatic representation of the RSL multi-channel HF-DF system as used during the campaign. In this system, the spaced array was composed of six Rhode

and Schwartz active measurement antennas. These were disposed in a field, according to the plan in Figure 3.2, and their positions accurately measured by professional surveyors using laser rangefinding theodolites. The direction of North was determined by placing a pole to the North of the array centre, in line with the sun at local midday. Errors in the measurement of the direction of North are due to: (a) a possible alignment error of  $\sim 0.5\text{m}$  in the positioning of this 'North pole' leading to an error of  $\sim 1.7^\circ$ , (b) A correction must be made in order to account for variations of the Earth's orientation relative to the Sun, when the array was surveyed, in early March, 'Sun time' was 11 minutes slow relative to 'Clock time'. This correction has not been applied, which would account for  $\sim 2.6^\circ$  of error. The measurements reported here are always relative to 'Array North' as measured. To correct for the differences between 'Array North' and 'True North',  $\sim 4.3^\circ$  should be subtracted from the measurements to result in a better estimate of the true DOA.

Each antenna was connected to separate inputs on a switch box, located at the centre of the array, via sections of large diameter, coaxial screened, cable cut to the same length, with an accuracy of 5mm. This ensured that any phase or amplitude differences introduced by the cables were minimised. A seventh input to the switch box was connected, via a programmable attenuator, to a phase continuous calibration source (a swept frequency synthesiser).

The six outputs from the switch box were connected, via lengths of low impedance coaxial cables, to separate HF receiver units mounted in a rack in a control cabin approximately 90m distant from the array. Depending on the state of a control signal sent via a cable from the computer, these outputs each carried either the separate signals from the antennas or identical calibration signals.

The separate HF receiver units depended on three (common) frequency stable local oscillators. Two of these were of fixed frequency while the frequency of the 3<sup>rd</sup> was controlled by the computer, via a GPIB bus, and set to the sum of 45MHz and the desired reception frequency. A separate control line from the computer controlled the (common) gain in the receivers. The baseband output of the receivers was connected to a 12 bit Analogue to Digital (A/D) card, mounted in the computer, where they were sampled simultaneously at 20kHz per channel and stored to disk. In order to maintain

time synchronisation with the transmitters the computer was also equipped with a GPS timing card which updated the system clock and provided a 1 pulse-per-second (1pps) timing signal which was simultaneously recorded on the trigger line of the A/D card.

### *3.1.1 The system scheduler*

The system's operation was controlled from a master schedule on the computer. This determined both the time of occurrence and the sequence of system activity for every event detailed in the master schedule file. A typical file is listed in Figure 3.3. This master schedule ensured that logging events occurred at the same time and frequency as the DAMSON transmissions.

There were two types of event that could be scheduled:

#### 1) A logging event

The event time and sounding frequency are read from the schedule file. The schedule program then executes a series of actions as follows:

- Local oscillator, LO3, is programmed to the sounding frequency + 45MHz, the calibration synthesiser is turned off.
- The switch box is switched to allow the antenna inputs through to the receivers.
- The most recently calculated gain, for the selected frequency, is accessed from memory and the selectable gains on the receivers are set to this value. If there is no gain value stored in the memory then a middle value gain of 35dB is used.
- The 1pps signal from the GPS card is enabled 1s before the event time.
- The receiver outputs are streamed to disk via the A/D card. Streaming begins ~0.2s before the expected transmission time and ends ~0.2s after transmission ends. The 1pps is recorded on the A/D trigger channel for use later in the analysis. The receiver gain value is also stored in this data file.
- The streamed data file is read back into memory and the maximum signal amplitude is found. The calculated gain is adjusted -5dB if this amplitude requires > 9bits of the 12bit A/D range and +5dB if it requires < 9bits. This

process maintains the dynamic range of the recordings. The previous gain value is stored in memory for use by the calibration routines.

## 2) A calibration event

The event time and sounding frequency are read from the schedule file. The schedule program then executes a series of actions as follows:

- The calibration synthesiser is programmed to generate a linear frequency sweep  $\pm 5\text{kHz}$  around the selected frequency.
- LO3 is programmed to the sounding frequency + 45MHz.
- The switch box is switched so that the calibration signal appears at the input to all the receivers.
- The selectable gains in the receivers are stepped, through the gains used in the previous data logging events on the selected frequency, at intervals of 1s, while the programmable attenuator is simultaneously set to the same values as the gains. This ensures that the receivers present similar signal levels at the inputs to the A/D card as those present during logging of a signal. The receiver outputs for each gain level are streamed to disk via the A/D card.

The data files resulting from the above operations were initially stored on the computer's local hard disk drive. This drive was periodically archived to digital audio tape (DAT), for long term storage and further processing.

## 3.2 DAMSON schedule and signal format

The DAMSON system software includes scheduler routines, which allow transmissions to occur at selected intervals over any chosen time period. During the period of the campaign, transmissions occurred at 10 different frequencies, between 2 - 22MHz, according to the schedule illustrated in Table 3.1. To avoid interference between transmitters, the Harstad transmitter ran the reverse frequency schedule to the Svalbard transmitter. Within each 1 minute frequency interval a sub-schedule of different sounding waveforms were transmitted.

Start time (minutes past each hour)	Duration of interval (minutes)	Svalbard TX frequency (MHz)	Harstad TX frequency (MHz)
5,15,25,35,45,55	1	2.8	21.9
6,16,26,36,46,56	1	4	20
7,17,27,37,47,57	1	4.7	17.5
8,18,28,38,48,58	1	6.8	14.4
9,19,29,39,49,59	1	9	11.1
0,10,20,30,40,50	1	11.1	9
1,11,21,31,41,51	1	14.4	6.8
2,12,22,32,42,52	1	17.5	4.7
3,13,23,33,43,53	1	20	4
4,14,24,34,44,54	1	21.9	2.8

Table 3.1 DAMSON transmission schedule

### 3.2.1 Signal format

Although the DAMSON system was designed to use a wide variety of sounding waveforms, of the waveforms in use during the campaign, the delay-Doppler (DD) waveform was the most appropriate to the experiment. The delay-Doppler waveform is designed to allow the determination of the multipath and Doppler characteristics of a channel. The waveform is made up of a series of bi-phase shift keying (BPSK) Barker-13 sequences modulated at 2400 bits per second, giving a time resolution, after processing, of approximately 0.4ms. The multipath window is defined by the frame width (time between successive sequences), which is 12.5ms wide. 128 frames are sent during 1.6 seconds of transmit time, resulting in a frequency resolution of 0.63Hz after processing. Figure 3.4 is a representation of the DD signal format.

This DD waveform is transmitted six times, at five second intervals, within each frequency transmission interval. The rest of the 1 minute interval is occupied by other sounding waveforms.

The receiver logging schedule implemented on the RSL multi-channel system during the collection campaign included all six DD transmissions in each frequency transmission interval and alternated between the 10 minute frequency schedules of each transmitter.

The revisit time between successive recordings at a given frequency from a particular transmitter was thus 20 minutes. Receiver calibration events were scheduled to occur immediately after the last DD transmission in the 1 minute time slot for a given frequency.

### **3.3 Post processing**

Prior to analysis the collected data files were processed in order to calibrate the system and to extract the delay-Doppler and direction finding information.

#### *3.3.1 Calibration*

The inputs to the DAMSON analysis routines and the SRDF algorithms must first be corrected for any amplitude and phase variations between receiver channels. The amplitude correction was achieved by multiplying the FFTs of each recorded channel by a factor derived from processing of the calibration files. The phase matching was done in a similar way by adding appropriate phases, derived from calibration file processing, to each channel.

Since the calibration synthesiser produces a waveform, which sweeps across the bandwidth of the receiver, the recorded data is in effect a frequency response for each receiver. This calibration data was first Hilbert transformed, to provide the complex amplitudes, then a Fast Fourier Transform was performed giving the frequency response of each channel in the frequency domain. Due to the nature of the calibration synthesiser, the waveform it produces is a digital sweep consisting of a finite number of discrete frequency steps over a given period and frequency range. The resulting FFT of the signal has an equal number of discrete peaks in the frequency domain. The energy under the discrete peaks in the FFT was determined from a 3 point rolling sum over the bandwidth. Only the resulting local maxima were of interest since it is only at these positions in the spectra that phase information has any significance, these were selected by finding the 3 point local maximum. The amplitude and phase responses of all the channels were then available, over the whole bandwidth of the system. Figure 3.5 represents the amplitude and phase frequency responses of one channel of the system tuned to 4.921650MHz, the phase response is measured relative to a reference channel. It is possible to use the amplitude and phase information at each frequency step across

the whole of the receiver bandwidth in the calibration corrections, however, this is computationally very expensive. A good approximation to the necessary corrections is obtained by taking the mean of the amplitude and phase responses over the 3kHz bandwidth window of the DAMSON transmissions. This is the calibration procedure that was used.

In order to correct the sampled baseband output of the receivers, contained in the data files, it was first necessary to apply a Hilbert transform to provide the complex signal amplitudes. A filter was then used to remove signals outside the DAMSON bandwidth. In order to use the standard DAMSON processing routines, the data was resampled at 9600 samples per second. The previously calculated calibration factors were then applied.

### *3.3.2 Time of flight corrections*

Although the transmit and receive timing was nominally synchronised to within  $\sim 10\mu\text{s}$  using the 1 pulse-per-second GPS time signals, there are systematic errors in the time of flight measurements due to delays in the transmit and receive equipment. In order to measure absolute time of flight, the delays were characterised for both the DAMSON transmitters and the RSL receiver system and have been used to correct the collected data during the post processing.

Data from the co-located DAMSON system was also made available for comparison in order to validate these time of flight corrections as applied to the RSL system.

### *3.3.3 DAMSON signal processing*

A number of signal processing techniques were used to obtain the standard DAMSON output illustrated in Figure 1.19.

- Digital Pulse Compression (by signal cross correlation with a perfect Barker-13 sequence)

As described earlier, the DD waveform is composed of a number of Barker-13 sequences, as represented in the first panel of Figure 3.6. In the same way as other pseudo random compression codes, when Barker sequences cross correlate with a perfect copy of themselves, they result in a complex correlated sequence with a large

peak having an amplitude equal to the length of the sequence. A special property of Barker sequences, however, is that the other elements of the correlated sequence only have an amplitude of either 1 or 0. The maximum sidelobe level of a Barker sequence is thus the reciprocal of the Barker sequence length compared to the peak. In the case of the DAMSON DD waveform this results in a pulse compression processing gain of 13, with sidelobes 13x (~22dB) smaller, as illustrated in the second and third panels of Figure 3.6. The pulse compression process has traded 13 times longer transmission time for a 13 times signal gain in the processing, whilst achieving a time resolution of 1/2400s (approximately 0.4ms).

- delay – Doppler processing

If no dispersion were introduced during signal propagation then the resulting complex correlation sequences for each frame would be identical and have a gain of 13 on one element and correlation time sidelobes with unity gain. This will not occur in the general case and the correlation sequences for each frame will be different. Any dispersion (delay and Doppler shifts/spreads) observed on the received signal would be due to ionospheric propagation effects.

The delay and Doppler dispersion of the incoming signal can be represented as a delay-Doppler surface, similar to that illustrated in Figure 1.19. The horizontal axis has units of time, with the maximum defined by the 12.5ms frame width, and represents the delay dispersion. The vertical axis has units of Hz and represents the Doppler frequency dispersion, with a maximum spread of  $\pm 40$ Hz. The colour scale has units of dBr and represents the power, relative to the peak, in each delay-Doppler signal component.

Figure 3.7 illustrates the process by which this delay-Doppler surface is generated. Each frame of the pulse compressed correlation sequence is composed of complex samples with a spacing of (1/9600) seconds. Samples from each of the 128 frames, corresponding to the same time offset within the frames, are grouped together and passed through an FFT algorithm. This is repeated for each of the 120 time offsets within a frame and results in 120 complex Doppler spectra. These Doppler spectra can be plotted against their time offset within the frame, the resulting surface has a value of the complex Doppler amplitude for every delay offset and Doppler frequency. In the

main panel of Figure 1.19 and Figure 3.7 the magnitude of the complex Doppler amplitude is plotted using a colour scale for display purposes.

Summing the Doppler amplitudes at each Doppler frequency across all time delays generates a Doppler profile for the entire waveform, represented in the right hand panel of Figure 1.19. A delay profile may be generated in a similar way by summing the amplitudes at each time offset across all Doppler frequencies, as in the top panel of Figure 1.19.

These processes are applied to the recorded outputs of each of the  $n$  HF receivers in the system, resulting in multiple complex delay-Doppler surfaces.

The DD surfaces presented in this thesis are the result of delay-Doppler processing each recorded 1.6s DD transmission. This is not the same as in the majority of DAMSON studies, where the DD surfaces presented are the result of incoherently averaging the six DD sounding measurements made on a given frequency in a minute. Because ionospheric variability occurs on the order of seconds it is felt that the advantages of being able to examine separate DD surfaces in each minute outweighed the advantages of increasing SNR by incoherent averaging.

It should also be noted that, due to differences in the local frequency references for the RSL 6 channel system, small offsets from zero on the frequency axis are present in the recorded data. These did not affect the signal processing and can be corrected for in the analysis if desired. For the most part it is relative values of Doppler that will be considered in the analysis.

### **3.4 First pass data selection.**

Over the course of the six DD recordings made in a transmission interval, the receiver gain will have been iteratively modified by the system according to the rules described in section 3.1.1. By the time of the last DD recording in a transmission interval, the receiver gain should have converged to its optimum value. This first pass analysis therefore uses only the last recorded sounding from a given transmission interval.

In order to determine if a DAMSON signal, with sufficient SNR for further processing is present in a given recording, the average value of the normalised time delay amplitude profile is calculated. If this is less than 0.75, then a DAMSON signal is deemed to be present. This test was empirically derived and worked well with the examples tested, one example is illustrated in Figure 3.8. For those cases where the wanted signal was evident, the 1000 cells within the delay-Doppler profile containing the most power were input to the direction finding algorithm. This first pass analysis produced 2884 cases for the Svalbard – Kiruna path and 1505 for the Harstad – Kiruna path.

### **3.5 Direction finding of received signals.**

In the examples discussed here, estimates of the direction of arrival of components of the ionospherically propagated DAMSON signals were made using a super resolution direction finding algorithm called Iterative Null Steering (INS), which is based on the IMP (*Brandwood [1994]*) and DOSE (*Zatman et al. [1993]*) algorithms. As described in section 2.2, the algorithm is capable of resolving multiple directions of arrival and provides the DOA of at least the strongest two (primary and secondary) incoming signals and is particularly robust at HF. This method of analysis is suitable for the processing of data from the RSL spaced antenna array.

The detailed operation and performance of the INS algorithm is not discussed here. An in depth description of the algorithm and performance comparisons of INS with an alternative SRDF algorithm, called MUSIC, have been carried out by *Warrington [1995(2)]*. However, it is necessary to identify some limitations in the direction finding capabilities of the system.

#### *3.5.1 Antenna sensitivity patterns and sidelobes.*

As has been discussed in section 2.2 an array can be made particularly sensitive to signals arriving from a given direction by the selection of an appropriate combination of phase corrections to the signals received at each element before coherently summing them together. It can be said that a sensitivity ‘beam’ has been steered in that direction. Figure 3.9 is a typical sensitivity pattern for the RSL 6 antenna array deployed in Kiruna. The colour scale represents the relative sensitivity of the array to signals

arriving from different directions in azimuth and elevation when a given combination of phases is added to make it most sensitive along  $300^\circ$  azimuth.

One of the consequences of the array geometry is that the main sensitivity lobe is relatively narrow in azimuth, which is good from a direction finding viewpoint, however, in elevation the lobe is very broad, which means that the resolution of the system in elevation is very poor.

Also of note is a secondary lobe of sensitivity along  $\sim 200^\circ$ , a 'sidelobe', this indicates that the combination of phases chosen to enhance sensitivity along  $300^\circ$  is very similar, to the combination of phases required to steer a beam along  $200^\circ$ . This similarity may introduce an ambiguity in the DF processing which can on occasion lead to the wrong DOA being reported.

### 3.5.2 *DD-DF calculation*

The information for calculating the DOA estimates comes from the multiple complex delay-Doppler surfaces described in section 3.3.3. Each of the  $n$  surfaces represents the incoming signal at a given antenna while each value in the  $120 \times 127$  element surface is a complex pair representing the phase and amplitude of the incoming signal for a given delay-Doppler offset. The phase and amplitude values, for the 1000 elements carrying the most signal power, together with the accurately surveyed antenna positions are passed to the INS algorithm. The algorithm returns azimuth and elevation estimates for each of these delay-Doppler offsets. The azimuth and elevation estimates are stored in data structures similar to the delay-Doppler surfaces, except that at each delay-Doppler offset an azimuth or elevation estimate is stored instead of a complex amplitude.

## 3.6 **Visualisation**

It is convenient to represent the delay-Doppler (DD) information and the direction finding information described above in a common format, known as a DD-DF plot. A typical DD-DF plot is illustrated in Figure 3.10. The upper frames of these figures show the received pulses (after digital pulse compression) with normalised amplitude on an absolute time delay scale. The Doppler spectra of the received signals, also on a normalised scale, are given in the right hand frames of the figures. The delay-Doppler surface is indicated in the upper colour plot of the figures with a colour scale on which

the amplitude of the peak power value is represented as 0dBr. The Barker13 pulse compression time sidelobes can be suppressed by setting to zero any points with relative amplitude  $< -18\text{dBr}$ , however, in most cases this has not been done. The middle colour plots indicate the primary measured azimuths on a colour scale as a function of absolute time delay and Doppler frequency. The lower colour plot displays the primary measured elevation angles in a similar manner. Although the SRDF algorithm calculates both primary and secondary DOAs, generally only primary bearings are considered in this analysis.

### **3.7 Data analysis**

In order to extract parameters of interest from the processed data files, a selection of characterisation routines were developed. The information of interest is stored in three data structures; the delay-Doppler surface, the Azimuth surface and the Elevation surface as described above. These surfaces are composed of individual pixels, which are indexed by the delay and Doppler offsets, and are thus amenable to certain image processing techniques for the extraction of parameters. Some of the techniques used in this investigation are described below.

#### *3.7.1 Thresholding*

Since the analysis is mainly concerned with signal parameters on the DD plane, it is useful to find the power level that separates the signal and noise power. This detection threshold is set based on the noise floor of the delay-Doppler surface. The calculation of this threshold, based on the method used by QinetiQ's DAMSON analysis software (*Angling* [1995(2)]), is presented below:

The DD surface (in linear power units) is first scaled so that its maximum has a value of 32767. The projection of this surface onto the time axis is calculated by taking the maximum of each Doppler spectrum for each time delay offset. This profile is then divided into 5 separate, equal length slices. The mean value of each slice is calculated and the noise floor level is taken as the smallest of these mean values. Figure 3.11 illustrates this process. A sliding threshold is calculated based on this noise floor using the logic presented in Table 3.2 below.

Any signal power above this threshold is retained and used in the data analysis while any power below this threshold is discarded. The resulting delay-Doppler surface indicates regions where there is sufficient signal power to exceed the threshold. These regions typically represent a propagation mode. It is the characteristics of these regions that are of interest.

Noise floor boundaries		
Lower	Upper	Threshold
0	653.8	$653.8 * 1.99$
653.8	1000	$(\text{noise\_floor} * 3.981) - 1301.7$
1000	12216.4	$(\text{noise\_floor} * 1.99) - 689.3$
12216.4	32767	25000

Table 3.2 Threshold calculation logic

### 3.7.2 Region finding, clustering and parameter extraction

In order to identify which pixels are associated with each thresholded region, the pixels are indexed (as a function of absolute time delay and Doppler offset). The indices are then associated with each other, using a grouping function, on a region by region basis.

These indices can be used to extract parameters of interest from the relative power, azimuth and elevation data structures. These derived parameters can be displayed or stored in a database format.

The following list is a subset of the more important parameters that were extracted from every case in the first pass data set and stored in a characterisation database for later use.

- Ttspr – total time (delay) spread per case

The time spread is measured in terms of the minimum width, in the time dimension, into which 80% of the indexed signal power falls. The disposition of the signal power into separate modes is not considered so even a single mode will have a measurable Ttspr. This parameter is a total for each case and not for each region.

- TDspr – total Doppler spread per case

The Doppler spread is measured in terms of the minimum width, in the Doppler dimension, into which 80% of the indexed signal power falls, in a similar way to the total time spread calculation described above. This parameter is a total for each case and not for each region.

- SNR – overall signal to noise ratio per case

This signal to noise ratio parameter compares the power in the selected regions with the overall noise power for the case. Because the power in the selected regions is itself a combination of signal power and noise power then a correction based on the already calculated noise floor is necessary. This value is normalised by 30/13 to account for the duty ratio of the uncompressed pulse train.

$$SNR = \frac{Power_{inallselectedregions} - Noise_{inallselectedregions}}{NoiseTotal} \left[ \frac{30}{13} \right]$$

Equation 3.1

This parameter is a total for each case and not for each region. It should be noted that this method of calculation of overall SNR differs from that used in subsequent papers (*Warrington et al.* [2000(2)] and [2001]). The treatment used here includes only signal power that has been selected on the basis of the applied threshold. The method used by *Warrington et al.* does not involve thresholding and therefore includes all the power in the DD domain in the SNR calculation. This leads to a difference in the actual values of SNR between authors for the same data.

Notwithstanding this difference in calculation method, it would not be possible to make direct comparisons of measured SNR with the already large body of DAMSON analysis for the following reasons.

- a) The RSL system antennas and receivers are not as sensitive as the co-located DAMSON system at Kiruna, therefore the SNR for the same signals measured by both systems will be worse for the RSL system.

- b) Differences in the calculation of the channel delay-Doppler surface. Most DAMSON studies are based on a DD surface created as an incoherent average of six individual DD measurements made in a frequency time slot, while in this study, only one of the DD measurement in a time slot is used.

Although the measured values of SNR will be different, trends in the behaviour of SNR should remain the same.

- $t_{mean}$  – mean propagation time per region

This is the mean of the delay offset for each indexed region in a thresholded DD plot.

- $D_{mean}$  – mean Doppler offset per region

This is the mean of the Doppler offset for each indexed region in a thresholded DD plot.

- $SNR_m$  – mean signal to noise ratio per region

The signal to noise ratio for a given region, calculated for each indexed region.

- MPE – Equivalent multipath parameter per case

The MPE parameter is an SNR weighted time difference between two signal modes in the DD plane and has units of time. The subscripts 1&2 represent the two signal modes.

$$MPE = (t_2 - t_1) \frac{\min(SNR_1, SNR_2)}{\max(SNR_1, SNR_2)}$$

Equation 3.2

In the case of one mode,  $MPE = 0$ . In the more complex case of 2 or more modes, the largest MPE of each combination of two modes is chosen. If two modes contain the same signal power (as is the case in the *Watterson* [1970] model of an HF channel), the MPE is the same as the actual time of flight difference between the modes. This parameter is used in the analysis of the larger DAMSON data set and is evaluated here to allow comparison between the DAMSON data set and this DD-DF data set. The parameter is a total for each case and not for each region.

- AZpwm – power weighted mean azimuth per region

The azimuthal DOA information for each delay-Doppler offset in an indexed region is weighted with the power in that index before the mean is taken. In this way the resulting value will be more representative of the direction of arrival of most of the useful signal power.

$$AZ_{pwm} = \frac{\sum_{selectedregion} AZ \cdot Power}{\sum_{selectedregion} Power}$$

Equation 3.3

This is calculated for each indexed region in a case.

- ELpwm - power weighted mean elevation per region

This parameter is calculated in the same way as AZpwm by substituting the elevation DOA information for each region.

- AZstd – power weighted azimuth standard deviation
- ELstd – power weighted elevation standard deviation

Some of the major characterised parameters are illustrated in Figure 3.12.

### 3.8 Interferer signals from ~165° azimuth.

On a number of occasions during the collection campaign, an interfering signal was observed on a frequency close to 9.04MHz at the same time as the DAMSON signal. The presence of interferer signal power on nearby frequencies contributes significantly to the delay and Doppler spread values for these cases.

Interfering signals may be much stronger than the DAMSON signal due to their proximity to the receiver. However, because the Barker-13 pulse compressed DAMSON signal achieves a 13:1 processing gain on reception (in ideal conditions), the processed DAMSON signal can still present more energy in the DD domain. In order for an interferer to have an effect in the receiver/processing chain it must not be significantly reduced through the pulse compression processing. Signal reduction may occur if the

interferer has a different format to the DAMSON transmissions, however, if it has similar properties to the DAMSON signal (such as bi-phase modulation and/or 2400 bit/sec chip) rate then there may only be a little interferer signal reduction.

In Figure 3.13 a sequence of DAMSON soundings at 9.04MHz illustrates occasions when an interferer has appeared in the collected data. Due to ionospheric variability the relative signal strengths of the DAMSON signal and the interferer at the receiver have changed over time. The interferer appears to be a parallel tone modem using nearby frequencies, this is particularly clear in the lowest panel. This lowest panel, a transmission over the Harstad – Kiruna path, indicates the presence of the same interferer as for transmissions over the Svalbard – Kiruna path. The azimuth of the interfering signal, at  $\sim 165^\circ$ , is clearly different to the DAMSON signals. These examples are from a sequence of cases where an interferer appeared at the same frequency over the course of several hours, starting around 19:00 on day 77.

For each propagation path, histograms of the azimuthal DOAs for all the characterised signal modes in the data set are presented in Figure 3.14. Both paths show evidence of signal energy arriving from  $\sim 165^\circ$ , it is interesting to note that, since the azimuth of these incoming signals is always  $\sim 165^\circ$ , the cause of them must be independent of the propagation path, they are most probably due to the interferer described above.

On examination of the 102 cases that have signal energy arriving from between  $160^\circ \rightarrow 170^\circ$  azimuth, on 9.04MHz, over both paths, 90 cases indicate the presence of an interferer. These cases are spread relatively evenly throughout the periods when data was collected.

Although soundings at 9.04MHz do appear to be more likely to be contaminated with interference, there are image processing techniques available to mitigate the effects of an interferer. Such a technique is illustrated in Figure 3.15. For each Doppler row of the DD surface the mean value for the row is subtracted from each pixel along the row. In the case of an interferer such as encountered here, the mean will be large at the interferer Doppler offsets and will have a large effect, while for the other Doppler offsets the mean is small and has little effect.

The technique is not perfect, however, and it may still be necessary to visually filter cases for the presence of an interferer before any detailed propagation analysis can be done.

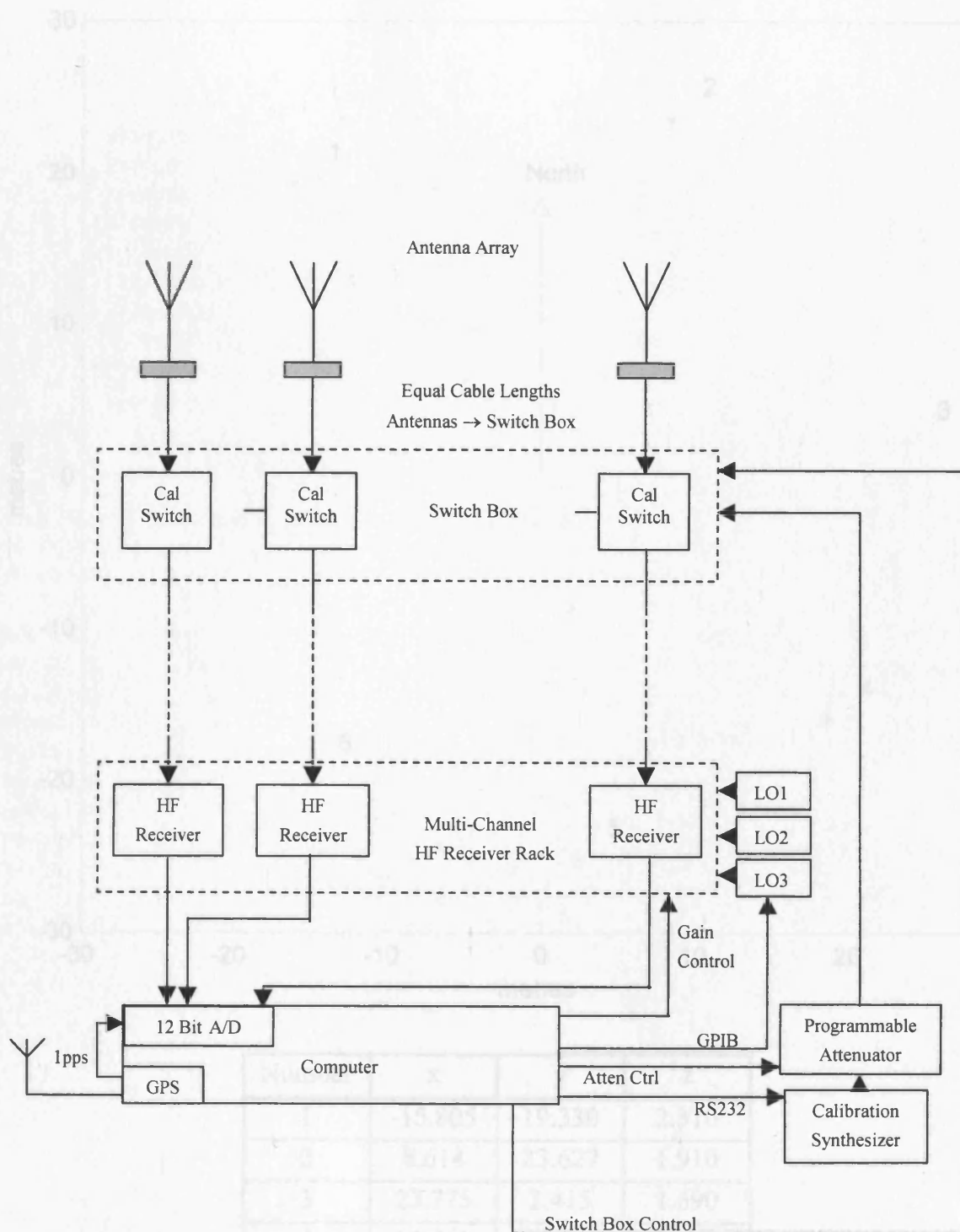
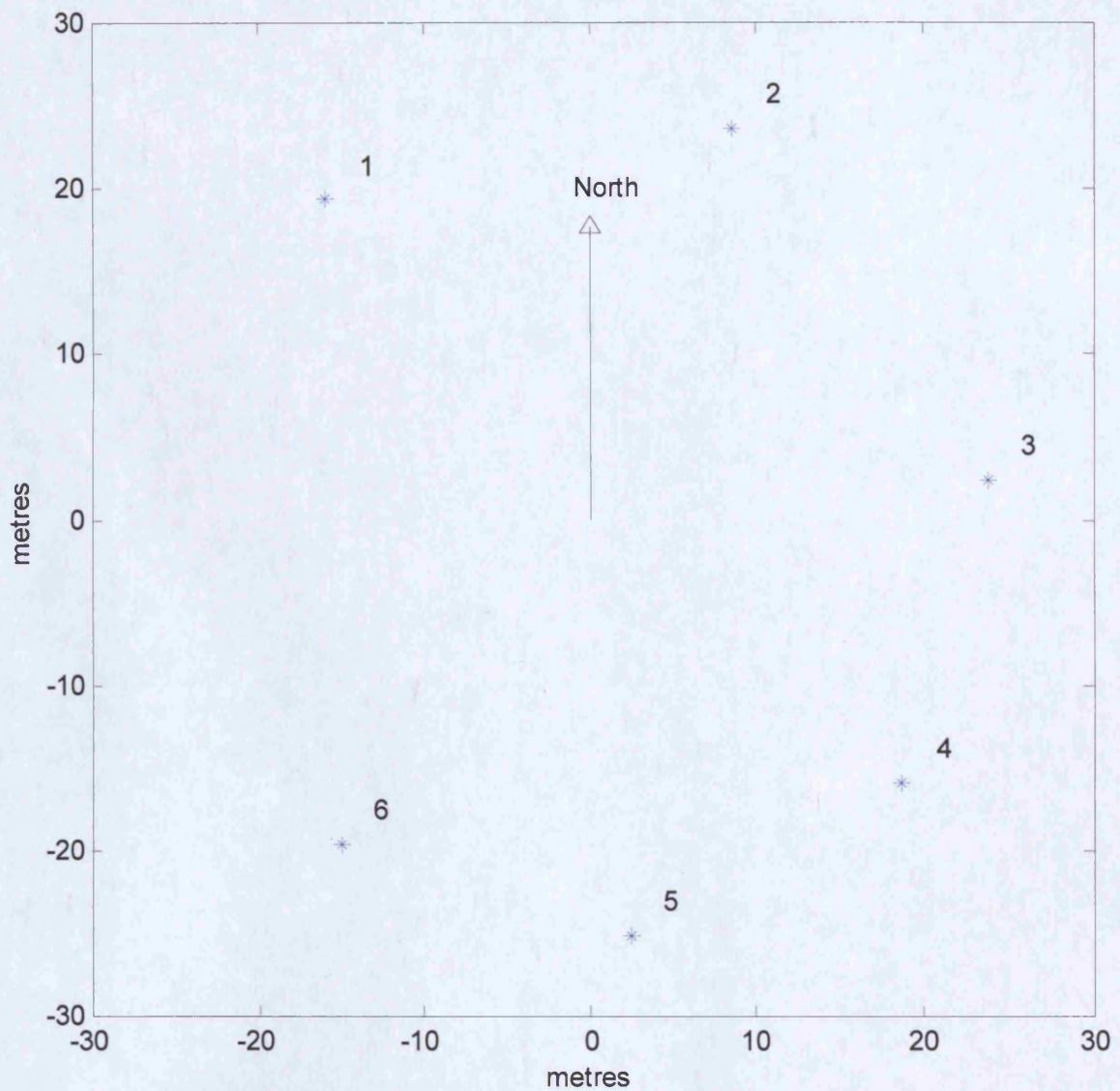


Figure 3.1 A diagrammatic representation of the RSL multi-channel HF-DF system



Number	x	y	z
1	-15.805	19.330	2.310
2	8.614	23.627	1.910
3	23.775	2.415	1.690
4	18.663	-15.889	1.740
5	2.389	-25.101	1.870
6	-14.993	-19.646	2.080

Figure 3.2 Disposition of antenna array, as used in Kiruna, March 1998

```

[ CHANNELS]
1 1 1 1 1 1 0 0
[ FREQLIST]
0      4920000
1      2830000
2      3950000
3      4700000
4      6780000
5      9040000
6      11175000
7      14360000
8      17450000
9      19950000
10     21880000
[ SCHEDULE]
98\03\20      10:45:00
600
time inc      freqnum  log    cal    gpsset
00:00:20     10      1      0      0
00:00:25     10      1      0      0
00:00:30     10      1      0      0
00:00:35     10      1      0      0
00:00:40     10      1      0      0
00:00:45     10      1      0      0
00:00:50     10      0      1      0
00:01:19     9       1      0      0
00:01:25     9       1      0      0
00:01:30     9       1      0      0
00:01:35     9       1      0      0
00:01:40     9       1      0      0
00:01:45     9       1      0      0
00:01:50     9       0      1      0

```

Figure 3.3 Partial listing of a typical schedule file used on the campaign.

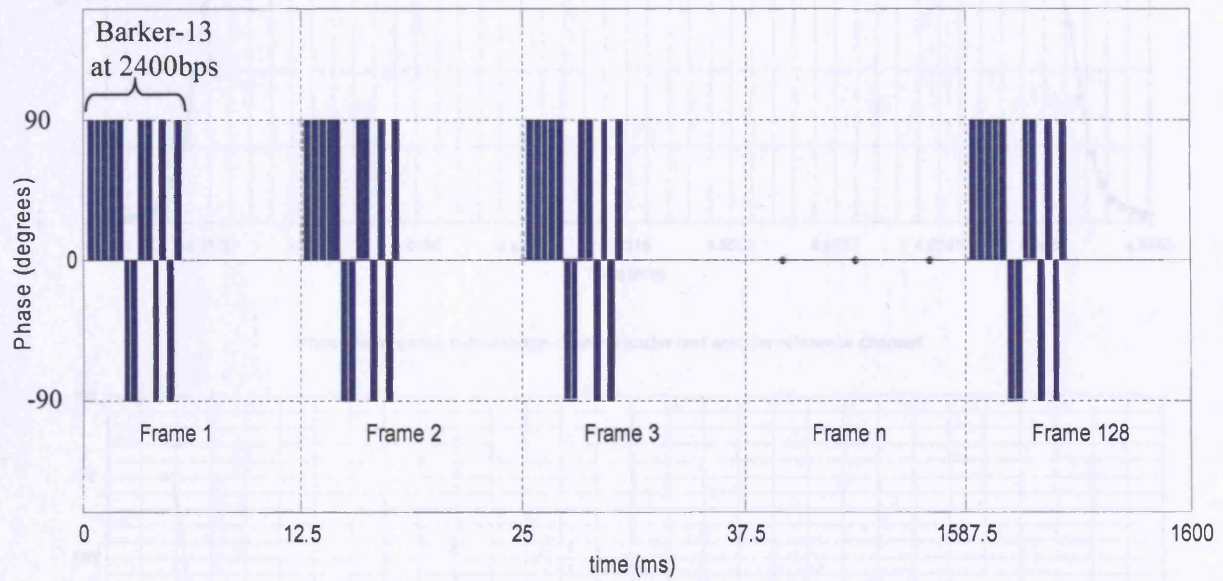


Figure 3.4 DAMSON delay-Doppler waveform, signal format.

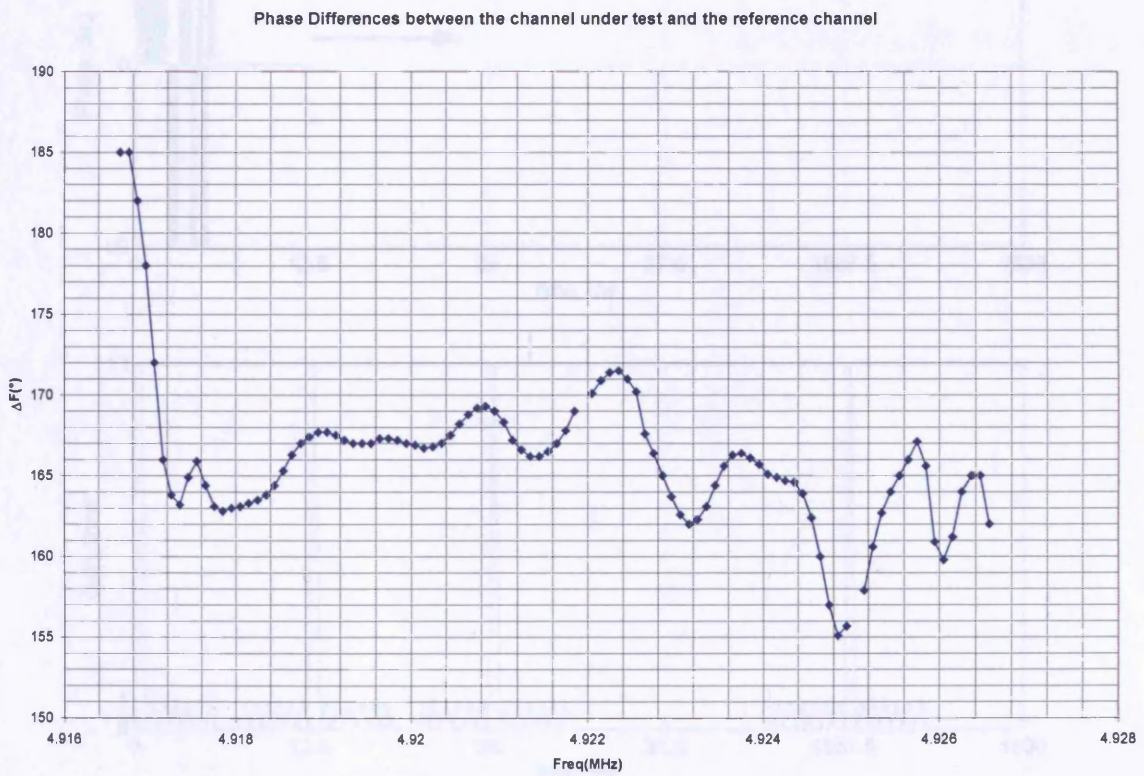
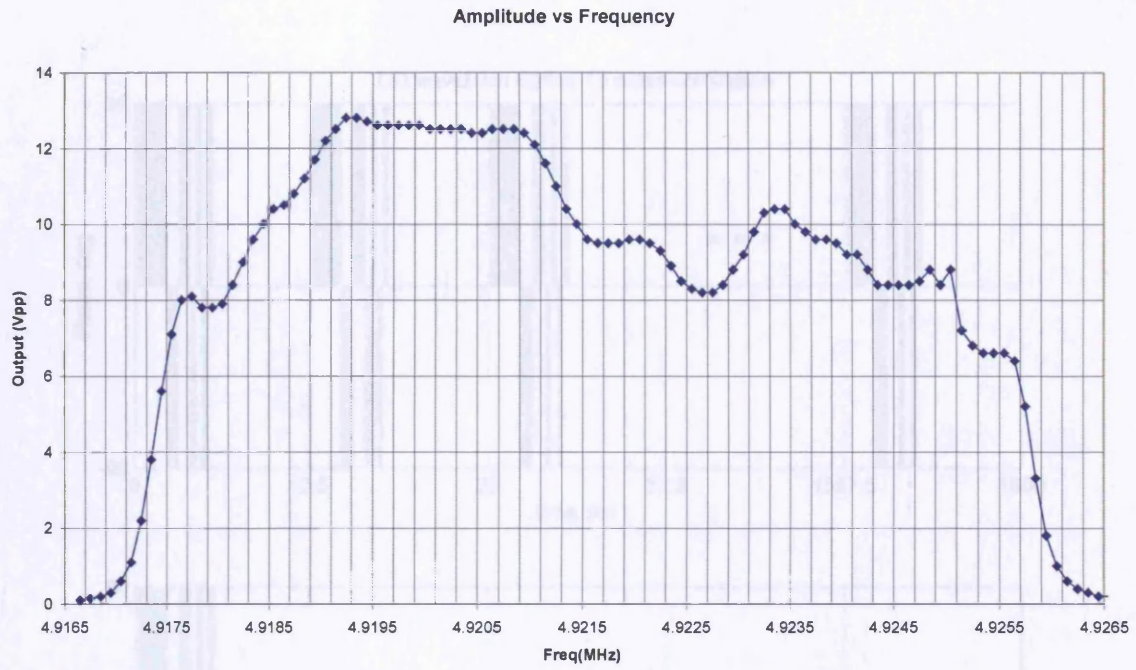


Figure 3.5 Frequency response of one channel of the RSL multi-channel system around 4.921650MHz

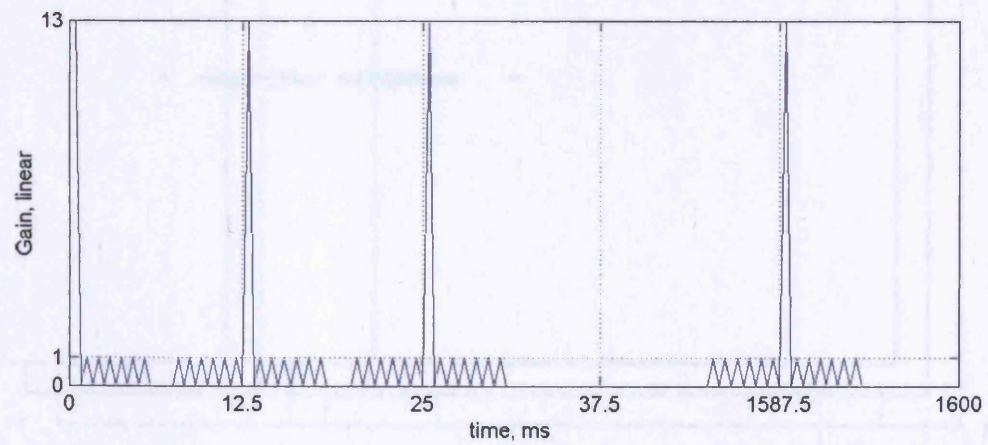
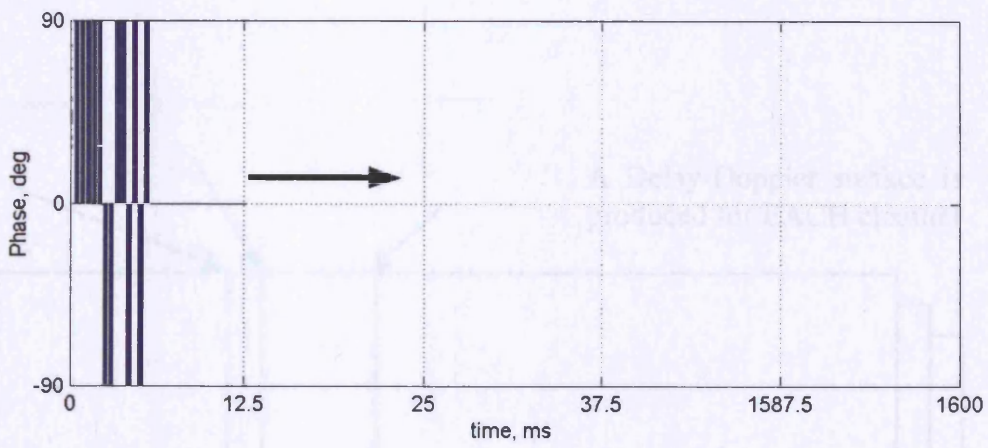
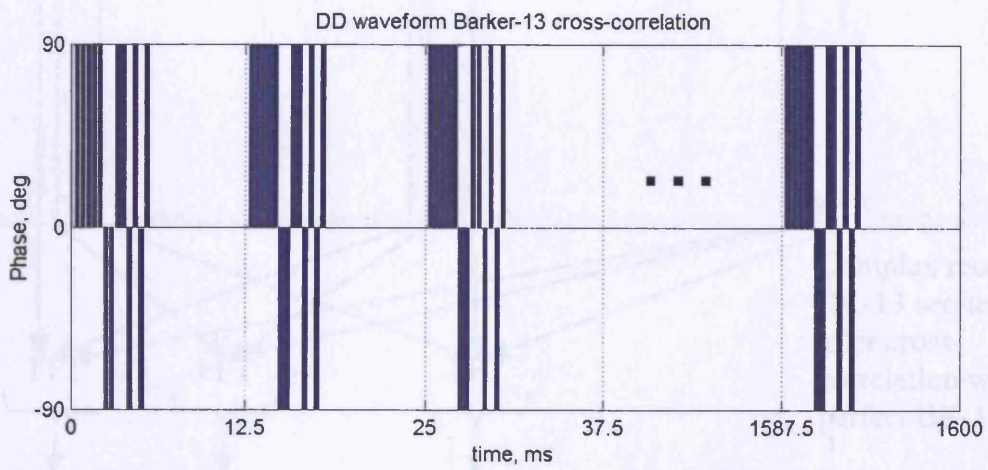


Figure 3.6 Cross correlation of the received DD waveform with a perfect Barker-13 sequence, resulting in a signal processing gain of up to 13x

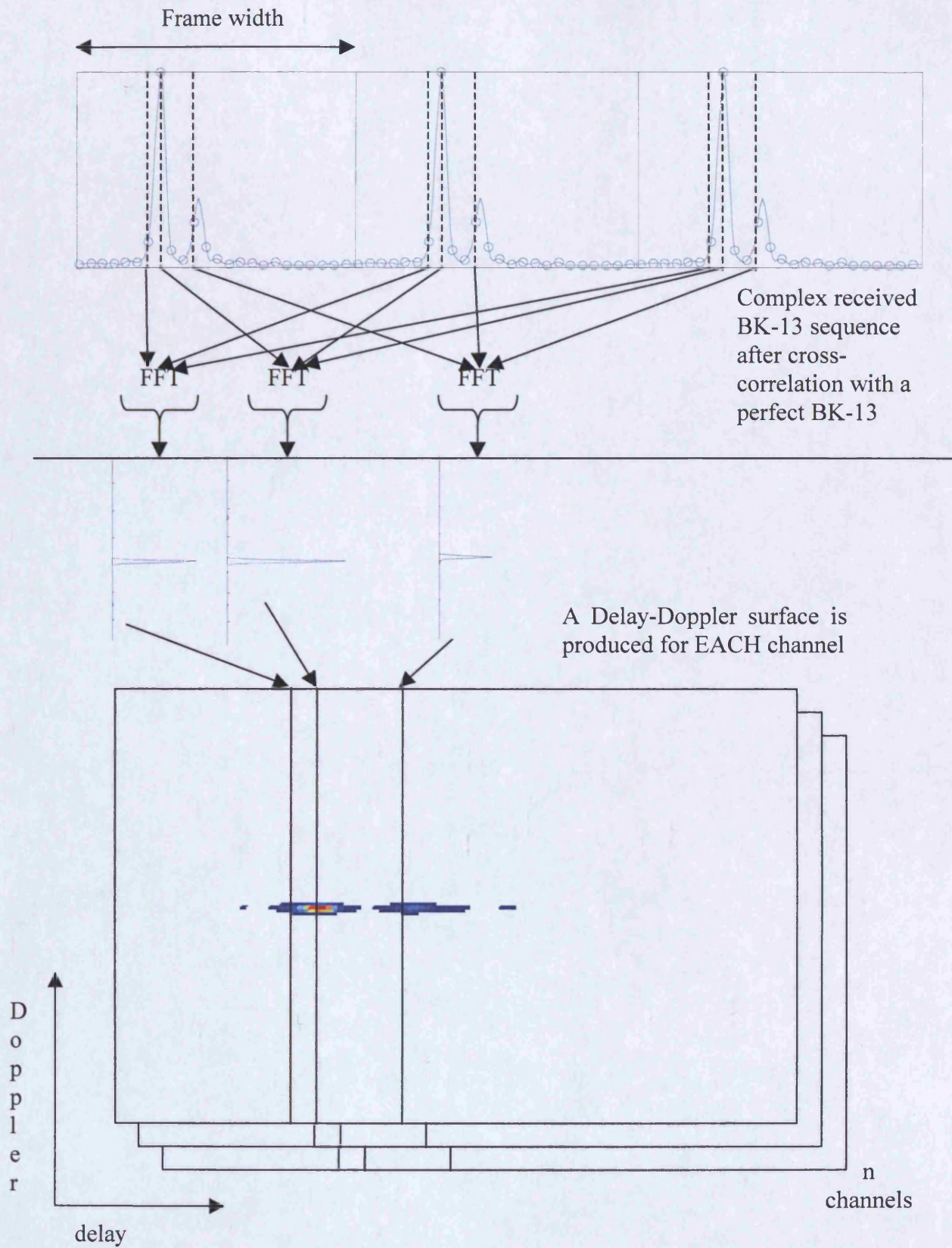


Figure 3.7 Calculation of the delay-Doppler surface

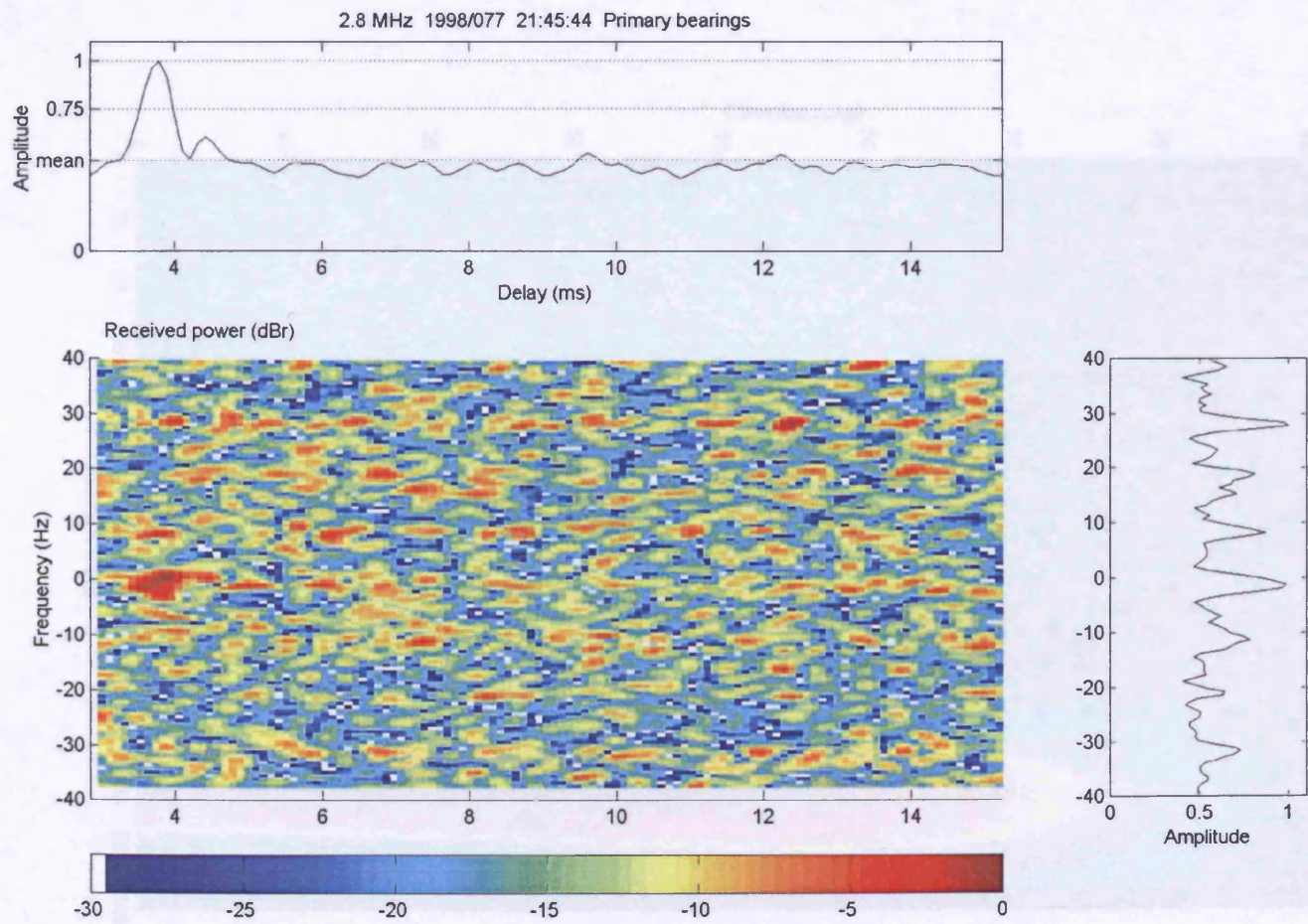


Figure 3.8 Example case that satisfies first pass selection criteria.

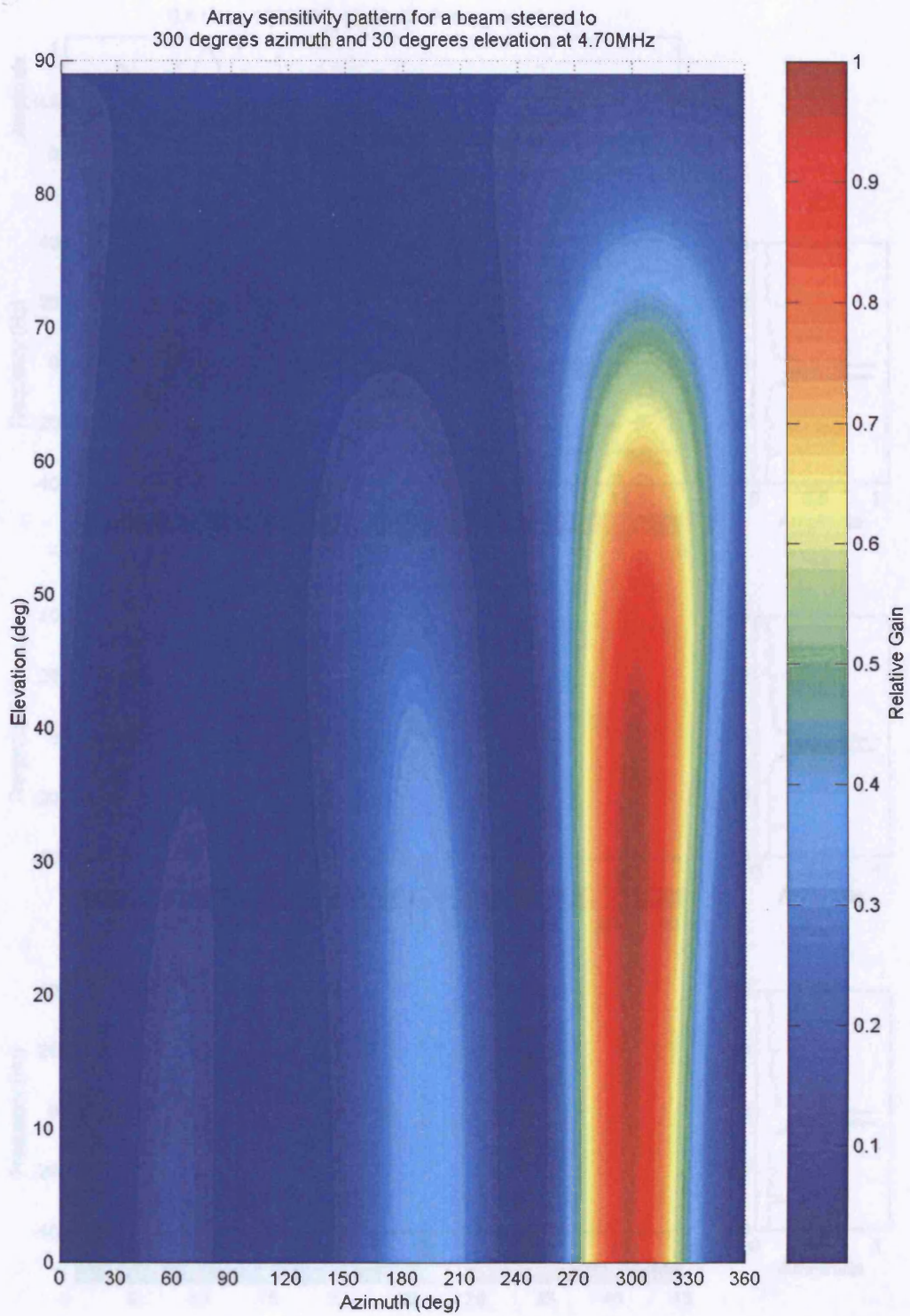


Figure 3.9 Array sensitivity pattern for a beam steered to 300° azimuth and 30° elevation at 4.7MHz.

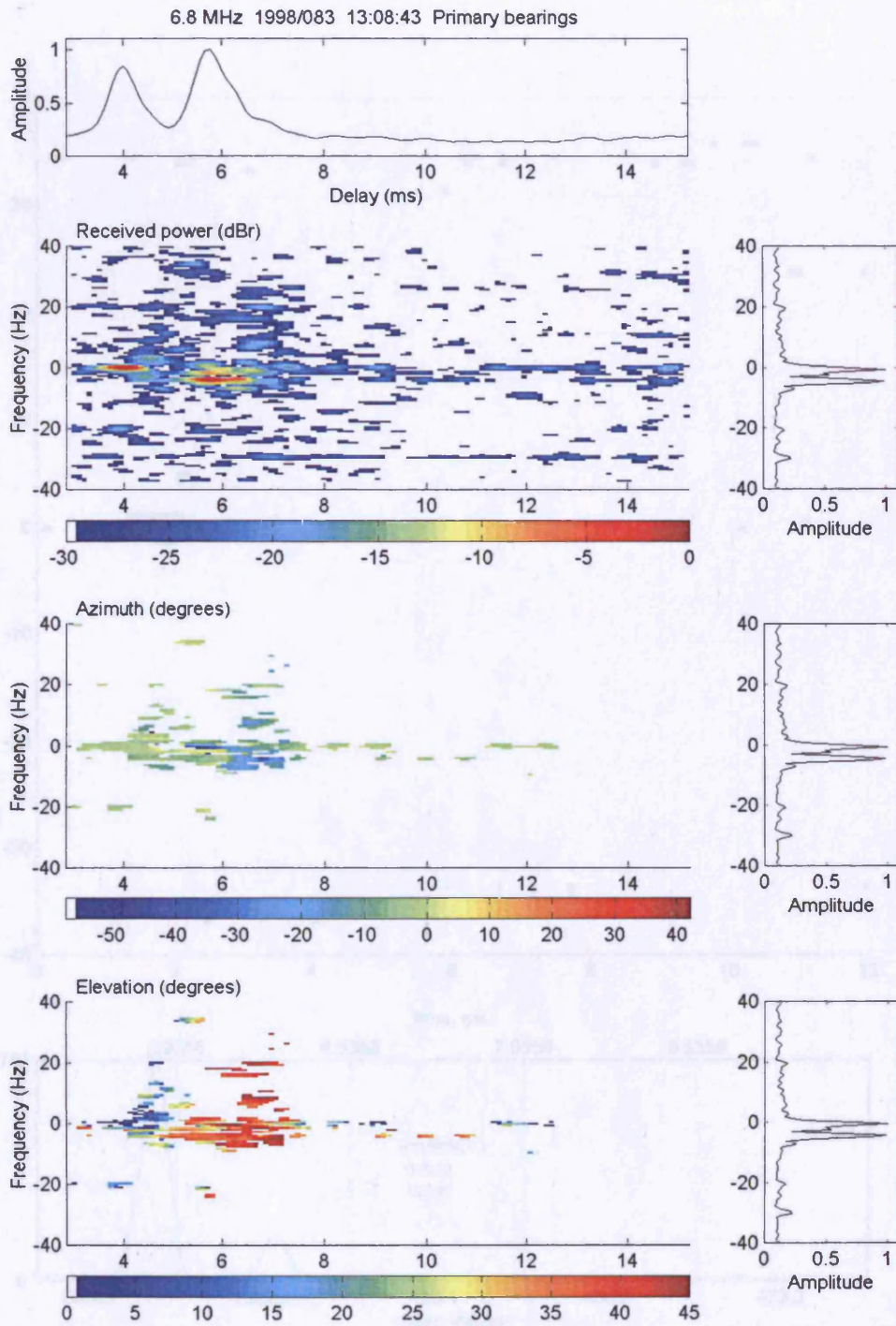


Figure 3.10 A Typical DD-DF plot illustrating a particular case from the Svalbard – Kiruna path.

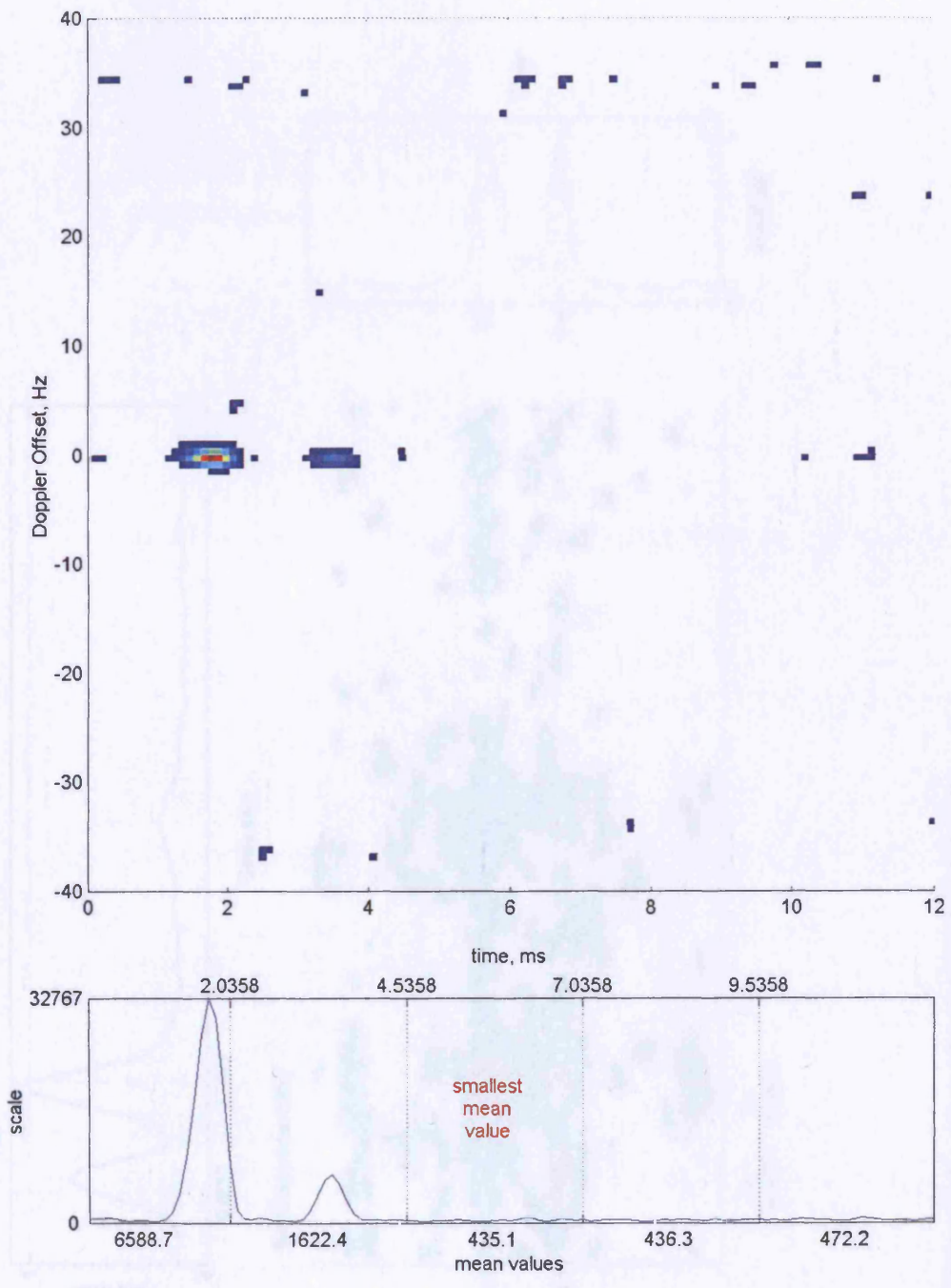


Figure 3.11 Calculating the noise floor

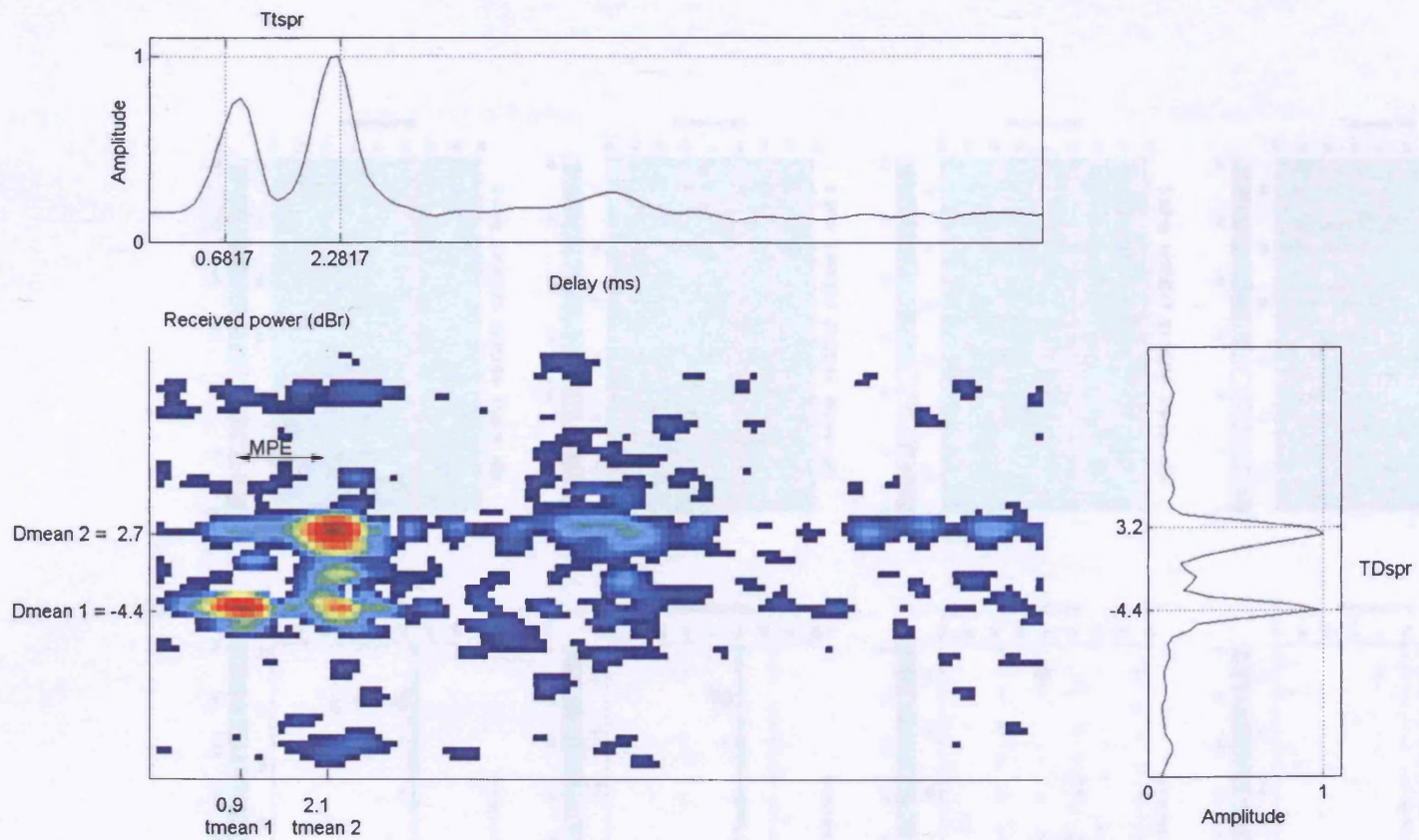


Figure 3.12 Illustration of some of the major characterised parameters.

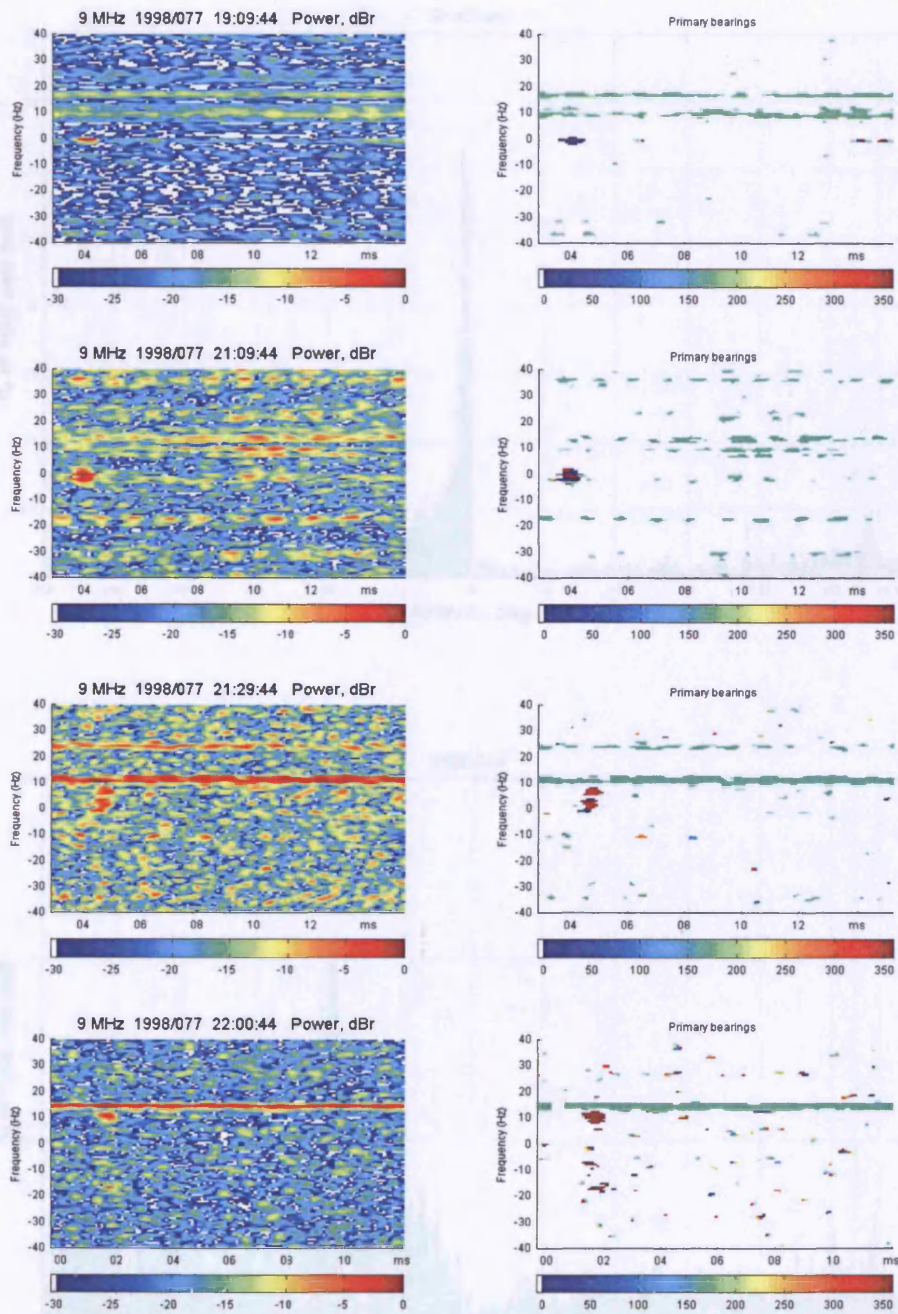


Figure 3.13 A sequence of soundings at 9MHz on 18<sup>th</sup> March in the presence of an interferer on a nearby frequency.

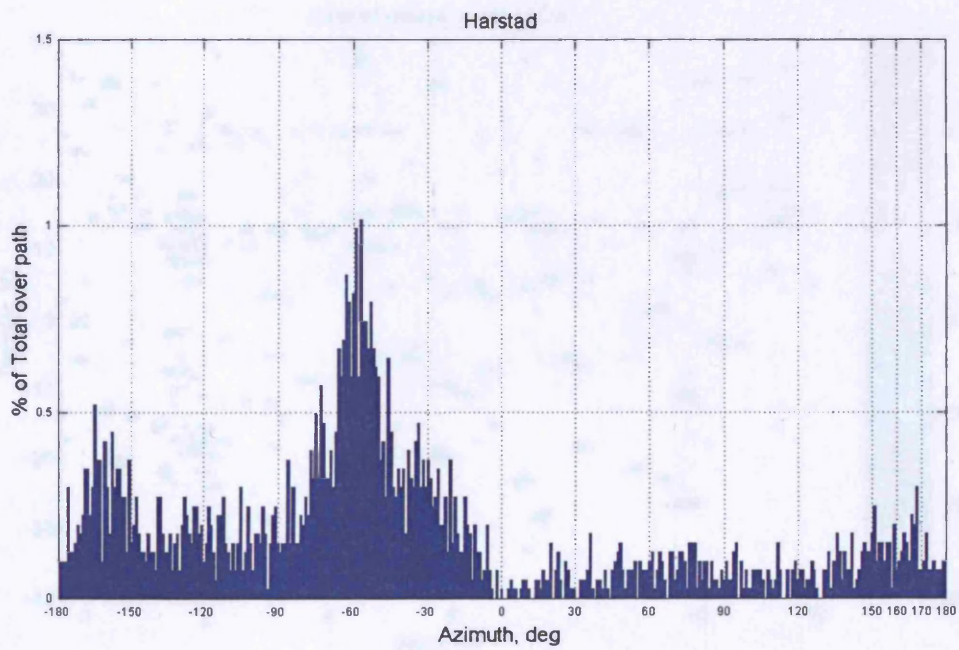
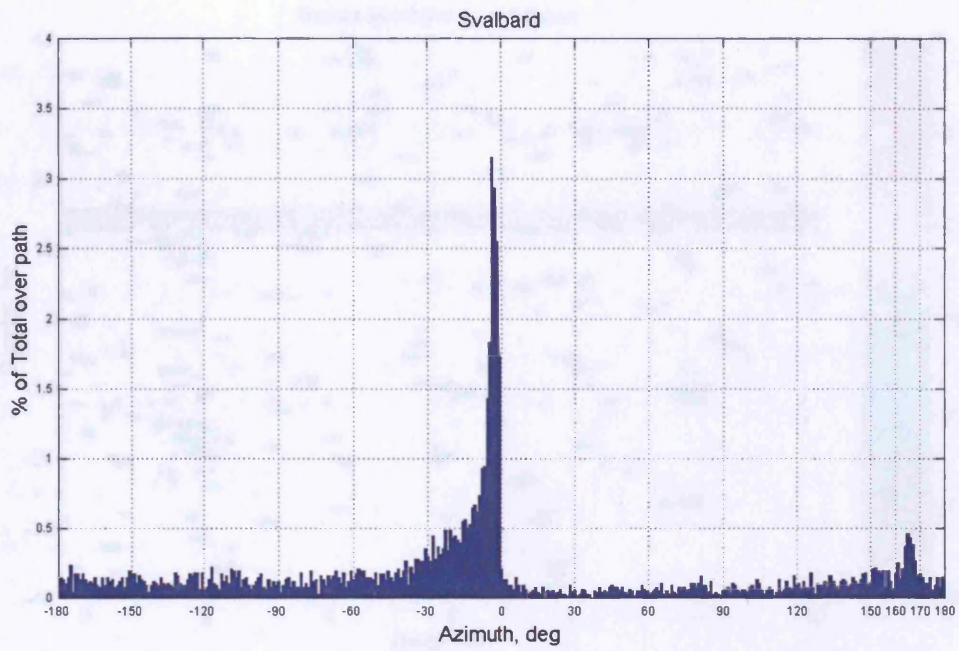


Figure 3.14 Histogram of all the selected azimuth measurements made over each path, (azimuth wraps at 180°).

#### 4. Survey of campaign data

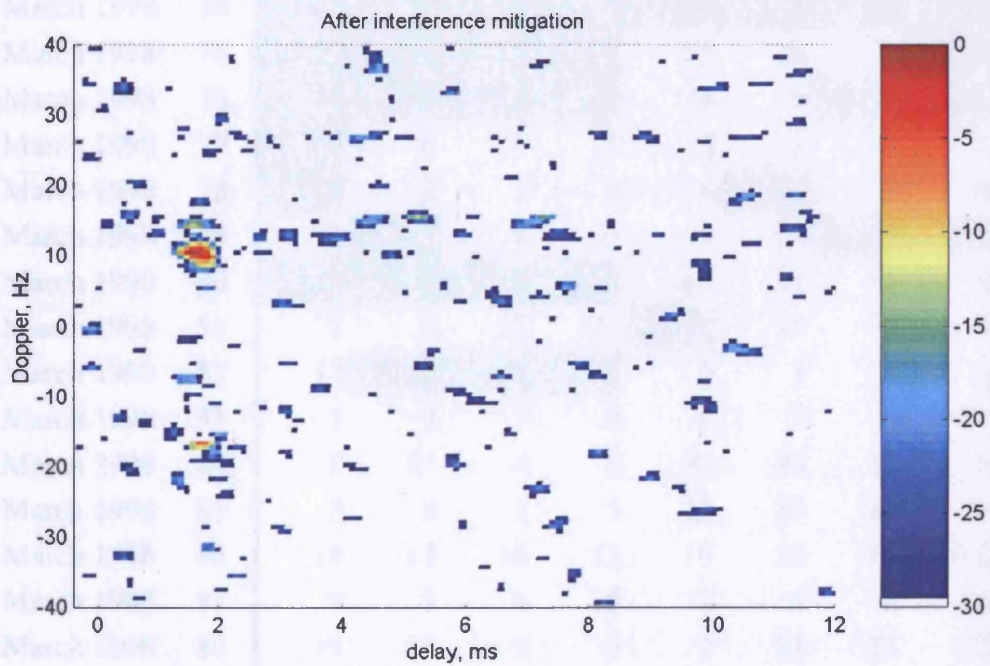
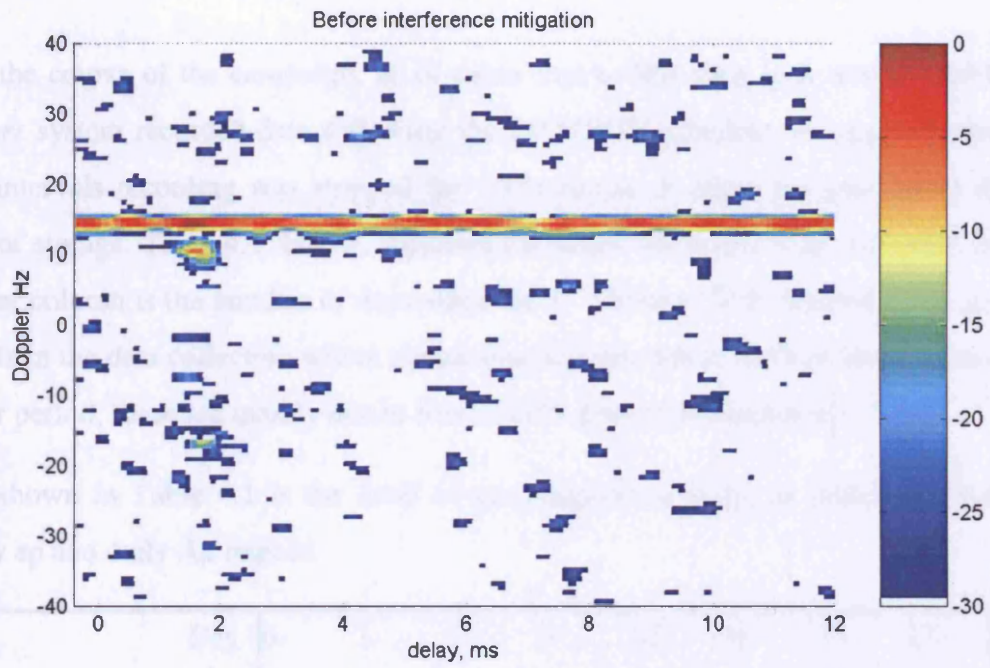


Figure 3.15 Effect of interference mitigation processing.

#### 4.1 First pass data analysis

### 4. Survey of campaign data

The first pass data set contains 2884 DO-DF cases over the Svalbard - Kongsfjord path and over the course of the campaign, at all times that a GPS time lock was available, the receiver system recorded data following the DAMSON schedule. At approximately 12 hour intervals recording was stopped for 100 minutes to allow the transfer of data to tape for storage. Table 4.1, below, indicates the times when data was collected, the day number column is the number of days since the 1<sup>st</sup> January 1998. Shaded times indicate periods in the data collection where measurements were made for less than 1 hour of the 3 hour period, these are mainly due to loss of GPS time synchronisation.

Also shown in Table 4.1 is the level of geomagnetic activity, as indicated by the 3-hourly ap and daily Ap indices.

Date	Day num	0-	3-	6-	9-	12-	15-	18-	21-	Ap
		3	6	9	12	15	18	21	24	
14 March 1998	73	6	3	5	9	9	22	15	15	10
15 March 1998	74	48	39	27	7	9	6	5	15	20
16 March 1998	75	22	15	12	7	12	18	7	4	12
17 March 1998	76	9	12	5	15	6	3	4	9	8
18 March 1998	77	3	6	3	2	2	3	3	7	4
19 March 1998	78	5	2	2	3	4	4	3	6	4
20 March 1998	79	12	3	4	7	7	15	9	9	8
21 March 1998	80	9	6	9	32	67	94	56	9	35
22 March 1998	81	7	9	15	22	12	18	12	4	12
23 March 1998	82	12	12	3	2	3	3	3	6	6
24 March 1998	83	2	3	7	6	9	5	7	15	7
25 March 1998	84	9	15	4	9	32	39	12	6	16
26 March 1998	85	3	6	2	9	22	27	15	9	12
27 March 1998	86	18	12	18	12	15	15	18	12	15
28 March 1998	87	9	15	6	15	12	6	6	18	11
29 March 1998	88	39	27	9	5	9	39	22	12	20
30 March 1998	89	5	6	12	7	7	9	5	12	8
31 March 1998	90	18	22	15	5	5	2	0	4	9

Table 4.1 Geomagnetic indices vs. date, with data collection periods superimposed.

It is clear that Day 80 is the most geomagnetically active day of the campaign, particularly in the early afternoon. Fortunately this coincided with a successful collection period.

## 4.1 First pass data analysis

The first pass data set contains 2884 DD-DF cases over the Svalbard – Kiruna path and 1505 DD-DF cases over the Harstad – Kiruna path. The number of first pass cases, collected over each path, are plotted on a colour scale against day number and time of day in Figure 4.1 while the distributions of first pass cases against transmit frequency are plotted in Figure 4.2.

Propagation over the longer Svalbard – Kiruna path was more successful than over the Harstad – Kiruna path. This success is due to the obliqueness of the path allowing propagation of the higher frequency transmissions to the receiver.

Both paths show evidence of preferential propagation in the afternoon and evening, this is more noticeable over the Svalbard – Kiruna path than the Harstad – Kiruna path. Although the empty data periods reported above generally occurred in the mornings, it is evident from examination of the colour plots in Figure 4.1 that even on the days when there were few empty data periods, propagation is more successful in the afternoon and evening. This coincides with expected peaks in the diurnal variation of ionospheric electron density as previously indicated in Figure 1.2.

The distribution against transmit frequency for the Svalbard – Kiruna path, in Figure 4.2(a), indicates that, while propagation is supported on each of the transmit frequencies, there is preferential propagation over the middle frequencies in the range. This is expected, since at the lower frequencies there is likely to be increased absorption while the higher frequencies may penetrate. The Harstad – Kiruna path distribution with regard to transmit frequency illustrated in Figure 4.2(b) is very different. There appears to be minimal or no support at the higher frequencies while there is very good support at the lower frequencies. Again this is expected since the path is much shorter and the maximum oblique propagation frequency for this path will be much lower than for the longer, more oblique, Svalbard – Kiruna path. Calculated values for the oblique propagation frequency, based on F2 virtual height and vertical critical frequency measurements made at Kiruna ionosonde and retrieved from the world data centre website (see references), are plotted in Figure 4.3. These indicate that the oblique propagation frequency for this path should never have exceeded 8.1MHz.

In order to assist in the analysis of this data, automatic characterisation scripts were developed which extract parameters of interest from each composite DD-DF case. These scripts use image processing techniques and have been described in section 3.7. They have been used to generate a parameter database for the first pass data set, which may be searched for cases exhibiting particular properties.

## 4.2 Time delay spreads

Delay spreading was observed in the first pass data sets for both the Svalbard – Kiruna and the Harstad – Kiruna paths. Figure 4.4 and Figure 4.5 are examples from each path. Delay spreading is often caused by signal propagation via multiple paths. Multiple paths may have reflection points distant from each other, generally leading to well separated modes in time (as can be the case for combined single and multi-hop propagation or combined great circle and off great circle propagation). However this is not always the case, reflection points may be clustered close to each other leading to an apparent delay spread mode or the time of flight difference between propagation paths may be smaller than the time resolution of the measurement system.

Two of the characterised parameters describing the amount of delay spreading on a signal are the 80% power time width ( $T_{tspr}$ ) and the equivalent multipath spread (MPE), these were described in section 3.7.2. In order to distinguish genuinely multi-moded cases, as opposed to broadly spread single modes, the time resolution of the system must be considered.

As described in section 3.2.1, the DD waveform has a time resolution of approximately 0.4ms, however, the incoming DAMSON signals were oversampled at a rate of 20000 samples per second and then interpolated down to 9600 samples per second for processing. The RSL system processing therefore has the same time resolution of 1/9600s (approximately 0.1ms) as the standard DAMSON processing. The extent of a perfectly propagated mode in the time dimension, after processing in this way, should be measurable at 0.4ms. With reference to Figure 4.4 and Figure 4.5, the assumption that a single mode has an approximately Gaussian shape seems reasonable. The measured 80% power widths of the individual modes in these cases is ~0.4ms, which is very close to the ideal compressed pulse width.

The minimum condition to resolve two modes is that the peaks of each mode must be separated to avoid the tails of the modes overlapping enough to look like a single mode, this will occur when the mode centres are separated by at least 0.65ms. When this condition is met the new 80% power width for the two modes is ~1.2ms (see Figure 4.6(a)).

In terms of the MPE parameter, the condition to resolve two separate modes is that the detected modes must be separated by at least one resolution cell. In practice many observations indicate that the extent of the signal energy above the detection threshold (as defined in section 3.7.1) is close to 1ms, even for a very cleanly propagated signal.

The example in Figure 4.6(b) has two modes of a given compressed pulse width,  $\tau$ , each with the same signal energy, separated by one resolution cell in time. This situation will give an Equivalent Multipath, MPE, value of  $(\frac{1}{2}\tau + \frac{1}{2}\tau + 0.1\text{ms})$ . For the observed, detected, pulse width of 1ms this gives a minimum resolvable MPE value of 1.1ms.

#### *4.2.1 Signal to Noise ratio considerations*

In low SNR cases there will be a number of noise spikes exceeding the detection threshold. The nature of random noise means that these spikes will be distributed across the whole DD plane. Some of these noise spikes will be very distant from the actual signal energy on the DD plane. The examples in Figure 4.7 illustrate the effect. If this occurs, the time term in the MPE equation (Equation 3.1) will dominate and the MPE parameter will be unrealistically large. The statistical nature of the Ttspr calculation, however, means that these noise spikes will not have such a large effect on the Ttspr parameter. Nonetheless, in order to reduce the uncertainty in the statistics, first pass cases that fell below an SNR threshold of 0.2 (-7dB) were discarded.

For the purposes of selecting cases for analysis, the Ttspr parameter appears to be an appropriate guide and based on the previous discussions, 1.2ms is a representative value of Ttspr, above which it is likely that multipath propagation is occurring.

Of the 4224 first pass cases remaining after the elimination of the low (<-7dB) SNR cases, 487 (11.5%) exceed this delay spread criteria of >1.2ms. Over the Svalbard – Kiruna path 310 (11.2%) of the 2773 remaining first pass cases for that path exhibit

such delay spread. Over the Harstad – Kiruna path the value is 177 (12.2%) out of 1451 cases.

Conversely, the number of cases with very little delay spread ( $T_{\text{tspr}} \leq 1.2\text{ms}$ ) is 3737 (88.5%) out of 4224 cases overall, with 2463 (88.8%) out of 2773 for the Svalbard – Kiruna path and 1274 (87.8%) out of 1451 for the Harstad – Kiruna path.

### 4.3 Doppler spreads

Due to the varying dynamic nature of the ionosphere, it was expected that Doppler spread propagation would be observable in the first pass data. Over the course of the campaign a number of examples were recorded.

Figure 4.8 is a DD-DF plot illustrating a Doppler spread example over the Svalbard – Kiruna path. In this case there is a large amount of Doppler spread (frequency dispersion) contained in a single mode having some time dispersion too. As discussed in section 2.1.1, *Wagner et al.* [1988 and 1995] suggest that such signal properties are due to propagation via scattering from drifting irregularities rather than a specular reflection process. They were unable to determine the drift direction from the scattergram alone. Direction of arrival information, however, may be able to resolve this ambiguity.

Doppler spreading can occur on any or all modes of a multi-moded signal. Some example case studies will be examined in detail in Chapter 5 with a view to forming an understanding of the propagation processes leading to such characteristics.

Section 1.7 describes the response to multipath and Doppler spread of two Mil-Std-188-110A modems (operating at 300bps and 1200bps respectively). These were measured using an HF channel simulator and presented in Figure 1.16 and Figure 1.17.

It was noted that there were boundaries, in terms of multipath and Doppler spread, in the performance of a given modem, beyond which it will fail to operate. These breaking points were seen at around 7ms multipath delay spread and 7Hz Doppler spread for the 1200bps modem, while the 300bps modem breaking points are around 7ms delay spread and 25Hz Doppler spread. For convenience, cases referred to here as having ‘Wide Doppler spread’ are those that exhibit Doppler spreads in excess of 7Hz, which is the

upper Doppler spread boundary on the performance surface of the Mil-Std-188-110A 1200bps modem.

#### *4.3.1 Signal to Noise ratio considerations*

Figure 4.9 is a plot of the SNR vs. Doppler spread for both paths. The red line indicates the 7Hz threshold, while the histogram displays the distribution of first pass cases having wide Doppler spread against SNR. It is clear that a significant number of wide Doppler spread cases have low SNR. It was noted that for many of these wide Doppler spread, low SNR, cases it is unclear whether there is a genuine Doppler spread due to dynamic propagation conditions or whether the applied thresholding process is capturing noise, which may appear over all Doppler offsets, as well as actual signal energy. Again Figure 4.7 illustrates the problem.

There appears to be no discernible signal in Figure 4.7(a), simply a lot of noise. It is surprising that this case passed the first pass criteria of mean power  $< 0.75 \times \text{peak power}$ . However, examination of the top panel of Figure 4.7(a), showing the normalised power vs. time, indicates that there might be a signal around 4ms delay and that it is this power that is allowing this case entry into the first pass data set. Nonetheless, with such a low SNR it is almost impossible to set an appropriate threshold in the DD domain and subsequently extract information about the propagation conditions.

The same is true of Figure 4.7(b), however, in this case the signal energy arriving around 4ms delay is more apparent in the top panel although there are no obvious peaks on the DD plane. This indicates that it probably is a genuinely Doppler spread case that also has very low SNR.

In Figure 4.7(c) the signal energy is more apparent, appearing around 4ms. A lot of the energy in this signal appears to be around 0Hz Doppler shift and is not very spread. However, the SNR of this case is also quite low and noise energy is again appearing above the detection threshold and contributing to the calculation of Doppler spread. In this instance there has been a misrepresentation of the propagation conditions where the characterisation indicates large Doppler spread on the signal when there is only modest Doppler spread and a poor SNR.

In order to address problems with low SNR, a threshold of -7dB has been used to eliminate first pass cases such as described above. Of the total 4224 cases with SNR  $\geq$ -7 dB, overall 473 (11.2%) have wide Doppler spread, which include 297 (10.7%) of the 2773 cases occurring over the Svalbard – Kiruna path and 176 (12.1%) of the 1451 cases occurring over the Harstad – Kiruna path.

Conversely, the number of cases which do not exceed the 7Hz threshold are 3751 (88.8%) out of 4224 overall, with 2476 (89.3%) out of 2773 over the Svalbard – Kiruna path and 1275 (87.9%) out of 1451 over the Harstad – Kiruna path.

#### 4.4 Summary

Figure 4.10 is a summary, over all frequencies, of the simultaneous distribution of delay and Doppler spread for all cases exceeding -7dB SNR over each path. Also marked are the breaking point boundaries for a Mil-Std-188-110A modem operating at 1200bps. It is interesting to note that no cases exceed the delay spread boundary, while a number do exceed the Doppler spread boundary. The hyperbolic line is a line of constant spread factor, where spread factor is the dimensionless product of delay spread and Doppler spread. In this case the spread factor has been fixed at  $7\text{Hz} \times 7\text{ms} = 49 \times 10^{-3}$ .

For the purposes of grouping the first pass data set, using the parameter database, boundaries on the definition of delay spread cases and Doppler spread cases have been chosen based on the discussions in sections 4.2 and 4.3. Any case having  $T_{\text{tspr}} > 1.2\text{ms}$  is characterised to be ‘Delay spread’ and any case having  $T_{\text{Dspr}} > 7\text{Hz}$  is characterised to have ‘Wide Doppler spread’. The numbers of first pass cases, which equal or exceed an SNR of -7dB, falling into each category, are summarised in Table 4.2.

From this table, it is clear to see that by far the most common form of characterised signal observed in the first pass data set are narrow in both delay and Doppler spread. These comprise 3454 (81.8%) of cases out of the total 4224 with 2282 (82.3%) out of 2773 over the Svalbard – Kiruna path and 1172 (80.8%) out of 1451 over the Harstad – Kiruna path. The low number of delay and Doppler spread cases reflects the generally quiet geomagnetic conditions prevalent during the campaign, resulting in relatively favourable propagation conditions. These numbers would be likely to increase as

geomagnetic activity increases and propagation conditions become less favourable. Nonetheless there are sufficient cases to justify a statistical treatment.

	Not delay spread ( $\leq 1.2\text{ms}$ )			Delay spread ( $> 1.2\text{ms}$ )			Total
	Svalbard	Harstad	Both	Svalbard	Harstad	Both	
Narrow Doppler ( $\leq 7\text{Hz}$ )	2282	1172	3454	194	103	297	3751
Wide Doppler ( $> 7\text{Hz}$ )	181	102	283	116	74	190	473
Total	2463	1274	3737	310	177	487	<b>4224</b>

Table 4.2 Numbers of cases falling into each category

#### 4.5 Occurrence statistics of both narrow delay and Doppler spreads

Since signals having both narrow delay and Doppler characteristics, as defined above, comprise the largest part of the first pass data set, they provide the most statistically stable sample. Figure 4.11 illustrates typical examples of these signals. This type of signal falls within the boundaries of operation of the Mil-Std-188-110A 1200bps modem, so should provide favourable operating performance.

On examination of the distributions of transmit frequency vs. time of day (Figure 4.12 and Figure 4.13) there is a distinct trend in propagation success of the different frequencies. During the course of the early hours of the morning, over the Svalbard – Kiruna path, support for the lower frequencies is good and for the middle frequencies improves during the morning towards midday. This support continues through the afternoon with success of higher frequency propagation evident in the early evening, after when support for the high and middle frequencies drops off towards midnight. This behaviour is consistent with the expected diurnal variation in ionospheric electron density, see Figure 1.2(a), including in the D-region which is responsible for absorbing the lower frequencies during the middle of the day. Over the Harstad – Kiruna path there is of course no support for the higher frequencies. Around midday there is increased

propagation towards the top end of the lower frequencies and a reduction in the propagation of the lowest frequencies, which tails off during the evening.

Direction of arrival and time of flight are plotted vs. time of day for each path respectively in Figure 4.14 and Figure 4.15. Each point is colour coded to the transmit frequency and histograms of the distributions are also shown. Due to the length of the Svalbard – Kiruna path, not much structure is visible in the time of flight plot, with measurements between  $\sim 4 \rightarrow 5$ ms. As expected, the majority of direction of arrival (DOA) measurements over the Svalbard – Kiruna path fall close to the GCP direction, however, there is a significant number of measurements spread across all DOA.

Over the Harstad – Kiruna path, increases in the time of flight, associated with support for higher transmit frequencies, during the daylight hours are clear, this is consistent with the diurnal variation in F-region height and oblique frequency (as indicated in Figure 4.3). Short flight times of around 1ms, at the lower frequencies, still occur throughout most of the day; these flight times are consistent with 1-hop E-region propagation, where the measured E-region virtual height was between 110km and 130km.

The DOA measurements for the Harstad – Kiruna path have a broad distribution around the GCP direction, with a small cluster of arrivals appearing around  $200^\circ$ . There are few arrivals from the North or the East of the receive site. The majority of the successful 6.78MHz transmissions, one of the higher frequencies supported on this path, appear from a direction North-West of the receiver, around  $\sim 340^\circ$ . As expected longer flight times are associated with non-GCP propagation, while the shorter times of flight are associated with lower frequency near-GCP E-region propagation. The variation in DOA appears to be greater for F-region propagation than for E-region.

Figure 4.16 presents azimuth histograms for the lowest four frequencies propagated over the Harstad – Kiruna path. It is clear that there is some variation in measured DOA against frequency with the peak directions of arrival at  $298^\circ$  and  $294^\circ$  for the lowest three frequencies and the previously noted daytime arrivals from  $\sim 340^\circ$  on 6.78MHz.

The small cluster of arrivals from the south at around  $200^\circ$  seems to occur on most days between approximately 0500  $\rightarrow$  1700 with the majority before midday. The preferred propagation frequencies for this DOA appear to be 3.95MHz and 4.70MHz. This

behaviour occurs consistently during the campaign. It is possible that these signals are arriving via reflections from the mid-latitude trough to the south of the path midpoint, however, during the campaign sunrise was slightly earlier than 0500 so that the path was in daylight during the time when these southern arrivals occurred. This would be inconsistent with the usual behaviour of the trough. The elevation measurements for these cases are higher than usual, while the flight times are similar to a normal F-region mode. This suggests that a local tilt or irregularities close to the south of the receiver might be producing these southern arrivals. Such ionospheric behaviour, however, is unlikely to occur as consistently as seen here. Although an interferer could be a more consistent feature, the cluster is clearly not due to an interferer since the times of flight are consistent with normal F-region propagation and it occurs on two frequencies. Importantly, the cases have been selected for both small delay spread and narrow Doppler spread, neither of which are characteristic of interferers.

Figure 4.17 illustrates this cluster more clearly using a time of flight vs. azimuth plot in the upper panel and an elevation vs. azimuth plot in the lower panel, both have a colour scale proportional to the transmission frequency. The lower frequency transmissions are generally associated with the shorter E-region times of flight. The cluster of arrivals around  $200^\circ$  azimuth is clearly visible, having a 1-hop F-region time of flight and transmit frequencies, similar to the  $\sim 300^\circ$  DOA arrivals, of 3.95MHz and 4.70MHz. The 3.95MHz and 4.70MHz cases are obviously split between  $\sim 300^\circ$  and  $\sim 200^\circ$  azimuth. Recalling the discussion in section 3.5.1 and examining the array sensitivity pattern in Figure 3.9 indicates that this could be a cluster of ambiguous measurements due to the array sidelobe characteristic, with the elevation preference due to slightly increased sidelobe sensitivity at those elevations. This does not depend on ionospheric behaviour and can occur quite consistently. The sidelobe is thus a likely cause of the cluster of measurements around  $200^\circ$  azimuth.

#### 4.5.1 Summary

The majority of first pass cases have small delay spread and narrow Doppler spread. The distribution of cases vs. time of day, frequency and DOA is as expected for the long and short paths respectively.

The statistical mode, mean and standard deviations of the power weighted time of flight and azimuthal DOAs of these cases, for each path are included in Table 4.3, along with the great circle path azimuths at the receiver. The tabulated values have been corrected for the 4.5° error in estimating the direction of North, described in section 3.1.

Path	Time of flight, ms		GCP, °	Azimuth, °		
	Mean	Standard deviation		Mode	Mean	Standard deviation
Svalbard – Kiruna	4.15	0.54	352.2	352.0	341.4	49.3
Harstad – Kiruna	1.64	0.81	294.6	293.5	284.9	51.0

Table 4.3

With the exception of bearings measured in a sidelobe of the array pattern, most of the measured azimuths are around the GCP direction. The Harstad – Kiruna path has a broader range of azimuths around the GCP, although the standard deviation of these is no larger than for the Svalbard – Kiruna path because that path exhibits a small number of arrivals from a very wide range.

There is a diurnal trend in propagation success of the different frequencies for both paths and for the Harstad – Kiruna path the diurnal variation of F-layer height is clearly seen in the time of flight measurements.

Most of the direction of arrival structure is seen over the Harstad – Kiruna path since this is the shortest and hence most sensitive to small changes in propagation geometry. An important observation as far as communications systems are concerned is the variation of DOA with transmission frequency over this path.

The DOA plots and Table 4.3 reveal that, although the cases examined were narrow in both delay and Doppler, there is considerable variation in the direction of arrival of these signals. This indicates that there must be some spatial variation in the ionosphere in these regions, which allows non-GCP propagation while not imposing Doppler spread in the same way as for propagation via irregularity regions.

## 4.6 Occurrence statistics of time delay spreads

Figure 4.18 and Figure 4.19 indicate the delay spreads for all cases having  $\text{SNR} \geq -7\text{dB}$  irrespective of whether this is due to single or multi-mode spreading. Some of these cases may also be Doppler spread, however, Doppler spread cases will be dealt with separately in section 4.7. The upper 10 panels are plots of the measured delay spread vs. time, in units of day number, for each transmitted frequency throughout the campaign, there is a dashed red line indicating 1.2ms of delay spread. The histogram in the right hand panel indicates the number of cases at each frequency that exceed this 1.2ms threshold while the histograms in the lower two panels represent the distribution of cases over all frequencies with delay spread that exceed 1.2ms vs. day number and time of day respectively. The time of day plot also has a superimposed blue trace representing the measured delay spreads  $>1.2\text{ms}$  over all campaign days. The total number of delay spread cases is identified in red to the right of these histograms.

The time of day histograms reveal that over the Harstad – Kiruna path there is a trend for less delay spread propagation during the daylight hours and more overnight. The lack of an absorbing D-region during the night allows more multipath propagation via longer (non-GCP) paths. Since non-GCP propagation over such a short path will lead to pronounced increases in delay compared to the GCP path, these cases will have larger delay spreads. Over the Svalbard – Kiruna path this effect is less apparent since it is already a long, oblique, path allowing the propagation of higher frequencies that are less affected by absorption.

When the Frequency distributions for each path are examined, the Svalbard – Kiruna frequency distribution for the delay spread cases demonstrates a preference for propagation at 4.7MHz, which is a lower frequency than for the overall distribution presented in Figure 4.2(a). Over the longer Svalbard – Kiruna path, a large proportion of the delay spread cases are likely to be due to multi-hop propagation. These multi-hop paths will have a lower MUF than the predominantly one hop single moded cases with delay spreads  $\leq 1.2\text{ms}$ . Since the Harstad – Kiruna path is already a short, near vertical incidence (NVIS), path where the time differences between 1-hop and multi-hop propagation is significant but the angle of incidence at the ionosphere is virtually the

same, the frequency distribution is very similar to the overall distribution in Figure 4.2(b), with most cases propagating at 4.7MHz and very few above this frequency.

Figure 4.20 and Figure 4.21 indicate the properties of each separate propagation mode, detected by the image processing scripts, for all delay spread cases propagated via the Svalbard – Kiruna and Harstad – Kiruna paths respectively. The top panel of Figure 4.20, which is colour coded for azimuth, reveals that most of the detected modes over the Svalbard – Kiruna path, with small times of flight, arrive from close to the GCP direction, while the longer delayed modes arrive from a range of azimuths. The lower panel of Figure 4.20 is plotted in polar coordinates with time of flight represented radially against azimuth and the points colour coded to the transmit frequency. It is clear that although there is a range of azimuths, there is a strong tendency for arrivals from the West. There is also a trend in delay apparent on this plot with the delay increasing as the direction of arrival moves from close to the GCP direction around to the West and then the South. A feature of this plot, however, is the ‘spoke’ of points, at the same frequency, aligned along  $\sim 165^\circ$ . This is clearly characteristic of the interferer described in section 3.8. Although the interference mitigation technique, described earlier, was used before the first pass data were processed by the characterisation scripts it has not been completely effective. Closer examination of the upper panel of Figure 4.20 indicates that the interferer only appears to be present between  $\sim 18:00$ hr and  $01:00$ hr each day, this has been confirmed using the histogram of frequency of occurrence of such signals vs. time of day in Figure 4.22. Given that this interferer has now been identified, the best way to reduce its impact is to ignore detected signal energy arriving from  $\sim 165^\circ$  at 9.04MHz during the times when it is expected to be present.

The upper plot of the Harstad – Kiruna data presented in Figure 4.21 shows a similar trend to that in Figure 4.20 whereby the shorter delay modes arrive from close to the GCP direction while the longer delay modes arrive from a range of azimuths. The lower, polar, plot reveals that most of the detected modes are arriving from the West.

## **4.7 Occurrence statistics of large Doppler spreads**

Figure 4.23 and Figure 4.24 display the Doppler spread statistics in a similar format to that used previously for the delay spread statistics. In these examples the y-axes of the upper 10 panels represent the measured 80% Doppler width of all the first pass cases

with  $\text{SNR} \geq -7\text{dB}$ , with a dashed red line indicating the 7Hz Doppler spread threshold above which a Mil-Std-188-110A modem operating at 1200bps will fail. The histograms represent the occurrence of such wide Doppler spread cases vs. frequency, day number and time of day respectively.

The largest numbers of wide Doppler spread cases occur on Day 84 for the Svalbard – Kiruna path, while for the Harstad – Kiruna path Days 80, 84 and 88 have the most. These times align well with the periods of higher magnetic activity as indicated in Table 4.1.

The wide Doppler spread cases appear to occur most frequently in the evening and night. These times approximately span midnight CGMLT (Corrected GeoMagnetic Local Time) at around 21:30 UT during the campaign. This is when the auroral oval reaches its most southern extent and thus when the propagation medium is most likely to be disturbed.

The shape of the distribution of Doppler spread cases vs. frequency over the Svalbard – Kiruna path is very similar to the overall distribution of all first pass cases vs. frequency for this path, irrespective of Doppler spreading (Figure 4.2(a)). The peak has moved from 6.78MHz to 9.04MHz, probably due to the higher levels of electron density in the ionosphere during the more disturbed periods when Doppler spreading occurs, which also allows higher propagation frequencies.

The shape of the distribution of Doppler spread cases vs. frequency over the Harstad – Kiruna path, however, is quite different compared to the overall distribution of all first pass cases vs. frequency for the path, irrespective of Doppler spreading (Figure 4.2(b)). The distribution has moved to higher frequencies with Doppler spread propagation appearing to occur most often at 4.7MHz and 6.8MHz and many fewer cases appearing at frequencies below these. The higher levels of ionisation during the disturbed periods allow the propagation of higher frequencies but causes absorption at the lower frequencies.

Histograms of the distributions of wide Doppler spread cases are plotted against azimuth in Figure 4.25 for each path. For the Svalbard – Kiruna distribution, while there appear to be slightly more Doppler spread signals arriving from close to the GCP, there are very few Doppler spread signals arriving from the North-East ( $\sim 0^\circ \rightarrow \sim 90^\circ$ ). The

most obvious feature of the distribution is the peak around  $\sim 165^\circ$  which is due to the interferer mentioned in section 3.8, this has been confirmed by verifying the frequency to be at 9.04MHz. It is clear that the interference mitigation technique described in section 3.8 has not been completely effective again. There is also an interferer peak around  $165^\circ$  in the Harstad – Kiruna distribution too. Apart from this there is not much structure in the distribution with Doppler spread cases arriving from all directions, although there does appear to be a slight preference for directions near to the GCP direction.

The small number of wide Doppler spread cases means that, beyond these relatively straightforward observations, not much more can be said about the distributions.

## **4.8 Concluding remarks**

The first pass data set has been surveyed with the aim of classifying the different types of propagation observed during the campaign. It is clear that there are a variety of propagation mechanisms occurring to cause the observed variation in the characteristics of the DD-DF plots.

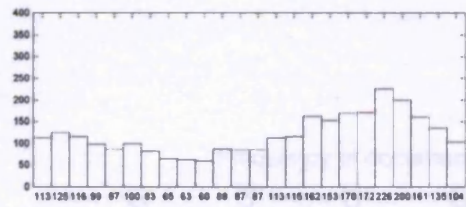
The data set was classified according to delay spread (narrow or wide) and Doppler spread (narrow or wide). Two useful parameters for the estimation of delay spread in a scattergram (MPE and  $T_{\text{spr}}$ ) were discussed in terms of the resolution of the DAMSON system and their sensitivity to poor SNR.  $T_{\text{spr}}$  was chosen to characterise delay spread because of its lower sensitivity to SNR. Similarly, Doppler spread was estimated with the  $T_{\text{Dspr}}$  parameter. Boundaries were placed on the definitions of narrow and wide delay and Doppler spread according to the performance of the DAMSON system and of the Mil-Std-188-110A 1200bps modem discussed in section 1.7. These boundaries were set at 1.2ms delay spread and 7Hz Doppler spread. The numbers of cases in the data set falling into each category are summarised in Table 4.2.

The majority of first pass cases are seen to have small delay spread and narrow Doppler spread. Due to the generally quiet geomagnetic conditions prevalent during the campaign, there are only a relatively small number of cases that exhibit complex properties related to the propagation environment.

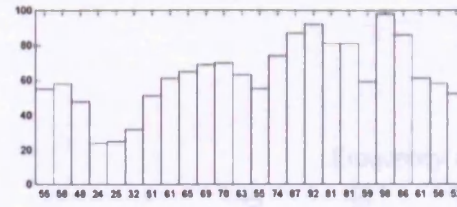
Since signals having both narrow delay and Doppler characteristics, as defined above, comprise the largest part of the first pass data set, they provide the most statistically stable sample. In general the occurrence statistics for these signals were as expected, with diurnal variation in successful propagation frequency and time of flight consistent with well understood changes in ionospheric structure during the day. Surprisingly, however, there was a significant statistical spread in the measured directions of arrival over both paths.

The statistical behaviour of the more complex delay or Doppler spread cases generally agrees with observations made previously by other authors involved with the DAMSON project. For the wide delay spread cases, analysis of the DF information did reveal that while much of the signal energy arriving at longer delays was from off GCP directions, the shorter delayed signal energy was often from the GCP direction. For the wide Doppler spread cases, signal energy was seen to arrive from a large range of angles with a small preference for directions close to the GCP. Doppler spreading was more prevalent around midnight CGMLT, which is when the auroral oval reaches its most southern extent and thus when the propagation medium is most likely to be disturbed

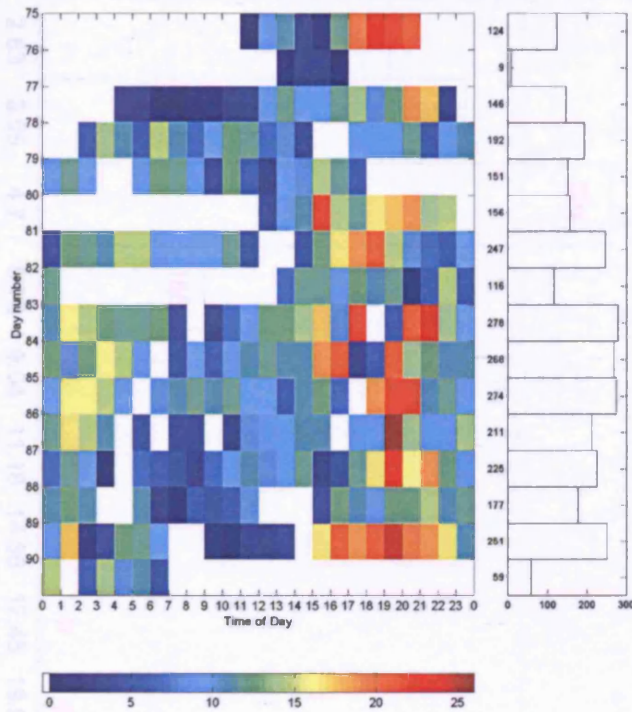
Since there is only a small number of these delay or Doppler spread cases available, the statistical value of this analysis is limited. Information regarding the short term behaviour of the channel, and the propagation environment, however, can be gained by studying a few cases in detail. This will also allow the best use of the available direction of arrival information.



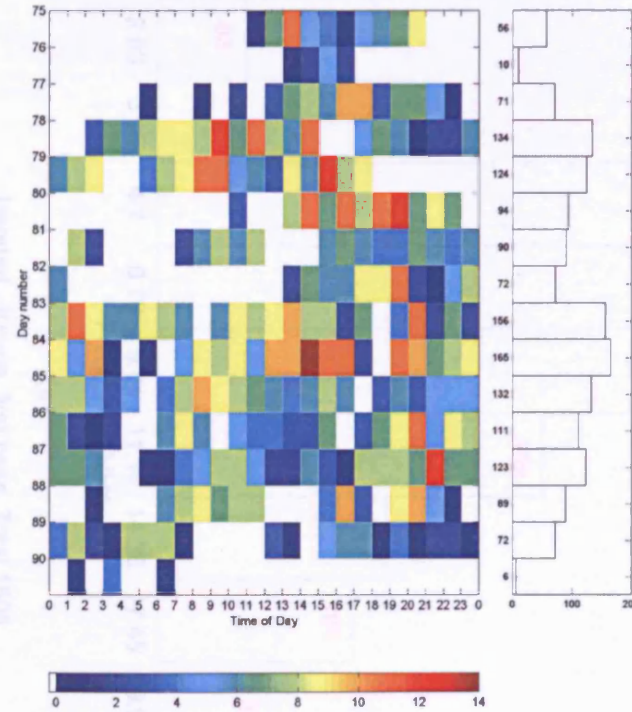
Total  
2884



Total  
1505

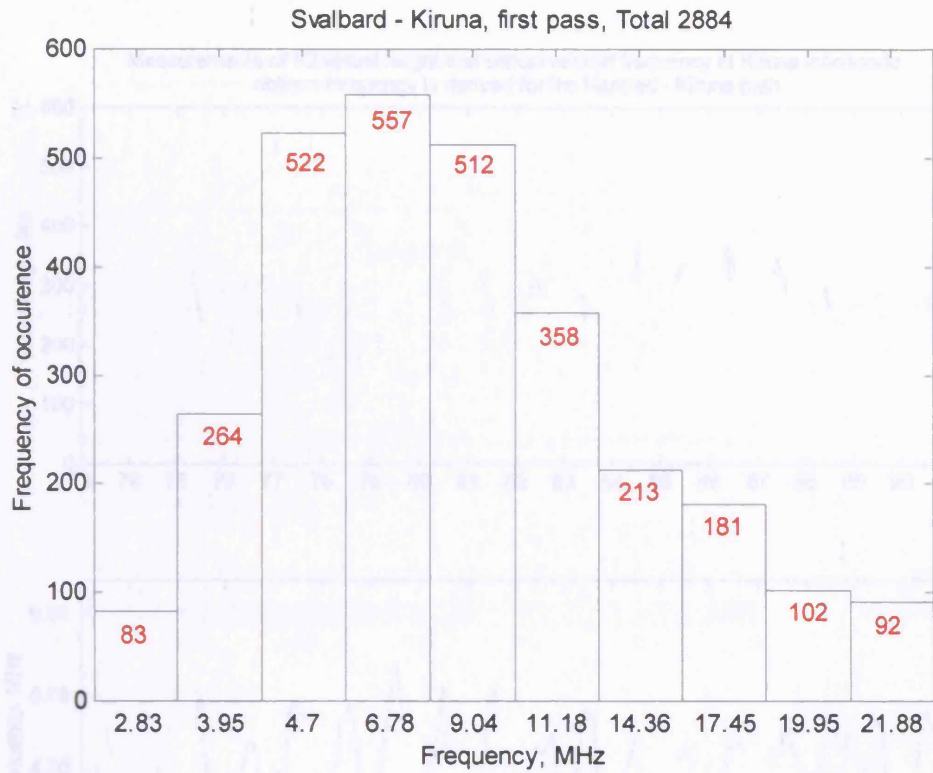


(a)

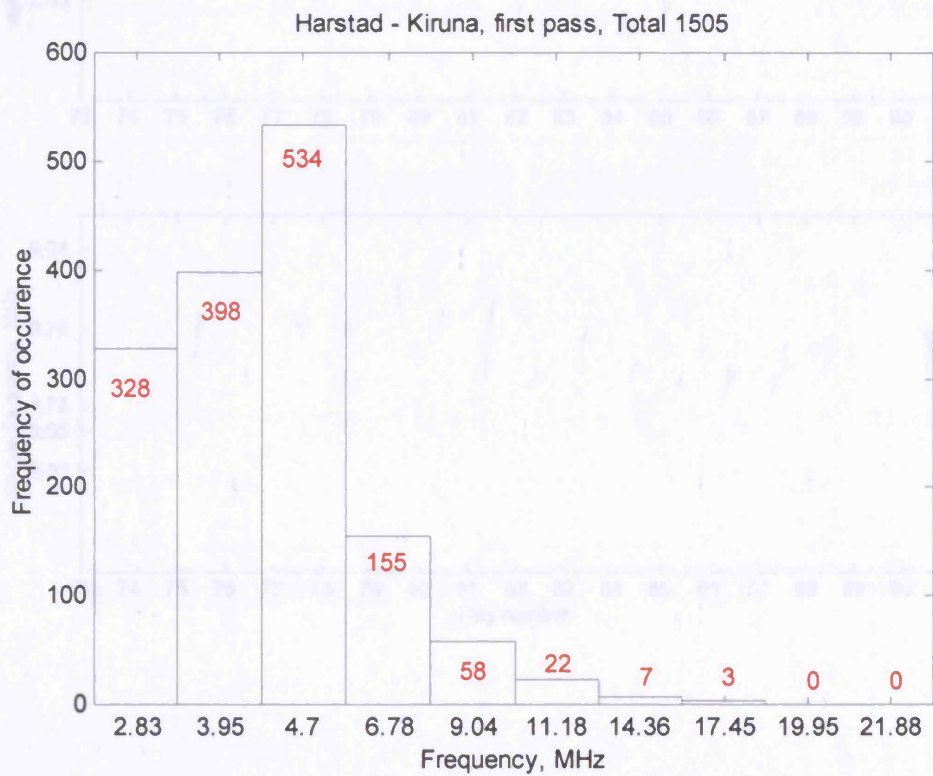


(b)

Figure 4.1 Distribution of first pass cases vs. Day number and Time of Day for (a) Svalbard – Kiruna path and (b) Harstad – Kiruna path.



(a)



(b)

Figure 4.2 Distribution of First Pass cases vs. Transmit Frequency for (a) Svalbard – Kiruna path and (b) Harstad – Kiruna path.

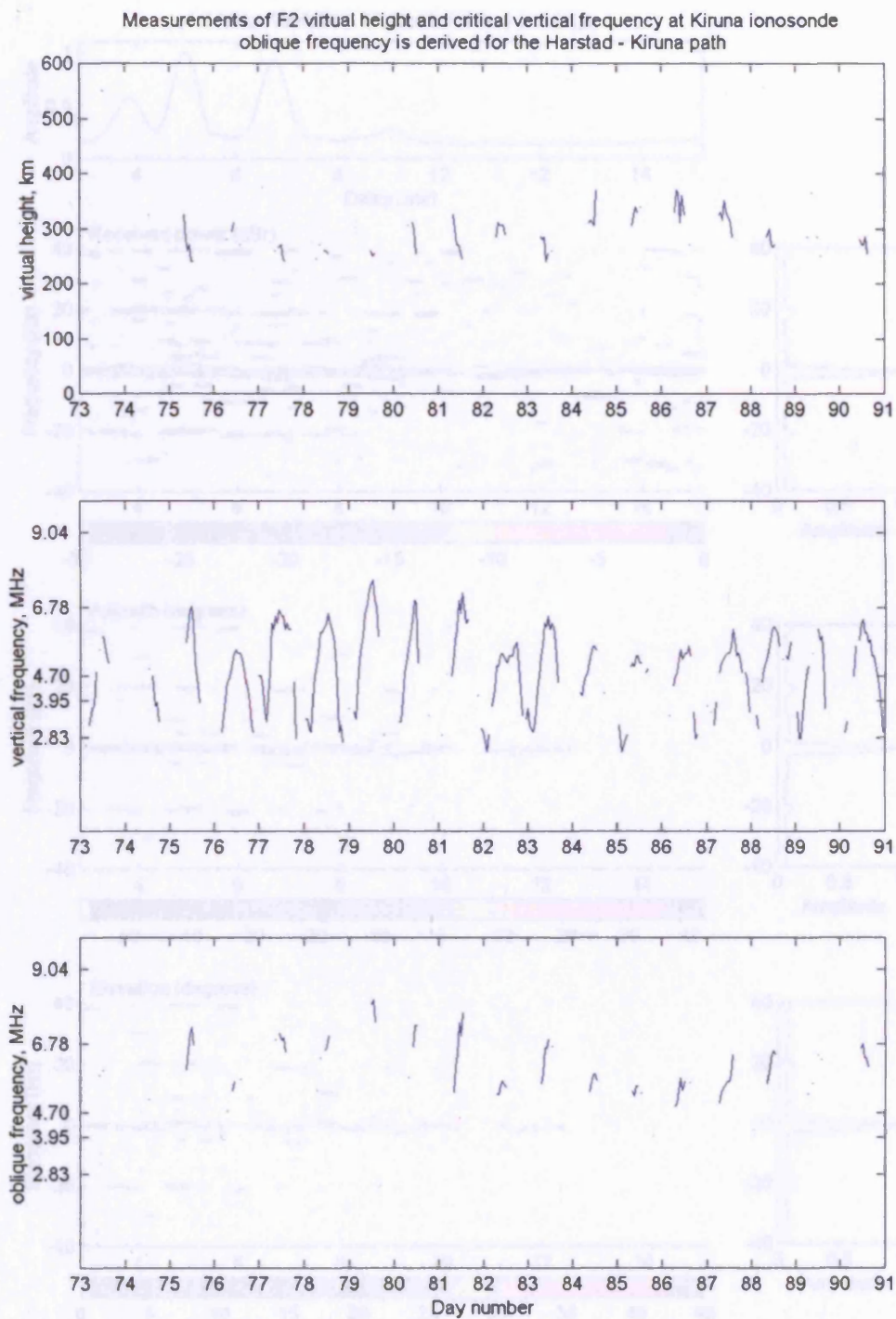


Figure 4.3 Measurements made at Kiruna ionosonde. The oblique propagation frequency is derived using the secant law with a flat Earth approximation.

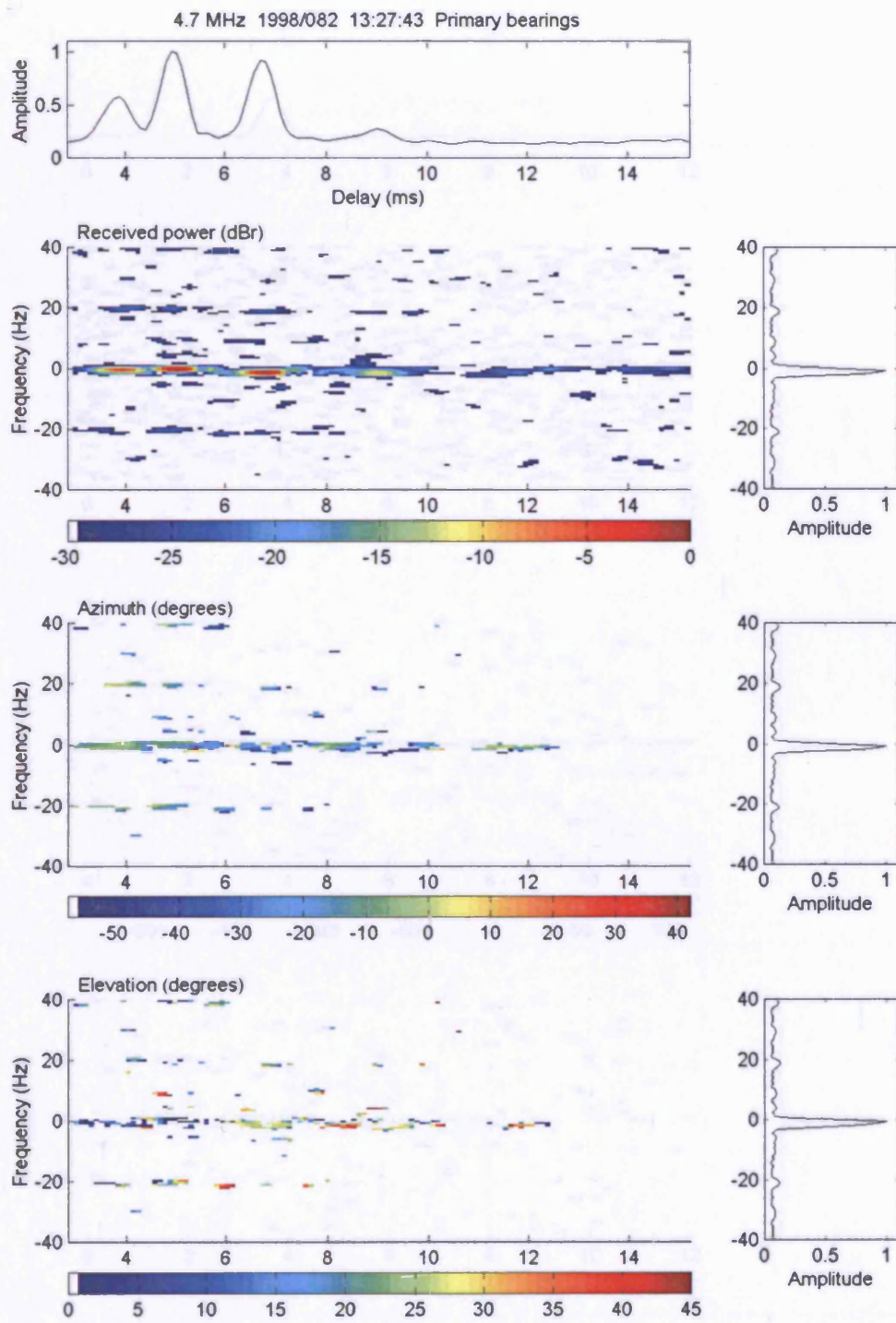


Figure 4.4 Svalbard – Kiruna multi path example.

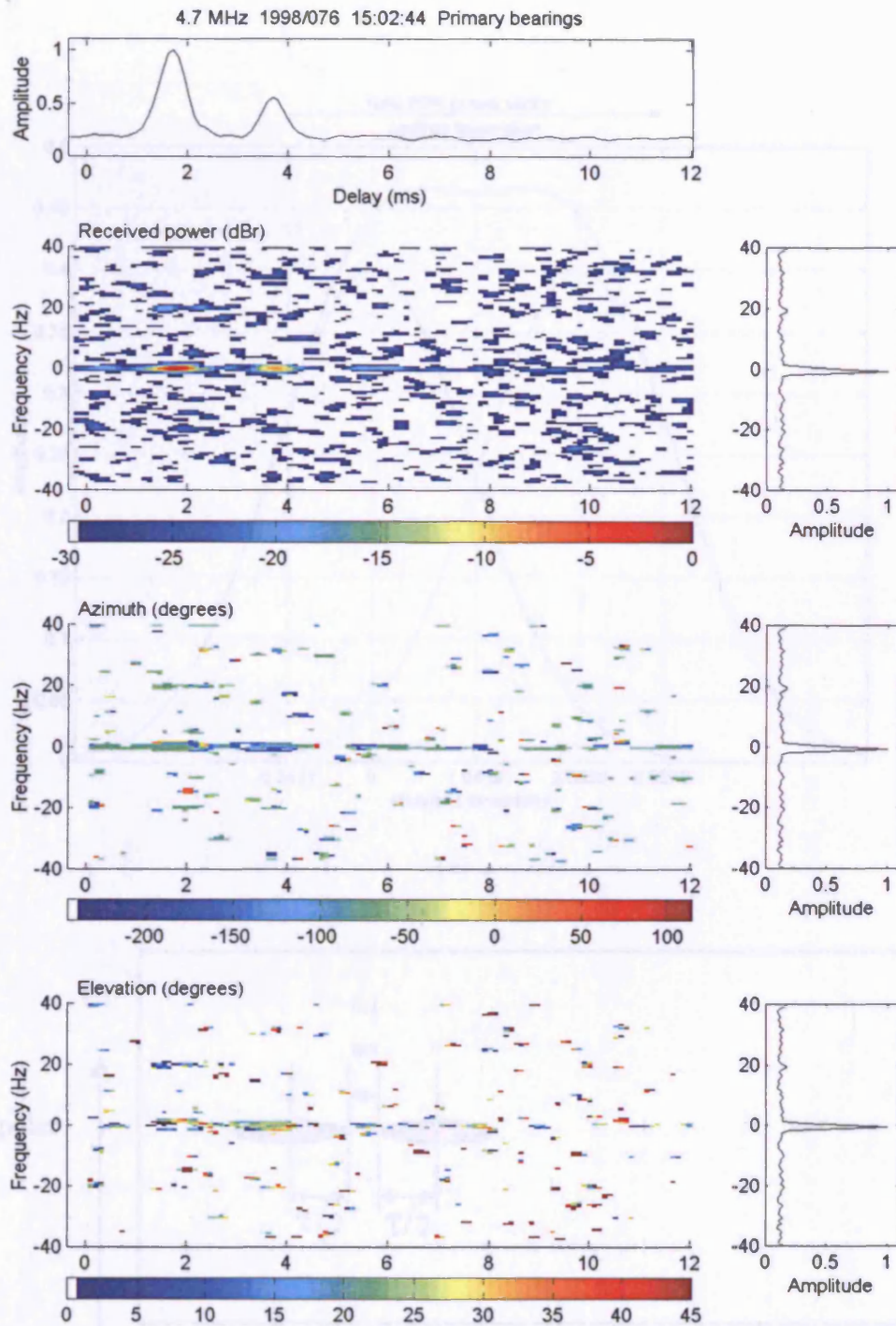
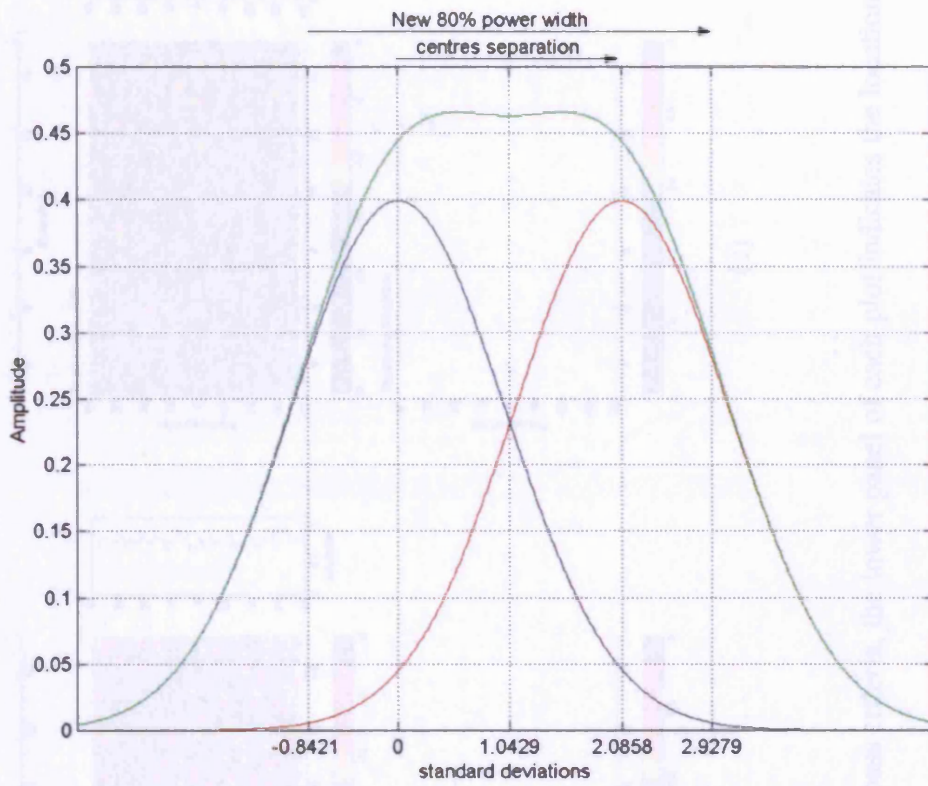
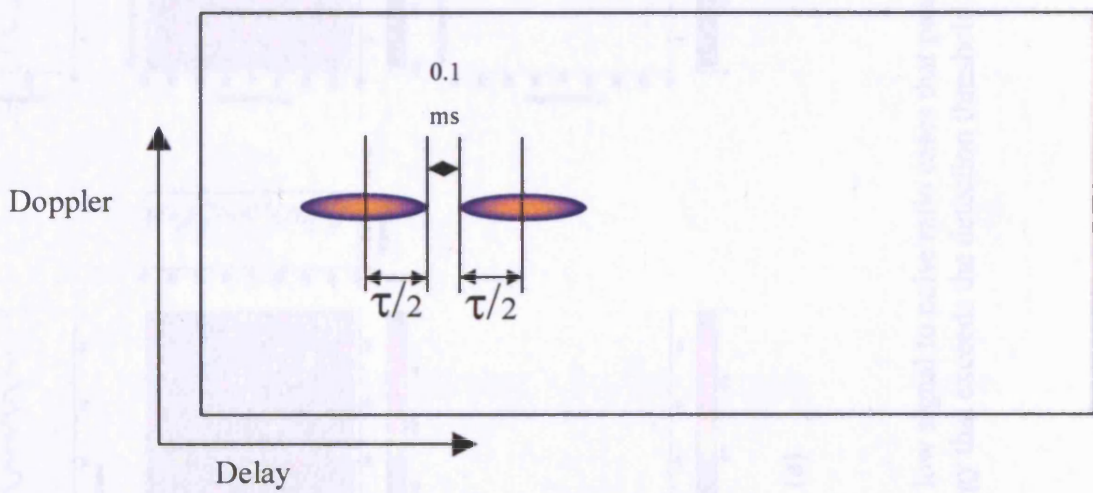


Figure 4.5 Harstad – Kiruna multipath example



(a)



(b)

Figure 4.6 (a) 80% power width of two overlapping gaussian modes. (b) Equivalent multipath spread of two equal power modes separated by one resolution cell

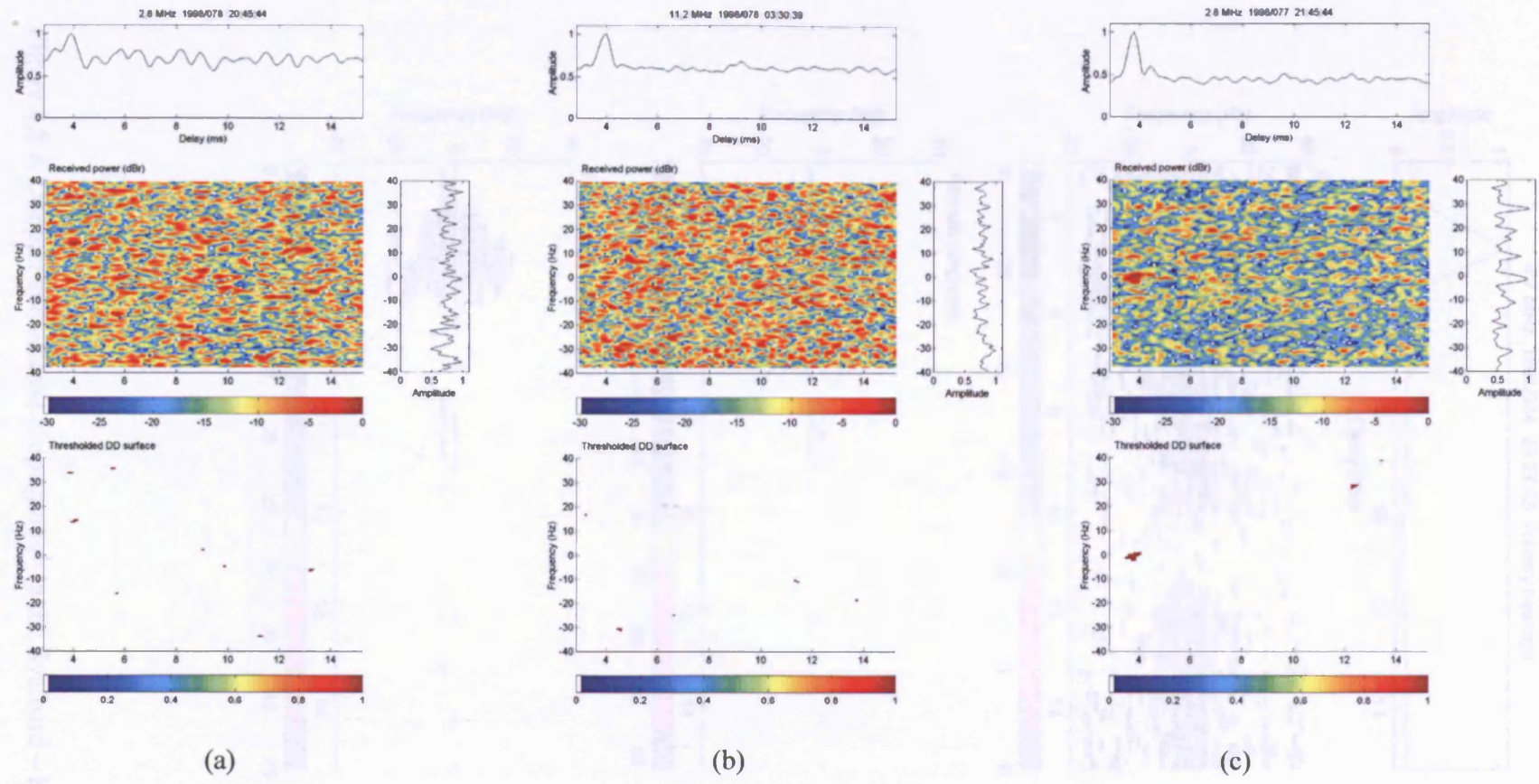


Figure 4.7 Three very low signal to noise ratio cases that pass the first pass criteria, the lower panel of each plot indicates the location on the DD plane of received energy that exceeds the detection threshold.

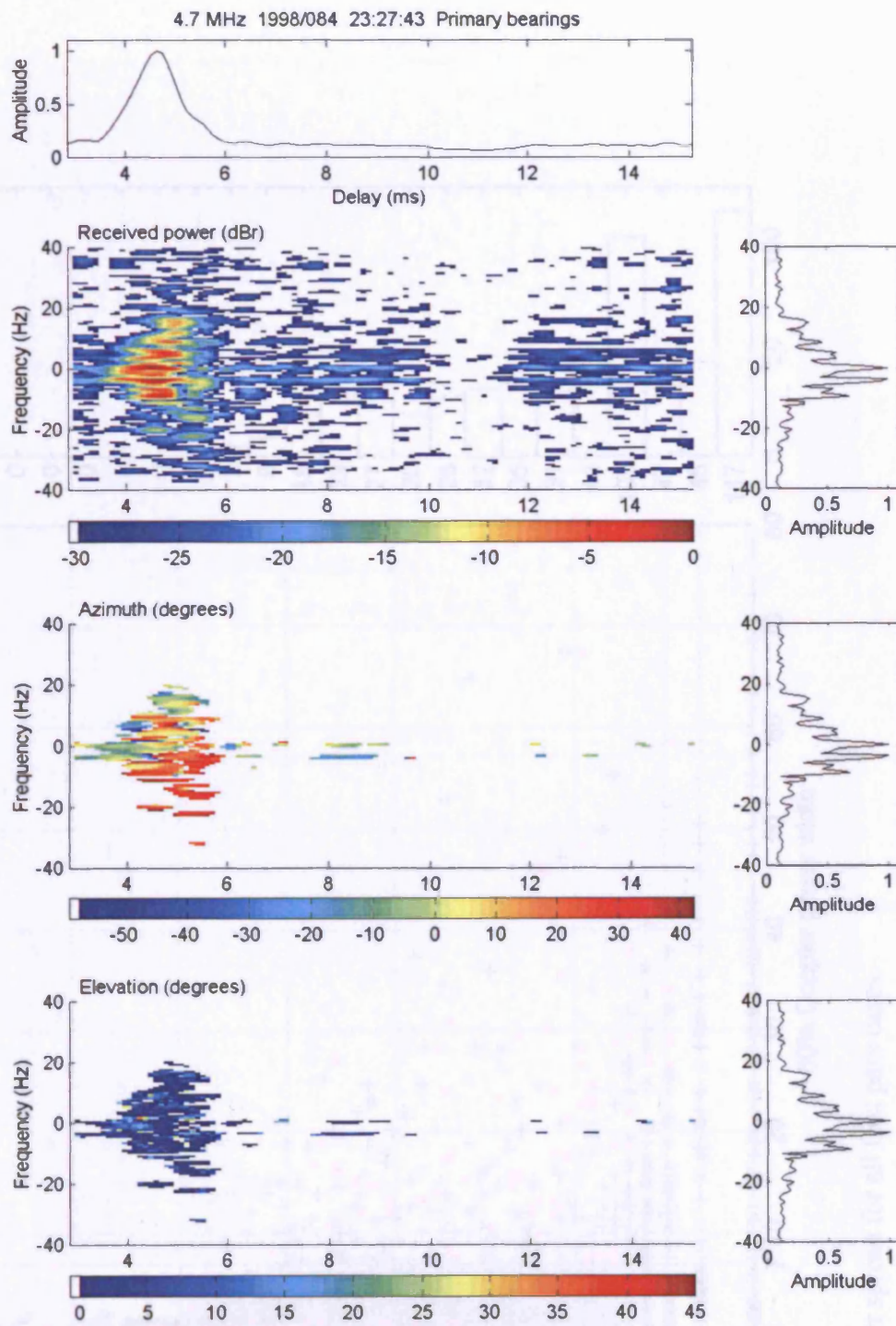


Figure 4.8 A Doppler spread case propagating via the Svalbard – Kiruna path.

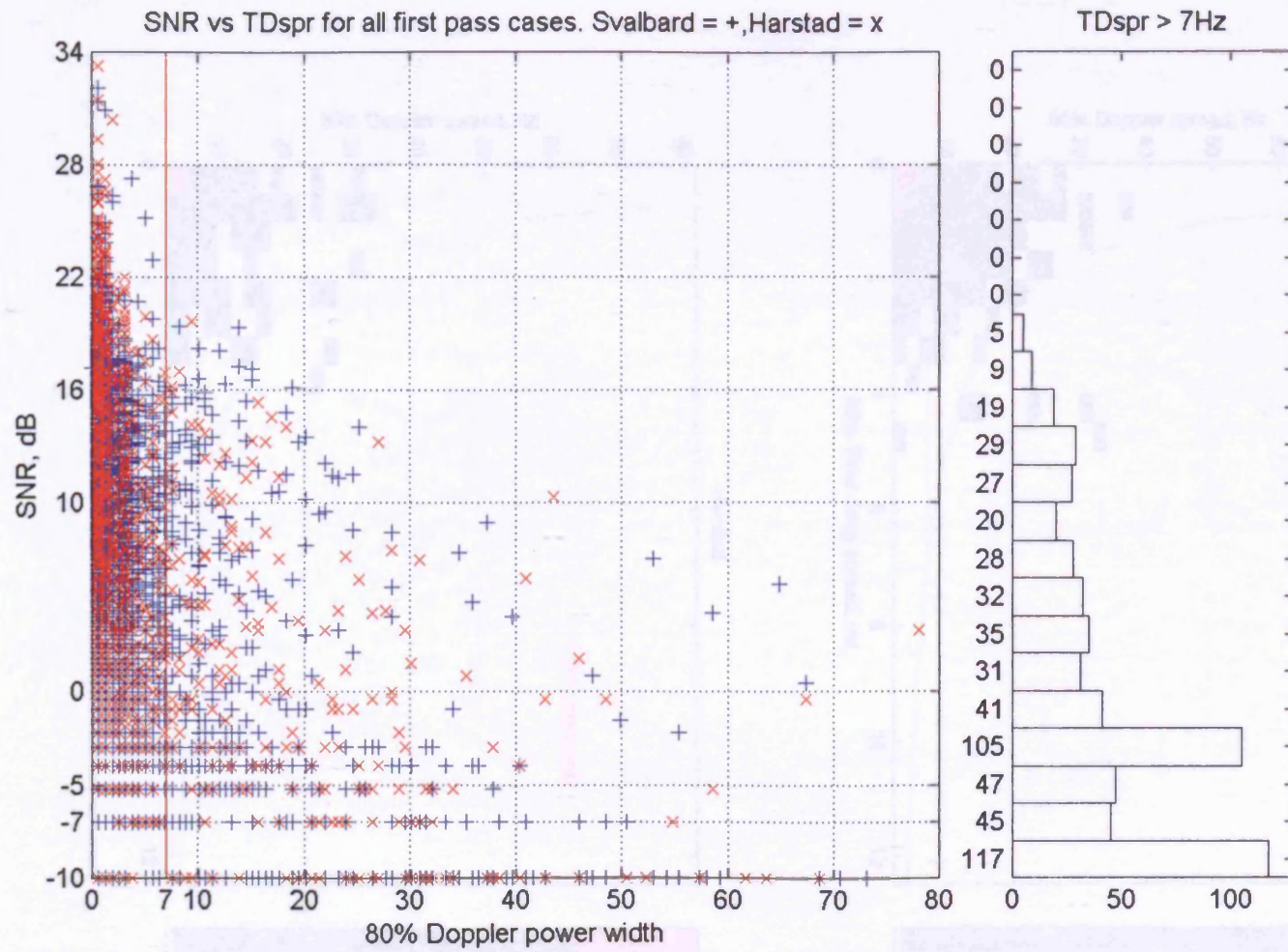


Figure 4.9 SNR vs. Doppler spread for all first pass cases.

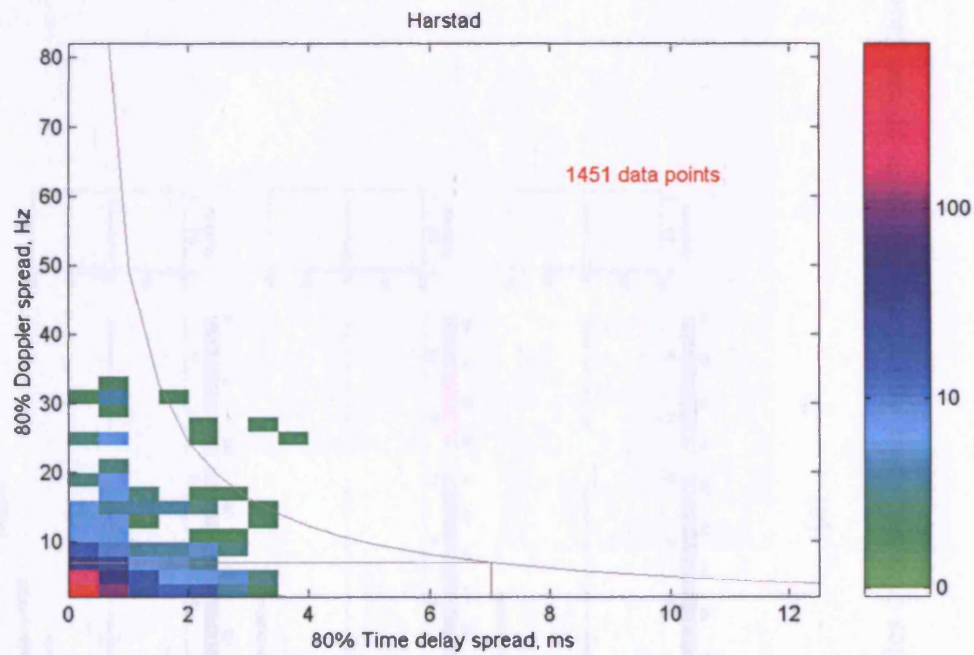
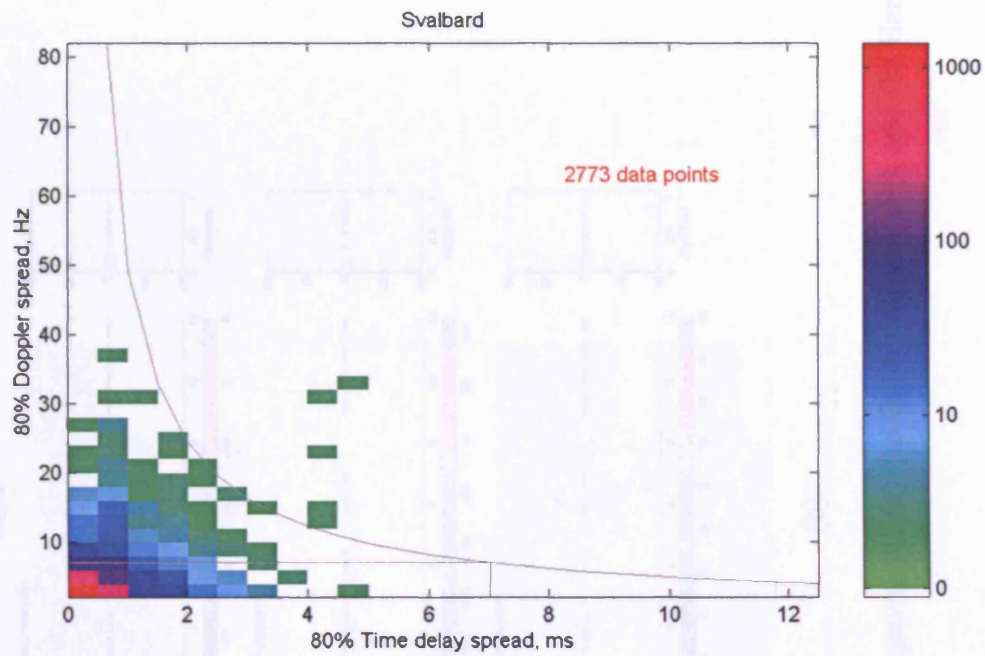


Figure 4.10 Two dimensional histograms of the simultaneous distribution of delay and Doppler spread for all cases exceeding  $-7\text{dB}$  SNR for each path. Note the different logarithmic colour scales.

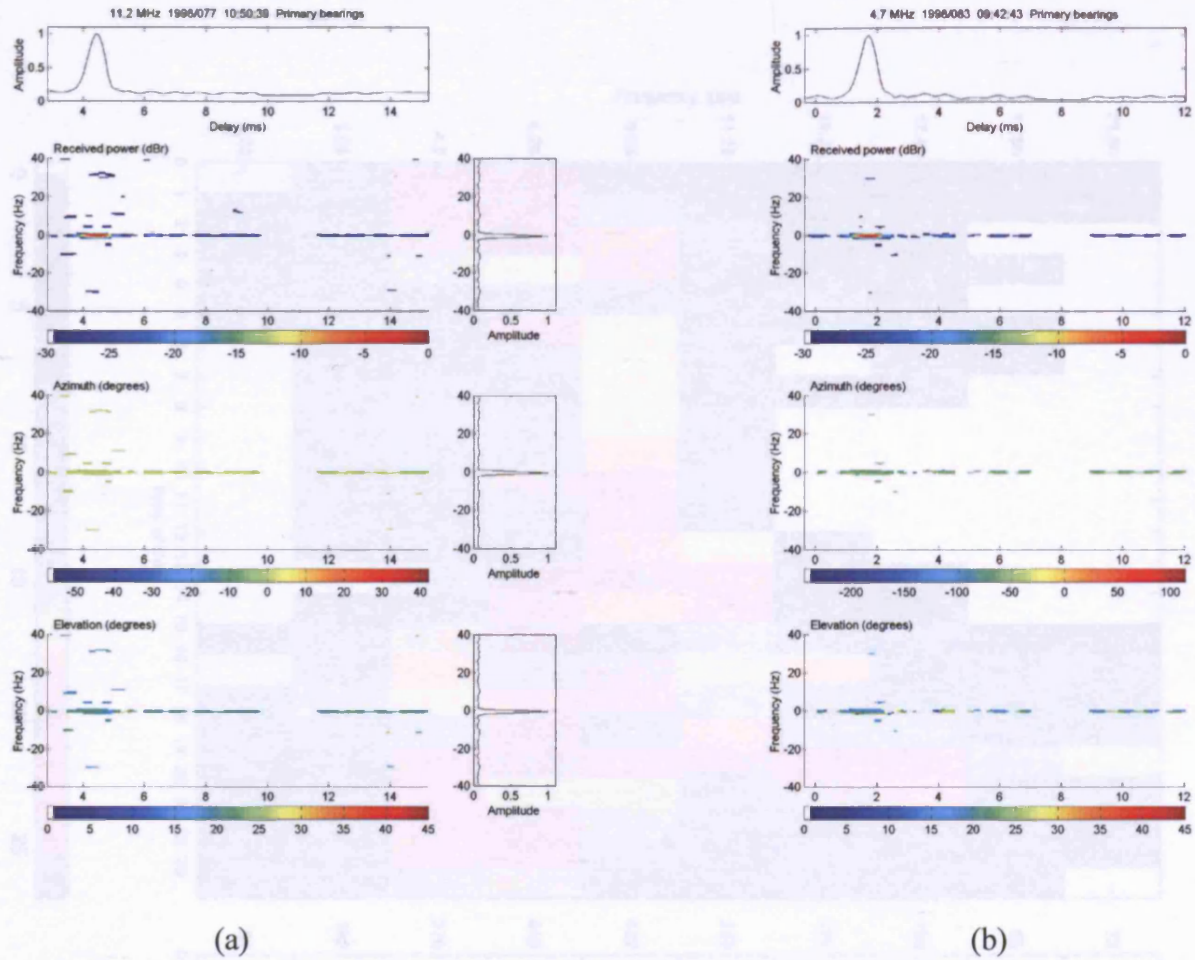
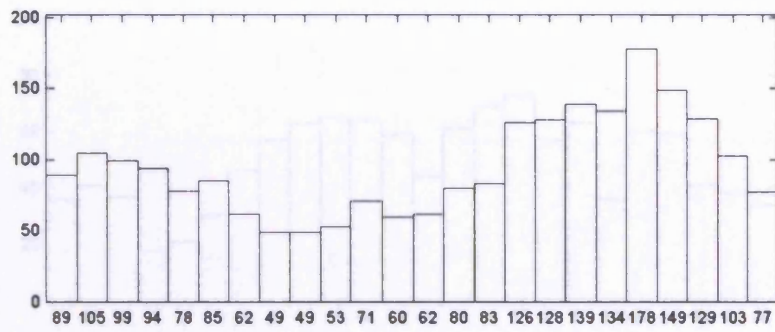


Figure 4.11 Typical examples of small delay and narrow Doppler spread cases propagating via (a) Svalbard – Kiruna path and (b) Harstad – Kiruna path



Total  
2282

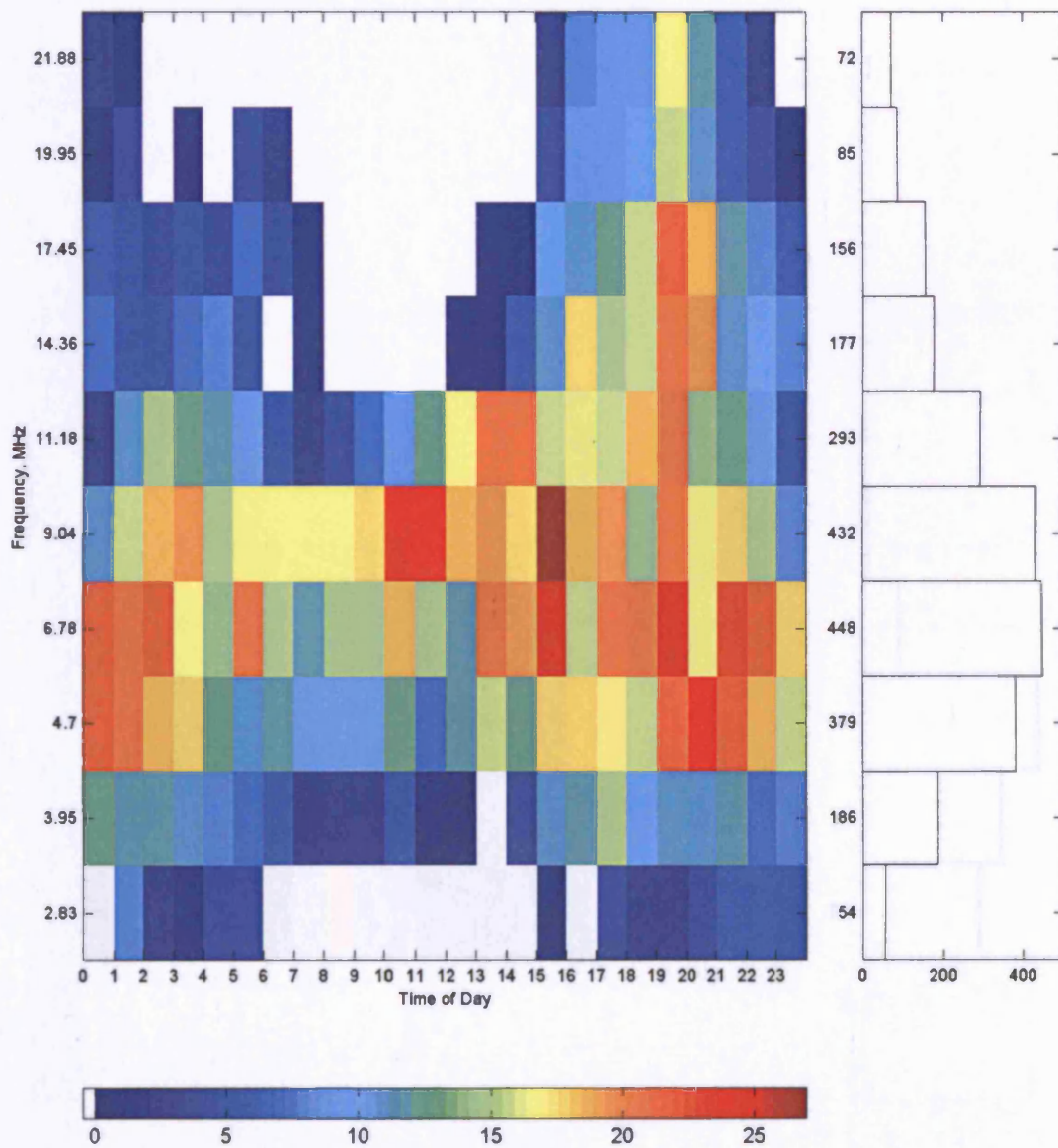


Figure 4.12 Svalbard – Kiruna, Distribution of Transmit Frequency vs. Time of Day for small delay, wide Doppler spread cases.

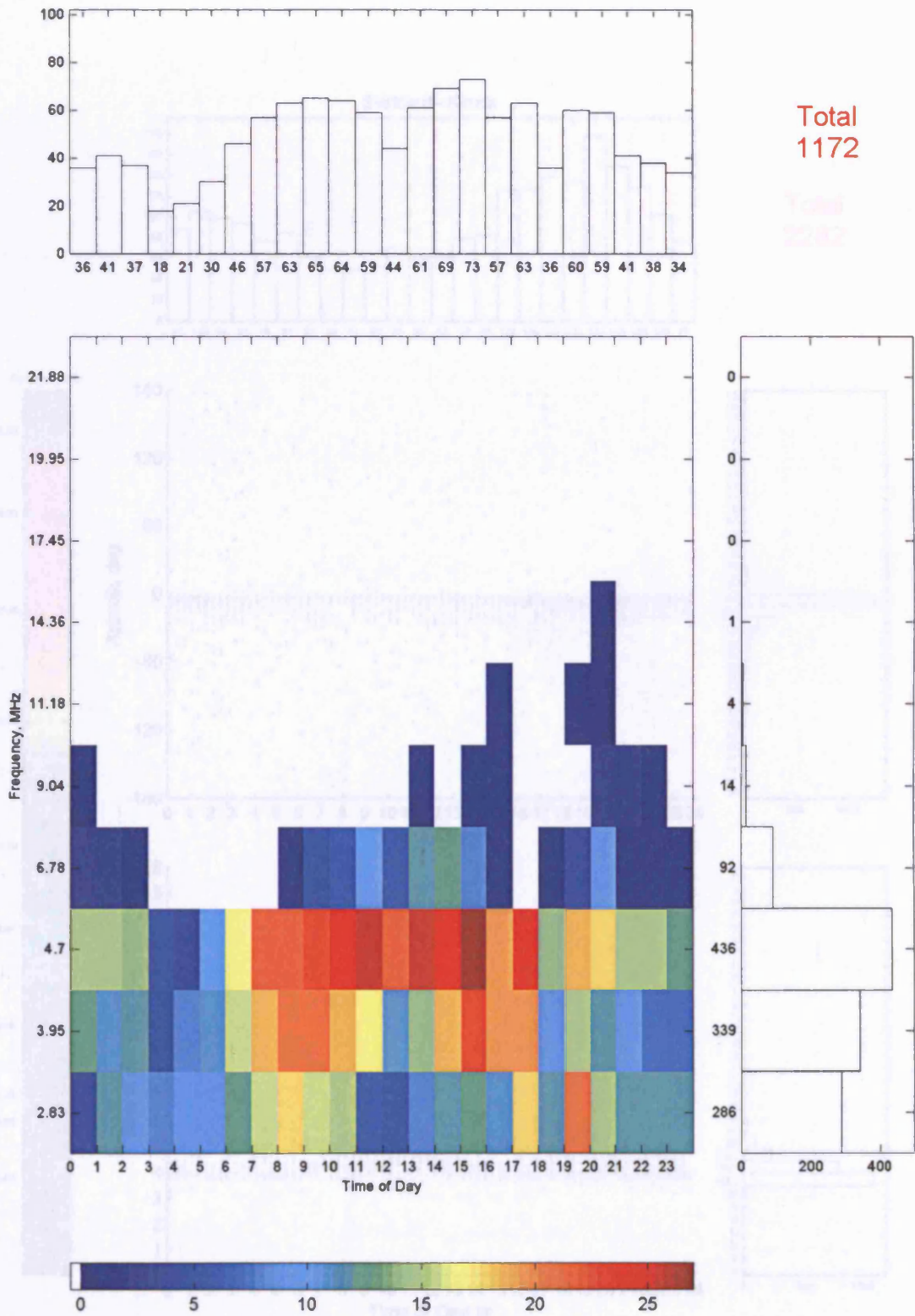


Figure 4.13 Harstad - Kiruna, Distribution of Transmit Frequency vs. Time of Day for small delay, wide Doppler spread cases.

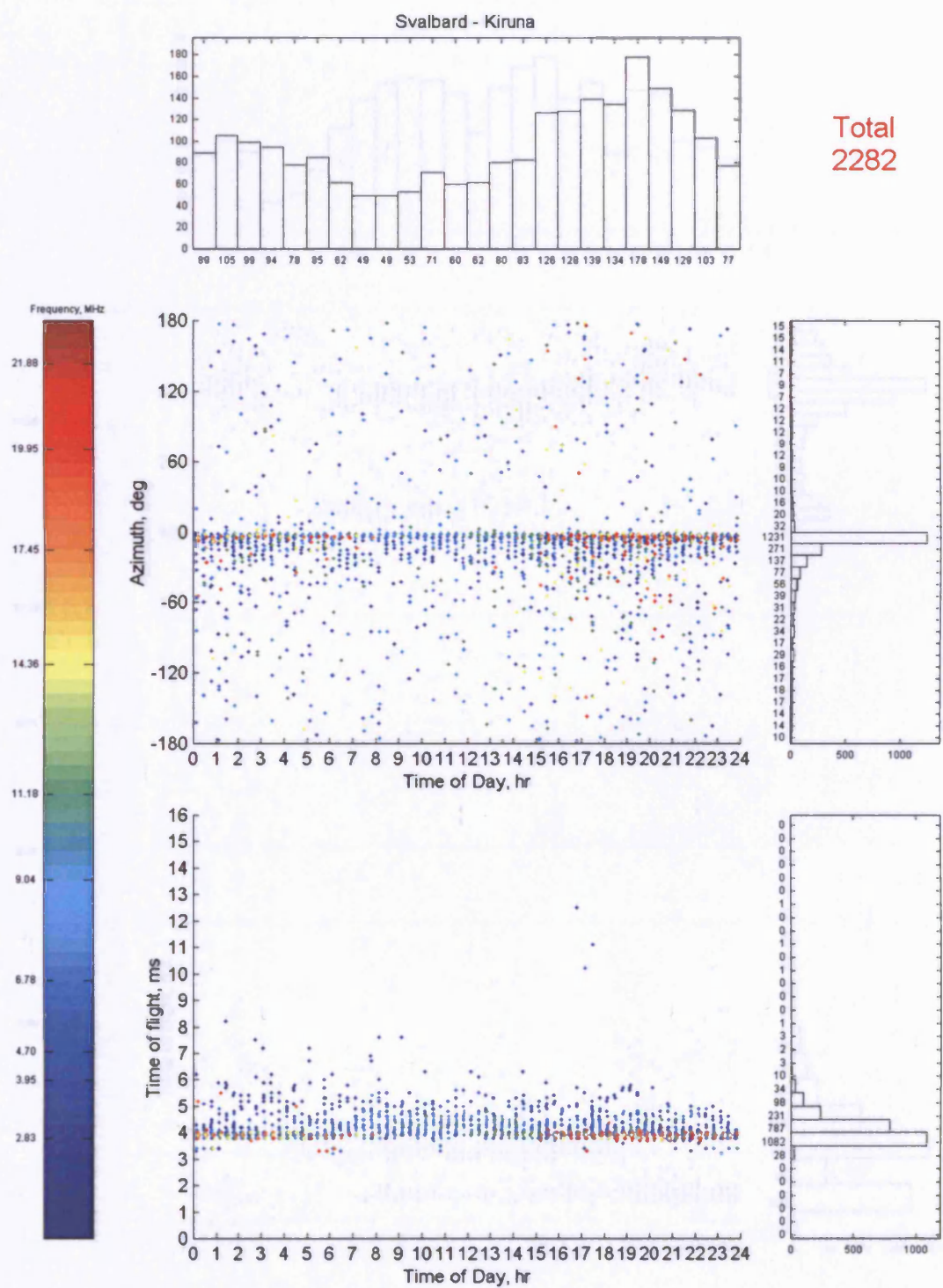


Figure 4.14 Svalbard – Kiruna. Azimuth and time of flight plots for small delay spread narrow Doppler spread cases. Colour scale indicates frequency.

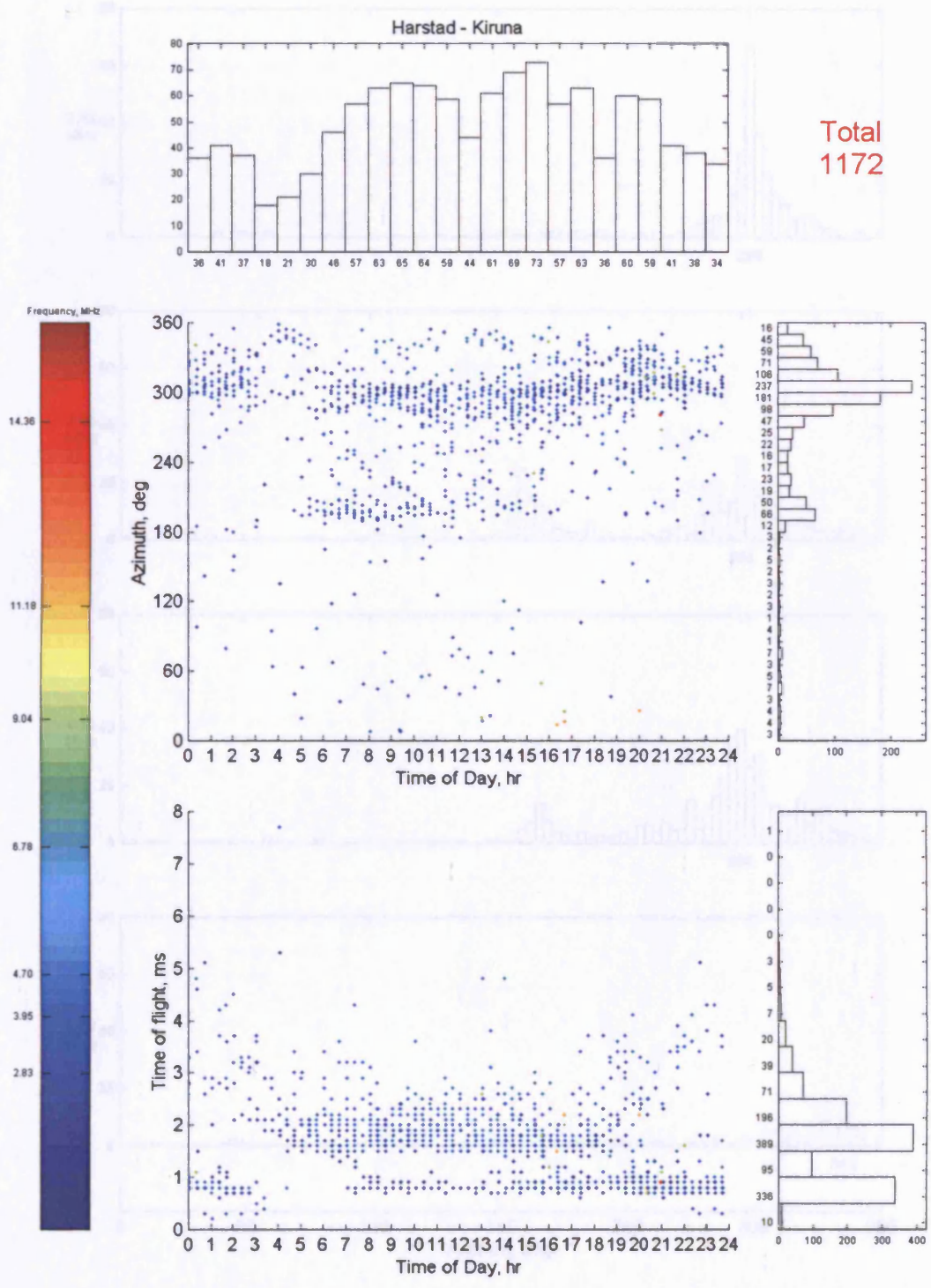


Figure 4.15 Harstad – Kiruna. Azimuth and time of flight plots for small delay spread narrow Doppler spread cases. Colour scale indicates frequency.

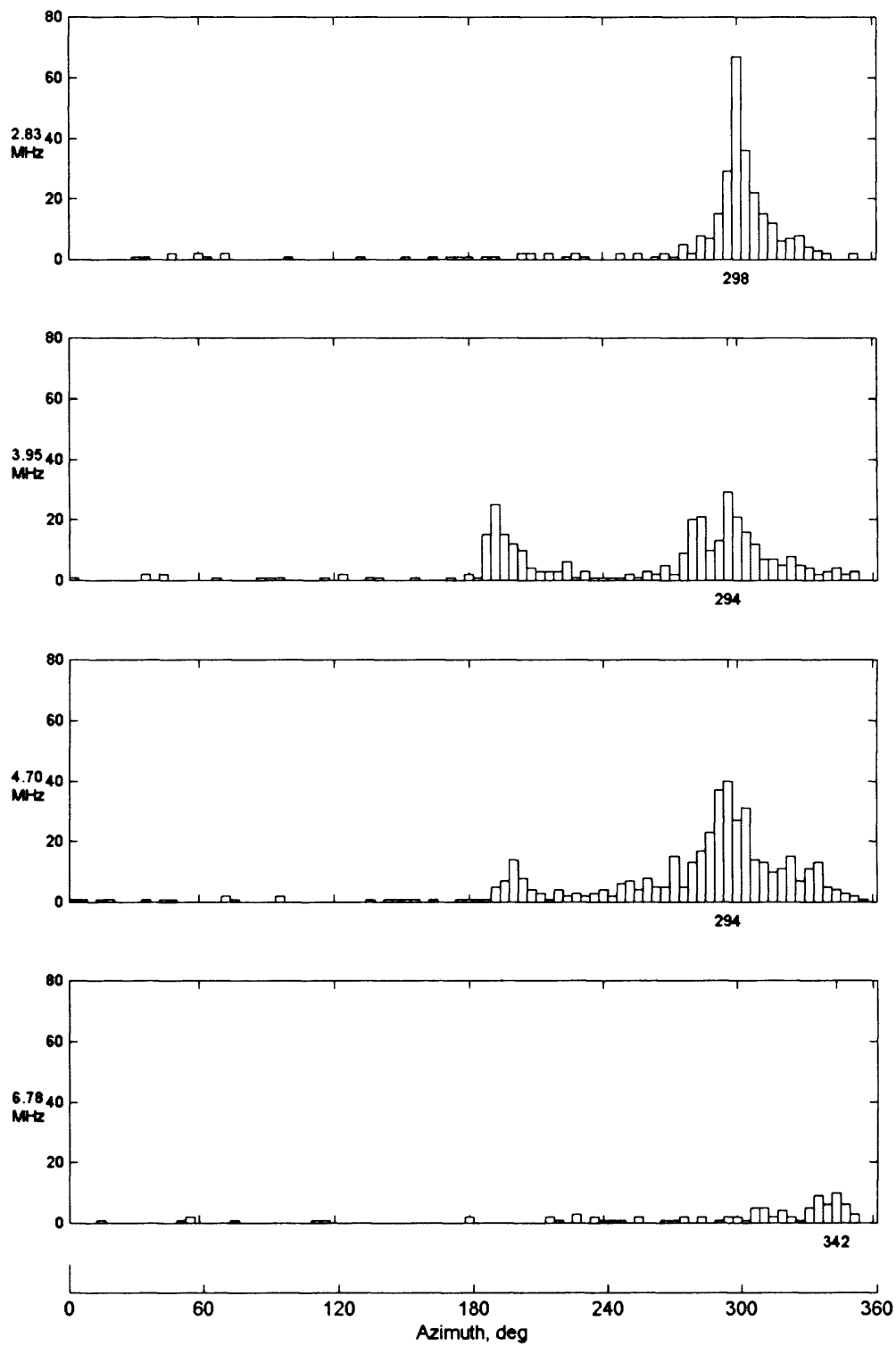


Figure 4.16 Harstad – Kiruna azimuth distributions vs. frequency, corrected for 4.5° measurement error.

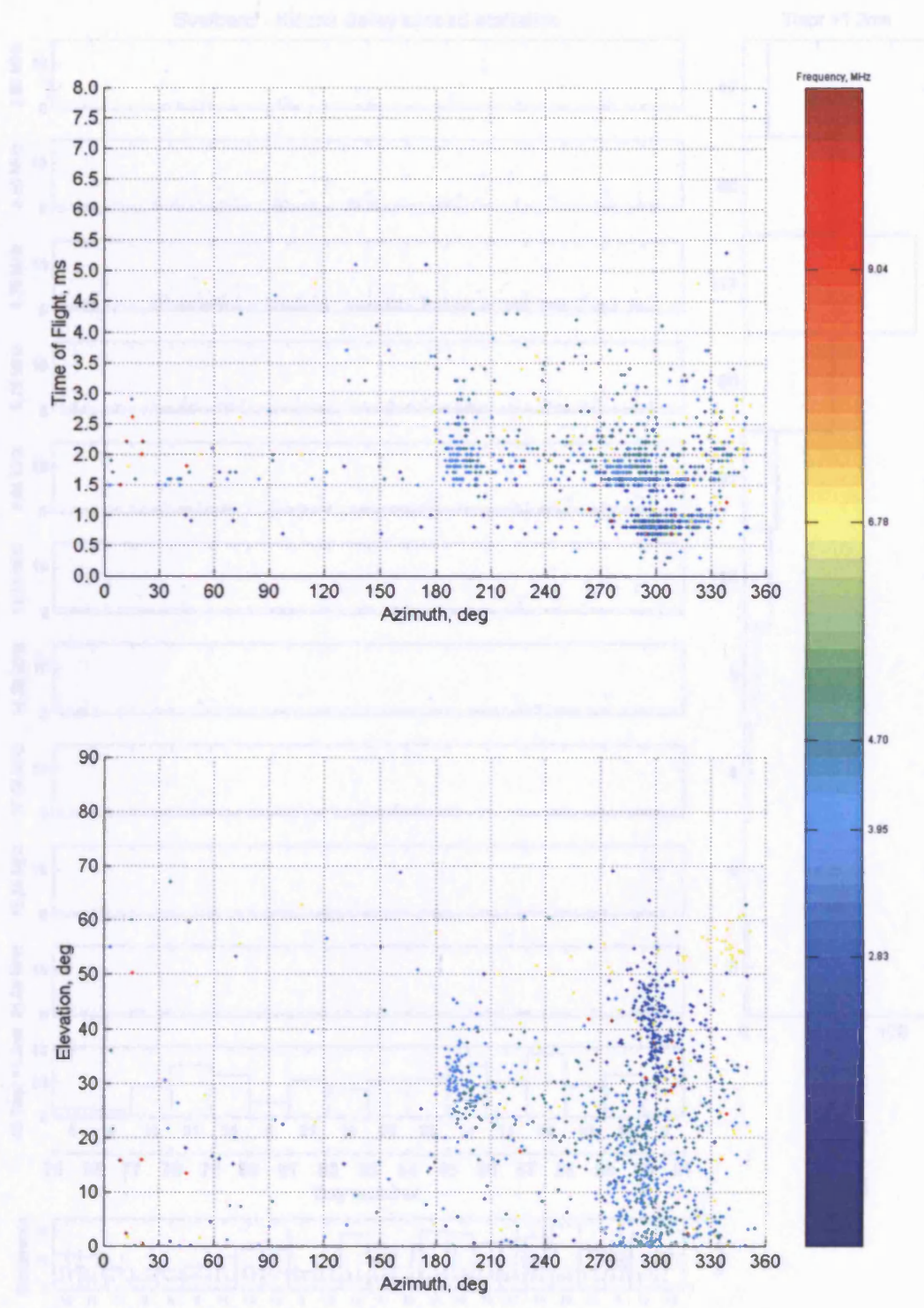
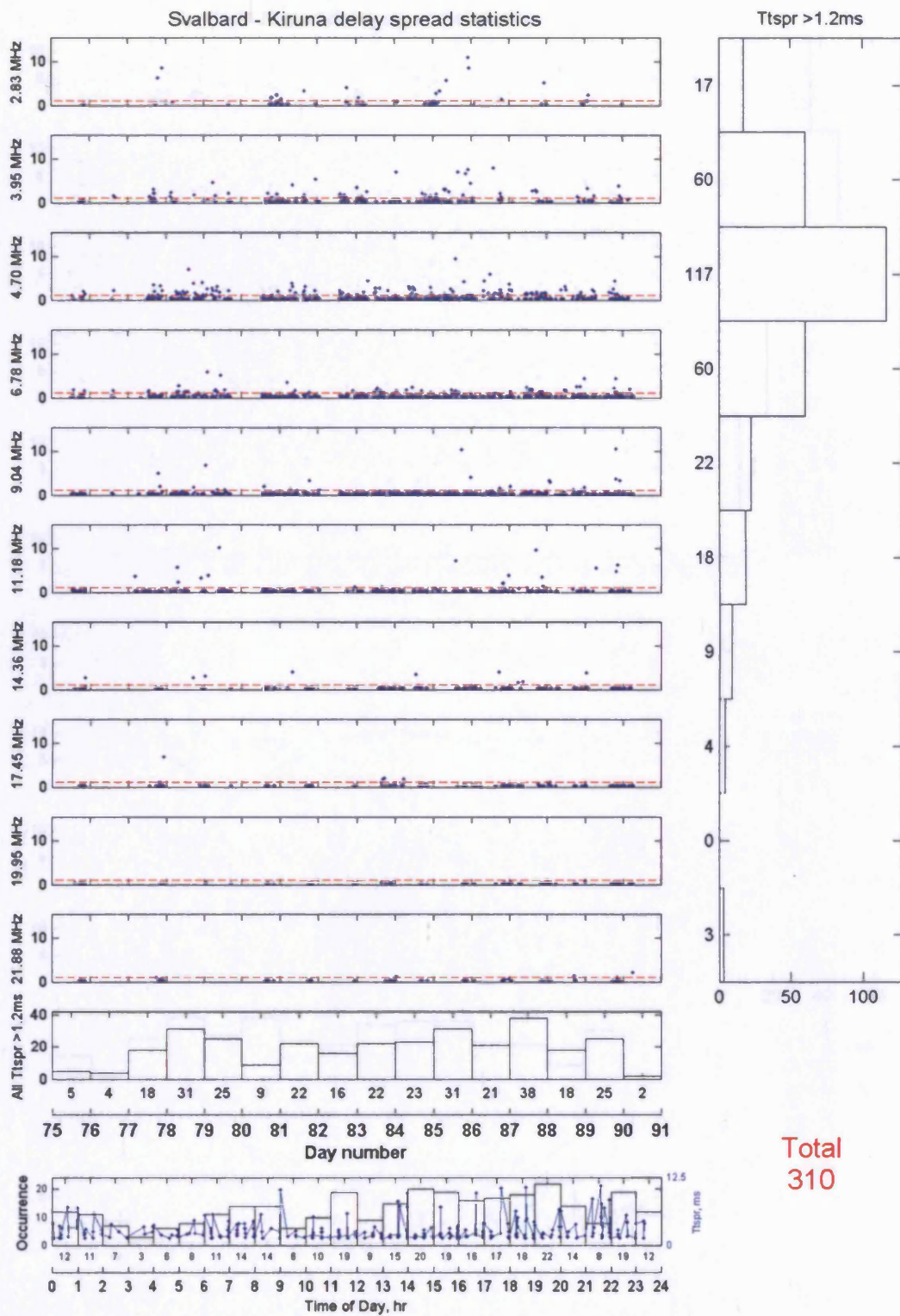


Figure 4.17 Harstad – Kiruna, Time of Flight vs. Azimuth (upper panel) and Elevation vs. Azimuth (lower panel). Colour scale represents transmit frequency.



Total  
310

Figure 4.18 Svalbard – Kiruna delay spread statistics

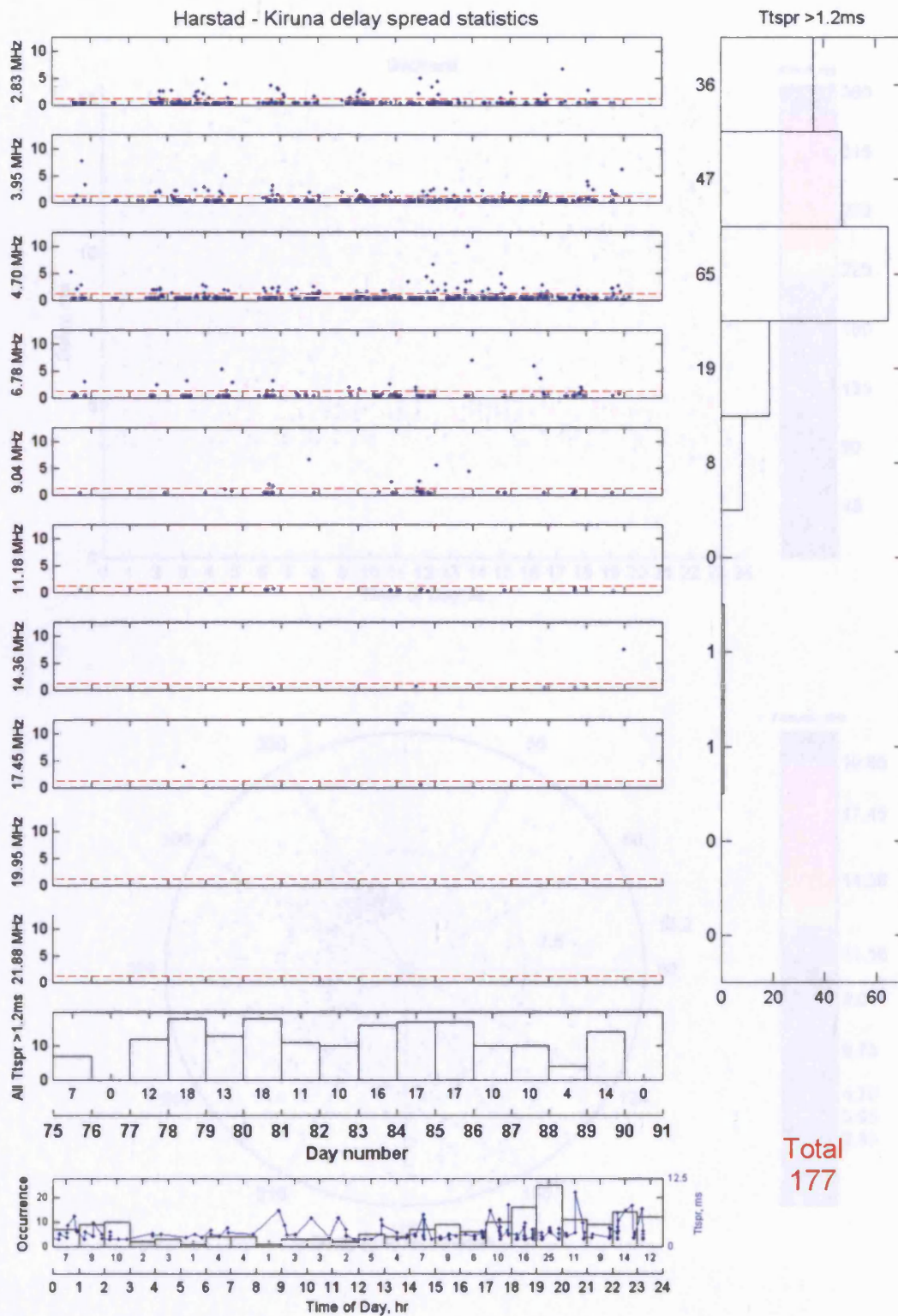


Figure 4.19 Harstad – Kiruna delay spread statistics

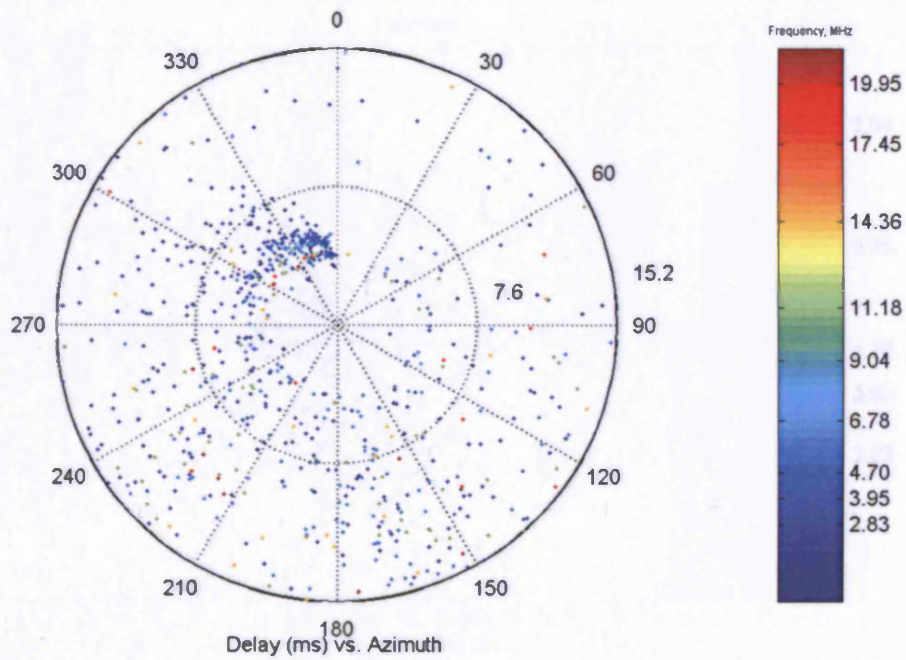
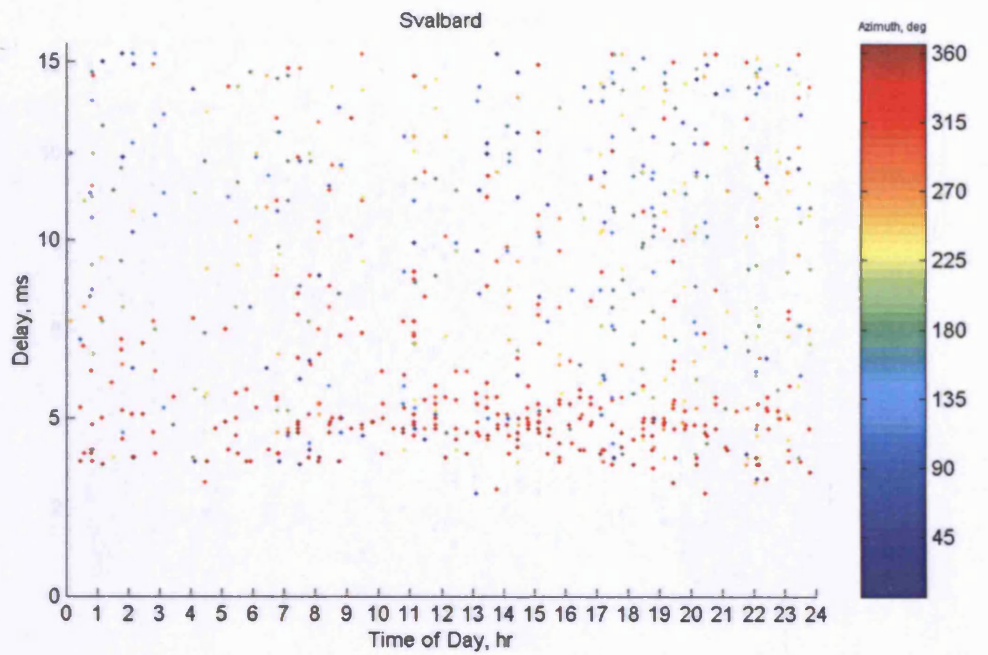


Figure 4.20 Direction of arrival statistics for the Svalbard – Kiruna path. Each point represents the properties of separate detected modes for all cases with delay spread >1.2ms.

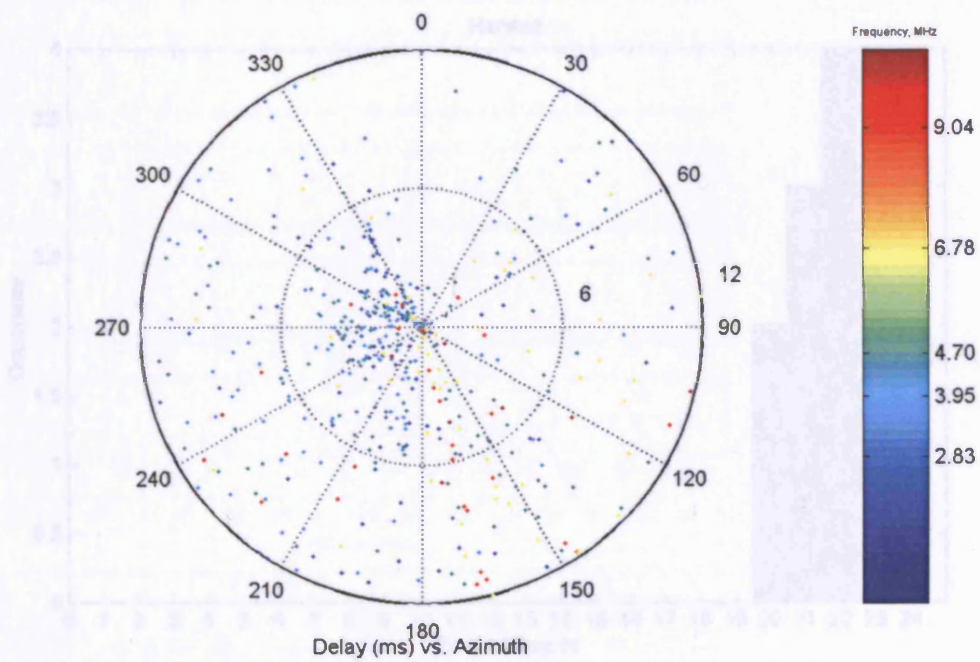
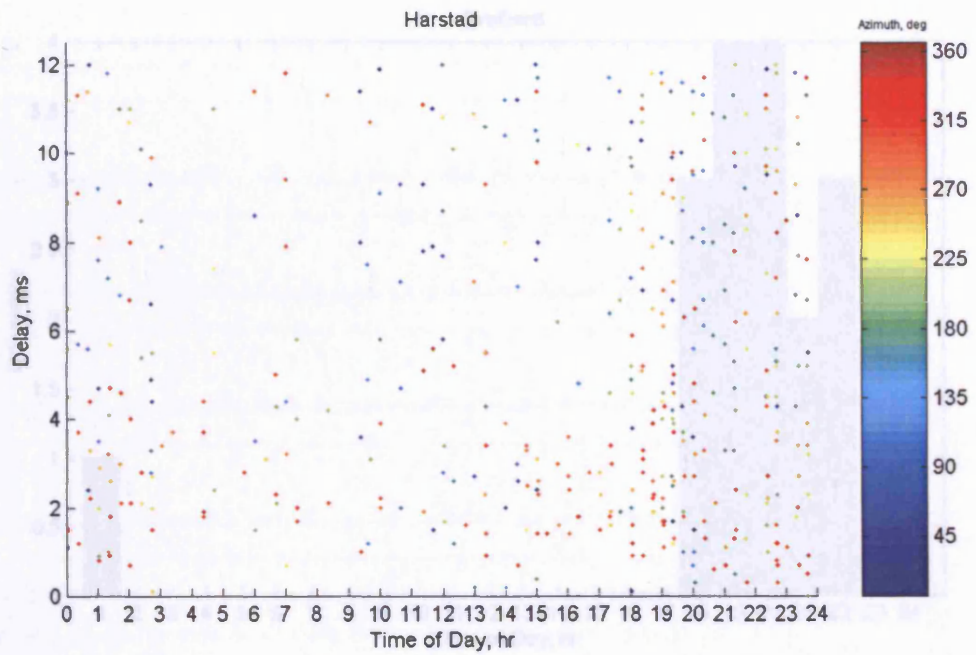


Figure 4.21 Direction of arrival statistics for the Harstad – Kiruna path. Each point represents the properties of separate detected modes for all cases with delay spread  $>1.2$ ms.

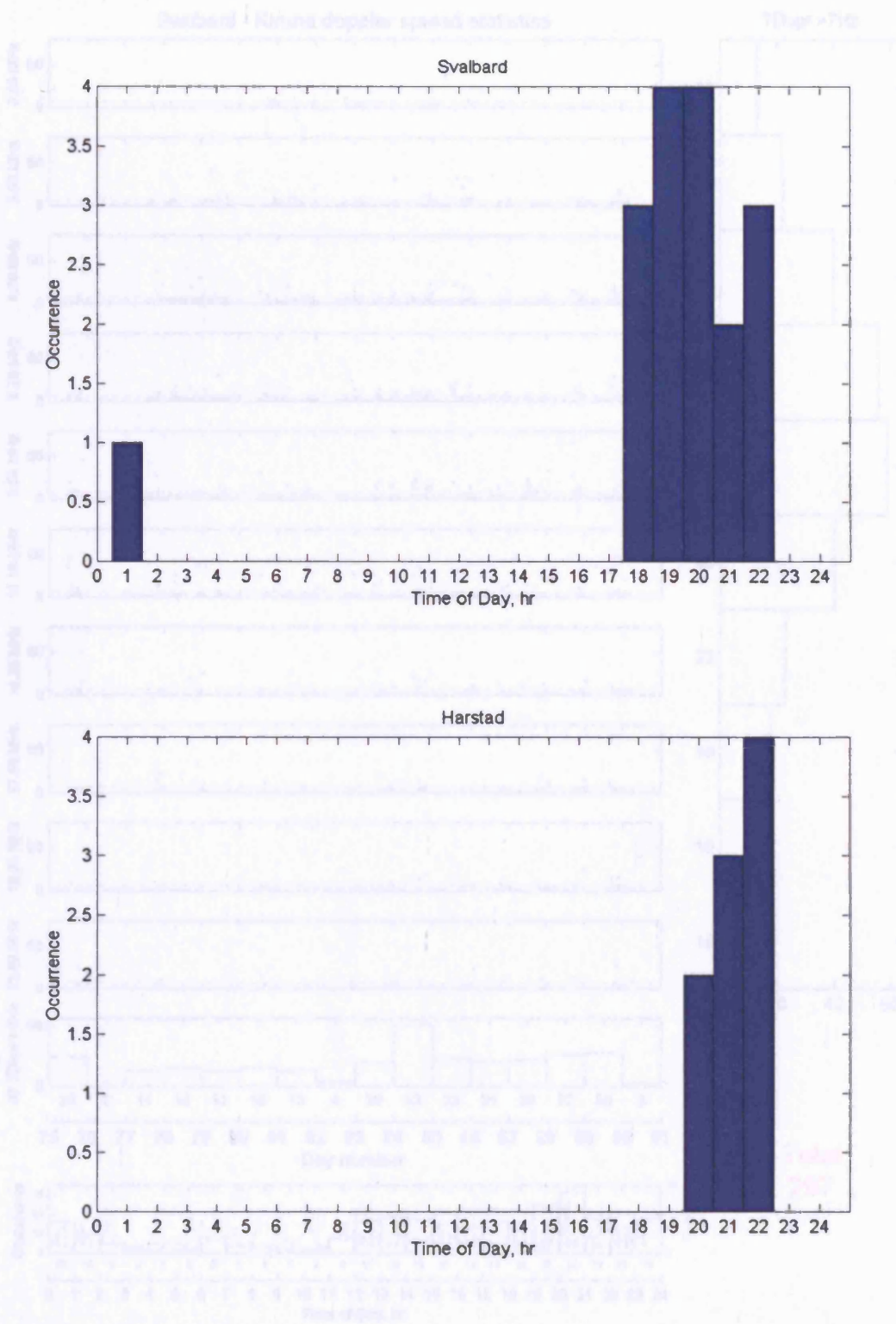


Figure 4.22 Times of day when interferer at  $\sim 165^\circ$  on 9.04MHz is present.

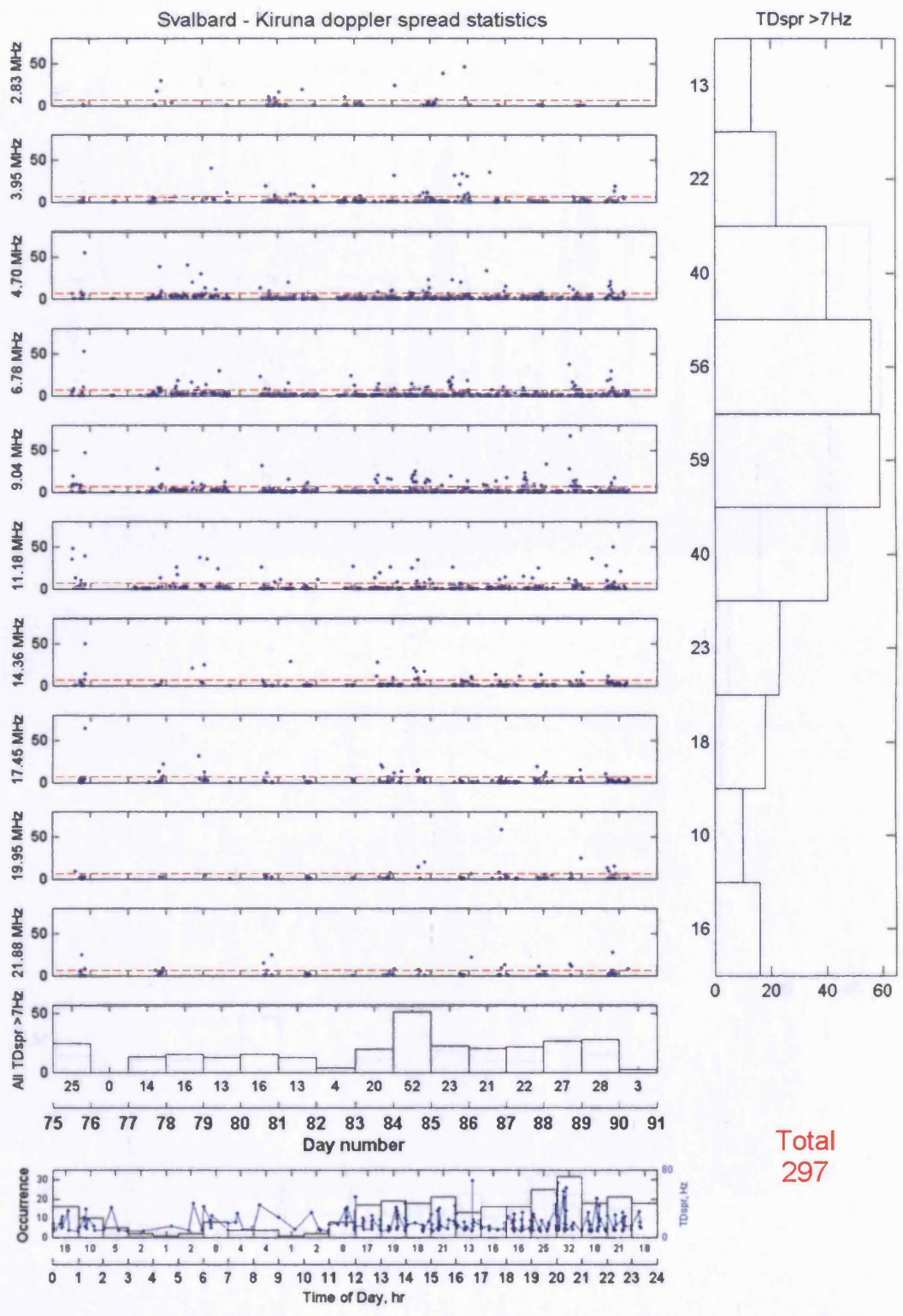


Figure 4.23 Svalbard – Kiruna Doppler spread statistics

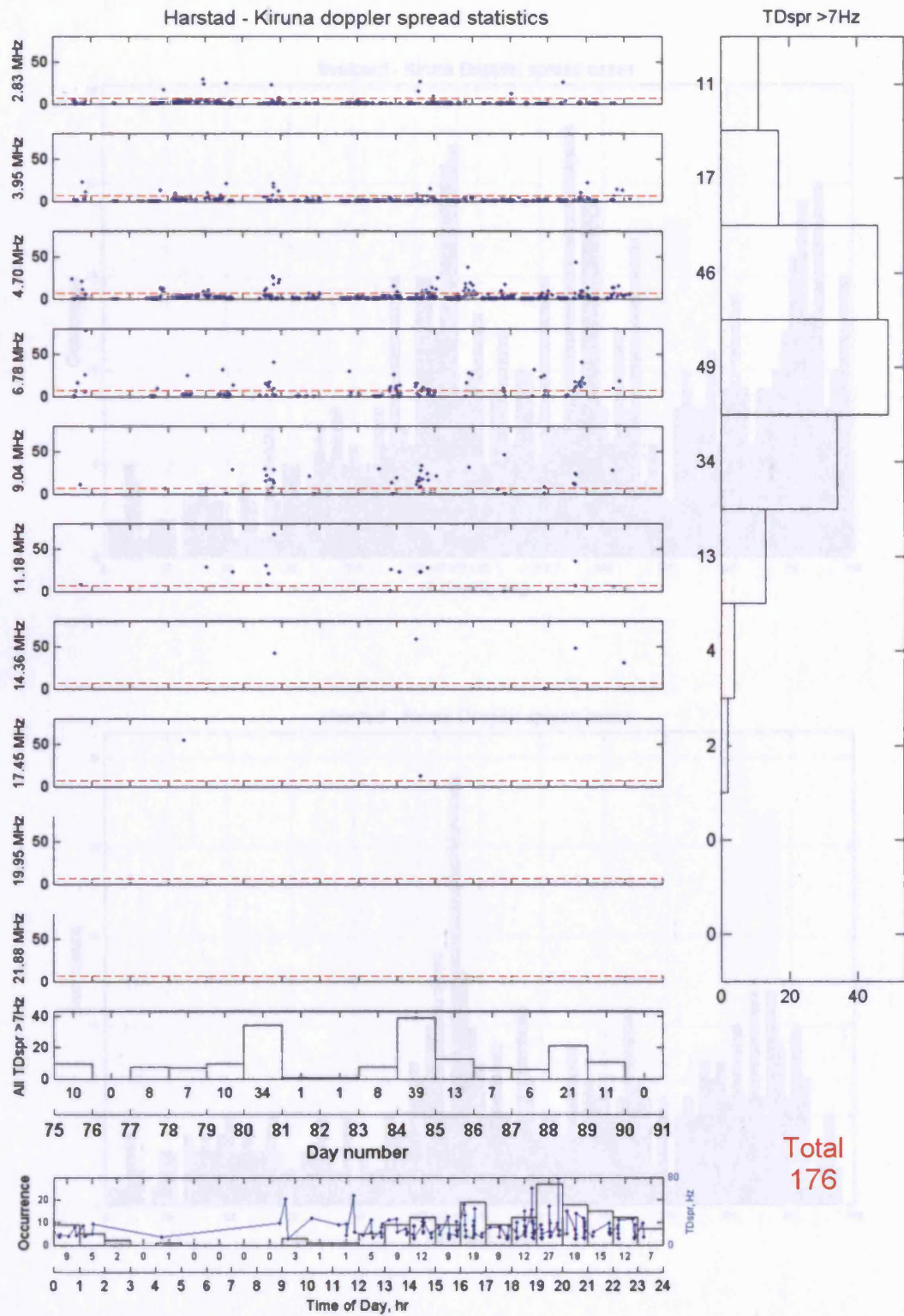


Figure 4.24 Harstad – Kiruna Doppler spread statistics

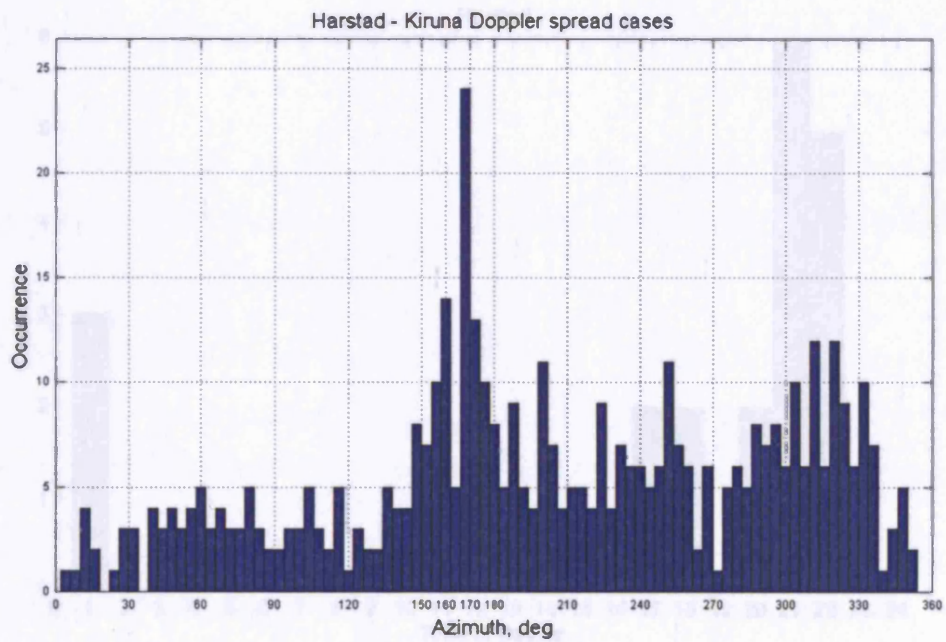
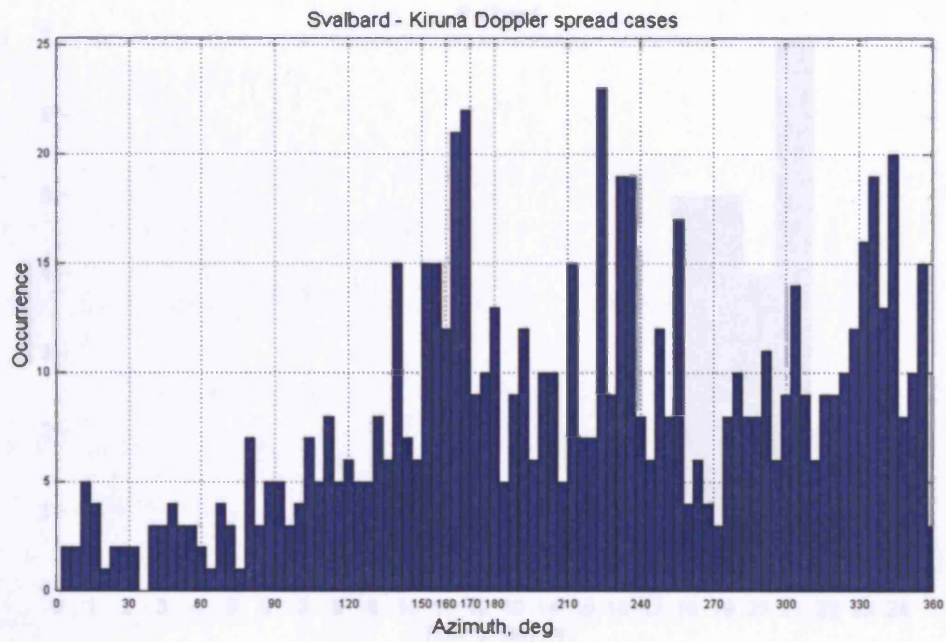


Figure 4.25 Histograms of occurrence of wide Doppler spread cases having SNR  $\geq$ -7dB vs. Azimuth.

## 5. Propagation analysis

### 5.1 Time delay spreads

The propagation of Day 21 (23<sup>rd</sup> March 1998) provides a number of cases displaying large delay spreads. Some of these are examined below.

5.1.1 *Harstad - Eureka, 13:00UT → 13:50UT, 27<sup>th</sup> March* (see Figure 4.25)

Data collected during the afternoon and evening of the 23<sup>rd</sup> March shows a number of

subsequent cases, Figure 5.1 → Figure 5.3 are DD-DP plots taken from the

Svalbard ground path for 13:27UT → 13:29UT (note that the path length is 1500 km)

related to 2100 Hz. They represent the first delay spread observed during this

afternoon.

correlation peaks with a small amount of Doppler shift on each (up to 1.5 kHz). Most

none of them have any appreciable Doppler spread. The delay separation between the

first and second peaks is approximately 500 ns, comparable to an excess path length of

150 km.

The power information indicates that the first peak is in the GCP region (13.2°E,

the second at 140°, and third at -330° and the fourth at both -30° and -330° (nearly

all GCP propagation is occurring).

The elevation angles for each peak are -5°, -2°, -30° and -30° (give a 1000 m

difference in elevation suggest that there is a change in the propagation path

propagation which will contribute towards the large delay spread.

The power of the correlation peaks in all three cases is shown in Table 5.1.

The expected correlation peaks in all three cases are shown in Figure 5.1.

The expected correlation peaks in all three cases are shown in Table 5.1.

that generally for off GCP propagation these elevation angles will reduce and the delay

time is increased with the excess path length increase).

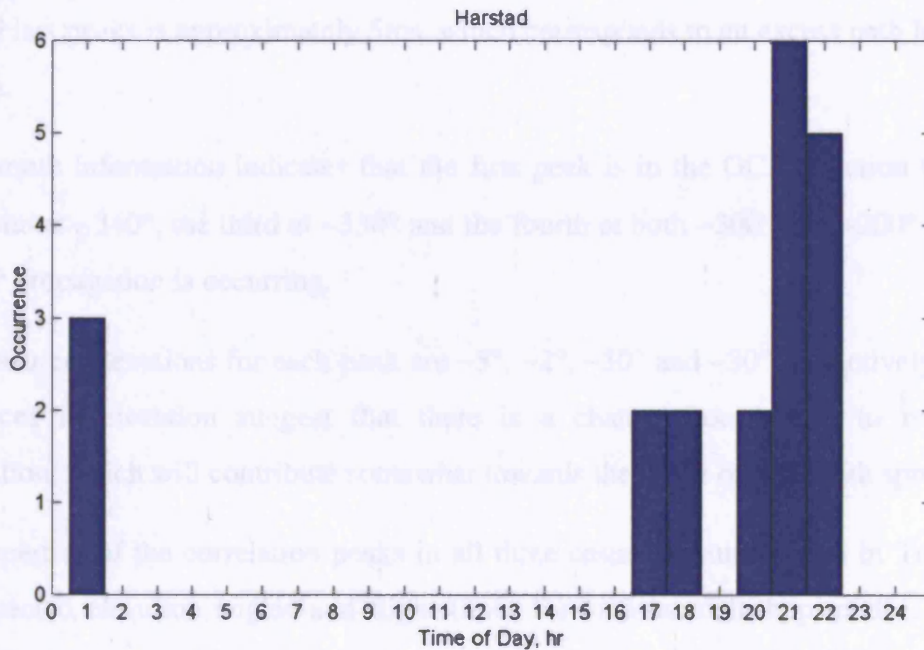
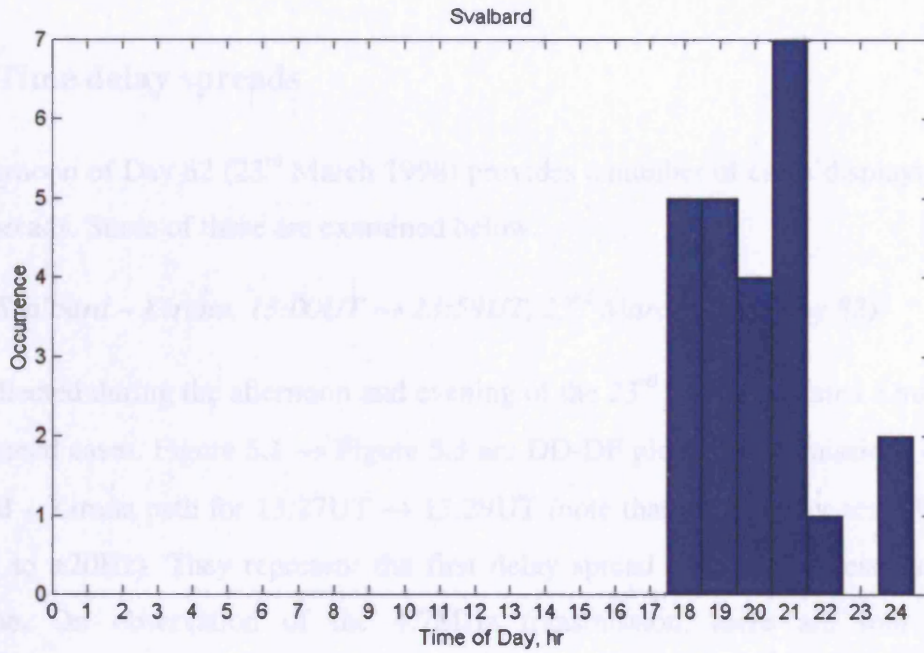


Figure 4.26 Times of day when interferer at  $\sim 165^\circ$  on 9.04MHz is present.

## 5. Propagation analysis

### 5.1 Time delay spreads

The afternoon of Day 82 (23<sup>rd</sup> March 1998) provides a number of cases displaying large delay spreads. Some of these are examined below.

#### 5.1.1 Svalbard – Kiruna, 13:00UT → 23:59UT, 23<sup>rd</sup> March 1998 (Day 82)

Data collected during the afternoon and evening of the 23<sup>rd</sup> March contains a number of delay spread cases. Figure 5.1 → Figure 5.3 are DD-DF plots of transmissions over the Svalbard – Kiruna path for 13:27UT → 13:29UT (note that the Doppler scale has been reduced to  $\pm 20$ Hz). They represent the first delay spread cases of interest during the afternoon. On observation of the 4.7MHz transmission, there are four distinct correlation peaks with a small amount of Doppler shift on each (never exceeding 3Hz), none of them have any appreciable Doppler spread. The delay separation between the first and last peaks is approximately 5ms, which corresponds to an excess path length of 1500km.

The azimuth information indicates that the first peak is in the GCP direction ( $\sim 352^\circ$ ), the second at  $\sim 340^\circ$ , the third at  $\sim 330^\circ$  and the fourth at both  $\sim 300^\circ$  and  $\sim 200^\circ$ . Clearly off GCP propagation is occurring.

The measured elevations for each peak are  $\sim 5^\circ$ ,  $\sim 2^\circ$ ,  $\sim 30^\circ$  and  $\sim 30^\circ$  respectively. These differences in elevation suggest that there is a change from single to multi-hop propagation, which will contribute somewhat towards the range of multipath spread.

The properties of the correlation peaks in all three cases are summarised in Table 5.1. The expected elevation angles and flight times for various multi-hop modes, using a curved Earth - curved ionosphere model for this path, are indicated in Table 5.2 (note that generally for off GCP propagation these elevation angles will reduce and the flight times increase as the excess path length increases).

Time - Date	Frequency (MHz)	Delay (ms)	Azimuth (°)	Elevation (°)	Doppler offset (Hz)
13:27 - 23/03/1998	4.7	3.9	352	5	-0.7
		5.0	340	2	-0.5
		6.7	330	30	-1.8
		9.0	200 and 300	30	-1.7
13:27 - 23/03/1998	6.8	4.1	0	0	-0.9
		5.9	356	30	-0.7
13:27 - 23/03/1998	9.0	4.0	0	1	-1.5
		4.8	0	16	-1.3

Table 5.1 Measured DD-DF properties

N° Hops	E <sub>100km</sub>		F <sub>250km</sub>		F <sub>300km</sub>		F <sub>350km</sub>	
	Elevation (°)	Delay (ms)						
1	7.1	4.0	20.3	4.3	24.2	4.5	27.8	4.7
2	17.6	4.2	38.9	5.2	44.0	5.7	48.3	6.2
3	26.3	4.4	50.9	6.4	55.7	7.3	59.6	8.1

Table 5.2 Svalbard – Kiruna, modelled elevation and delays for different layer heights

For the 4.7MHz case the time of flight of the first peak, at 3.9ms, is consistent with GCP propagation via an E-region at an altitude of ~100km. It is not clear whether this is via 1- or 2-hops since the time of flight resolution is not fine enough to discriminate, however, the elevation measurement is small suggesting 1-hop propagation. Although the second peak's elevation is low, the antenna beam pattern in elevation is very broad and the time of flight of 5.0ms is consistent with 1-hop F-region propagation at an altitude of ~300km (see Figure 4.3) and an offset of ~12° in azimuth from the GCP direction. The third peak's elevation is much larger and the time of flight is also consistent with 2-hop F-region propagation, this time with an azimuth offset of ~22° from the GCP direction.

The fourth peak contains enough signal energy and has azimuths away from the GCP direction and the azimuths of the other peaks, to indicate that it is not simply a Barker-13 correlation time sidelobe. However, the analysis for the fourth peak is somewhat complicated by its very large time of flight and multiple DOA estimates. For an

azimuth of  $300^\circ$ , the excess delay due to multiple hops, does not account entirely for the observed time of flight for the fourth peak. If, however, an azimuth of  $200^\circ$  is used, then signal power is arriving from behind the receiver and therefore introducing significant excess path length, which may account for the large time of flight. This does not account for some of the measured bearings arriving from  $300^\circ$ , however, when the secondary bearings are examined, most of the secondary signal power for this peak is arriving from  $\sim 200^\circ$ . The array sensitivity pattern at this frequency for a beam steered to  $200^\circ$  has a sidelobe at  $300^\circ$ . There is thus a directional ambiguity similar to that discussed in section 3.5.1. It appears that the fourth peak may have an actual azimuth of  $200^\circ$ , which accounts for the excess path delay, and that the DF algorithm is selecting the wrong ambiguity for some of the pixels in the DD-DF plots.

As expected for multi-hop propagation, the number of peaks present in the scattergrams of the higher frequency soundings is much fewer. At 6.8MHz there are only two peaks, both within a few degrees of the GCP direction, they have a time of flight and elevation consistent with 1-hop E-region and 2-hop F-region propagation respectively. The much smaller peaks, at the same Doppler offset and azimuth, beyond about 6ms are Barker-13 correlation sidelobes this time.

The 9MHz case at first appears to be composed of a single E-region mode, however, there is a shoulder in the correlation peak which suggest that a small amount of signal power may be arriving at 4.8ms via a 1-hop F-region mode. Elevation estimates do indicate that this signal power is arriving from a higher elevation than the E-region mode.

Less oblique multi-hop paths have increased angles of incidence at the ionospheric reflecting layers. At the higher frequencies, signals attempting to propagate via these paths will penetrate the ionosphere. This accounts for the reduction in the number of multipath peaks as the transmission frequency increases.

None of the DD plots in the figures show evidence of large Doppler spread, which suggests that propagation is not via irregularity regions. The 3 hourly ap index for the time 12:00  $\rightarrow$  15:00, was 3 (see Table 4.1). The time of day (being close to local midday) means that the statistically modelled auroral oval will be displaced northwards and the mid-latitude trough will be absent. The control points for both single and multi-

hop propagation will be outside the auroral oval disturbed regions where irregularity structures are most likely to be found. The off GCP propagation does indicate, however the presence of electron density gradients in the ionosphere to the West of the great circle path.

Figure 5.4 and Figure 5.5 are the delay-Doppler scattergrams for all of the 4.7MHz transmissions collected between 13:00UT and 23:59UT. They indicate that this type of complex multipath propagation continues throughout the afternoon, until sunset at approximately 17:30 UT after when the propagation conditions begin to change leading to a reduction in SNR and an increase in Doppler spread. The delay spreading continues, but the discrete structure of the modes is lost as the correlation peaks broaden in delay. These conditions change around 21:30UT after when there is less successful propagation at this frequency and the SNR drops further, this roughly coincides with the time of Corrected Geomagnetic midnight at 21:21UT for Kiruna when the ionosphere is likely to be most disturbed as the auroral oval moves to its southernmost extent. The remaining few detected cases appear to be single F-region modes with little delay or Doppler spread.

### *5.1.2 Harstad – Kiruna, 13:00UT → 23:59UT, 23<sup>rd</sup> March 1998 (Day 82)*

Data collected over the shorter, Harstad – Kiruna, path, also contains a number of delay spread cases in the afternoon and evening of 23<sup>rd</sup> March. The number of cases is less than for the Svalbard – Kiruna path since the oblique critical frequency for this short path is lower. In addition, multi-hop propagation over this path will be limited by the large angles of incidence at the ionospheric reflecting layers of the multi-hop rays. Multiple paths, however, are still possible via regions of enhanced electron density and tilts away from the GCP direction.

Figure 5.6 and Figure 5.7 show DD and DF information for cases collected between 18:00UT and 23:00UT on 2.8MHz. There is very little delay spread propagation on this path before 18:00UT or after 20:00UT. The azimuth information is represented in the colour coded pixels of the right hand panels, a feature of most of the delay spread plots is that the azimuth of the delayed signal power is from the North of the GCP direction.

The example at 19:04UT is displayed in more detail in Figure 5.8 and the properties of each correlation peak listed in Table 5.3.

Delay, ms	Azimuth, °	Elevation, °
1.7	352	27
3.3	280	61
4.4	337	42
5.8	326	56

Table 5.3 Properties of the delay spread case collected at 19:04UT on Day 82

N° Hops	E <sub>100km</sub>		F <sub>250km</sub>		F <sub>300km</sub>		F <sub>350km</sub>	
	Elevation (°)	Flight Time (ms)	Elevation (°)	Flight Time (ms)	Elevation (°)	Flight Time (ms)	Elevation (°)	Flight Time (ms)
1	46.7	0.9	69.0	1.8	72.1	2.1	74.4	2.4
2	64.8	1.5	79.1	3.4	80.8	4.1	82.1	4.8
3	72.6	2.1	82.7	5.1	83.9	6.1	84.7	7.1

Table 5.4 Harstad – Kiruna modelled elevation and delays for different layer heights

The first peak, arriving at 1.7ms, has a time of flight consistent with 1-hop F-region propagation for a layer height of ~250km. The azimuth measurement for this peak indicates that signal energy is arriving from ~ +50° away from the GCP direction. Although the extra distance travelled is not enough to affect the time of flight measurement too much, the reflection points are closer to the horizon with respect to the receiver array, which results in a lower elevation measurement.

The second peak's time of flight and elevation are consistent with 2-hop F-region propagation, this time with an azimuth ~ -25° away from the GCP. The third and fourth peaks are probably due to 2- and 3-hop propagation respectively, where the multi-hop reflection points are from tilts in the F-region, occurring in geographically different locations at different altitudes.

Measurements made at Kiruna ionosonde, presented in Figure 4.3, confirm that the F2 critical frequency was ~5MHz, which means that, being a near vertical incidence path, multi-hop propagation is only possible at frequencies below ~5MHz. The 23<sup>rd</sup> March 1998 was geomagnetically quiet so the auroral oval will be small and the ionosphere

relatively 'smooth'. At this time of day the D-region will be absent so there will be little absorption.

Under these conditions it has been seen that multi-hop propagation over either Svalbard – Kiruna or Harstad – Kiruna paths is successful, although there are clearly still ionospheric tilts, mainly to the North, which lead to the non GCP directions of arrival.

In terms of communication system performance, under these geomagnetically quiet conditions, significant multi-hop spread could cause problems for high data rate modems, taking the conditions outside the boundaries of operation as discussed in section 1.7.

## **5.2 Large Doppler spreads**

In Chapter 4 the occurrence statistics for measured cases exhibiting Doppler spreads in excess of 7Hz were examined. It was noted that while in general this type of signal could arrive from almost any direction of arrival, it was observed that there was a small preference for arrivals from the North. In this section consideration will be given to the detailed spatial characteristics of cases with large Doppler spread on a case-by-case basis for some of the more interesting examples.

### *5.2.1 Direction of arrival considerations*

When measuring direction of arrival of Doppler spread signals it is important to take into consideration the following points:

- Over the longer Svalbard – Kiruna path, even small deviations in DOA could correspond to large geographic distances between reflection points for different signal components. Conversely, the DOA of signals propagated over the short Harstad – Kiruna path will be much more sensitive to spatial dispersion.
- When a mode is Doppler spread, there may also be a random or systematic variation in the direction of arrival with respect to Doppler offset. Thus although it is possible to measure a mean (or power weighted mean) direction of arrival this value may not always be representative of all the directions of arrival within a Doppler spread mode.

### 5.2.2 Doppler offset as a function of azimuth

It was observed that there could be considerable variation in the direction of arrival of the components of an incoming signal. In some cases this variation may be systematically related to Doppler offset. Figure 5.9 shows a sequence of 9MHz soundings exhibiting Doppler spread collected over the Svalbard – Kiruna path between 13:00UT and 14:30UT on 25<sup>th</sup> March (Day 84). In most of them there is a distinct trend in Doppler offset with azimuth. These soundings at 9MHz appear to be the only cases around this time of day exhibiting significant Doppler spread. Such spreading is characteristic of scatter propagation via irregularities. The scale size of irregularities is important and in these cases may only be appropriate to cause scattering for signals close to 9MHz.

Figure 5.10 represents such a Doppler spread case, measured at 13:29UT, in more detail. There is a small 1-hop E-region GCP mode arriving at 4ms delay followed by a broad Doppler spread mode at ~ 4.5ms. This Doppler spread mode appears to be composed of two separate spread modes centred at -10Hz and +10Hz with azimuths 351° and 12° and elevations of 1.5° and 15° respectively. On closer examination it can be seen that the signals arriving from around 351° have a mean time of flight of 4.6ms while the signals arriving from 12° have a mean time of flight of 4.7ms. This is consistent with modelled off great circle propagation via a curved ionosphere height of ~250km over a curved Earth.

Figure 5.11 plots the Doppler offset vs. the DOA estimates of the signal components. Both azimuth and elevation plots exhibit clustering as well as a trend in Doppler offset, which is much more evident in azimuth than in elevation. There is a very clear trend whereby the Doppler offset changes from positive to negative as the azimuth changes from East to West and the elevation changes from high to low.

In order to assist in the analysis of such cases, a set of tools have been developed which allow the presentation of the DD-DF information on a ‘Radar’ style plot superimposed over associated geographical information such as coastlines. These plots in essence indicate the location of the virtual reflection points for the various signal components. The properties of the signal components, such as relative power and Doppler offset, can be colour coded.

Figure 5.12 displays two radar plots for this example. To generate these plots both DOA and range information must be used. Clearly DOA information is available directly from the DD-DF data (and is corrected for the  $4.5^\circ$  error in array orientation). The calculation of range, however, is a more complex issue. In the plots illustrated in Figure 5.12, a simplistic calculation is made using the assumptions that for a model Earth with a given radius the reflecting ionospheric layer is fixed in altitude and that the range from the receiver to the reflection point is  $\frac{1}{2}c.t$  (where  $c$  is the speed of light in free space and  $t$  is the validated time of flight of the signal component). The range is thus based on a ‘Radar’ calculation. These assumptions only hold for 1-hop propagation in the absence of strong group retardation, nonetheless valuable insight may still be gained using this method.

The upper panel of Figure 5.12 is colour coded to relative signal power in dBr and clearly shows the two regions of interest spanning the great circle propagation path. The lower panel is colour coded to Doppler offset, with the colour scheme reversed in line with convention, where ‘red-shift’ indicates a negative Doppler offset. The change from blue-shift to red-shift from East to West is obvious. This type of Doppler spread is characteristic of propagation via drifting irregularity regions, as suggested by *Wagner et al.* [1988 and 1995]. In this example the direction of arrival information indicates that the irregularities are drifting in an East  $\rightarrow$  West direction. Signal components scattering from irregularities to the East of the GCP, where the movement of the irregularities tends to shorten the path, will suffer a positive Doppler shift while components scattered from the West of the GCP will suffer a negative Doppler shift as the movement tends to lengthen the path.

Irregularity regions may be embedded in ionospheric convection flows, these have been modelled as described in *Lockwood* [1993] and discussed in section 1.2. The geographic behaviour of the flow is dependent on the magnitude and direction of the interplanetary magnetic field ( $B_y$  and  $B_z$ ). These parameters are available from the Coordinated Data Analysis Web (CDAWeb) database maintained by NASA Goddard Space Flight Center (see references) and have been plotted in Figure 5.13 for the relevant day. At 13:29:45UT  $B_y$  is positive and  $B_z$  negative, however, over the course of the middle of the day,  $B_y$  changed sign a number of times while  $B_z$  remained negative. The modelled convection flow patterns are illustrated in Figure 1.6. For the magnetic conditions

described, the flow could have been in any one of the states illustrated in the top row of the figure. Considering the time of day and latitude of the reflection points it seems most likely that they are within the lower latitude return flows, moving towards the night side, rather than part of the cross polar flows. This is consistent with the observed East → West irregularity movement.

Figure 5.14 illustrates the movement of these observed scattering regions in time, using radar plots, colour coded for relative Power and Doppler offset respectively (note that the radar plots for 13:29UT have not been included). It is clear that the movement of the main scattering features, as indicated by the Power plots, is consistent with the sense of the convection flows, deduced from the Doppler measurements above, and indicated in the Doppler plots. Table 5.5 lists the properties of the Doppler spread, F-region reflections for each case, while Table 5.6 lists the calculated distances moved and consequent mean velocities between measurements, assuming a 1-hop virtual reflection height of 250km, which is consistent with the measured times of flight. Where there is more than one DOA associated with these Doppler spread modes, as is the case for 13:29UT, both values are tabulated. This also means that there will be multiple possible velocity estimates whenever this case appears in Table 5.6.

Time of Day	Time of Flight, ms	Azimuth, °
13:09:43	4.8	14
13:29:43	4.6	351
	4.7	12
13:49:43	4.6	349
14:09:43	4.5	339
14:29:43	4.8	323

Table 5.5 Properties of Doppler spread, F-region reflections

Times of Day	Distance moved, km	Mean velocity, km/h	Mean velocity, m/s
13:09:43 →	267	801	223
13:29:43	29	87	24
13:29:43 →	28	84	23
13:49:43	254	762	212
13:49:43 →	109	327	91
14:09:43			
14:09:43 →	184	552	153
14:29:43			
Overall	588	1764	123

Table 5.6 Mean velocities between measurements

Figure 5.15 illustrates the propagation geometry for signals scattered from irregularities away from the GCP direction, where measurements to the East are positive. Ignoring changes in elevation and assuming that the irregularities are drifting perpendicular to the GCP, the rate of change of path length as a function of crossing velocity, as the irregularities move from East → West, is indicated in Equation 5.1.

$$2 \frac{dx}{dt} \sin \theta = \frac{dR}{dt}$$

Where:  $\frac{dR}{dt}$  = Rate of change of path length  
 $\theta$  = Azimuth offset from GCP direction  
 $\frac{dx}{dt}$  = Crossing velocity

Equation 5.1

At the same time, the Doppler equation, Equation 5.2, indicates the amount of Doppler shift,  $f_d$ , imposed for a given rate of change of path length.

$$f_d \lambda = -\frac{dR}{dt}$$

Where:  $f_d$  = Doppler offset  
 $\lambda$  = Signal wavelength

Equation 5.2

Combining Equation 5.1 and Equation 5.2 results in an expression for the crossing velocity:

$$\frac{dx}{dt} = -\frac{f_d \lambda}{2 \sin \theta}$$

Equation 5.3

It is possible to apply this relationship to every pixel in the DD-DF data structure, to determine the crossing velocity for each pixel. The resulting crossing velocities are presented in Figure 5.16 and Figure 5.17 where the colour scales of the DD plots in the left-hand panels indicate crossing velocity and the right-hand panels plot crossing velocity vs. time of flight.

All of these cases have relatively narrow, close to zero velocity, 1-hop E-region returns. The F-region returns for each case, however, do exhibit a variety of crossing velocities. This would indicate that the convection flows the scattering irregularities are embedded

in are not rigid but that reflection/scattering points are moving at different velocities within the flows.

Histograms of the F-region crossing velocities for each case, plotted in Figure 5.18, confirm that there is a spread in crossing velocity, however, there is usually a distinct peak in the velocity distributions corresponding to the statistical mode. The velocity statistics are listed in Table 5.7:

Time of Day	Velocity estimate, m/s		
	Mean	Median	Mode
13:09:43	1474	1009	1025
13:29:43	1005	862	125, 1125
13:49:43	624	669	675
14:09:43	368	698	975
14:29:43	343	66	275

Table 5.7 Doppler crossing velocity statistics

The magnitudes of these Doppler derived velocity values are close to the 1200m/s estimated by *Wagner et al* [1995], despite the experimental path geometry being different. Although the trends are similar, they do not agree with the velocities calculated from the movement of the main scattering features over time, indicated in Figure 5.14 and listed in Table 5.5 and Table 5.6.

While it is possible that these soundings are illuminating the same set of irregularities as they convect across the path, this is unlikely since the Doppler calculated crossing velocities do not agree with the observed movement of the major scattering features. It is more likely that the observed scattering region is large in extent and/or composed of a number of separate scattering regions. Since the amount of scatter propagation is dependent on aspect angle the returns are strongest near to the GCP and the observed scattering regions are different from sounding to sounding. This would certainly explain both the variations in Doppler crossing velocity from case to case and the difference in magnitude between the Doppler velocity estimates and movement velocity estimates. The movement velocity estimates are thus not representative of the true convection flow velocities.

### 5.2.3 *E-region ~GCP modes*

When Doppler spreading occurs on multi-moded cases, a common feature is the presence of a mode with an E-region time of flight, this is not unexpected. Figure 5.19 illustrates a number of such cases at 4.7MHz over the Svalbard – Kiruna path between 11:00UT and 12:30UT on 25<sup>th</sup> March (Day 84). In most cases these E-region modes have very small Doppler offsets, very narrow Doppler spread and an azimuth very close to the GCP direction.

Figure 5.20 is an example showing an E-region GCP mode and a spread mode in more detail. The E-region mode arrives at 3.9ms with an azimuth of 354° (~GCP), Doppler spread and azimuth standard deviation of 1.3Hz and 0.8° respectively. The second mode, arriving at 5.2ms delay, has a large Doppler spread of 15.7Hz and an azimuth spread of 5.2° around 339° azimuth. There is also a trend in azimuth, which varies systematically with Doppler offset in a similar way to that described previously. The trends to increased time of flight at the Doppler extremes of this mode are associated with the increased path length at those azimuths. There is a third mode arriving at 7.5ms delay with a Doppler spread of 7Hz, low SNR and most of the signal power arriving from 184°.

When this example is displayed on a radar plot, as in Figure 5.21, it becomes clear that although the second mode appears to contain the most signal power, as indicated by the amplitude of the correlation peaks, this power is spread across a range of delay, Doppler and azimuth. Geographically, the best signal power density is to be found in the first, E-region GCP mode, indicated by the red region at the path midpoint (in this radar plot, the E-region mode has been displayed at the wrong range with respect to the receiver because a virtual reflection height of 250km is assumed to give the correct range for the F-region spread signals). In general, when an E-region mode is present in a sounding, its direction of arrival is usually close to the GCP direction and it often has a low Doppler spread.

### 5.2.4 *Doppler spreading observed over both paths.*

Large Doppler spreading is apparent on the evening of 25<sup>th</sup> March on both the Svalbard – Kiruna and Harstad – Kiruna paths, in common with many Doppler spread cases there is also some azimuth spread. A number of examples over the Harstad – Kiruna path on

4.7MHz have large times of flight for the Doppler spread modes and a mean azimuth of arrival to the North-West. The 4.7MHz soundings for the Svalbard – Kiruna path were recorded a few minutes later. They also show considerable Doppler and azimuth spreading at relatively large delays. Figure 5.22 illustrates these examples.

Given the time of flight and azimuth information it is possible that the scattering regions for both paths lie geographically close to each other. Figure 5.23 and Figure 5.24 are radar plots for illustration. It is clear that, although the signal power on the Harstad – Kiruna soundings is lower, for both paths the Doppler spread modes are arriving from the same geographic areas.

The three hourly ap for these times is quite low and the magnetic  $B_y$  and  $B_z$  are both positive and greater than 5nT (see Figure 5.13). This indicates that the convection flows should be similar to the modelled three cell pattern illustrated in the bottom right panel of Figure 1.6. The flow is complex with flow vectors moving in a number of directions, which would account for the large observed spreads. The auroral oval for these conditions is somewhat shrunken, which may account for why these reflection points are so far North.

### **5.3 Concluding remarks**

Over the Svalbard – Kiruna path, a trend in the form of a reduction in the number of multipath peaks as the transmission frequency increased was attributed to the increase in the angle of incidence at the ionospheric reflecting layers. The more delayed peaks propagate via less oblique, multi-hop paths, which at the higher frequencies may penetrate the ionosphere. Since there is only small Doppler spread, it was concluded that propagation in these cases was via geographically distributed tilts in an otherwise undisturbed ionosphere. This type of propagation breaks down after sunset and around midnight CGMLT as the auroral oval has a larger effect. Over the Harstad – Kiruna path, much of the multipath propagation is due to propagation via tilts to the North of the path.

When large Doppler spreads are considered it can be seen that many Doppler spread cases show a trend in direction of arrival with Doppler offset, these have been attributed to scatter propagation via drifting irregularity regions. The ambiguity in the direction of

irregularity drift as described in *Wagner et al.* [1988 and 1995] has been resolved using DF information and the flow direction has been related to modelled convection flows in the high latitude ionosphere which in turn are dependent on solar terrestrial magnetic conditions. The observed movement over time of the major scattering features is consistent with the Doppler trends. However, analysis of the crossing velocity of the irregularities, derived from both Doppler measurements and movement of the major scattering features over time, reveals that the flow velocities are actually much larger than appears from the movement calculations and that each sounding is illuminating different sets of irregularities embedded in a turbulent bulk convection flow.

It was observed that in many Doppler spread cases, a 1-hop E-region return is also visible. In general, when an E-region mode is present in a sounding, its direction of arrival is close to the GCP direction and it often has a low Doppler spread. The geographic distribution of signal energy from such a mode is much better than for the F-region Doppler/azimuth spread modes.

A set of soundings displaying long delays on the Harstad – Kiruna path were examined. By using a radar plotting tool it was seen that these returns arrived from the same geographical region as returns seen almost simultaneously on the Svalbard – Kiruna path.

Finally, the correlation of Doppler spread with direction of arrival, both in terms of the observed drifting irregularities and the localised nature of many E-region modes, may potentially be useful for communication systems in the sense that it allows the possibility of eliminating unwanted (Doppler spread) power from the channel while leaving wanted, unspread, power for a modem equaliser to operate on. This is discussed in the next chapter.

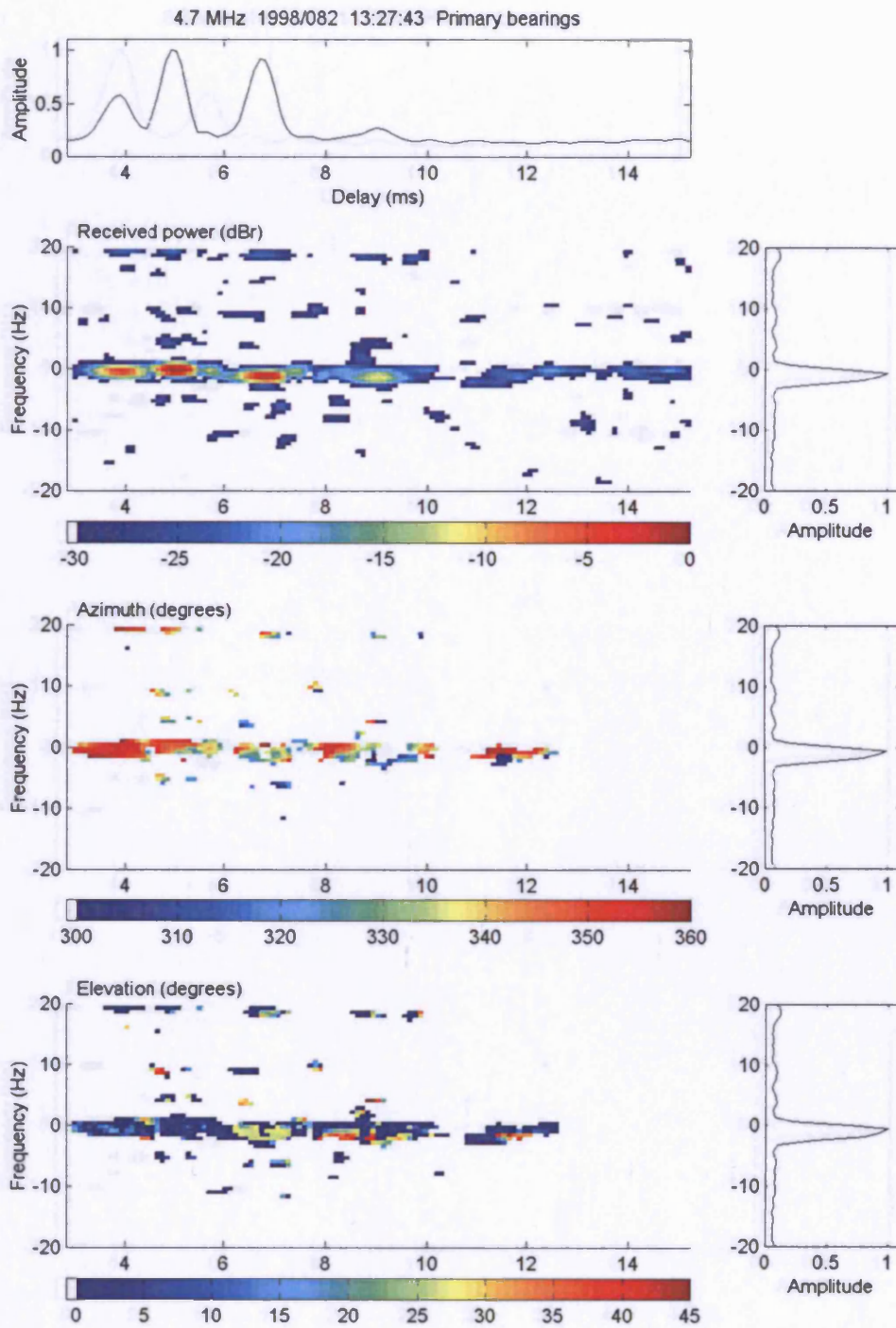


Figure 5.1 4.7MHz sounding over the Svalbard – Kiruna path at 13:27UT on 23<sup>rd</sup> March (note that the Doppler scale has been reduced to  $\pm 20$ Hz)

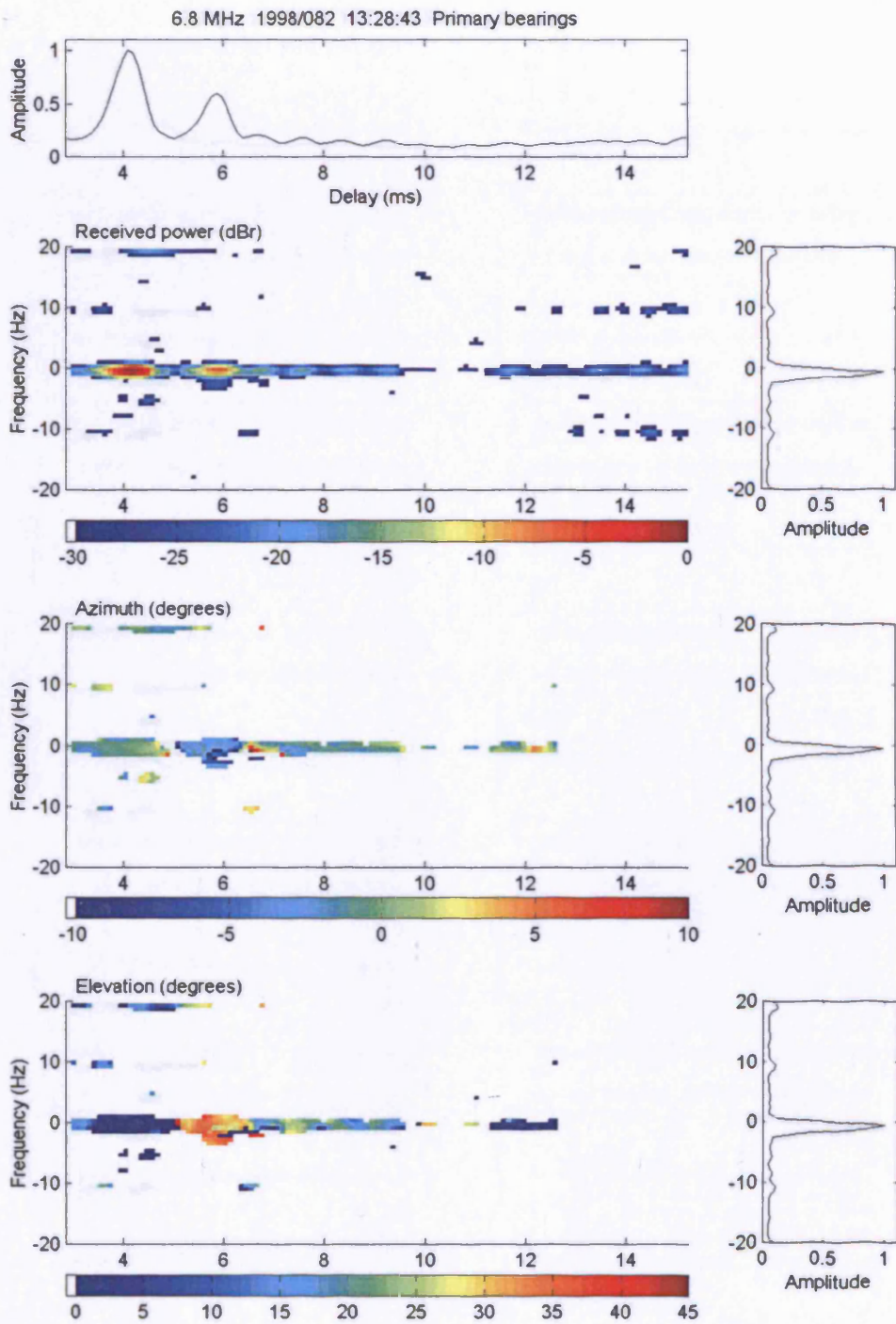


Figure 5.2 6.8MHz sounding over the Svalbard – Kiruna path at 13:28UT on 23<sup>rd</sup> March (note that the Doppler scale has been reduced to  $\pm 20$ Hz)

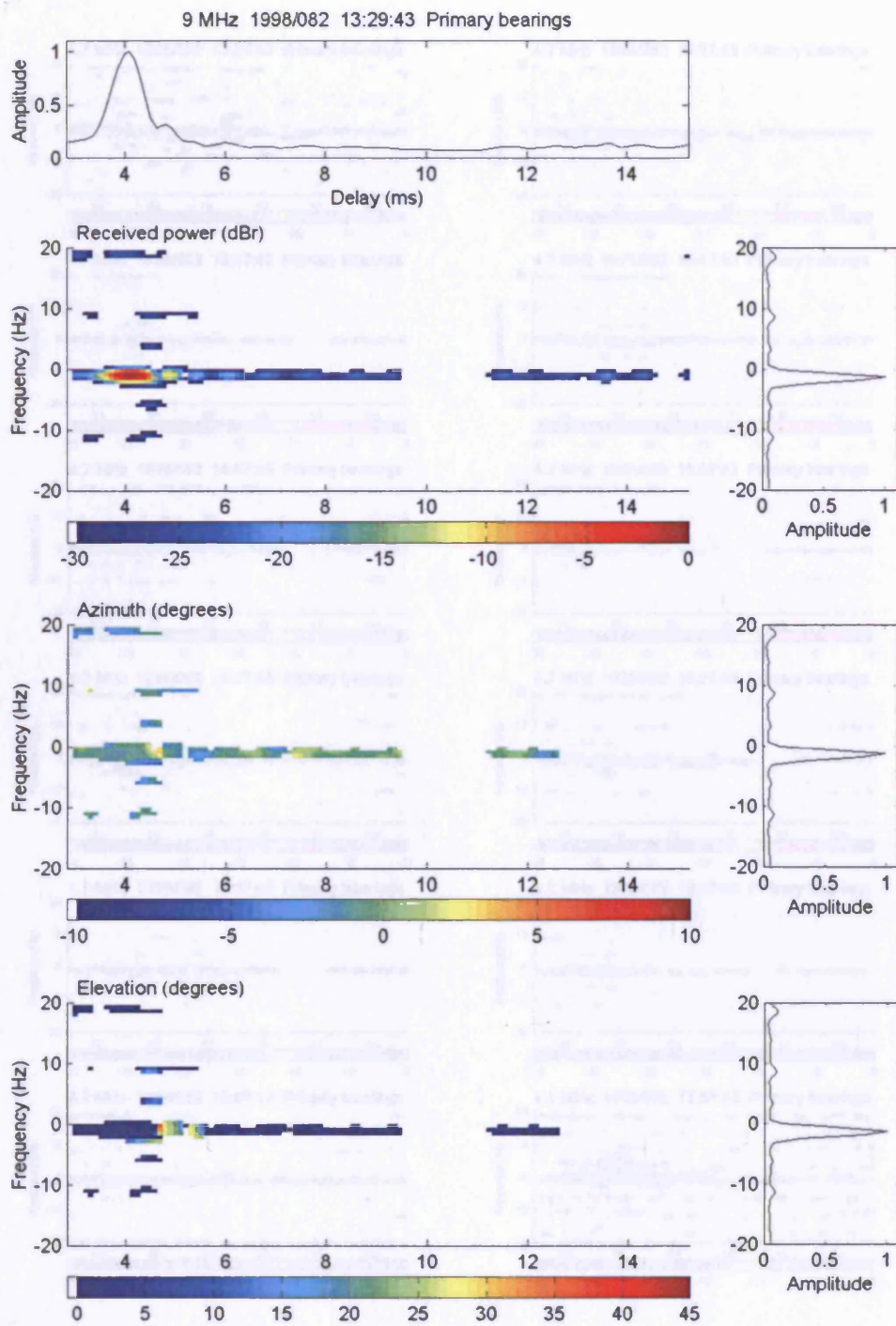


Figure 5.3 9MHz sounding over the Svalbard – Kiruna path at 13:29UT on 23<sup>rd</sup> March (note that the Doppler scale has been reduced to  $\pm 20$ Hz)

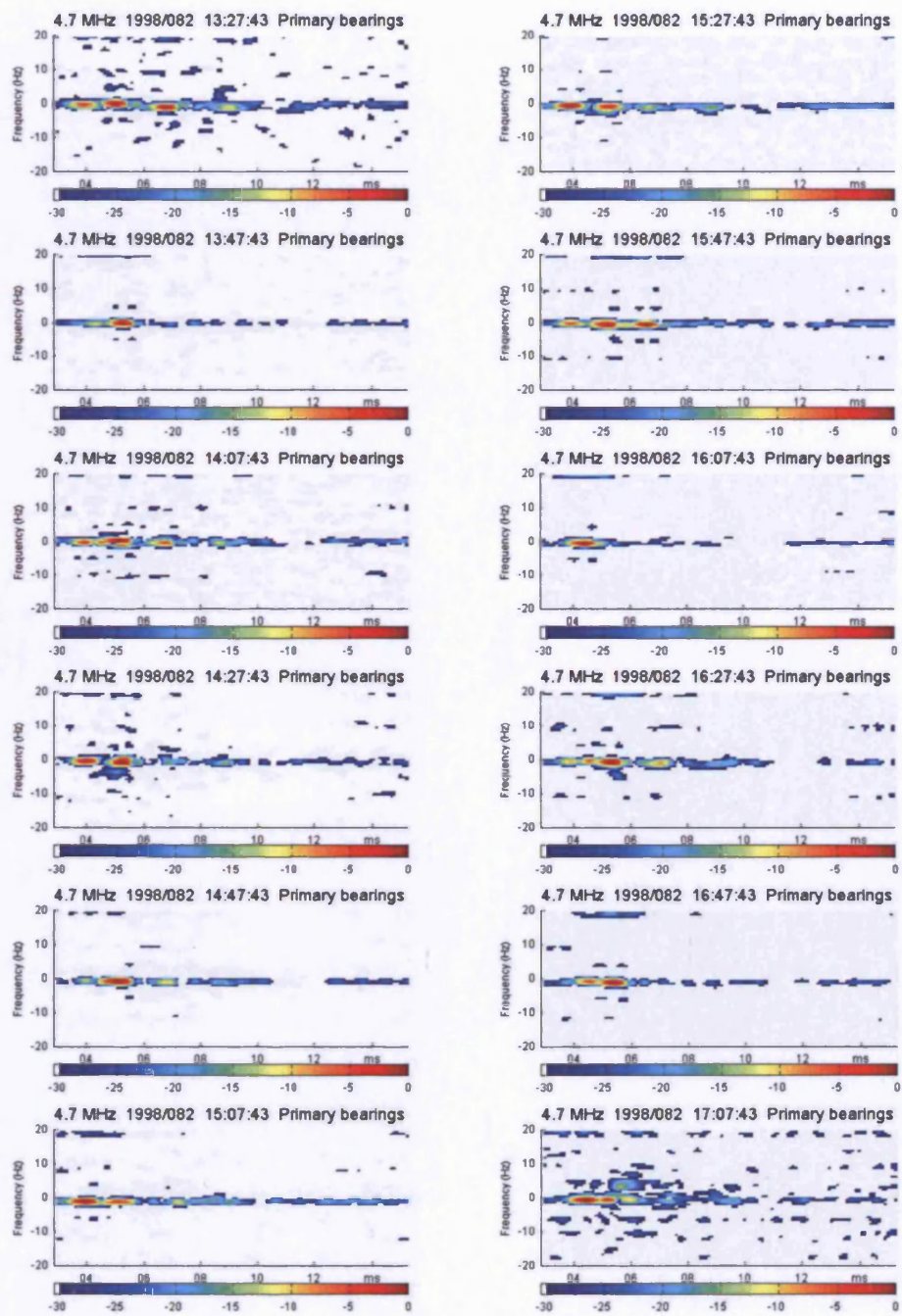


Figure 5.4 delay-Doppler scattergrams for all of the 4.7MHz Svalbard – Kiruna soundings collected between 13:00UT and 17:07UT on 23<sup>rd</sup> March (note the reduced Doppler scale)

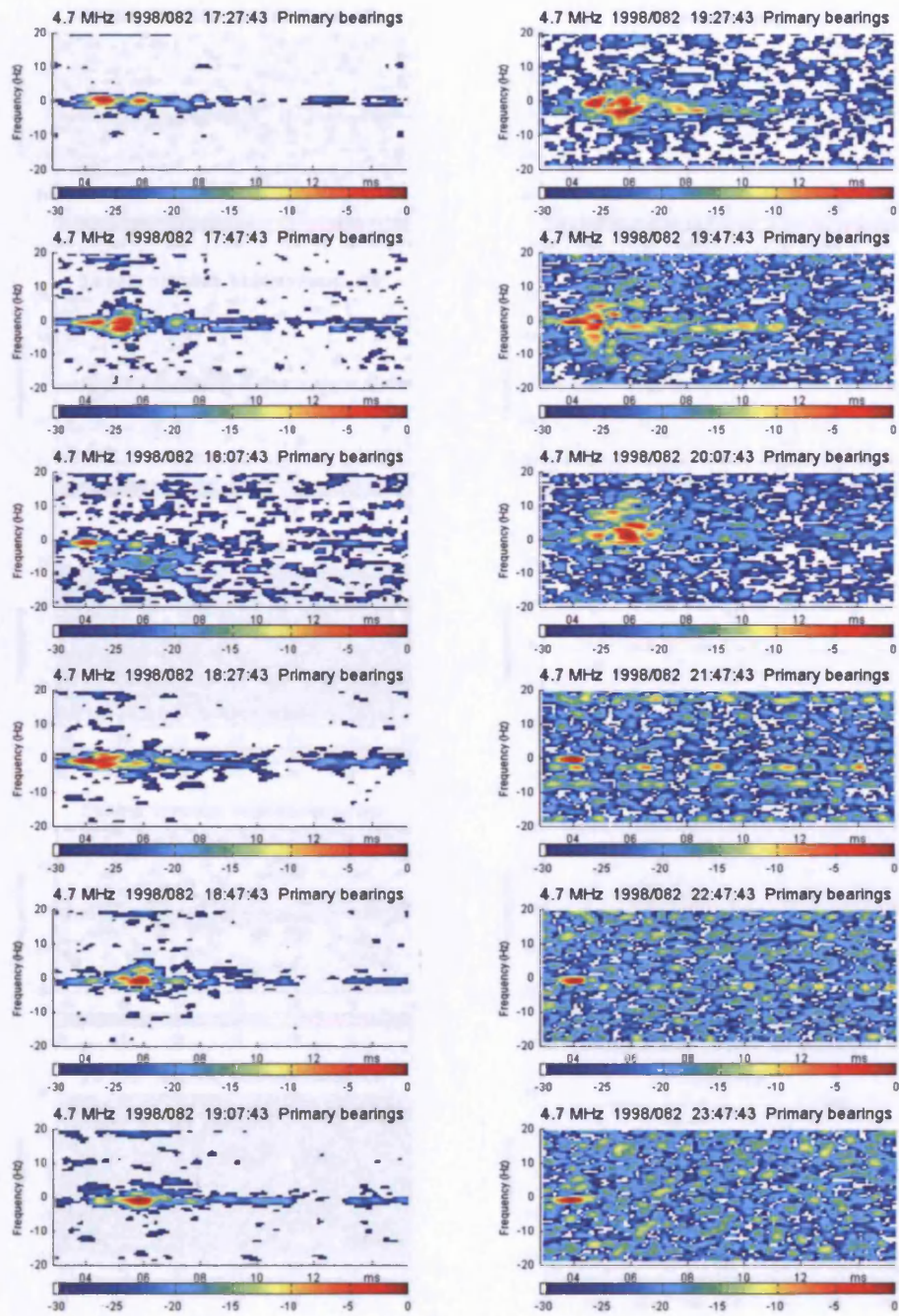


Figure 5.5 delay-Doppler scattergrams for all of the 4.7MHz Svalbard – Kiruna soundings collected between 17:27UT and 23:47UT on 23<sup>rd</sup> March (note the reduced Doppler scale)

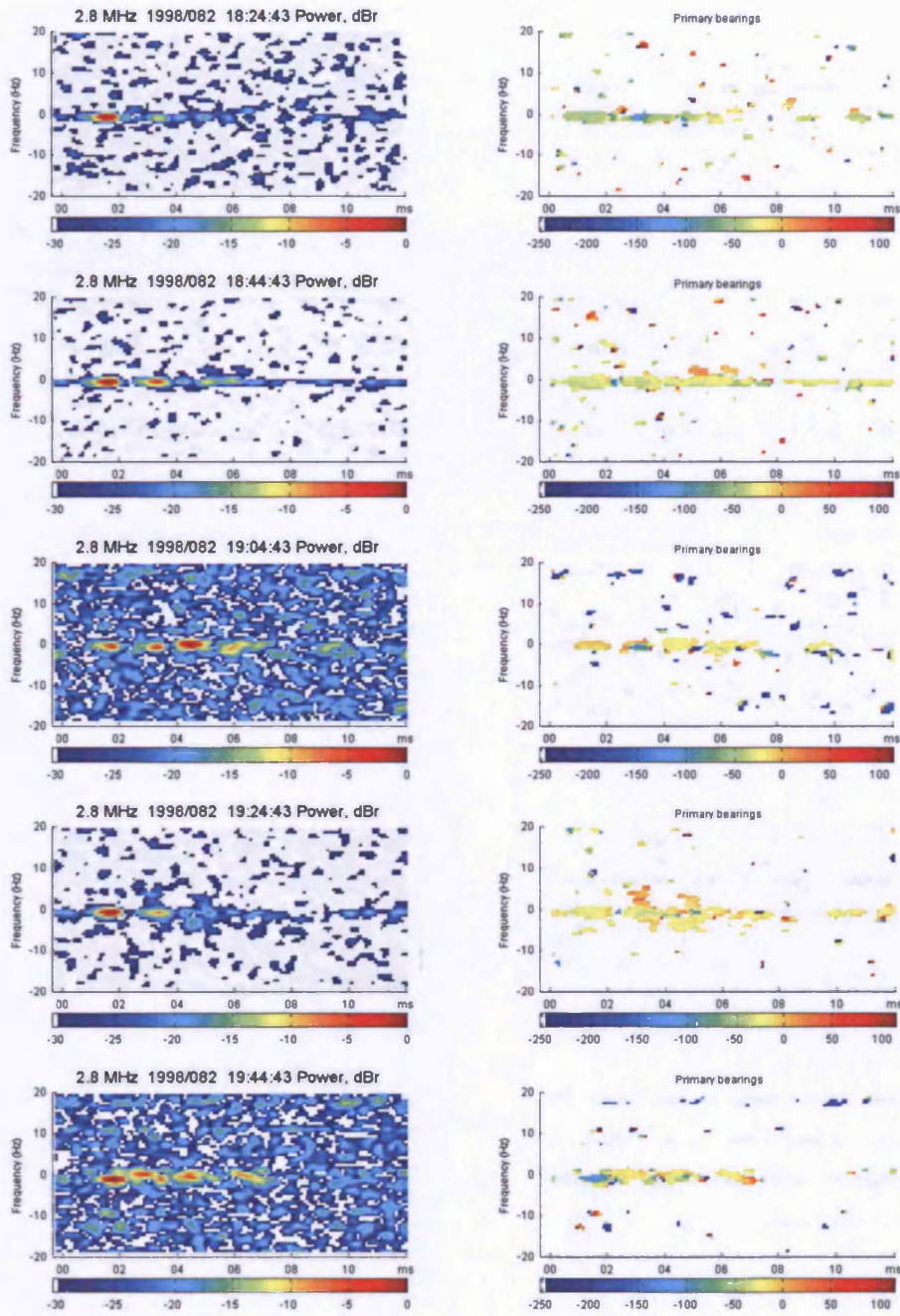


Figure 5.6 delay-Doppler scattergrams for all of the 2.8MHz Harstad – Kiruna soundings collected between 18:00UT and 19:44UT on 23<sup>rd</sup> March (note the reduced Doppler scale)

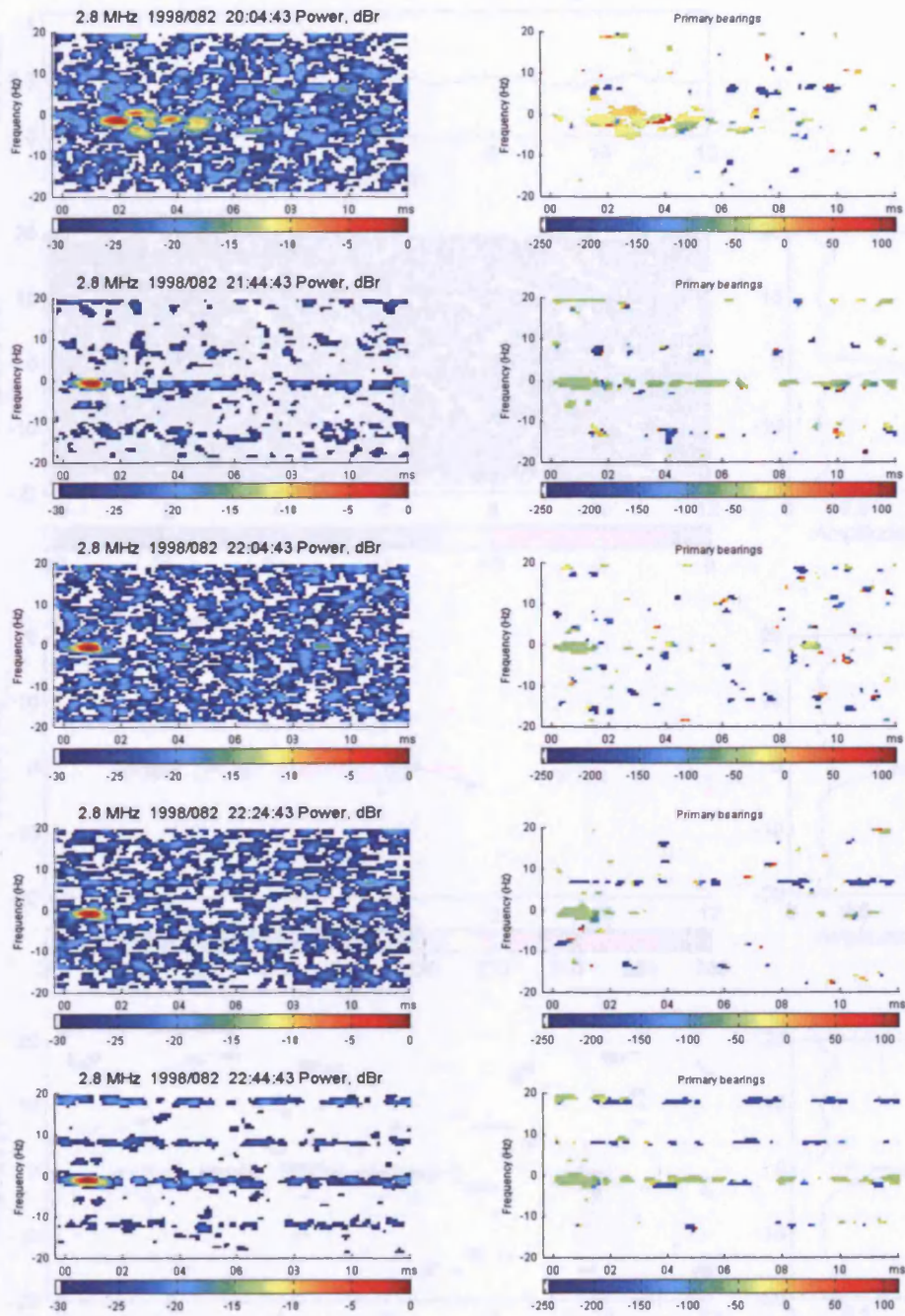


Figure 5.7 delay-Doppler scattergrams for all of the 2.8MHz Harstad – Kiruna soundings collected between 20:04UT and 22:44UT on 23<sup>rd</sup> March (note the reduced Doppler scale)

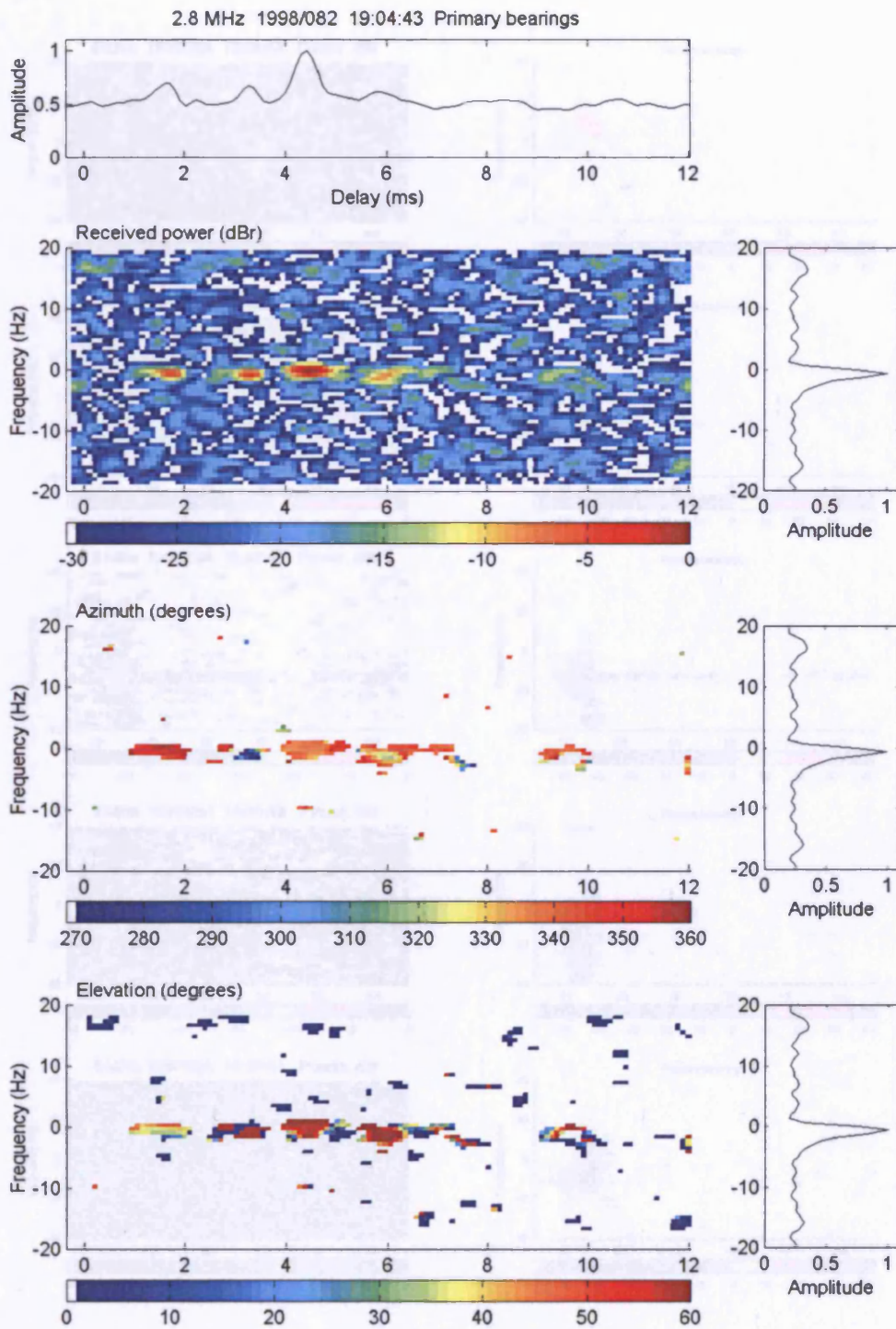


Figure 5.8 2.8MHz sounding showing multipath spread over the Harstad – Kiruna path at 19:04UT on 23<sup>rd</sup> March (note that the Doppler scale has been reduced to  $\pm 20$ Hz)

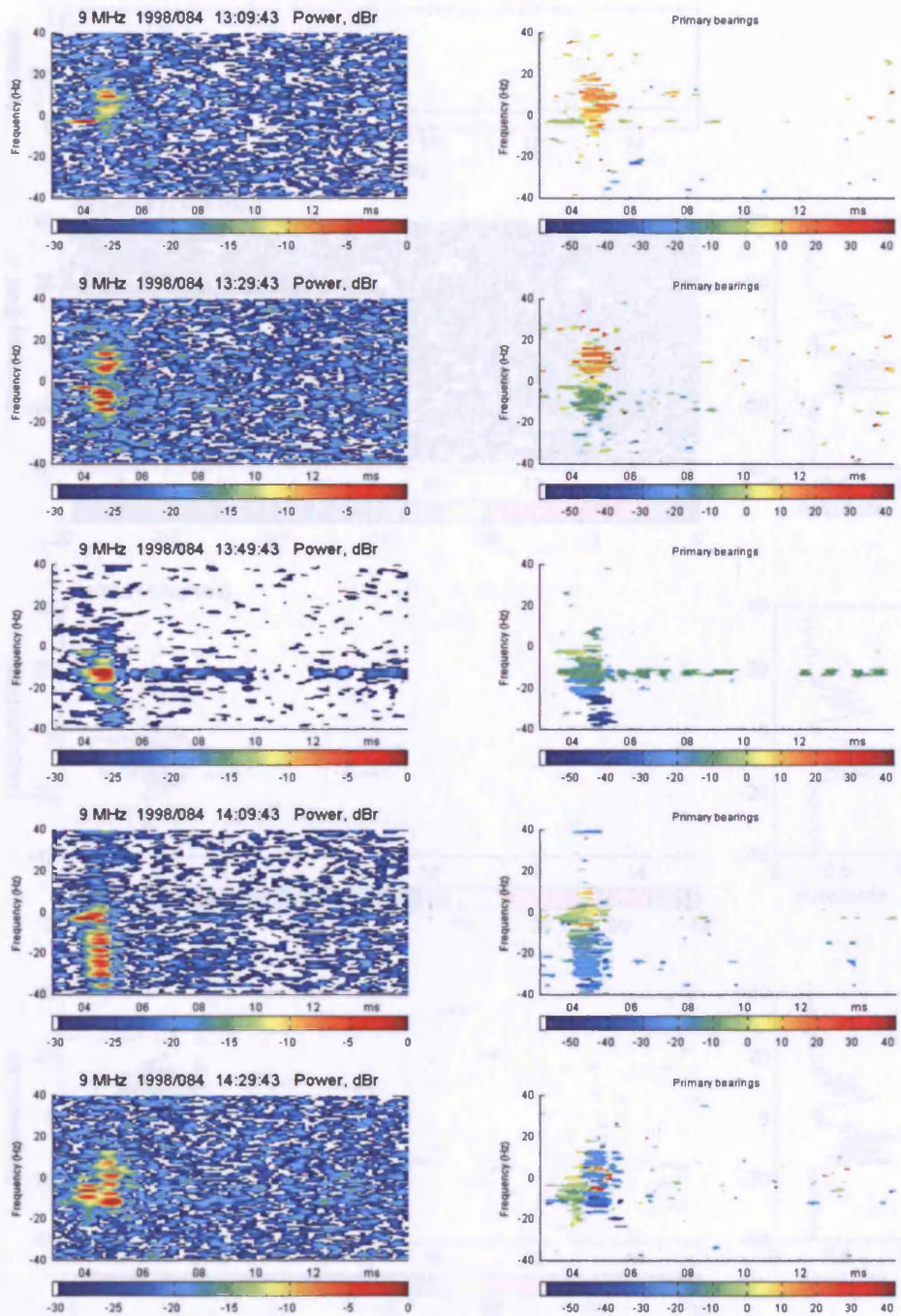


Figure 5.9 A sequence of Doppler spread cases, collected between 13:00UT and 14:30UT on 25<sup>th</sup> March, showing a systematic relationship between Doppler offset and azimuth.

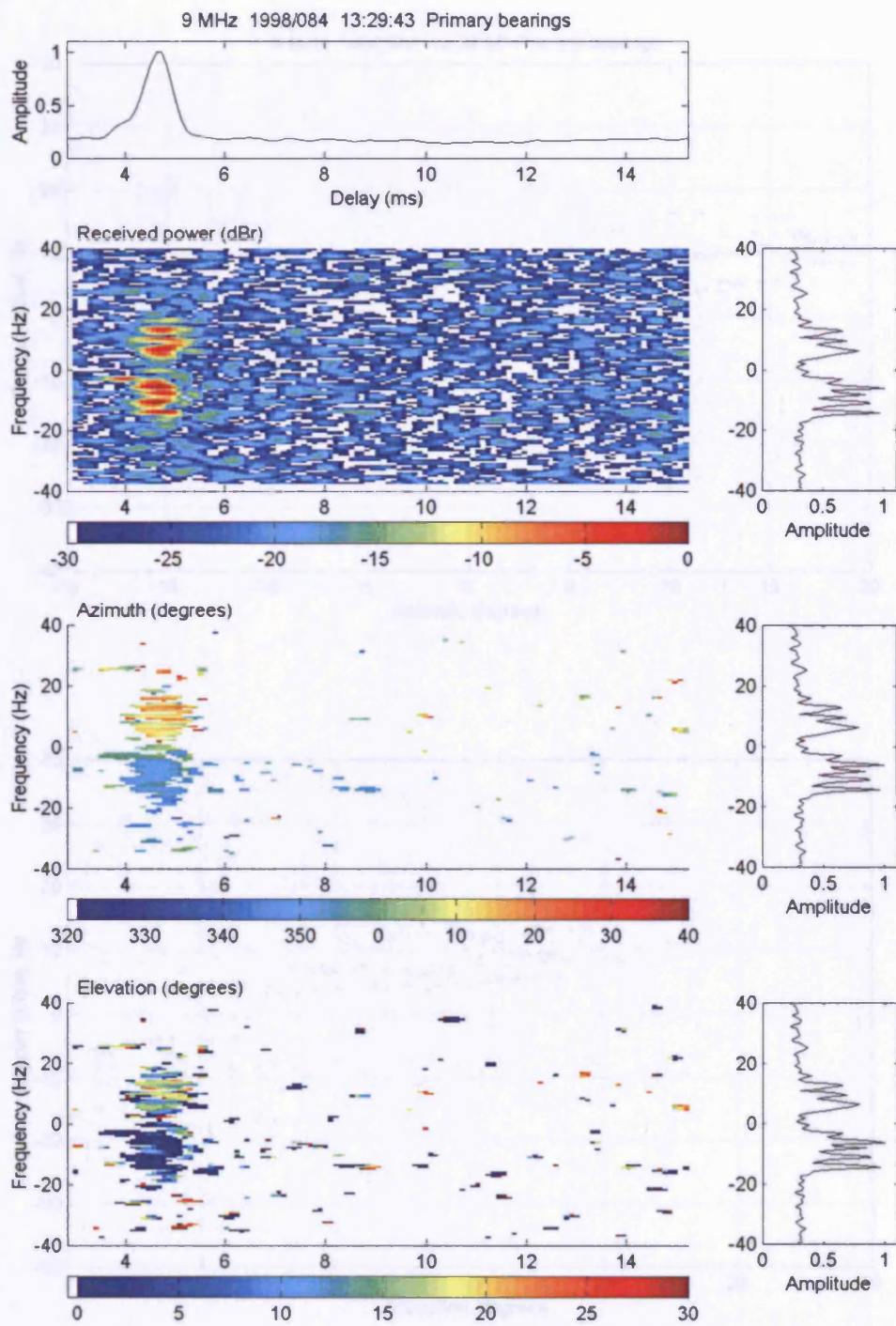


Figure 5.10 A selected Doppler spread case with a clear relationship between Doppler offset and azimuth

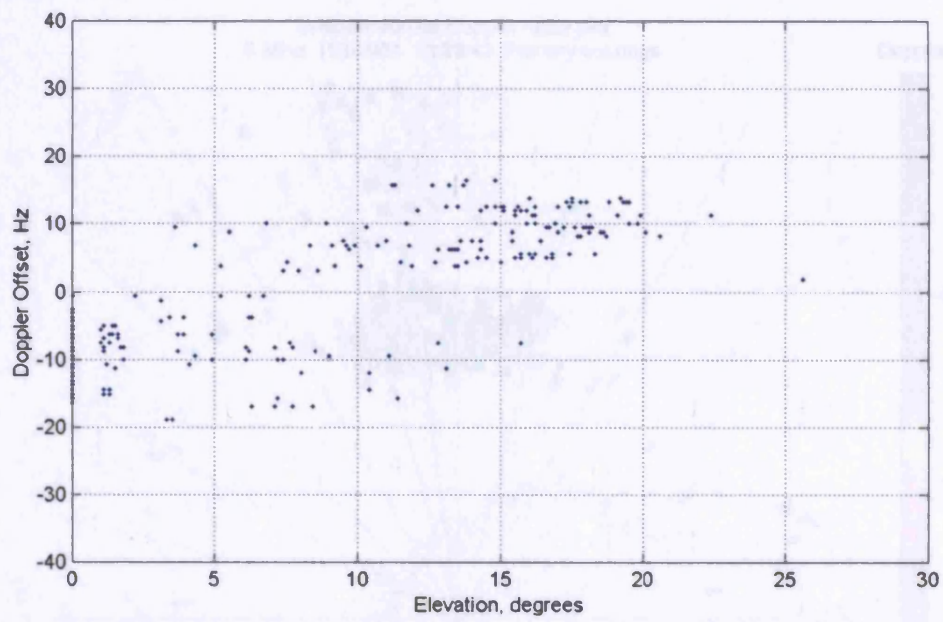
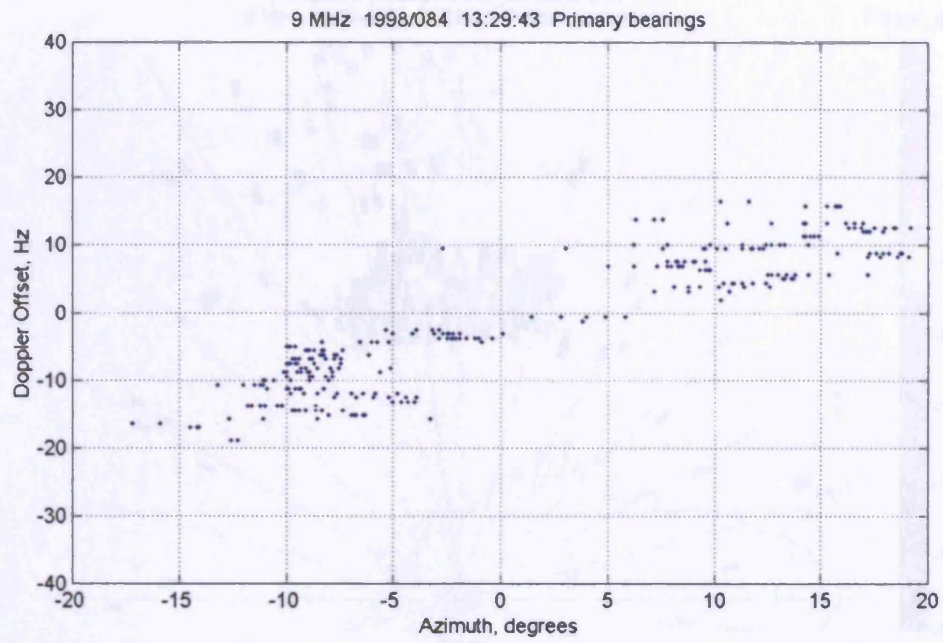


Figure 5.11 Doppler offset vs. DOA estimates of the signal components for the 9MHz sounding at 13:29UT on 25<sup>th</sup> March. Upper panel

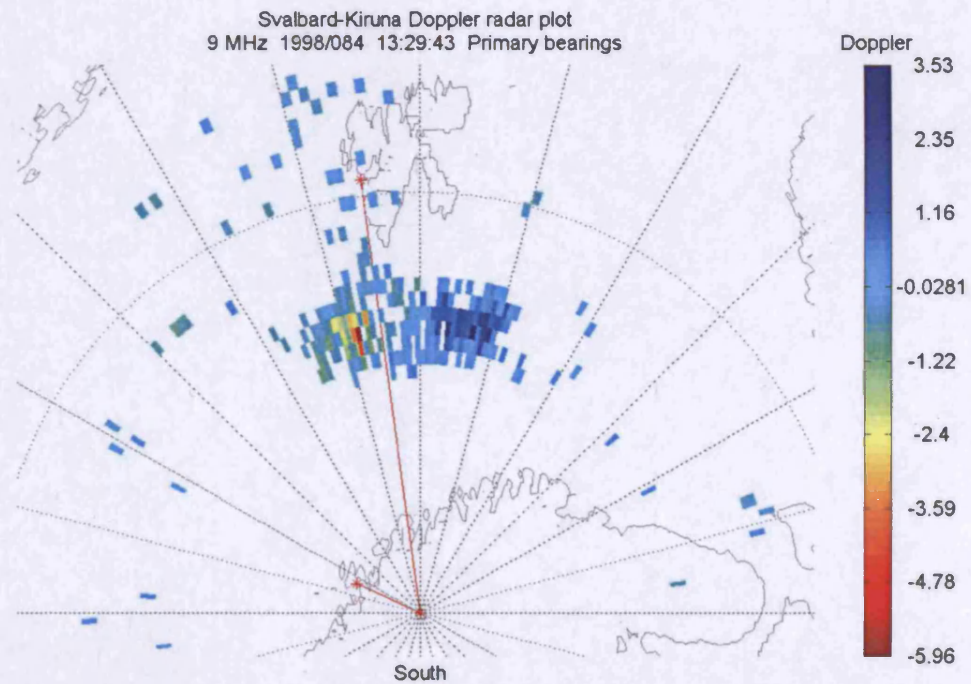
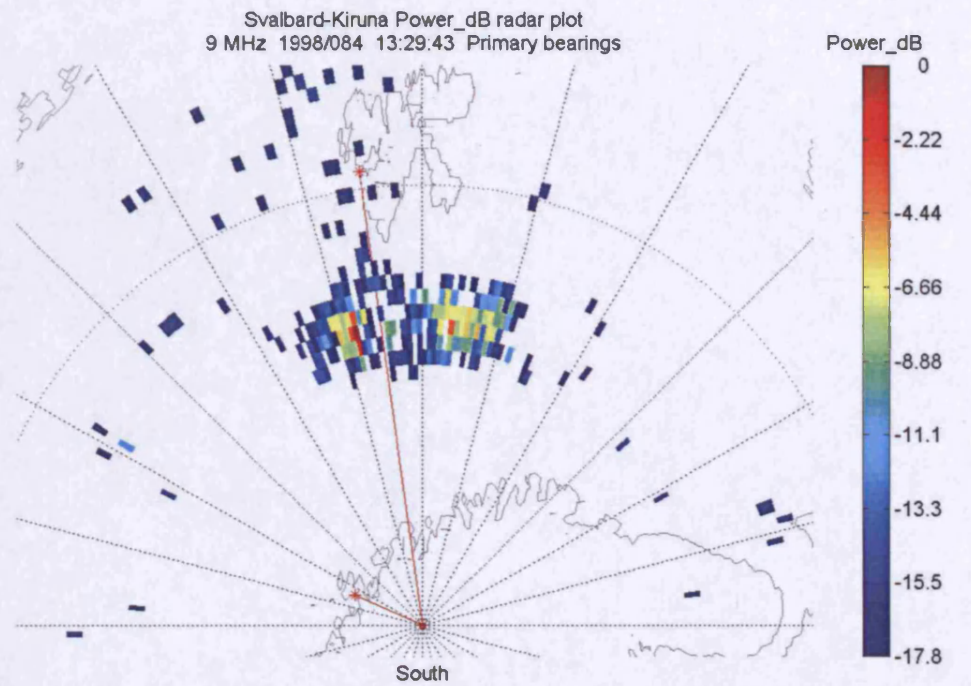


Figure 5.12 Radar plots for the 9MHz sounding at 13:29UT on 25<sup>th</sup> March. Upper panel colour scale is in dBr, lower panel in Doppler Hz (note the reversed scale)

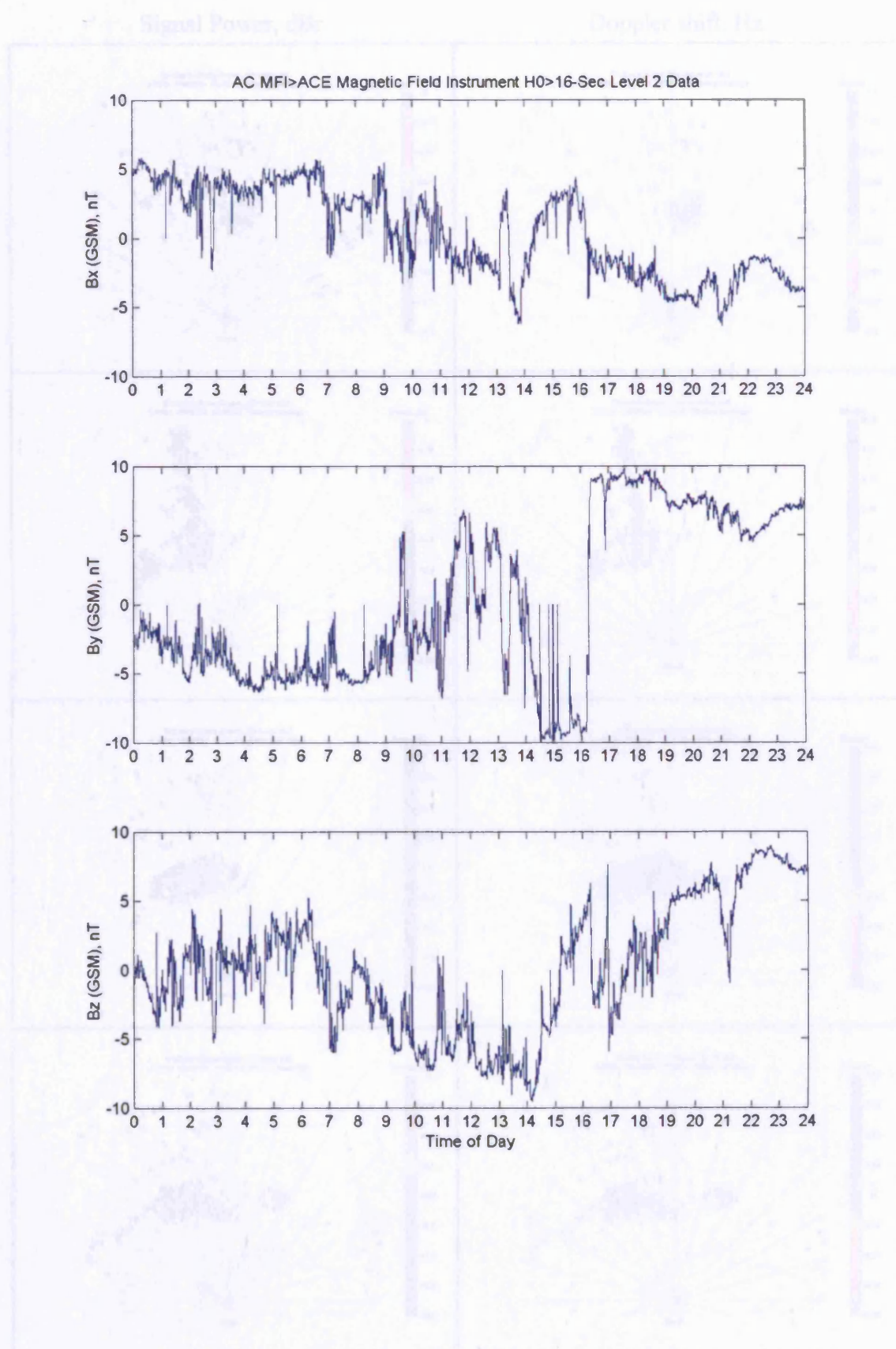


Figure 5.13 Magnetic Bx, By and Bz indices for 25<sup>th</sup> March 1998. Data courtesy of N. Ness (Bartol Research Institute) and NASA's CDAWeb (see References).

Signal Power, dBr

Doppler shift, Hz

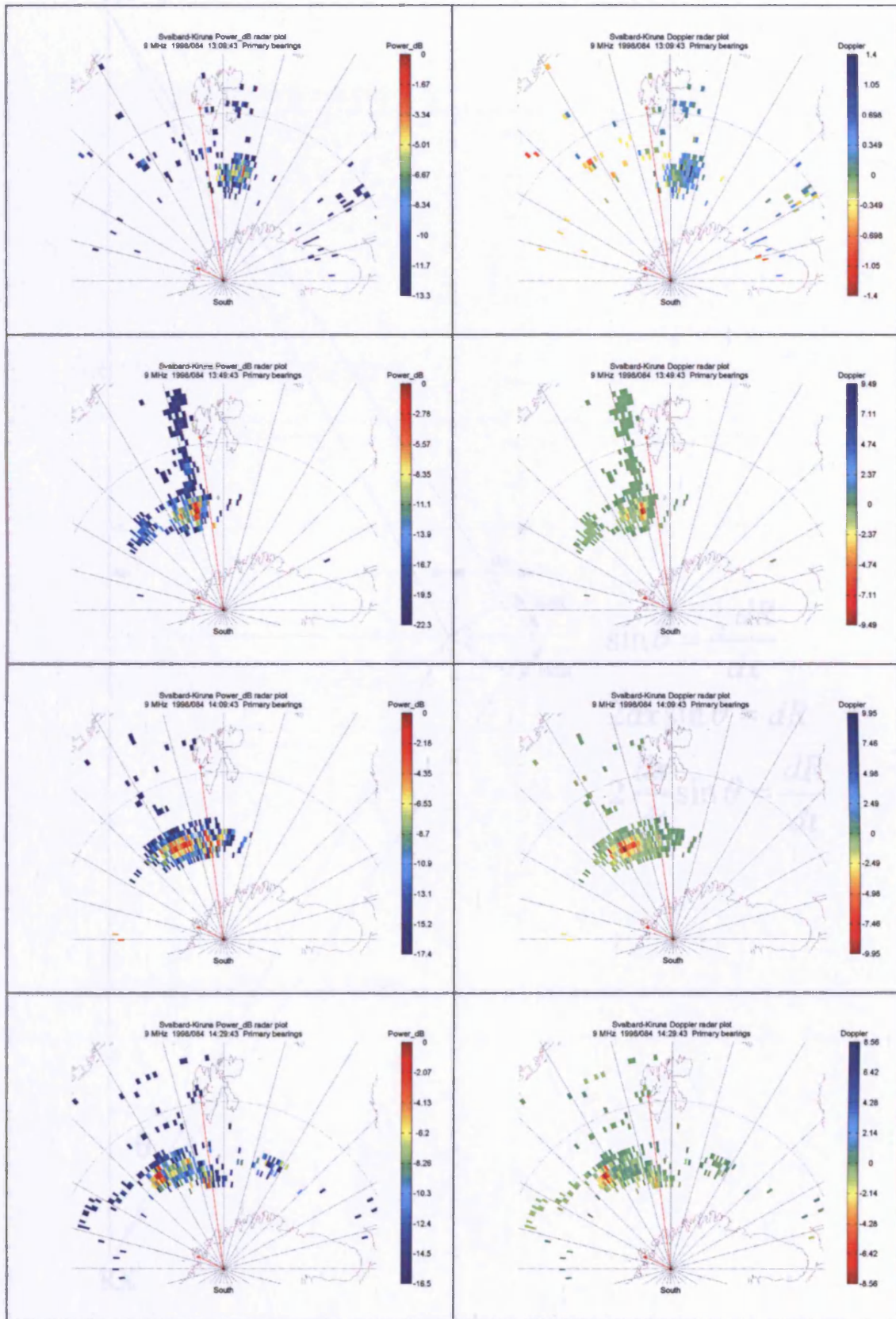


Figure 5.14 Temporal development of convecting scattering regions.

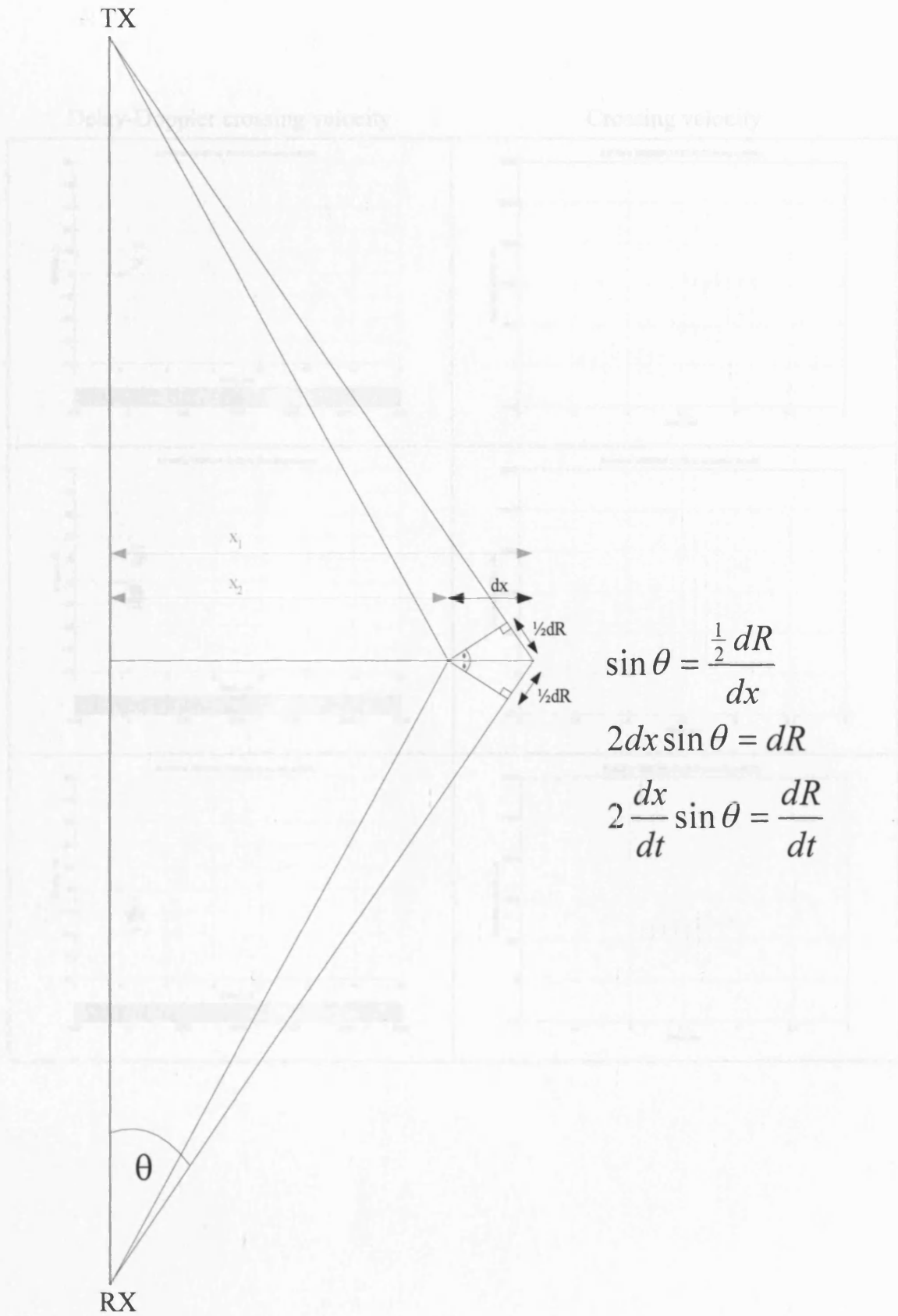


Figure 5.15 Path length change geometry for the calculation of crossing velocity

### Delay-Doppler crossing velocity

### Crossing velocity

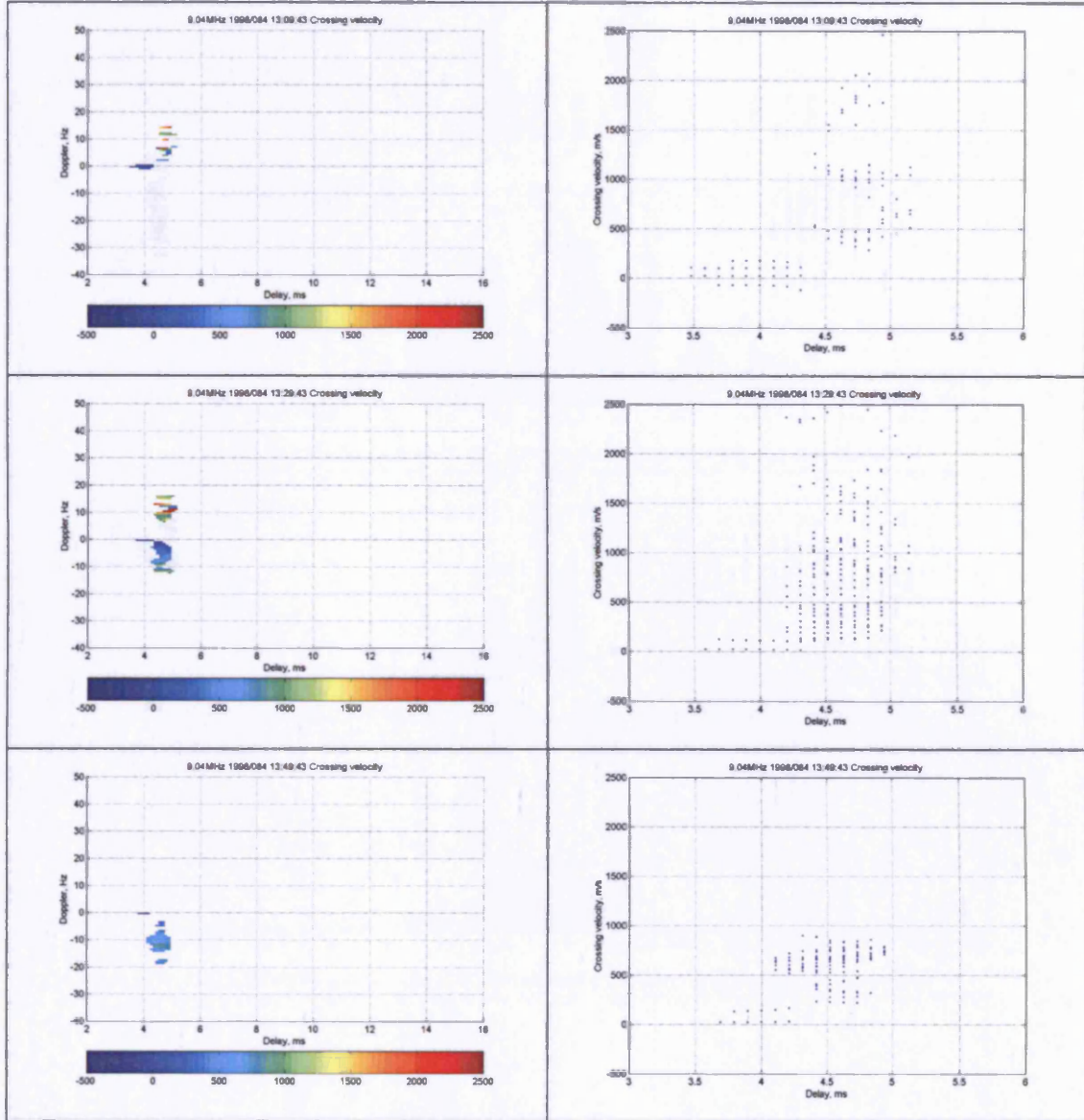


Figure 5.16

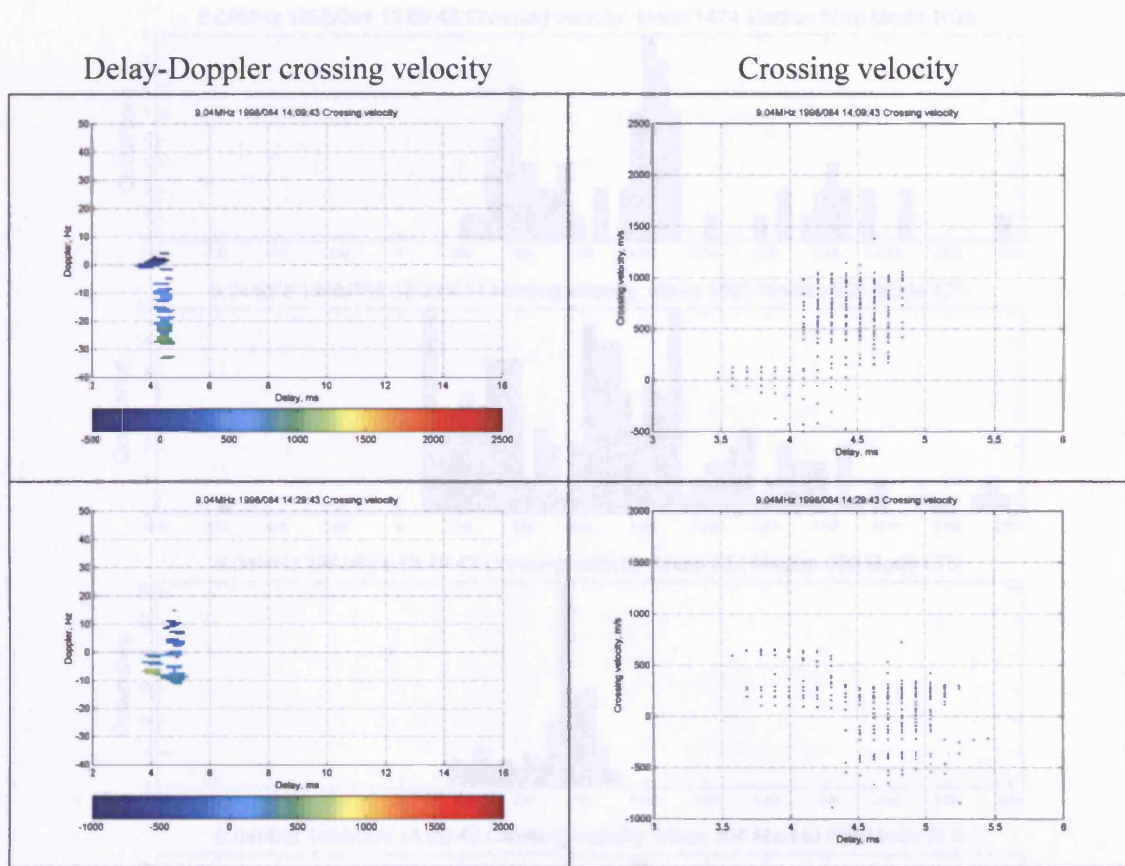


Figure 5.17

Figure 5.18 Doppler spread F-region crossing velocity histograms for each case.

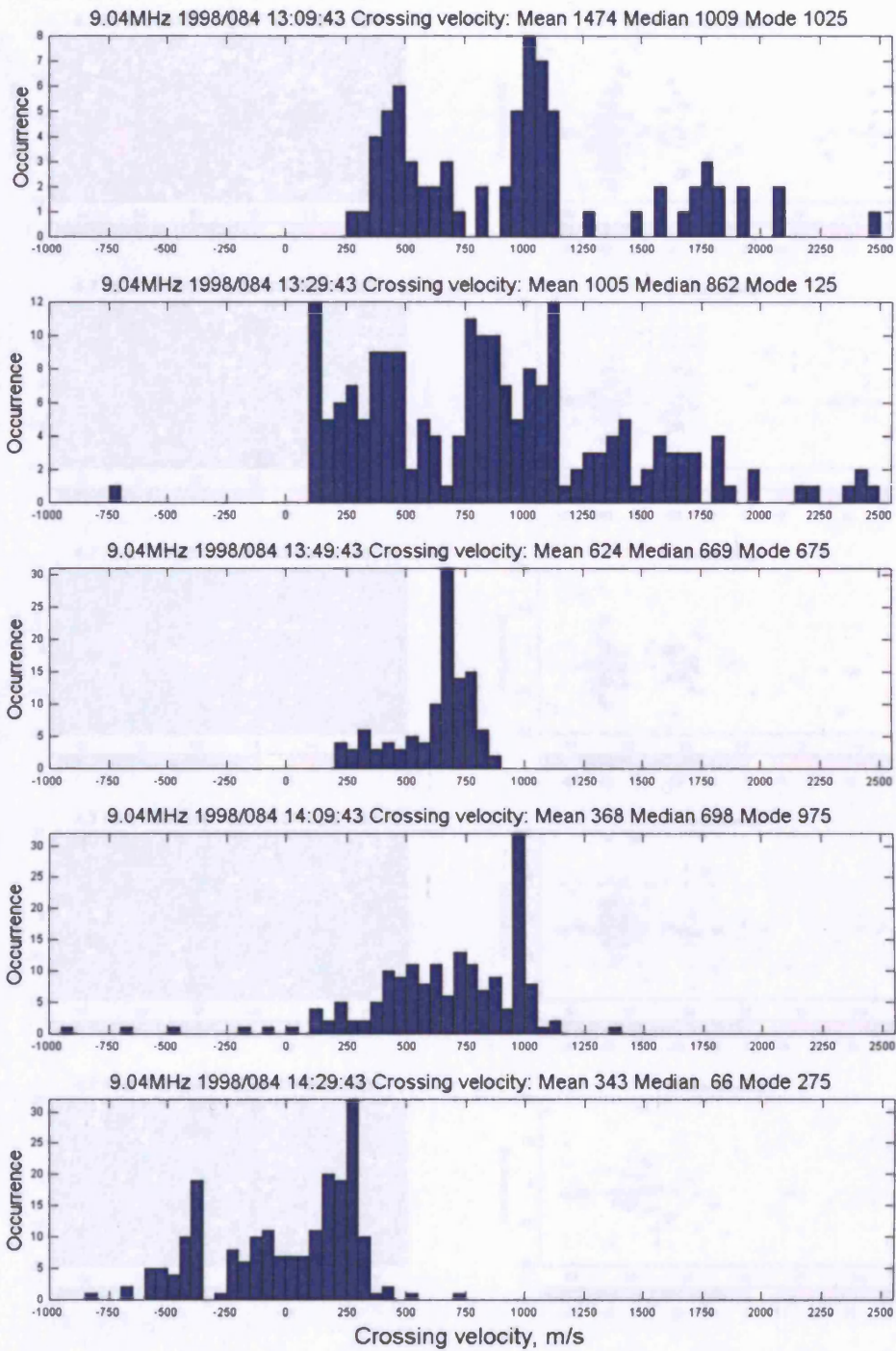


Figure 5.18 Doppler spread F-region crossing velocity histograms for each case.

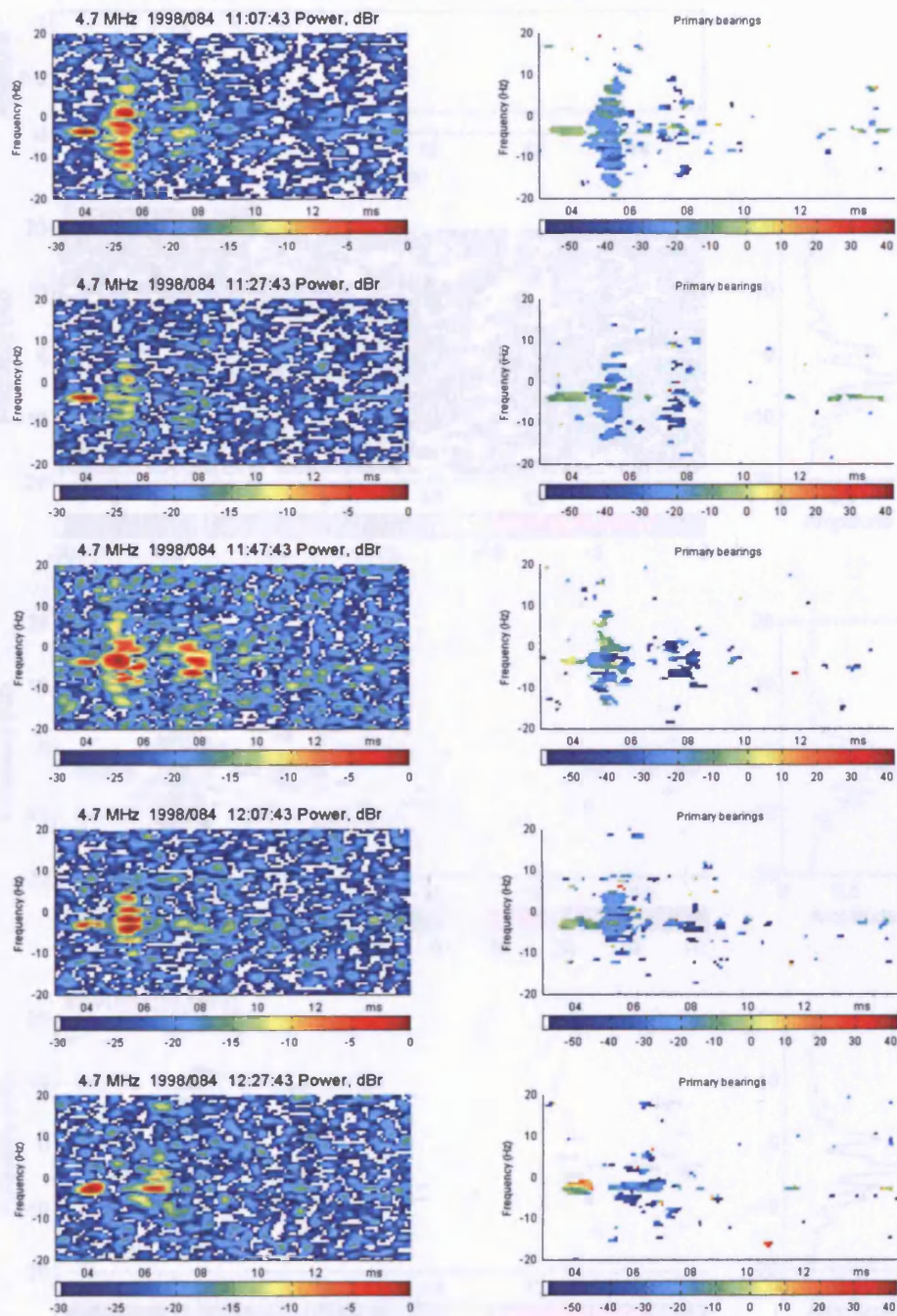


Figure 5.19 A sequence of soundings, containing an E-region mode, at 4.7MHz over the Svalbard – Kiruna path between 11:00UT and 12:30UT on 25<sup>th</sup> March (note the reduced Doppler scale)

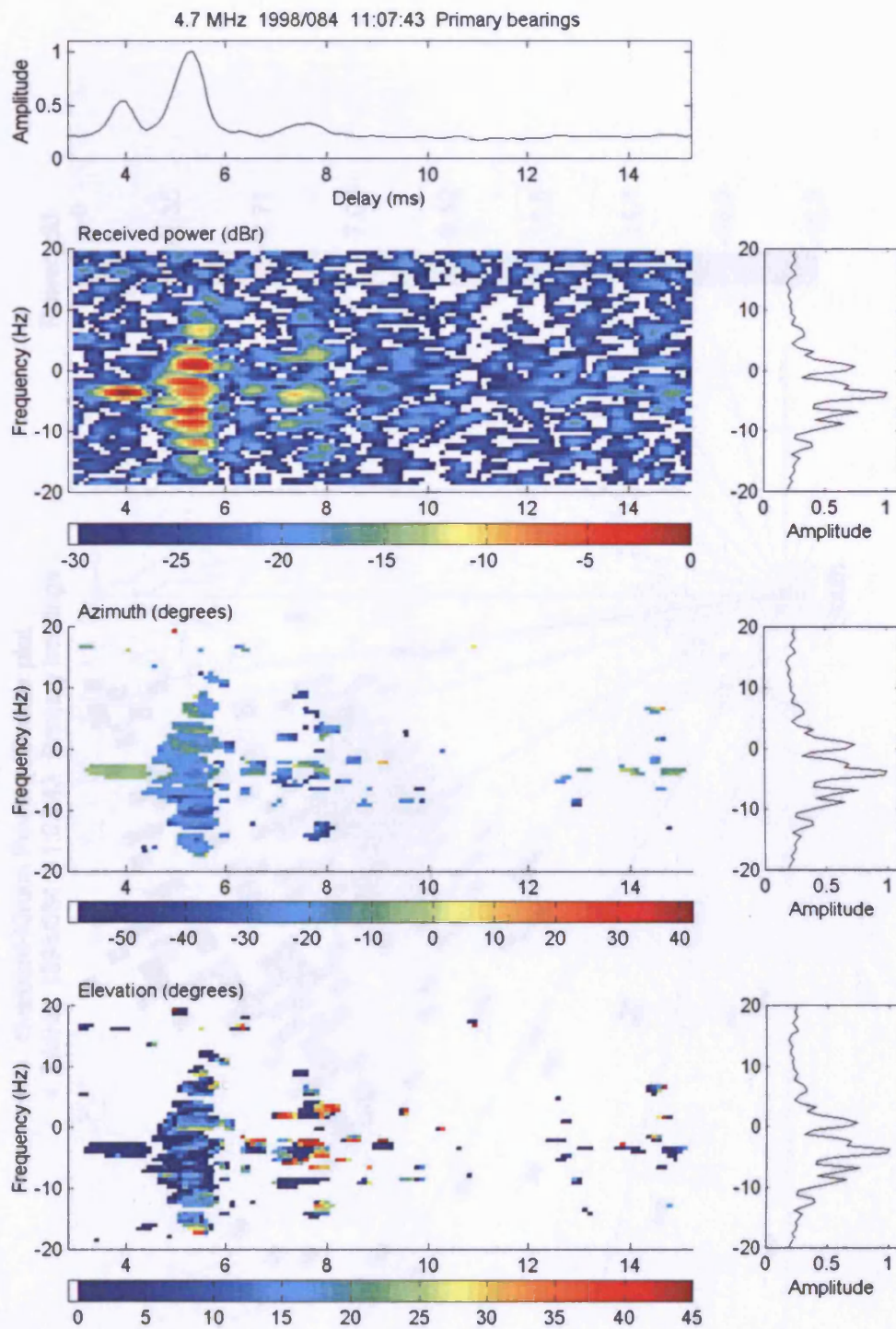


Figure 5.20 4.7MHz sounding, over the Svalbard – Kiruna path at 11:07UT on 25<sup>th</sup> March, showing an E-region GCP mode and a spread mode in more detail

Figure 5.21 4.7MHz sounding, showing Doppler spread in large -1100, over both paths

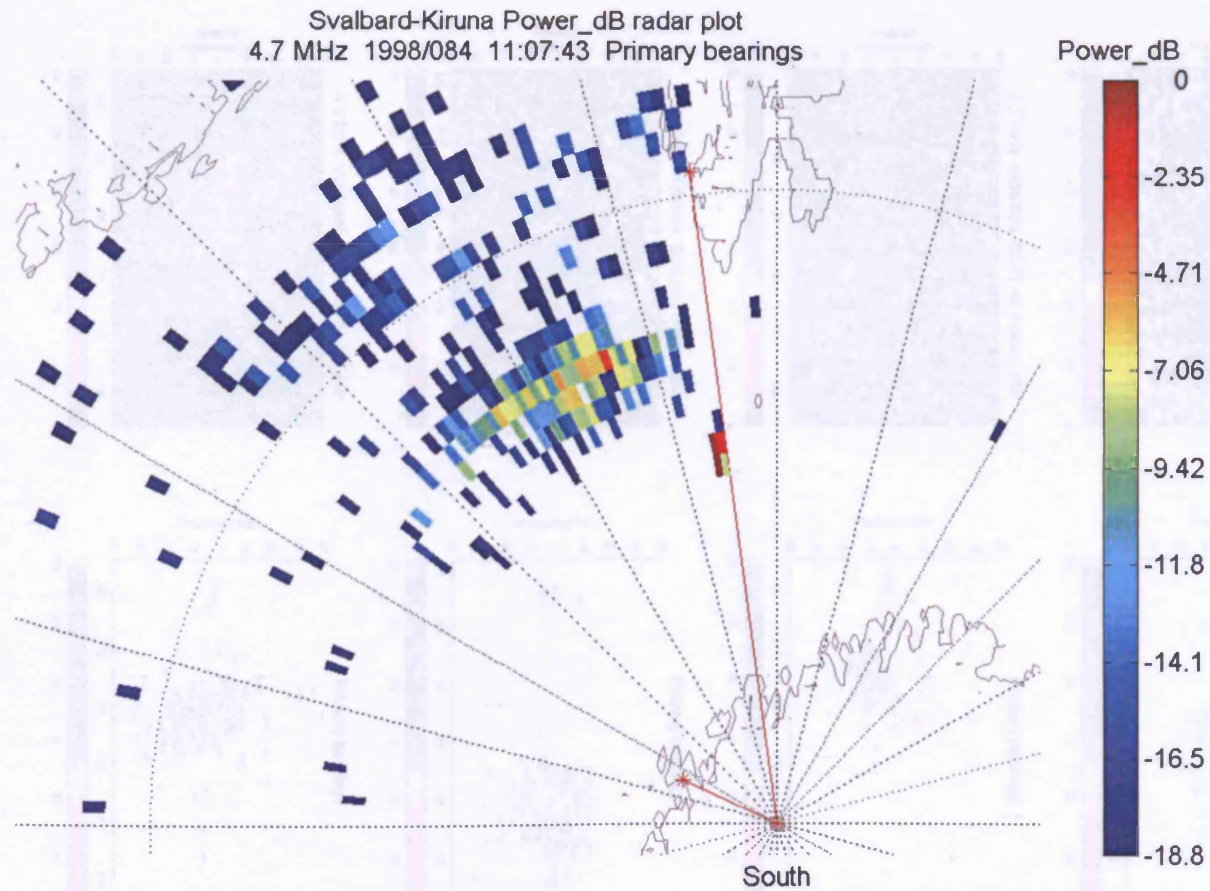


Figure 5.21 Radar power plot of the 4.7MHz sounding over the Svalbard – Kiruna path at 11:07UT on 25<sup>th</sup> March.

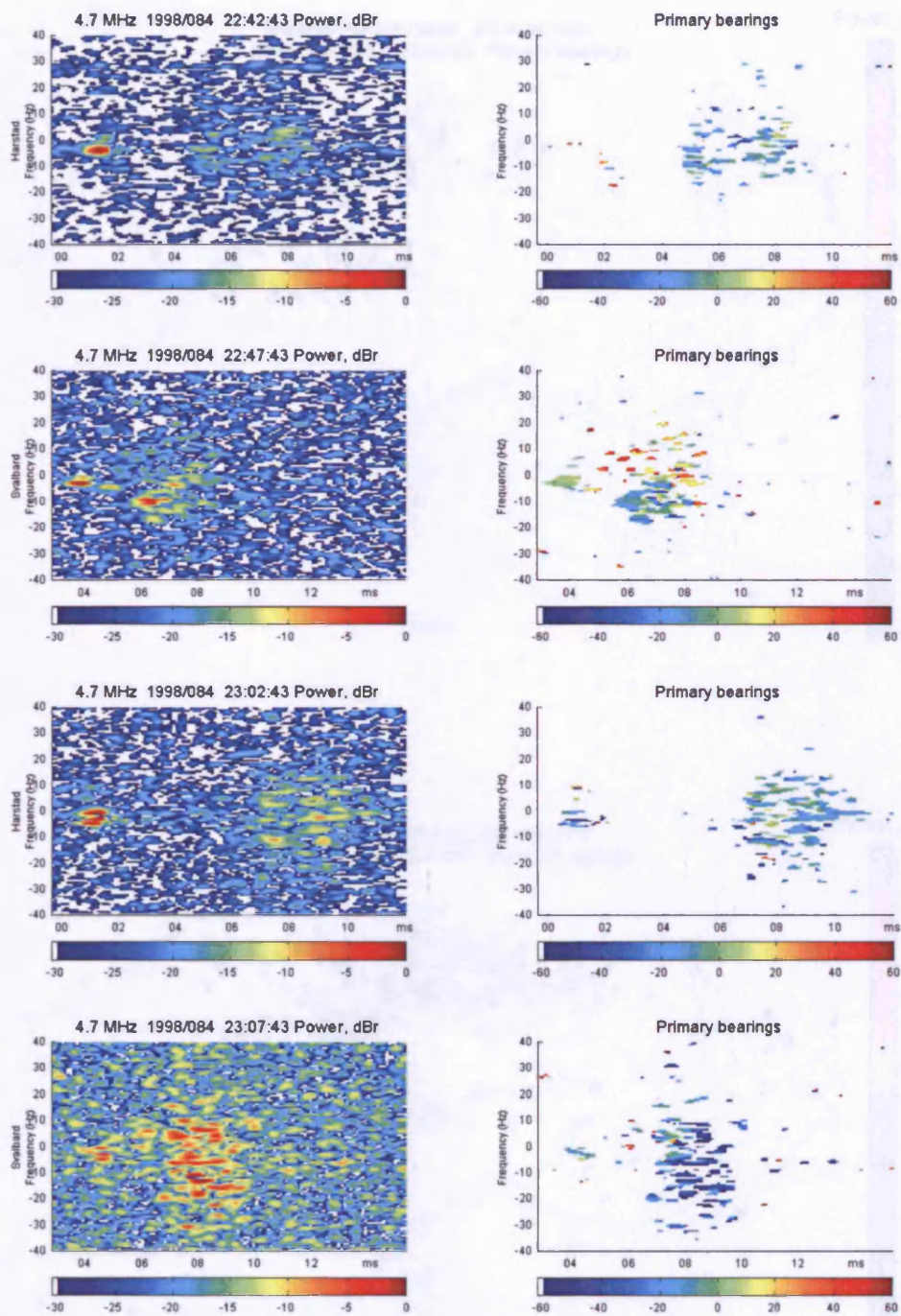


Figure 5.22 4.7MHz soundings, showing Doppler spread at large delays, over both paths taken around 23:00UT on 25<sup>th</sup> March

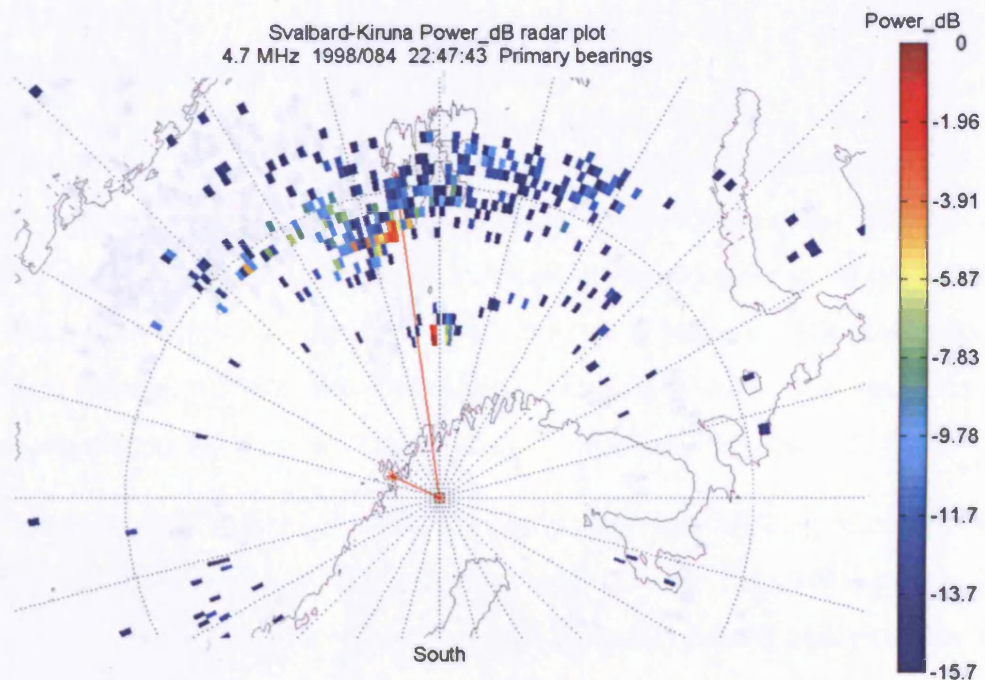
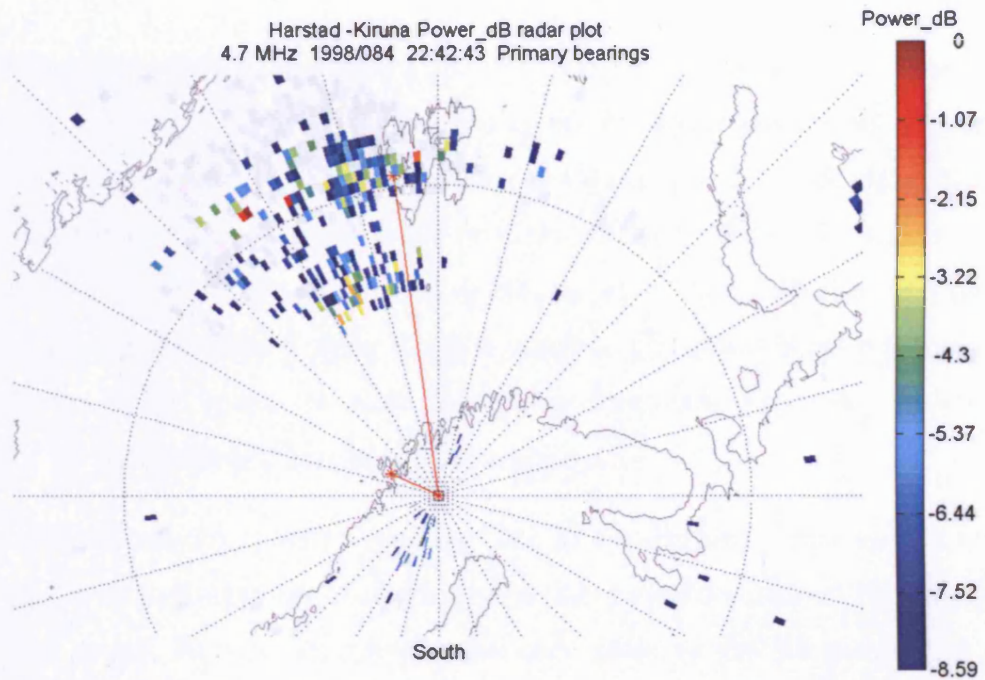


Figure 5.23 Radar plots of 4.7MHz soundings over both paths with considerable Doppler spread at large delays. The reflection points are geographically close

## 6; Spatial Filtering

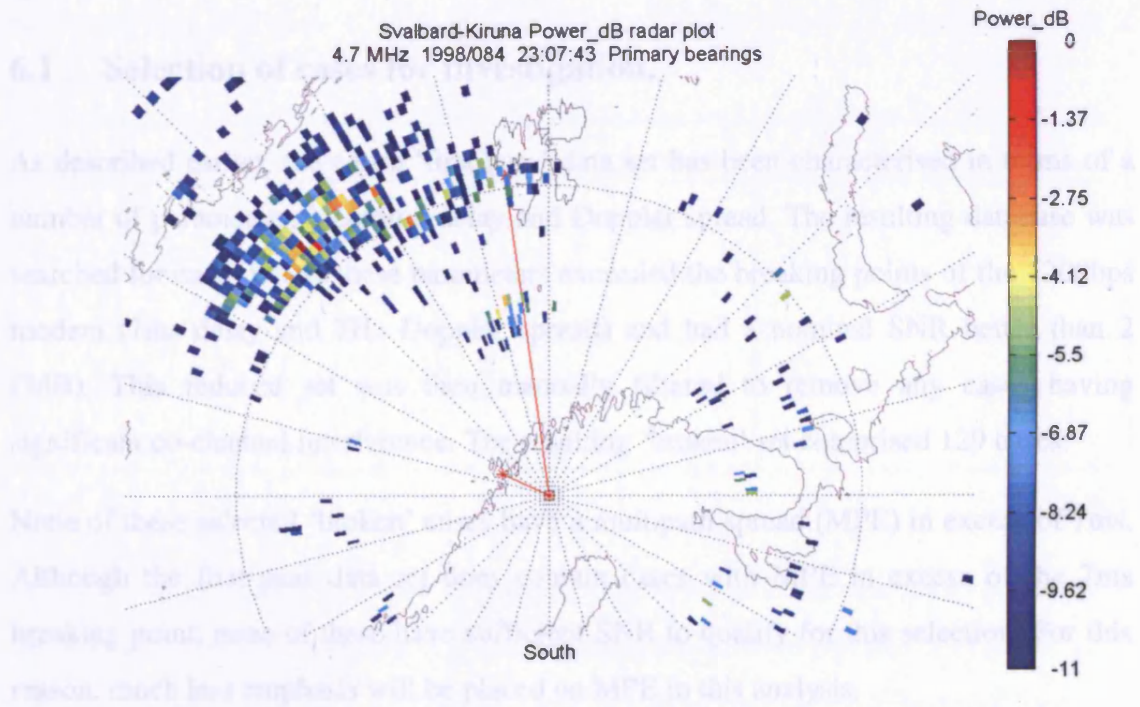
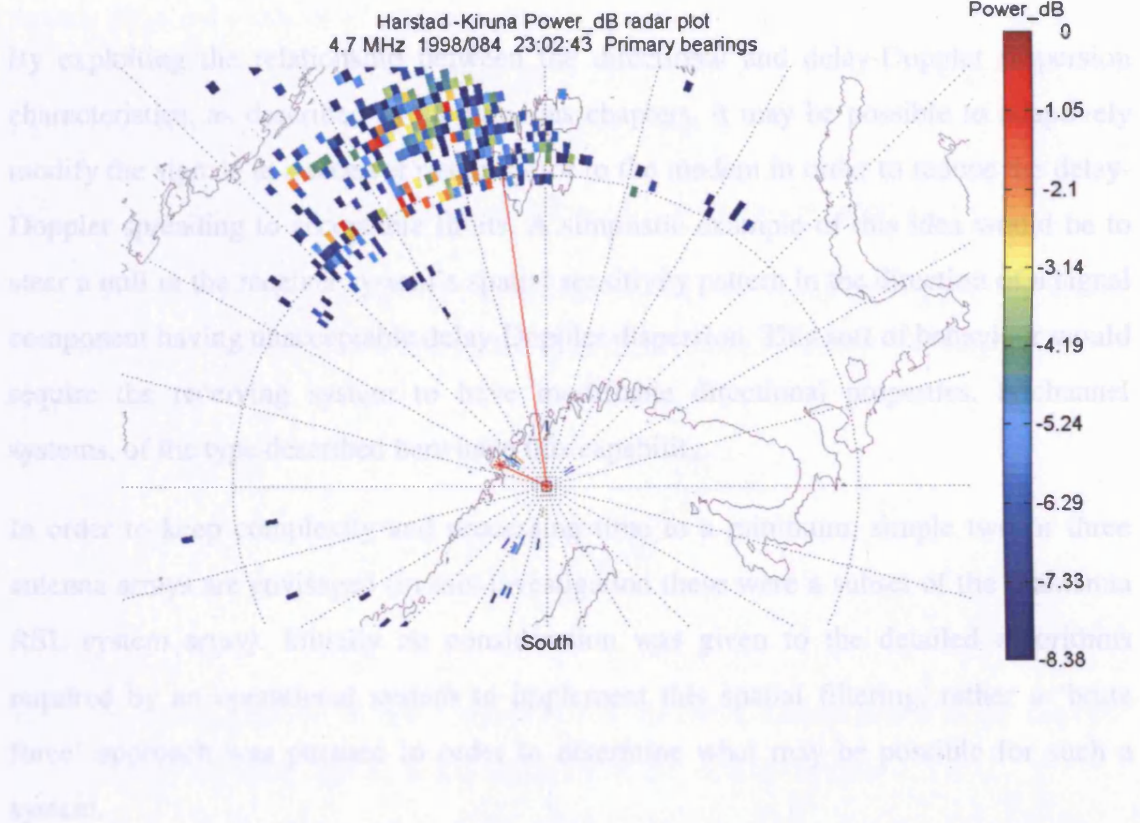


Figure 5.24 Radar plots of 4.7MHz soundings over both paths with considerable Doppler spread at large delays. The reflection points are geographically close

## **6. Spatial Filtering**

By exploiting the relationship between the directional and delay-Doppler dispersion characteristics, as described in the previous chapters, it may be possible to adaptively modify the signals in a receiver system prior to the modem in order to reduce the delay-Doppler spreading to acceptable limits. A simplistic example of this idea would be to steer a null in the receiver system's spatial sensitivity pattern in the direction of a signal component having unacceptable delay-Doppler dispersion. This sort of behaviour would require the receiving system to have modifiable directional properties. N-channel systems, of the type described here have this capability.

In order to keep complexity and processing time to a minimum, simple two or three antenna arrays are envisaged (in this investigation these were a subset of the 6 antenna RSL system array). Initially no consideration was given to the detailed algorithms required by an operational system to implement this spatial filtering, rather a 'brute force' approach was pursued in order to determine what may be possible for such a system.

### **6.1 Selection of cases for investigation.**

As described earlier, the entire 'first pass' data set has been characterised in terms of a number of parameters, including delay and Doppler spread. The resulting database was searched for cases where these parameters exceeded the breaking points of the 1200bps modem (7ms delay and 7Hz Doppler spread) and had a nominal SNR better than 2 (3dB). This reduced set was then manually filtered to remove any cases having significant co-channel interference. The resulting 'broken' set comprised 129 cases.

None of these selected 'broken' cases have a multipath spread (MPE) in excess of 7ms. Although the first pass data set does contain cases with MPE in excess of the 7ms breaking point, none of these have sufficient SNR to qualify for this selection. For this reason, much less emphasis will be placed on MPE in this analysis.

## 6.2 Signal processing for spatial filtering.

Several different methods of effecting spatial filtering were tried. All of them used 2 or 3 antenna subsets of the RSL 6 antenna array and combined the received signals in such a way as to attempt to reduce the resulting Doppler spread.

### 6.2.1 Two element arrays (constant amplitude, variable phase summation)

The simplest beam/null forming method combines the complex signals from two antennas, after subjecting one to a phase shift relative to the other. This may simply be expressed as:

$$S = S_A + S_B \cdot e^{\frac{j \cdot 2 \cdot \pi \cdot \psi}{360}}$$

Equation 6.1

Where  $S_A$  and  $S_B$  are the complex signals from the two antennas and  $\psi$  is the required phase shift, in degrees, applied to the signal from the second antenna.

With reference to Figure 3.3, the RSL 6 antenna system allows 15 combinations of 2 antennas as follows:

Pair Number	Antennas	Pair Number	Antennas	Pair Number	Antennas
1	1,2	6	2,3	11	3,5
2	1,3	7	2,4	12	3,6
3	1,4	8	2,5	13	4,5
4	1,5	9	2,6	14	4,6
5	1,6	10	3,4	15	5,6

Table 6.1

For each 'broken' case, the recorded signals from each antenna pair were combined in the way described by Equation 6.1. The resulting signal combinations, for values of  $\psi$  varied between  $1^\circ \rightarrow 360^\circ$  in  $1^\circ$  steps, were DD processed (as described in Chapter 3) and estimates of the new delay and Doppler spread with the associated SNR were calculated. The value of  $\psi$  that resulted in the smallest Doppler spread was recorded, along with the resulting values of delay spread, Doppler spread and SNR. In the case of

more than one value of  $\psi$  giving the same Doppler spread, the  $\psi$  giving the best SNR for this Doppler spread was selected. The process was repeated for each antenna pair.

### 6.2.2 Two element arrays (variable amplitude, variable phase summation)

The situation where the signals are summed after both an amplitude and phase shift is considered here. This may be simply expressed as:

$$S = S_A + A.S_B.e^{\frac{j.2.\pi.\psi}{360}}$$

Equation 6.2

Where  $S_A$  and  $S_B$  are the complex signals from the two antennas,  $A$  is the amplitude weighting factor and  $\psi$  is the required phase shift.

This method is a superset of that described in 6.2.1 above (where  $A$  was constrained to be 1). However, although relaxing the constraint on  $A$  may provide even better Doppler spread reductions, the magnitude of the computing task increases dramatically. In order to reduce the amount of computer time necessary for this analysis, only Pair 9 was considered (preliminary analysis of results indicated that Pair 9 performed well in comparison to the other combinations).  $A$  was allowed to take values between 0.5  $\rightarrow$  2.0 (excluding 1.0) in increments of 0.1.

### 6.2.3 Three element array (constant amplitude, varying phases)

A subset of three antennas from the six antenna array was chosen. The signals from these antennas were combined as follows:

$$S = S_A + S_B.e^{\frac{j.2.\pi.\psi_1}{360}} + S_C.e^{\frac{j.2.\pi.\psi_2}{360}}$$

Equation 6.3

Where  $S_A$ ,  $S_B$  and  $S_C$  are the complex signals from the three antennas with  $\psi_1$  and  $\psi_2$  being the two required phase shifts.

The selected antennas were 1,3 and 6 since these provided a large aperture and were evenly spaced in a triangular formation, giving this sub-array an aperture in all directions along the ground.

The introduction of another variable to the problem increases the computational load, however, it is not possible to limit the range of the new variable as in 6.2.2 above since it is necessary to maintain the whole range of  $\psi_2$  ( $1^\circ \rightarrow 360^\circ$ ). Each example took in excess of one week of computer time, thus only 3 cases were examined.

### **6.3 Analysis - Two element arrays**

The 129 selected cases were processed using the methods described in 6.2.1 and 6.2.2 above and analysed for improvements in Doppler spread. It was thought that the variable amplitude and phase approach might effect even better Doppler spread improvements than the phase only method. However, preliminary results indicated no significant benefit was gained by using variable amplitudes and because of the increased computer time necessary for the processing the method was not pursued further. The analysis in this section therefore deals only with the results of the two antenna constant amplitude, variable phase, spatial filtering method

#### *6.3.1 Case studies and examples*

A selection of example cases for both paths are included in Figures 6.1  $\rightarrow$  6.14. These illustrate the directional characteristics of the Doppler spread signals and the outcomes of the spatial filtering process. Also presented in these examples is the behaviour of the resulting Doppler spread and SNR as the phase angle,  $\psi$ , is changed along with antenna pair sensitivity plots for the best antenna pair / phase angle combination.

The first example, in Figure 6.1, appears to be single moded with a broad Doppler spread. The extremes of the Doppler spread energy do appear to be slightly delayed in time, leading to a somewhat extended delay spread. There is a trend in the direction of arrival as the Doppler offset moves from negative to positive. The energy around 0Hz offset towards the front of the pulse arrives from approximately the GCP direction. This example appears to be a part of the set discussed in Section 5.2.3 where there is often a narrow Doppler spread E-region GCP mode, in this case the GCP mode is embedded into the Doppler spread mode. The overall DOA spread covers several tens of degrees of

azimuth. Figure 6.2 represents the case after the application of spatial filtering. The top panels show the digital pulse compressed amplitude, the Doppler spectra and the delay-Doppler surface in the same way as a standard DD plot. The middle panel represents the variation of the resulting Doppler spread for the best antenna pair with applied phase angle and the bottom panel shows the variation of SNR with phase angle. The colour plot to the right of these two panels is the two antenna sensitivity pattern for the best phase.

In this instance antennas 2 and 3 were found to reduce the Doppler spread from 16.4Hz to give the least Doppler spread, of 8.2Hz, when a phase angle of  $227^\circ$  is used. This results in a SNR of 50.2. The variation of Doppler spread with  $\psi$  is quite smooth, with a well defined minimum. The SNR variation with  $\psi$  is quite different, although the best  $\psi$  results in a good SNR, nearby values of  $\psi$ , which still give good Doppler spread, result in significantly lower SNR. The DD panel reveals that signal energy at negative Doppler offsets, with DOA between  $\sim 20^\circ \rightarrow \sim 40^\circ$ , appear to have been mostly eliminated. Energy at the positive Doppler offsets is slightly reduced, leaving the energy around 0Hz offset and  $\sim 350^\circ$  azimuth relatively untouched. The two antenna sensitivity pattern has significant nulls in azimuth present at elevations below  $\sim 60^\circ$ . One of these is clearly steered to around  $35^\circ$  and is wide enough to significantly reduce signal energy arriving from anywhere between approximately  $10^\circ$  to  $60^\circ$ . The sensitivity lobe centred on  $330^\circ$  is large enough to maintain the signal energy at low Doppler offsets.

The second example, with an original Doppler spread of 18.9Hz is shown in Figure 6.3. The modal structure of the signal is evident with the first mode an un-spread E-region mode arriving along the GCP direction at  $\sim 354^\circ$  and having a delay of just under 4ms. The second mode, arriving at 5.2ms delay and azimuth  $\sim 337^\circ$ , has broad Doppler spread while a third, high elevation, mode arriving from a similar direction at  $\sim 7.5$  ms, carries much less signal energy.

In this example, Figure 6.4 reveals that antennas 4 and 6 give the best Doppler spread of 6.3Hz when a phase angle of  $95^\circ$  is applied. Although, as expected, the variation of Doppler spread with  $\psi$  is not the same as the previous example, it is smooth and there is only one minimum. Compared to the previous case the SNR curve is smoother and is not at a minimum for the  $\psi$  with the best Doppler spread. In azimuth the two antenna

sensitivity pattern indicates a null at  $\sim 330^\circ$ , which has significantly reduced the energy in the second and third Doppler spread modes, the edges of the null are steep and give enough gain at around  $352^\circ$  to maintain the un-spread E-region mode. The resulting Doppler spectrum is much narrower and there has been a marked enhancement of the un-spread E-region mode relative to the second mode in the delay profile.

Figure 6.5 illustrates the third example. In this case the delay profile indicates a single, slightly broadened mode, however, the Doppler profile indicates two Doppler spread regions offset from each other by  $\sim 20\text{Hz}$ , resulting in an overall Doppler spread of  $27.7\text{Hz}$ . The azimuthal direction of arrival of these two regions is separated by in excess of  $20^\circ$ . The results after spatial filtering are presented in Figure 6.6. It is clear that the second Doppler spread region, with an offset of around  $10\text{Hz}$ , has been almost totally eliminated while the first region remains. Consequently the overall Doppler spread has been dramatically reduced to  $10.1\text{Hz}$ .

The variation of Doppler spread with  $\psi$  has two local minima, the lowest value of  $10.1\text{Hz}$  occurs with a phase angle of  $340^\circ$  between antennas 4 and 5. The other local minimum occurs around  $226^\circ$  of phase. When this value is used in place of  $340^\circ$  to calculate the DD surface, it results in the first Doppler spread region, with an offset approx.  $-10\text{Hz}$ , being eliminated, leaving the second Doppler spread region and a consequent Doppler spread value of  $17.0\text{Hz}$ .

Examination of the two antenna sensitivity patterns, for  $340^\circ$  of phase, reveals a null at around  $20^\circ$  in the direction of the upper Doppler spread region and sensitivity in the direction of the lower region. When  $226^\circ$  of phase is applied to this pair the situation is reversed with a null in the direction of the lower region and sensitivity in the direction of the upper.

Figure 6.7 is the first of the examples from the Harstad – Kiruna path. This has a complex structure with a large delay and Doppler spread region, there is no obvious modal structure and the signal energy tails off at the extremes of delay and Doppler. The region is composed of signal energy arriving from nearly all directions of arrival. Spatial filtering does reduce the Doppler spread from  $18.9\text{Hz}$  to  $15.7\text{Hz}$  by appearing to remove energy from between approximately  $300^\circ \rightarrow 360^\circ$  at the lower edge of the region. The

variation of Doppler spread with  $\psi$  is again smooth and not surprisingly has a wide shallow minimum.

The second example from the Harstad – Kiruna path is illustrated in Figure 6.9. There is a distinct modal structure, with a narrow 1-hop E-region mode evident, followed by a broad mode around 3ms delay, there is also a small amount of signal energy arriving at about 7.5ms. The direction of arrival of the second mode is spread between  $300^\circ \rightarrow 360^\circ$ . The spatial filtering significantly reduces the energy in the second mode, resulting in enhancement of the E-region mode in comparison. The overall Doppler spread reduces from 24.6Hz to 1.3Hz

Figure 6.11 is the third example from the Harstad – Kiruna path. Two Doppler spread modes are apparent, separated in delay by about 1ms. The DF information reveals that the first mode is composed of a relatively narrow mode at 0Hz offset and azimuth  $\sim 250^\circ$  along with broad Doppler spread energy arriving from around  $340^\circ$ . The second mode is predominantly from around  $0^\circ$ . There is also marked elevation differences between the modes, with the first mode arriving at a much higher elevation than the second. The spatial filtering reduces the Doppler spread from 25.2Hz to 6.9Hz. The resulting DD surface reveals that the energy in the second mode has been much reduced while the Doppler spread energy in the first mode has also been reduced. This is consistent with the two antenna sensitivity pattern in azimuth, which shows a broad null covering most of the interval between  $-30^\circ \rightarrow +60^\circ$  and a lobe with significant gain along  $\sim 250^\circ$ .

The final example over the Harstad – Kiruna path is illustrated in Figure 6.13. There are two modes, the first, an un-spread E-region mode and the second a very broadly spread mode around  $\sim 2$ ms delay. The first mode has an azimuth  $\sim 300^\circ$  while the second mode's azimuth ranges between  $\sim 150^\circ \rightarrow \sim 220^\circ$ . The results of the spatial filtering, illustrated in Figure 6.14, show that the second mode has been virtually eliminated, with the corresponding relative enhancement of the E-region mode in comparison. The Doppler spread has been reduced by a factor of  $>10$  from 46.0Hz down to 4.4Hz.

### 6.3.2 *Statistical treatment*

Figure 6.15 indicates potential Doppler spread improvement using spatial filtering with two antennas, constant amplitude and variable phase. The black line represents the

Doppler spread of each 'broken' case before spatial filtering while the yellow bars represent the best Doppler spread achieved after spatial filtering, regardless of antenna pair, sorted into the same order as the black line. The two red lines at 7Hz and 25Hz indicate the approximate 'breaking points' of the 110A modems. The difference between the black line and the yellow bars is the Doppler spread improvement. Although in some cases the improvement is small, there are a number of very large improvements, clearly the Doppler spread improvements vary on a case by case basis. In some of the broken cases with the largest original spreads, the improvements due to the spatial filtering results in them passing the 7Hz spread criteria. It is clear that for each case examined there are potential improvements in Doppler spread possible through spatial filtering. At the low Doppler spread end of the scale, the spatial filtering has improved many cases from failing the spread criteria and 'breaking' to passing.

These results are also presented in Figure 6.16 in the form of a cumulative probability distribution. For the points plotted on each line of such a graph, the y-values represent the Doppler spread measurements, while the x-values represent the percentage of points with a Doppler spread less than the current y-value (remembering that all of these cases were originally selected to exceed 7Hz spread). As an example, in the case of the black line, representing the Doppler spreads before spatial filtering, the intersection with the upper red line indicates that nearly 75% of cases do not exceed 25Hz spread and 25% do. The blue dots represent the best Doppler spreads obtained with the 15 different antenna pairs and the blue line is the mean of these values. Finally the purple line represents the spreads achievable by selecting the best antenna pair on a case by case basis and sorting into order of spread.

It is clear that this form of spatial filtering can lead to significant reductions in Doppler spread. Indeed examination of the shape of the curves in Figure 6.16 implies that although there will be improvements in the case of the 110A modems, these points fall on relatively steep parts of the cumulative probability curves. Even better improvements may be possible for a hypothetical modem, operating at an intermediate data rate, with a breaking point around 15Hz, where the cumulative probability curve is relatively flat and a small change in Doppler spread leads to a large change in cumulative probability.

Table 6.2 summarises the improvements around the breaking points.

	<7Hz, % (1200bps)	<15Hz, % (Hypothetical)	<25Hz, % (300bps)
Before spatial filtering	0	27.9	73.6
Mean Dspread after spatial filtering	6.2	57.4	89.9
Best Dspread on a case by case basis	19.4	73.6	95.4

Table 6.2

In terms of the 110A modem performance, when the best result is chosen on a case by case basis, the difference between the percentage passing the spread criteria after spatial filtering compared to before (i.e. the % being ‘fixed’) is around 20% for both the 300bps and 1200bps modems. For a hypothetical modem with a breaking point around 15Hz the figure is 45%.

An operational system is unlikely to have the ‘luxury’ of selecting the best performing pair from an array, however, on average, these results do indicate that in ~6% of cases an improvement in the mean Doppler spread after spatial filtering may ‘fix’ a 1200bps modem. While in ~30% of cases spatial filtering may ‘fix’ the hypothetical modem.

Since the propagation characteristics of the signals are both path and frequency dependent, Figure 6.17 and Table 6.3 detail subsets of these overall results separated by path and frequency.

For completeness, histograms of the number of times a given antenna pair results in the best Doppler spread after spatial filtering are shown in Figure 6.18. There is no obvious trend, although, pair 9 does occur most often on both paths.

Transmitter	Frequency MHz		No. Cases	<7Hz %	<15Hz %	<25Hz %
Svalbard	All	Before spatial filtering	<b>87</b>	0	31.0	79.3
		Mean after spatial filtering		6.9	64.4	92.0
		Best (case by case basis)		20.7	79.3	95.4
	3.95	Before spatial filtering	1	0	0	100
		Mean after spatial filtering		0	100	100
		Best (case by case basis)		0	100	100
	4.70	Before spatial filtering	16	0	56.3	87.5
		Mean after spatial filtering		12.5	87.5	100
		Best (case by case basis)		37.5	93.8	100
	6.78	Before spatial filtering	28	0	35.7	78.6
		Mean after spatial filtering		7.1	67.9	89.3
		Best (case by case basis)		17.9	78.6	92.9
	9.04	Before spatial filtering	24	0	25	87.5
		Mean after spatial filtering		4.2	62.5	95.8
		Best (case by case basis)		25	79.2	100
	11.18	Before spatial filtering	6	0	0	33.3
		Mean after spatial filtering		0	50	83.3
		Best (case by case basis)		16.7	83.3	100
	14.36	Before spatial filtering	1	0	0	100
		Mean after spatial filtering		0	100	100
		Best (case by case basis)		0	100	100
	17.45	Before spatial filtering	5	0	40	100
		Mean after spatial filtering		0	60	100
		Best (case by case basis)		0	80	100
	19.95	Before spatial filtering	2	0	0	100
		Mean after spatial filtering		0	50	100
		Best (case by case basis)		0	50	100
21.88	Before spatial filtering	4	0	0	25	
	Mean after spatial filtering		0	25	50	
	Best (case by case basis)		0	25	50	
Harstad	All	Before spatial filtering	<b>42</b>	0	21.4	61.9
		Mean after spatial filtering		4.8	40.5	85.7
		Best (case by case basis)		16.7	61.9	95.2
	3.95	Before spatial filtering	1	0	0	100
		Mean after spatial filtering		0	100	100
		Best (case by case basis)		0	100	100
	4.70	Before spatial filtering	17	0	41.2	82.4
		Mean after spatial filtering		11.8	47.1	94.1
		Best (case by case basis)		23.5	64.7	100
	6.78	Before spatial filtering	17	0	11.8	58.8
		Mean after spatial filtering		5.9	41.2	94.1
		Best (case by case basis)		17.6	64.7	100
	9.04	Before spatial filtering	6	0	0	16.7
		Mean after spatial filtering		0	16.7	50
		Best (case by case basis)		0	50	83.3
11.18	Before spatial filtering	1	0	0	0	
	Mean after spatial filtering		0	0	0	
	Best (case by case basis)		0	0	0	

Table 6.3

### 6.3.3 SNR considerations.

The concept of spatial filtering is to eliminate unwanted signal components, by signal combination, before being processed in a modem. As described, this process has been constrained to give a reduction in signal Doppler spread, since this usually involves removing signal energy, the signal SNR may also decrease.

The subsequent treatment will use as a reference the original SNR of the received signals before spatial filtering is applied.

Figure 6.19 plots the resulting SNR values of each case, after spatial filtering to reduce Doppler spread, in dB relative to the SNR of each case before spatial filtering. In 52% of cases there is actually an improvement in SNR after spatial filtering. The red lines represent the  $\pm 6$ dB levels, 97% of the cases remain above the  $-6$ dB level but only 3% exceed the  $+6$ dB level. It is interesting to note that in most cases the SNR changes are approximately evenly spread around 0dB. However, towards the right hand end of the graph, where the original SNR values were higher to start with, there is a definite trend towards negative SNR changes. Because the SNR values were large to start with the resulting SNR is still not very low. The worst case appears to experience a reduction of  $\sim 8$ dB relative to the original SNR, since the original was  $\sim 18$ dB this reduces the SNR to  $\sim 10$ dB.

## 6.4 Analysis - Three element arrays

The results of the analysis, as described in 6.2.3, are presented in Table 6.4 below. Since only three cases were examined, due to the size of the computational load each one presented, it is not appropriate to draw firm conclusions. However it is not clear that there is any performance improvement over the two antenna methods. Since the three antenna method does present a massively increased computing load and initially appears to lack an appreciable performance improvement over the constant amplitude, two antenna approach, it will not be pursued further.

Date	Time	Freq MHz	Path	Doppler Spread, Hz					
				Original	3 antennas	Best pair	Pair 1,3	Pair 1,6	Pair 3,6
98075	124944	9	S	10.1	8.8	8.2 (3,5)	10.1	10.1	8.8
98083	222243	4.7	H	24.6	1.3	1.3 (1,6)	12.0	1.3	6.9
98087	130944	9	S	13.2	9.4	7.6 (2,5)	10.7	8.2	12.0

Table 6.4

It is interesting to note, however, that the Doppler spread reductions achieved when the three antennas were used was no better than when the constituent pairs were employed singly. In one case, a constituent pair out performed the triplet.

## 6.5 Analysis – Fast solver method

The Doppler spread (TDspr) vs. phase angle ( $\psi$ ) curves for the two antenna, constant amplitude, variable phase method (described in section 6.3.1) are in general smooth and well behaved. It may thus be possible to use fast minimum finding solver algorithms to select the phase angle resulting in the smallest value of Doppler spread.

In the analysis presented earlier, the TDspr parameter was calculated repeatedly at  $1^\circ$  intervals of  $\psi$  over the range  $1^\circ \rightarrow 360^\circ$  using a looping mechanism, the best  $\psi$  was chosen on the basis of selecting the result having the smallest TDspr. If more than one  $\psi$  gave the smallest TDspr, then the  $\psi$  resulting in the best SNR was used.

A similar approach was taken in this analysis, however, the looping mechanism was replaced by a standard 1D minimum finding solver function (fminbnd()) as supplied with MATLAB R11, this also outputs information about the algorithm used and solver performance). The problem presented was to find the  $\psi$  resulting in the smallest value of TDspr (SNR was not considered in this formulation). The ‘Golden section search’ solver algorithm was selected as the most appropriate for the problem. In common with many algorithms of this type, the  $\psi$  corresponding to the smallest value of TDspr is returned when the latest iteration of the solver returns a value within a small tolerance of the previous result. Since speed of calculation is important, the termination tolerance is a critical parameter. A number of different values were tried initially on a subset of

cases, resulting in the decision to use a value of  $0.1^\circ$  for the entire broken data set (129 cases). In all these cases the solver successfully converged on a solution.

Figure 6.20 represents the values of TDspr after spatial filtering using both the looping mechanism (blue line) and the fast solver method (green line). The resulting values of TDspr are in close agreement, particularly for the high original spreads, with 97/129 cases resulting in the same value of TDspr. In the analysis of the looping method results there are a number of cases having two distinct minima in the TDspr vs  $\psi$  curves. It is possible that some of the cases, where the solver calculated Doppler spread is larger than the looping method result, the solver has selected the wrong minima to optimise.

Figures 6.21 and 6.22 are cumulative probability curves for the results over both paths combined and separately. It appears that the solver method does result in slightly increased values of TDspr after spatial filtering compared to the looping method. This result will be affected by the selected termination tolerance, the smaller the tolerance the better the result should be.

When Figures 6.23 and 6.24 are considered, it is clear that the solver method does not always result in the same antenna pair or  $\psi$  angle selection. These results indicate that in 87/129 cases the same antenna pair was selected and in 1/129 cases the same  $\psi$  was selected. This is most probably due to the different minimising criteria being used. In the looping mechanism a phase angle resulting in the smallest TDspr having the best SNR was selected, in the solver method only TDspr was minimised. In order to improve the performance of the solver method, it may be appropriate to minimise a composite parameter combining both TDspr and SNR (TDspr/SNR perhaps) instead of the simple TDspr. At the same time it may also be possible to introduce a time spread parameter (Ttspr or MPE) to attempt delay spread reduction in the same way.

The performance and speed of the solver method is illustrated in Figure 6.25 with curves of number of iterations before convergence and CPU time required for each path separately. The mean convergence time was 17.3 seconds for an average of 15.9 iterations of the solver. These results depend strongly on the termination tolerance selected. When compared with the looping method this is at least an order of magnitude faster. This speed improvement also allows the opportunity of considering arrays of more than two antennas. If the case where a three-element array, with apertures in all

directions (as described in 6.4) is considered, it is still relatively quick to calculate the best performing pair (out of 1-2, 1-3 and 2-3) using the solver method.

Clearly this solver method has merit, particularly as all cases examined quickly converged to a successful solution which was smaller than the original Doppler spread before spatial filtering and in most cases close to the brute force spatial filtering results presented in 6.3.2. Remembering that the looping method operated at  $1^\circ$  steps in  $\psi$ , there is scope for even better Doppler spread values at non integer values of  $\psi$  using the solver method if performance parameters such as termination tolerance are optimised.

If these results are considered alongside work on the stability of the validity of  $\psi$  in time (Warrington *et al.* [2000(2) and 2001]) it may be possible to recalculate  $\psi$  at small enough time intervals to demonstrate the feasibility of an operational system using spatial filtering. Further improvements in calculation time may also be possible if the optimisation constraint is to reduce TDspr below a given boundary (7Hz for example) rather than to find a global minimum. As well as speeding up calculation time, this will minimise the reduction in SNR due to spatial filtering. A drawback of this method, however, will be that the selected phase angle will not be valid for a very long time compared to the global minimum phase and the system would need to probe the channel and update its estimate more frequently, thus reducing throughput compared to the optimum.

## 6.6 Concluding remarks

A selection of examples from the campaign data set have been chosen on the basis of exceeding the working boundaries of the modem performance surfaces presented in Figure 1.16 and Figure 1.17. Three different approaches to implementing spatial filtering on this data set, using a simple array were applied. Each method can lead to reductions in the important Doppler spread parameter, however, this may be at the cost of SNR.

Although the 129 cases examined is a limited data set, and geomagnetic conditions were relatively quiet during the campaign, a large variety of Doppler spread propagation conditions are represented in this set and the spatial filtering technique was shown to be

effective against many of them. While in some cases the improvements were not large, in others there were marked improvements in the Doppler spread parameters.

The spatial filtering methods used varied in computational complexity and this must be taken into account when considering an operational system. In light of the performance and simplicity of the constant amplitude two antenna approach, this would seem to be the most appropriate spatial filtering method to pursue.

It is clear that this form of spatial filtering can lead to significant reductions in Doppler spread and thus improvements in the availability of modems operating over such a channel. Examination of the shape of the cumulative probability curves indicates that there will be improved availability in the case of the Mil-Std-188-110A 300bps and 1200bps modems. The improvement in availability possible for a hypothetical modem, with a breaking point around 15Hz is much more significant. The cumulative probability curves around this value are relatively flat and a small change in Doppler spread leads to a large change in cumulative probability.

In terms of Mil-Std-188-110A modem performance, when the best result is chosen on a case by case basis, the difference between the percentage passing the spread criteria after spatial filtering compared to before (i.e. the % being 'fixed') is around 20% for both the 300bps and 1200bps modems. For a hypothetical modem with a breaking point around 15Hz the figure is 45%. An operational system is unlikely to have the 'luxury' of selecting the best performing pair from an array, however, on average, these results do indicate that in ~6% of cases an improvement in the mean Doppler spread after spatial filtering may 'fix' a 1200bps modem. While in ~30% of cases spatial filtering may 'fix' the hypothetical modem.

The variation of Doppler spread with the phase angle,  $\psi$ , was examined and in most cases appears to present a smooth curve with one or more minima, depending on the propagation conditions. It is reassuring to note that the minima in the Doppler spread curves do not coincide with minima in the SNR curves. It is also interesting to note that in many cases, all values of  $\psi$  actually led to a reduction of Doppler spread.

Fast solver methods were applied to the optimisation of  $\psi$  and were found to be both robust and quick, with all cases converging to a good solution, comparable to the looping method solution, many times faster than the looping method. The performance

improvements are such that it may be feasible to consider the implications of using these techniques in an operational system.

Although it performs well, the solver method has not been fully optimised to the spatial filtering problem. There are a number of ways forward to further improve the performance of the solver method. These include investigations into the following:

- Introducing a composite TDspr, Ttspr and SNR parameter
- Alternatives to the Golden section search algorithm
- Optimisation of the termination tolerances
- Optimisation of the underlying Doppler spread calculation, since this is the most computationally intensive component of the cycle. Compilation of the MATLAB code is an option that may significantly speed up execution time.

While this analysis has selected the best performing antenna pair from the RSL six antenna array, the preliminary three antenna results indicate that although applying two sets of phases is too computationally intensive, it may be practical to select the best performing pair from a carefully arranged three antenna array.

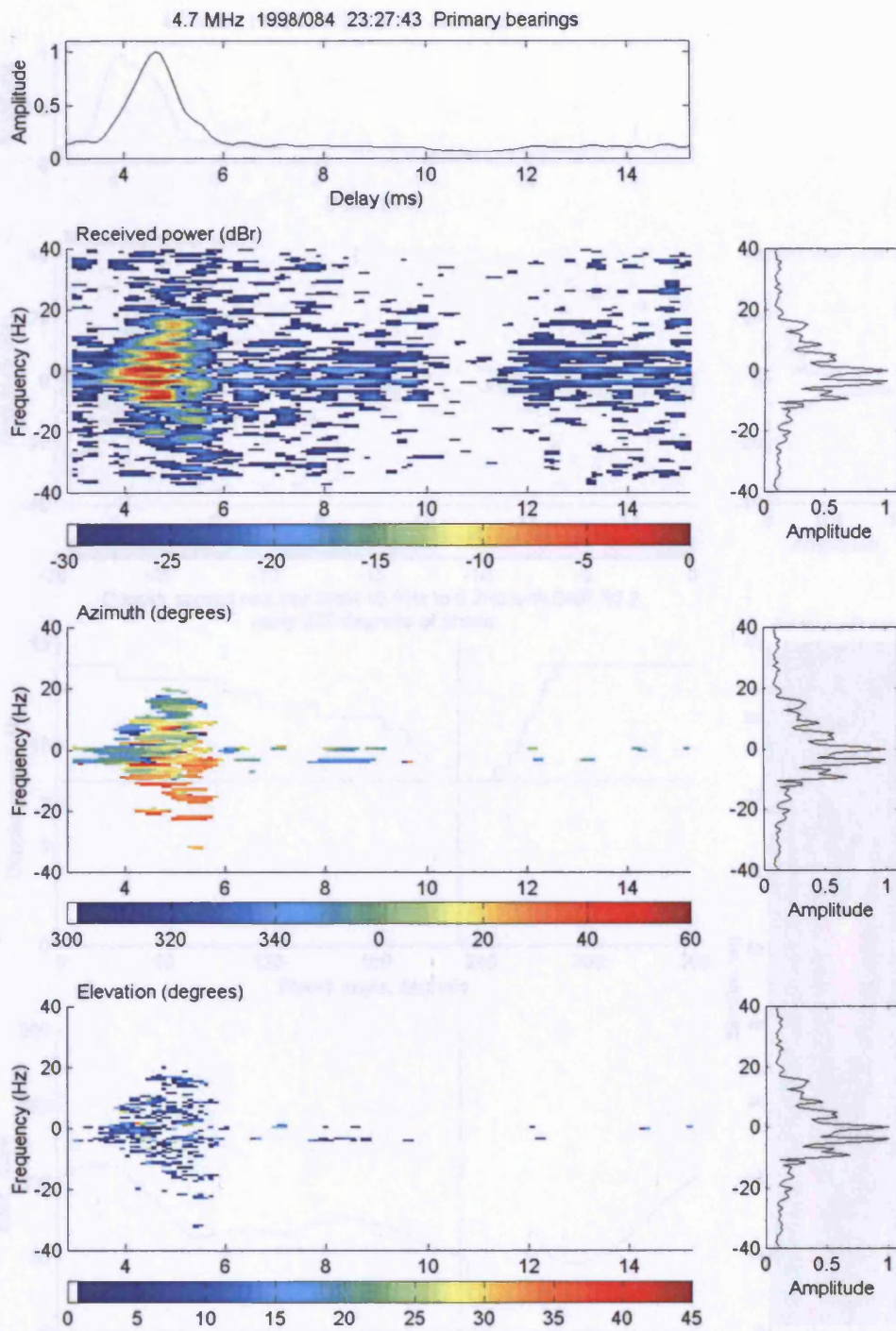


Figure 6.1 4.7MHz Svalbard – Kiruna, received at 23:27UT, 25 March 1998 before spatial filtering. Doppler spread, 16.4Hz

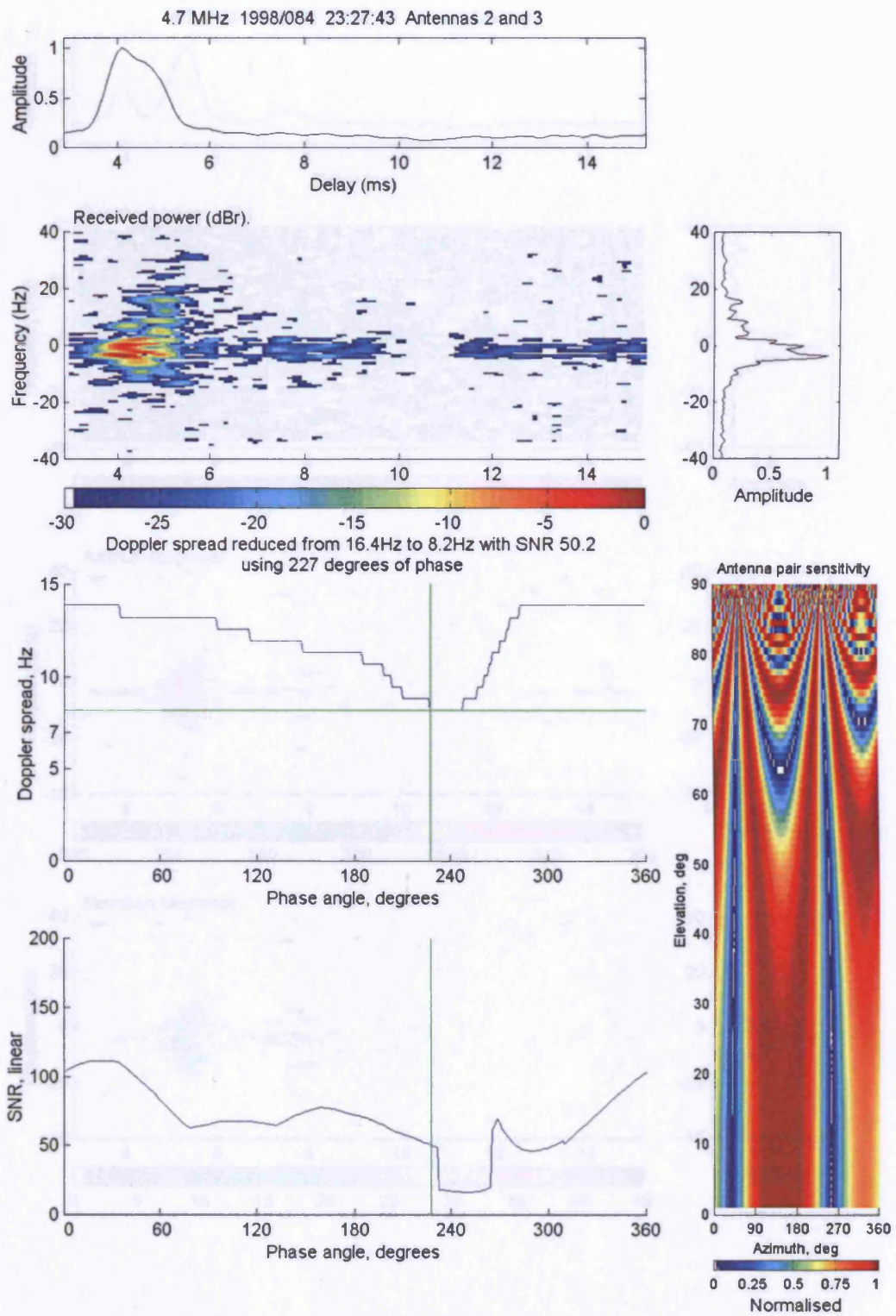


Figure 6.2 4.7MHz Svalbard – Kiruna, received at 23:27UT, 25 March 1998 after spatial filtering. Doppler spread, 8.2Hz

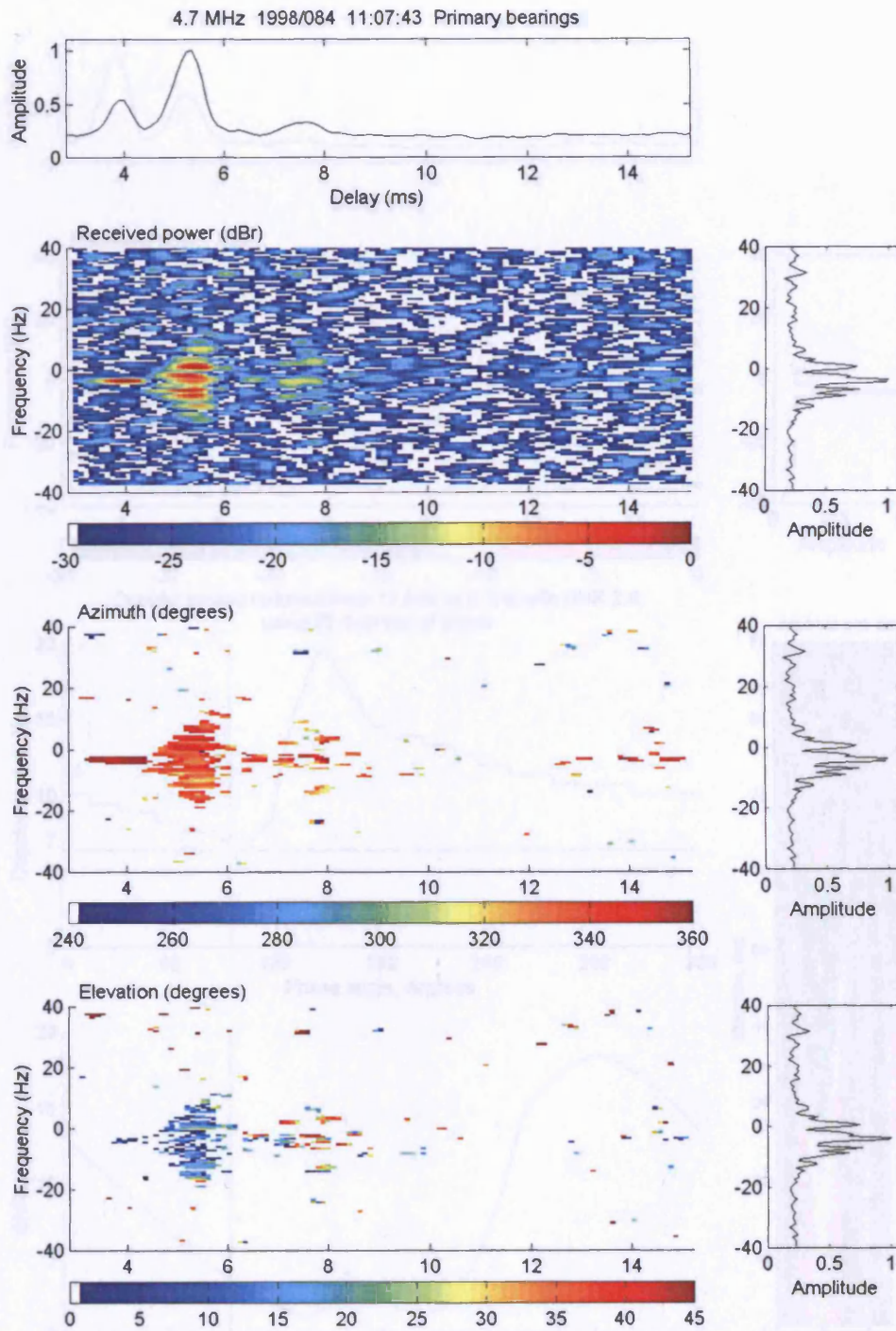


Figure 6.3 4.7MHz Svalbard – Kiruna, received at 11:07UT, 25 March 1998 before spatial filtering. Doppler spread 18.9Hz

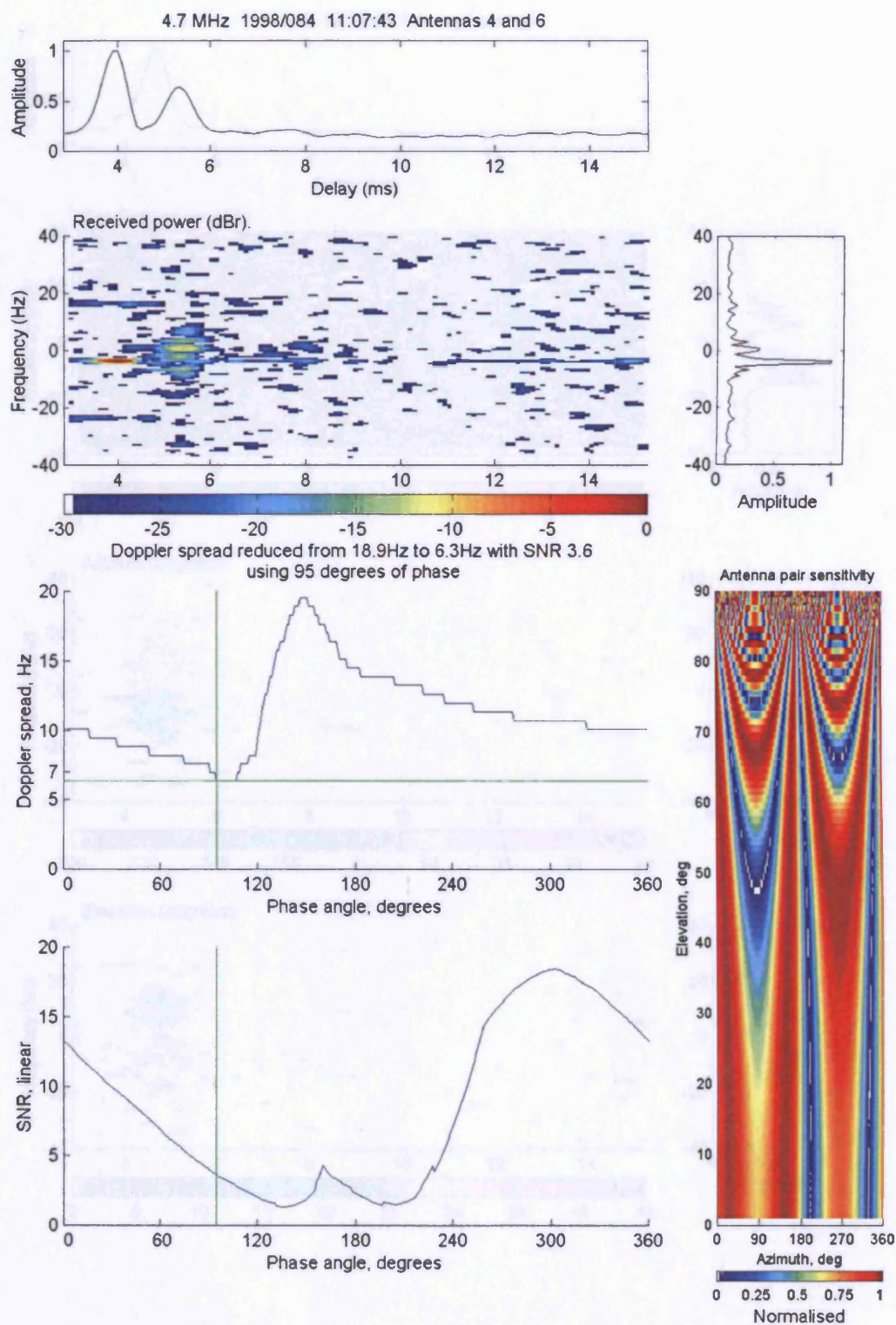


Figure 6.4 4.7MHz Svalbard – Kiruna, received at 11:07UT, 25 March 1998 after spatial filtering. Doppler spread 6.3Hz

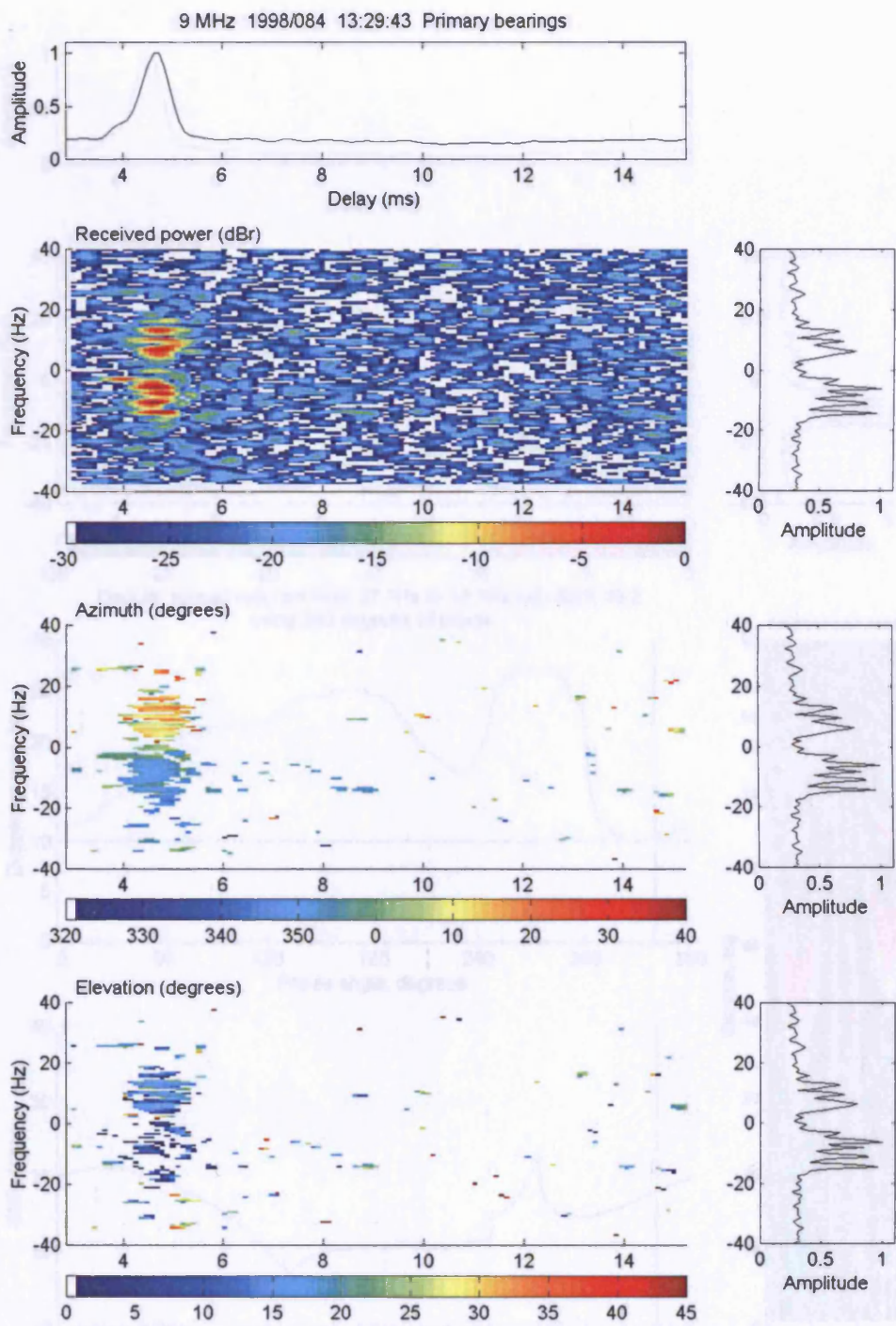


Figure 6.5 9MHz Svalbard – Kiruna, received at 13:29UT, 25 March 1998 before spatial filtering. Doppler spread 27.7Hz

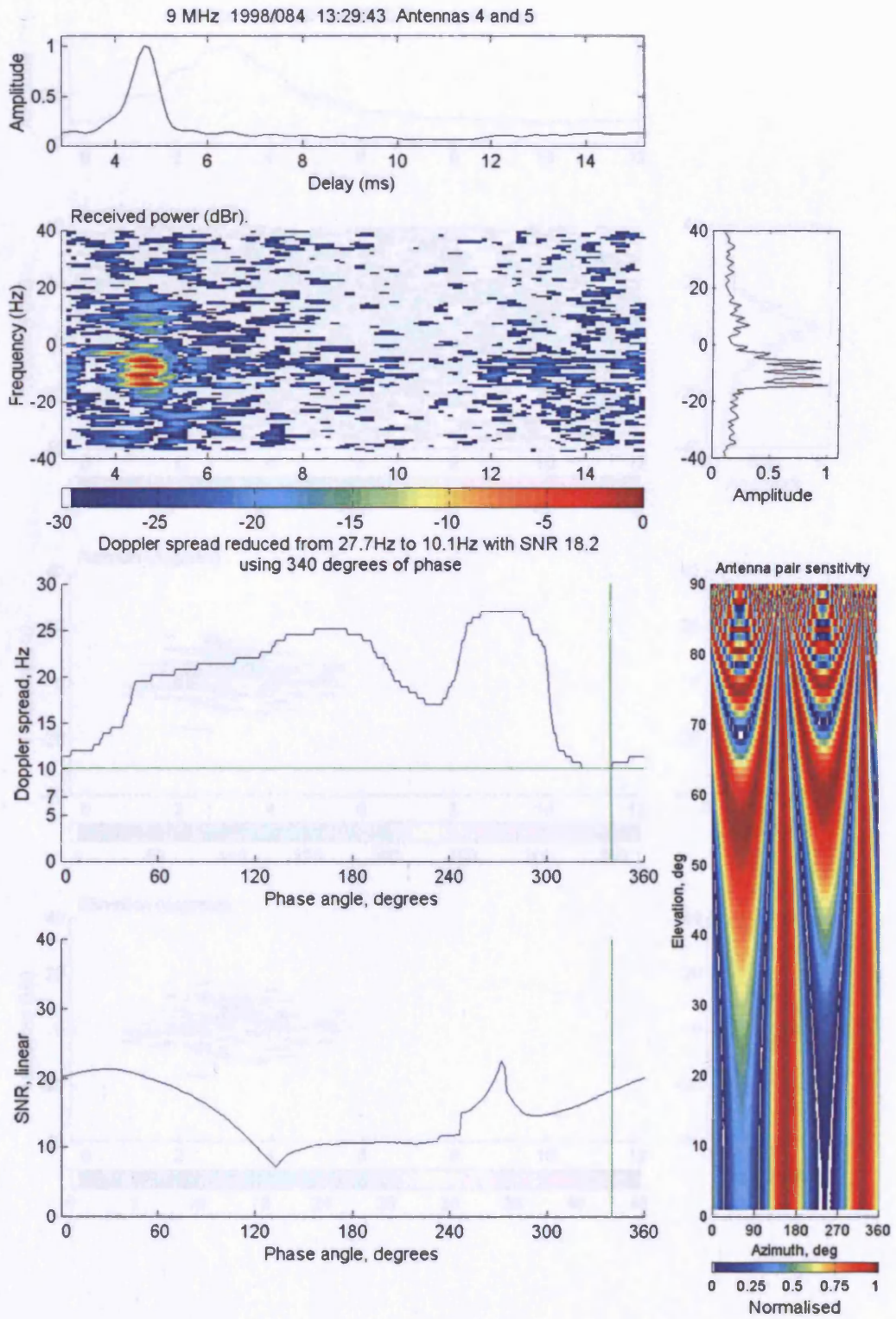


Figure 6.6 9MHz Svalbard – Kiruna, received at 13:29UT, 25 March 1998 after spatial filtering. Doppler spread 10.1Hz

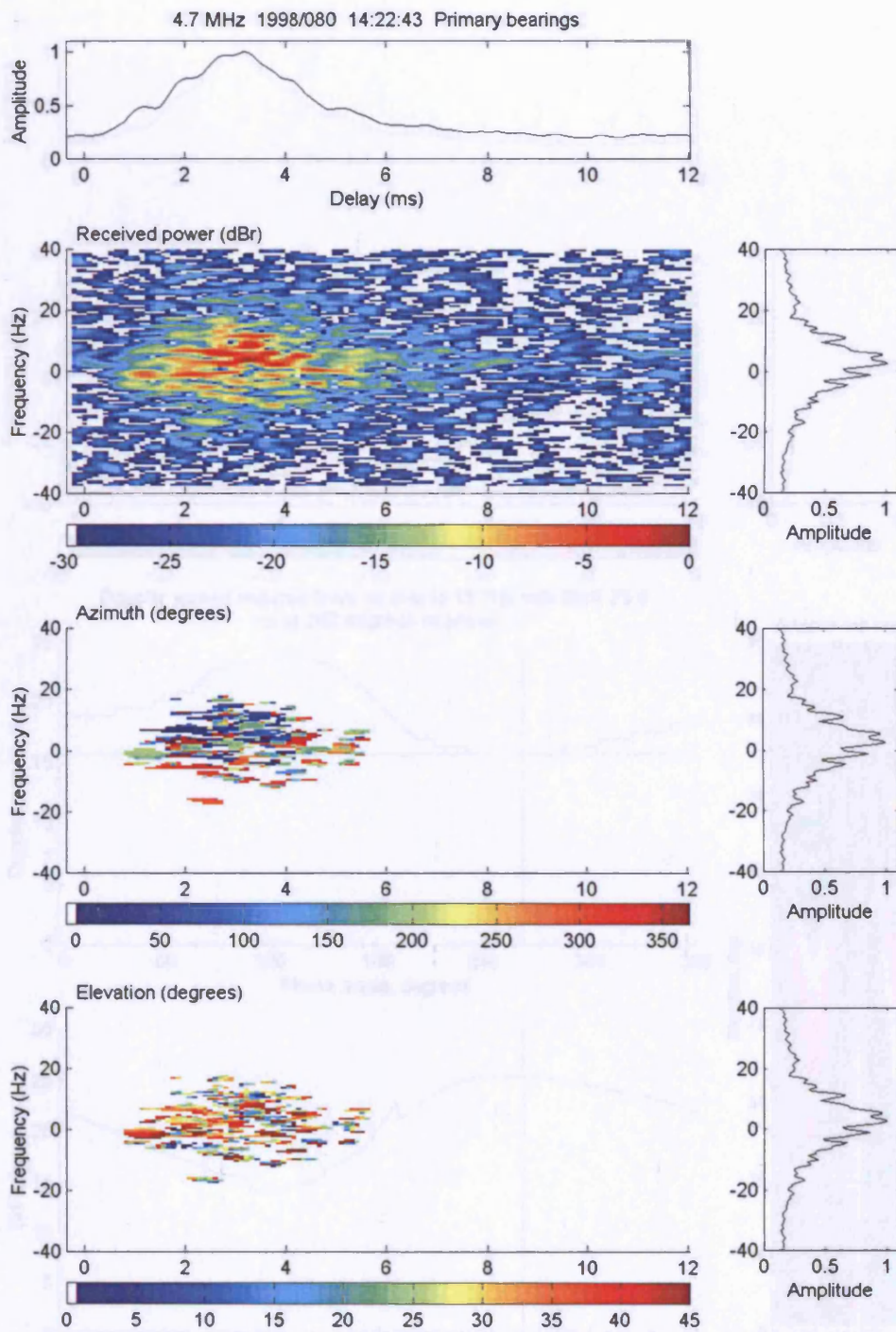


Figure 6.7 4.7MHz Harstad – Kiruna, received at 14:22UT, 21 March 1998 before spatial filtering. Doppler spread 18.9Hz

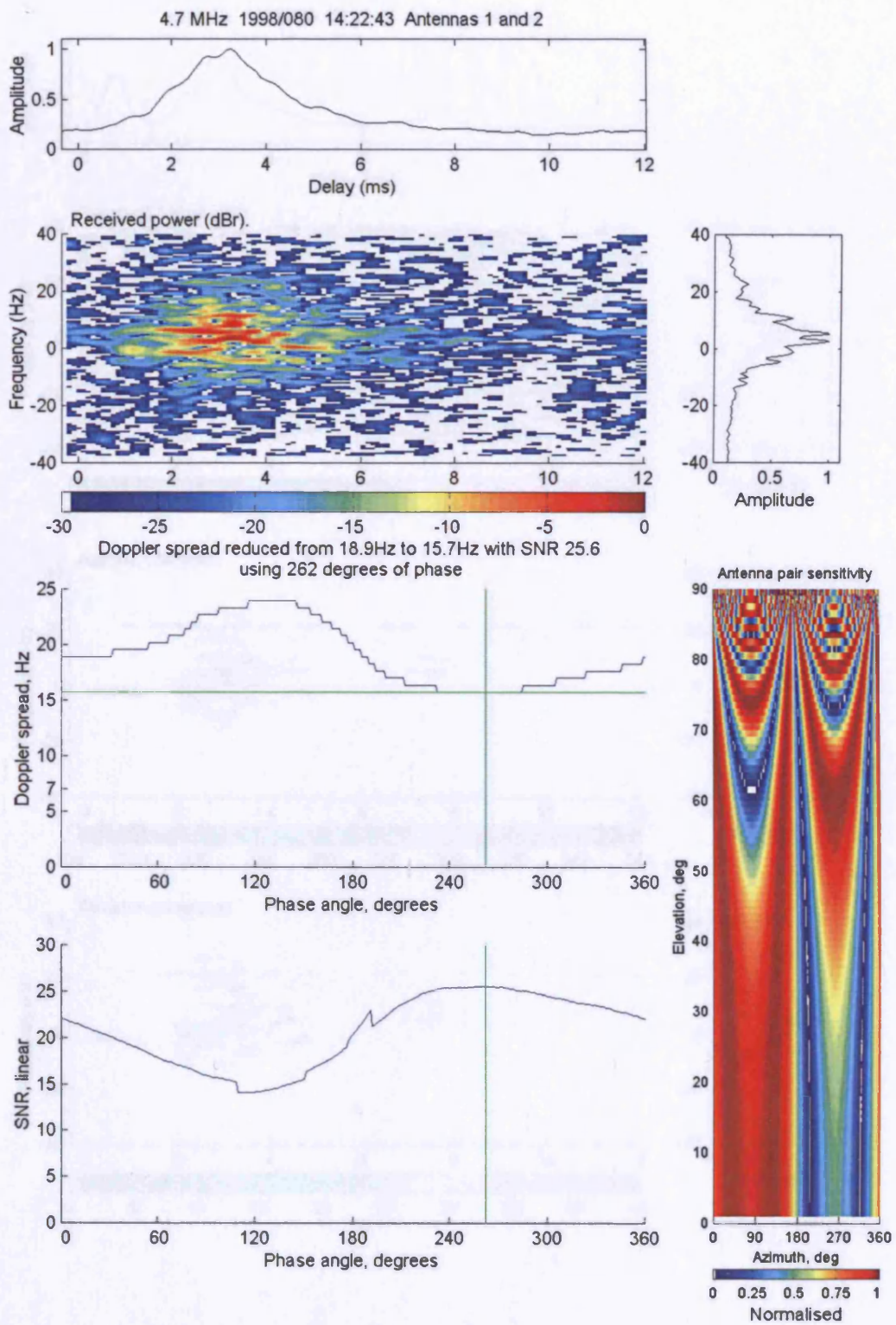


Figure 6.8 4.7MHz Harstad – Kiruna, received at 14:22UT, 21 March 1998 after spatial filtering. Doppler spread 15.7Hz

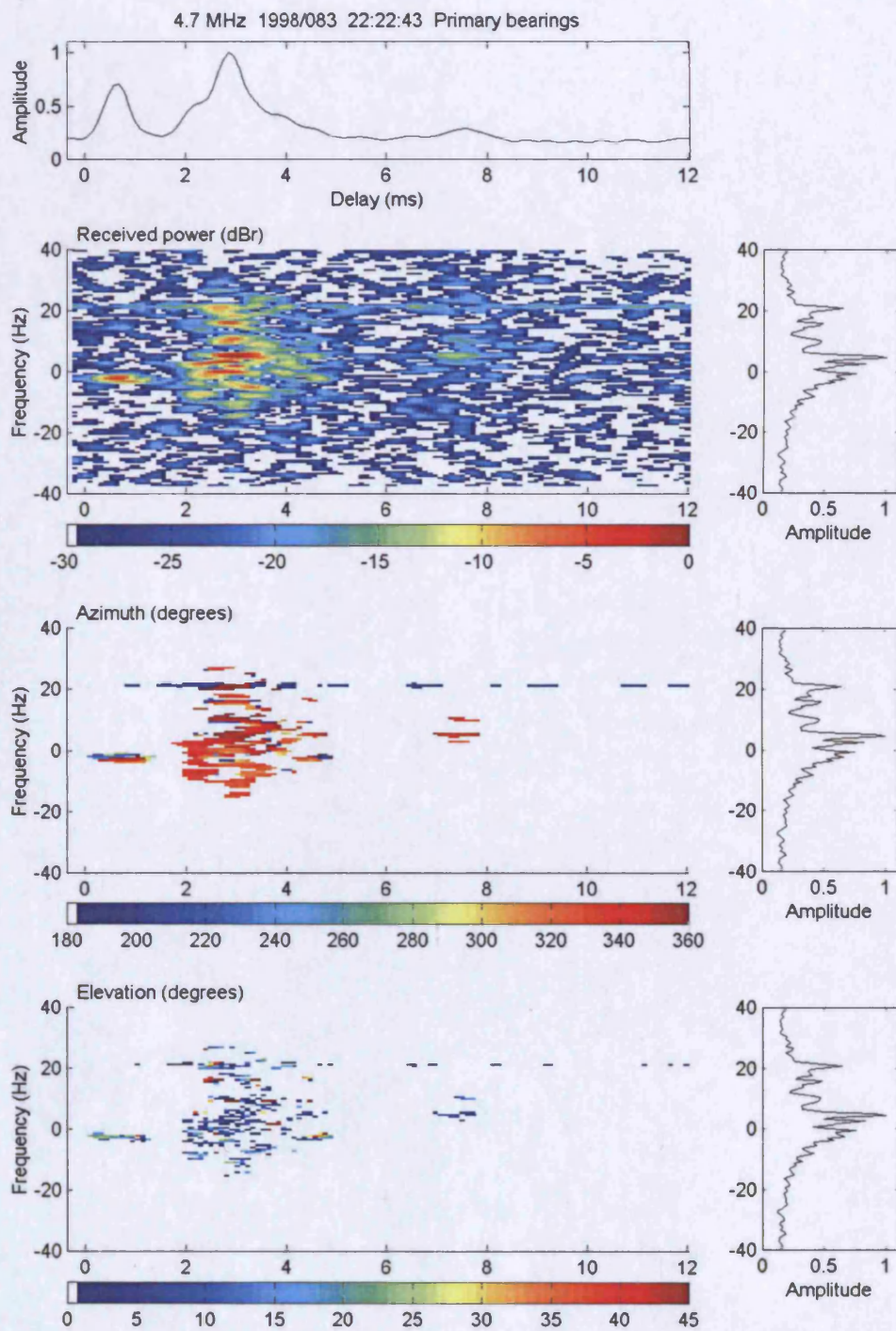


Figure 6.9 4.7MHz Harstad – Kiruna, received at 22:22UT, 24 March 1998 before spatial filtering. Doppler spread 24.6Hz

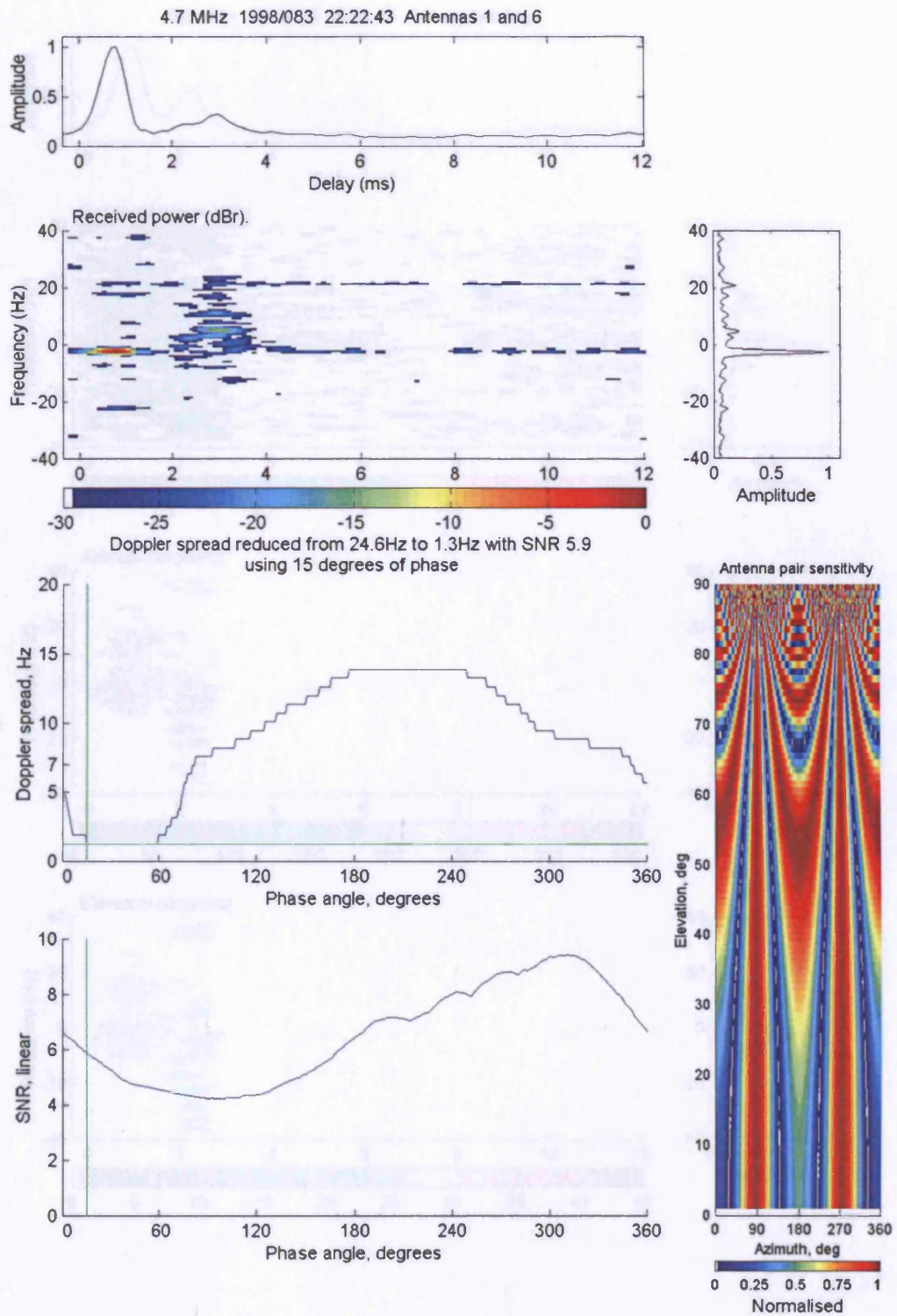


Figure 6.10 4.7MHz Harstad – Kiruna, received at 22:22UT, 24 March 1998 after spatial filtering. Doppler spread 1.3Hz

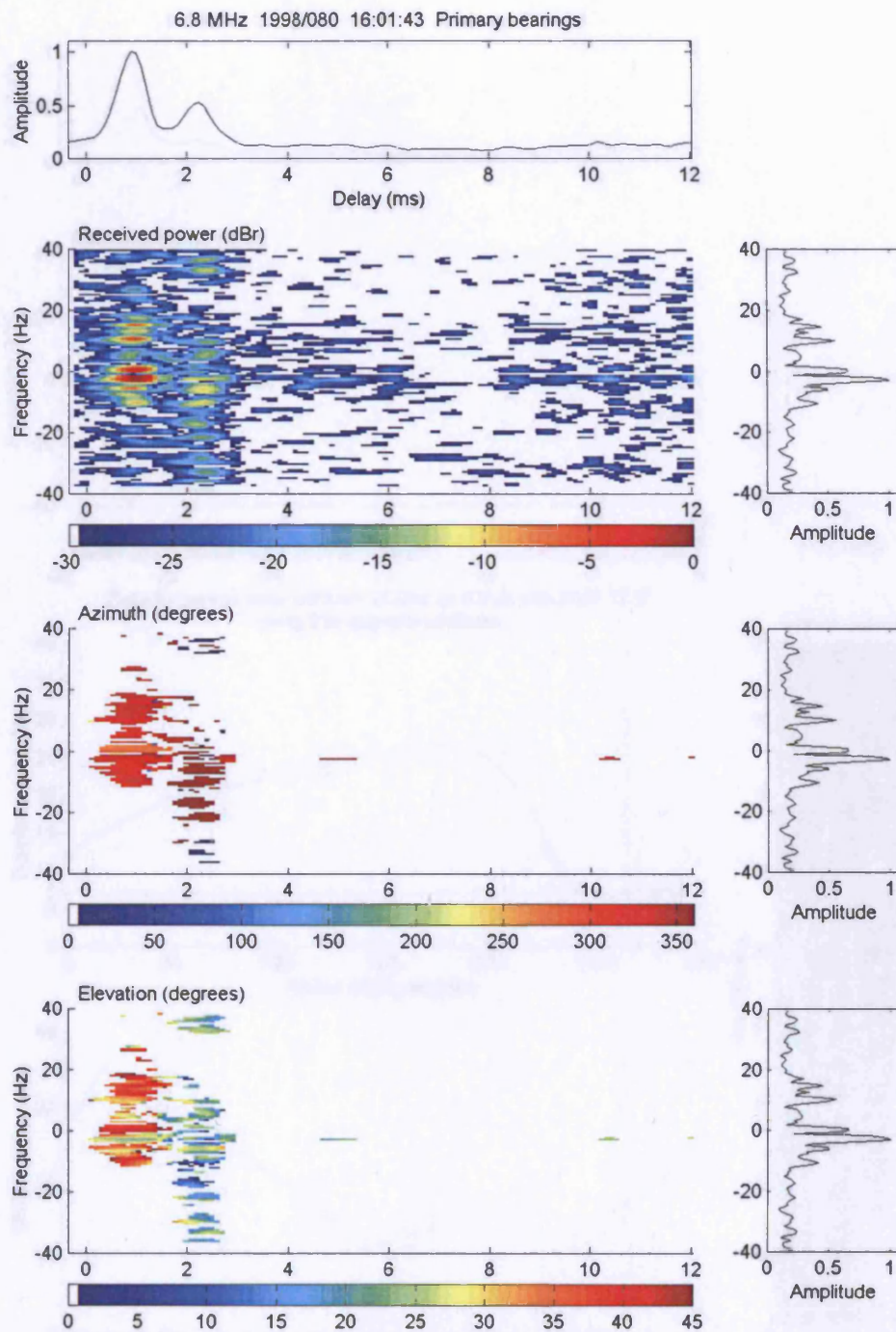


Figure 6.11 6.8MHz Harstad – Kiruna, received at 16:01UT, 21 March 1998 before spatial filtering. Doppler spread 25.2Hz

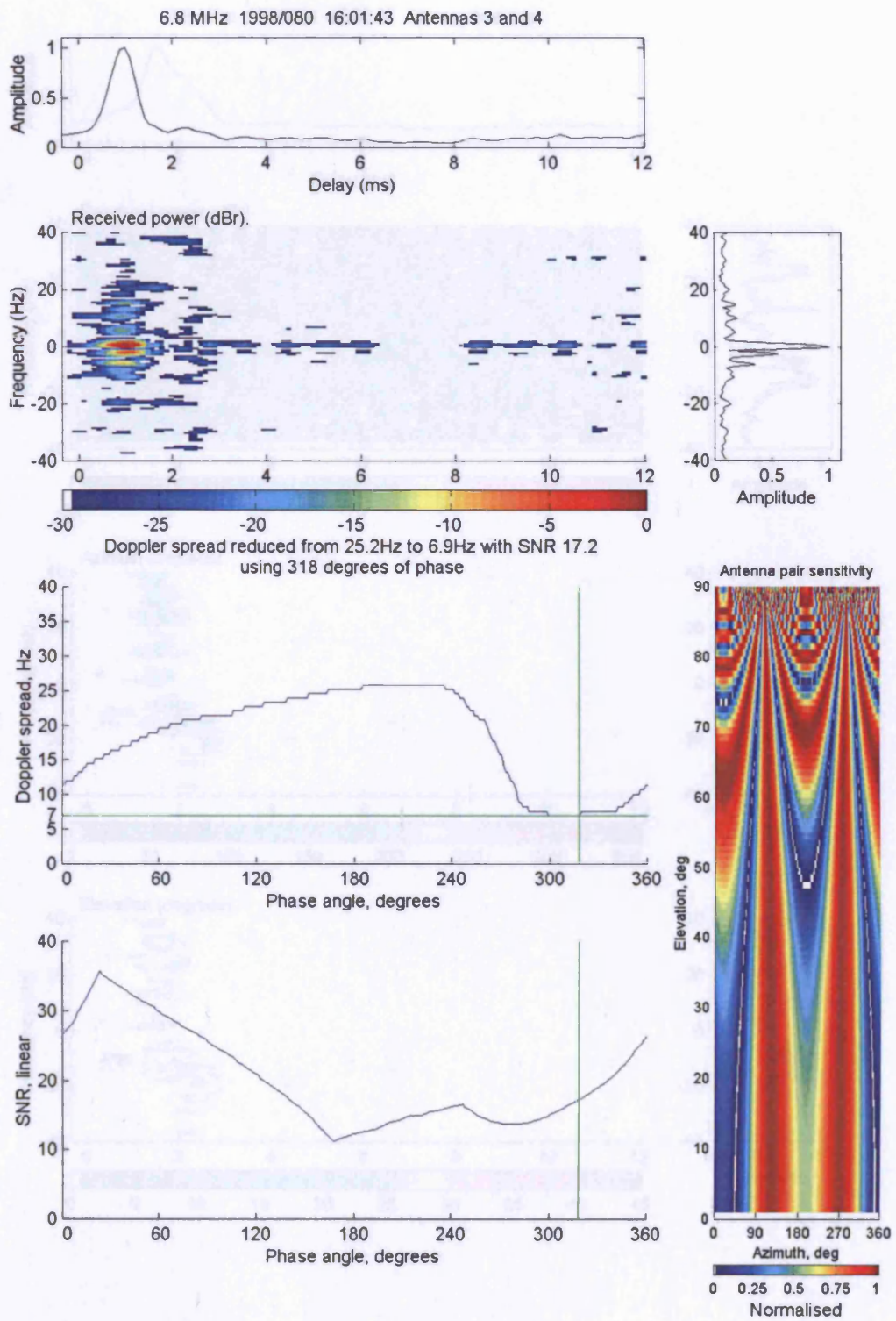


Figure 6.12 6.8MHz Harstad – Kiruna, received at 16:01UT, 21 March 1998 after spatial filtering. Doppler spread 6.9Hz

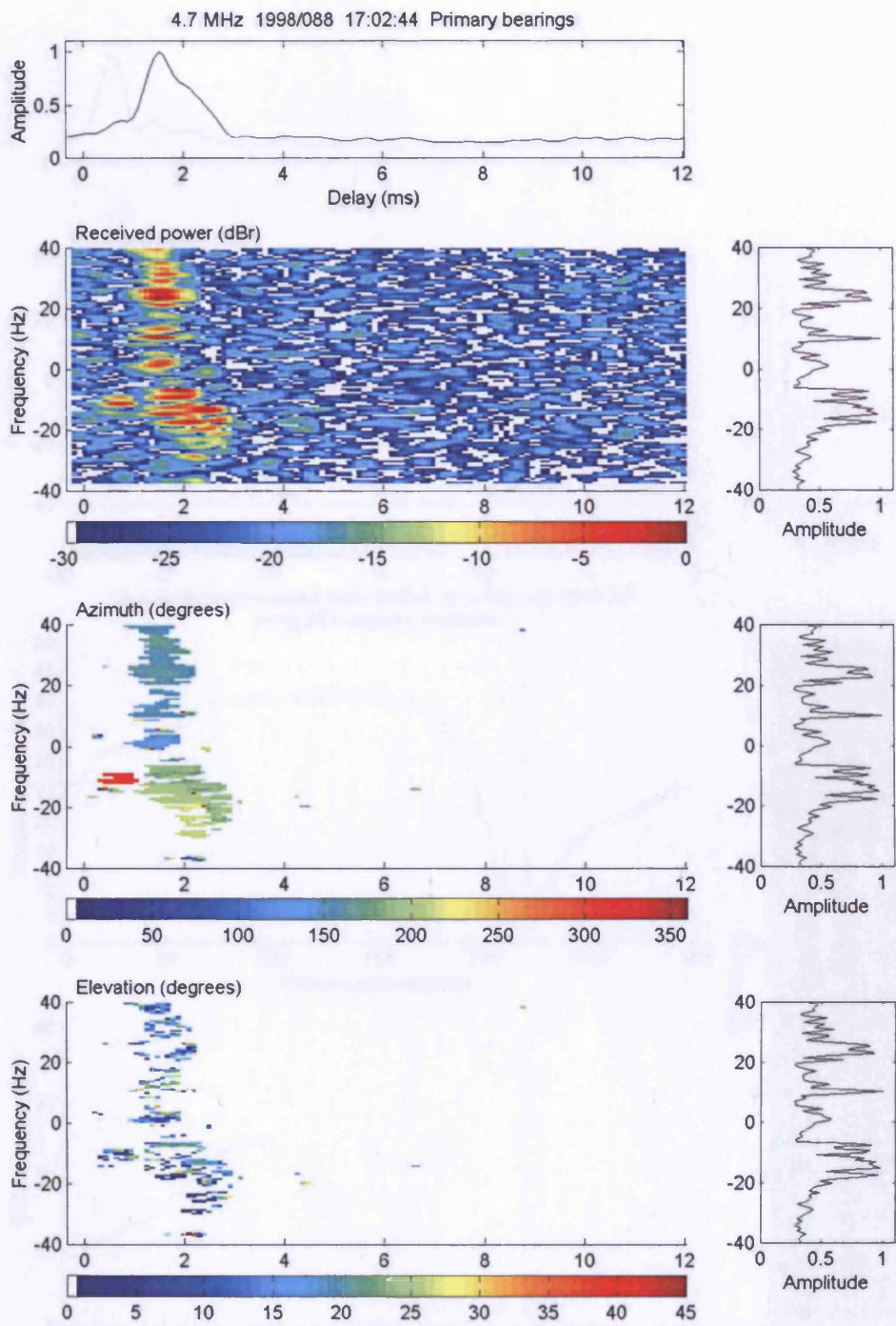


Figure 6.13 4.7MHz Harstad – Kiruna, received at 17:02UT, 29 March 1998 before spatial filtering. Doppler spread 46.0Hz

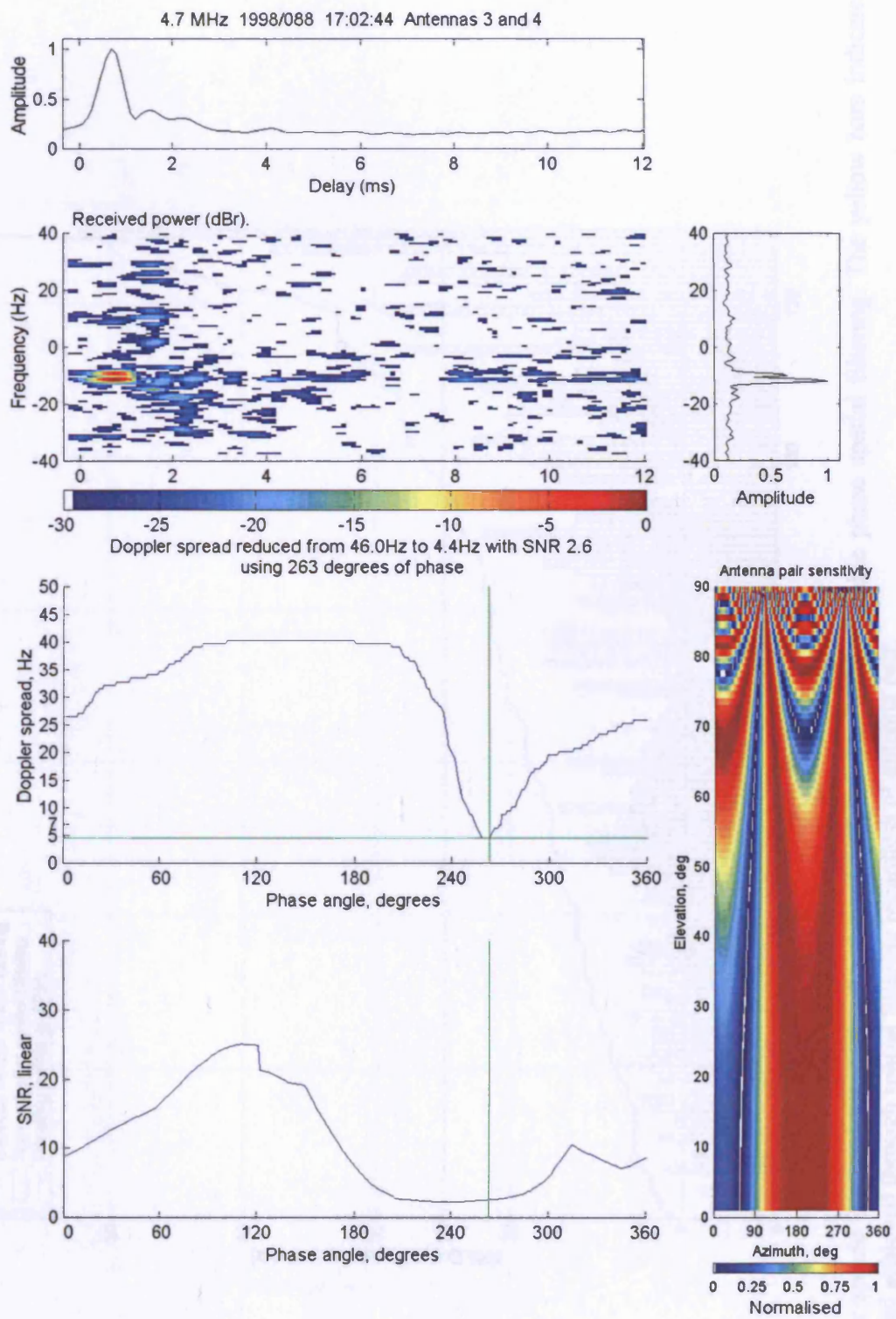


Figure 6.14 4.7MHz Harstad – Kiruna, received at 17:02UT, 29 March 1998 after spatial filtering. Doppler spread 4.4Hz

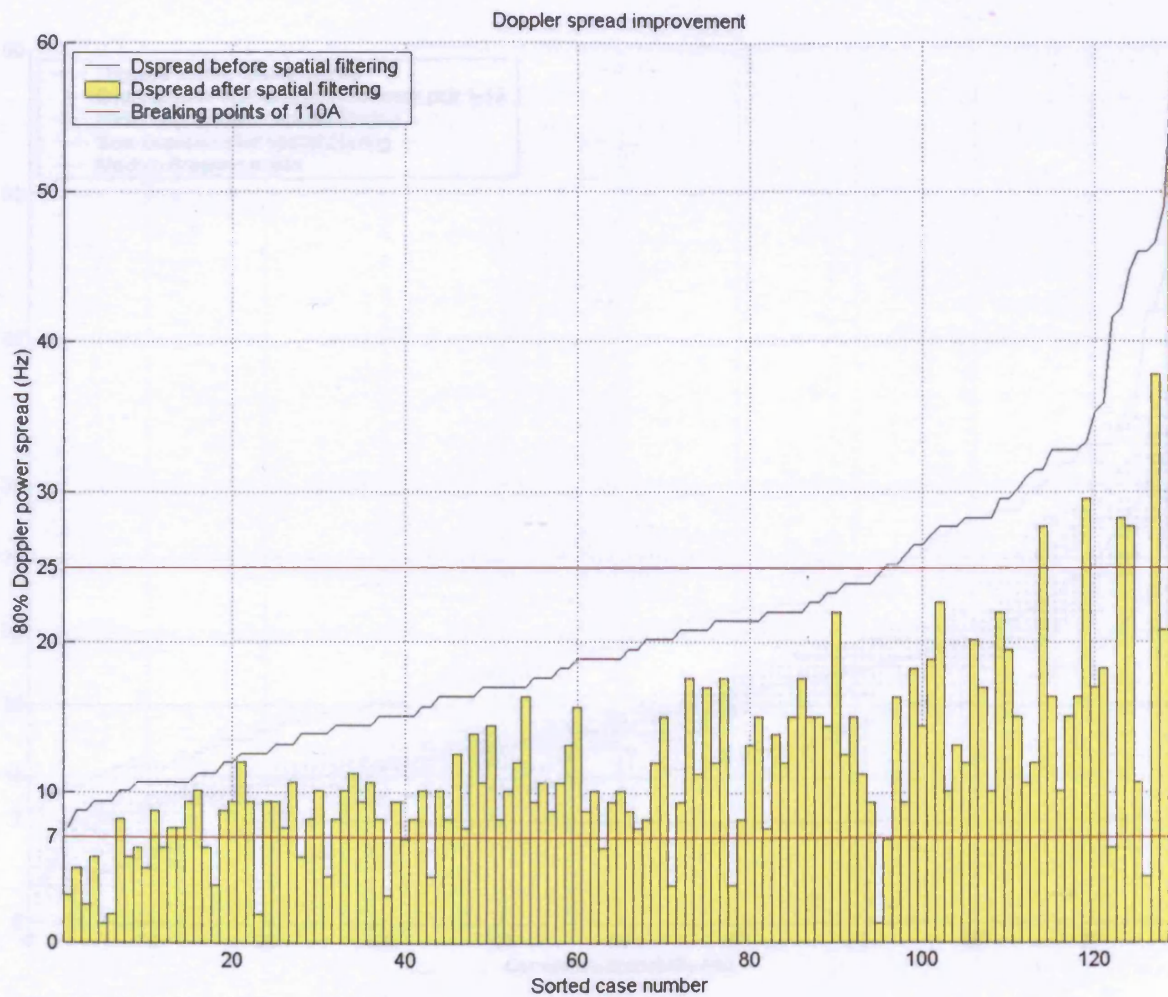


Figure 6.15 Doppler spread improvements after 2 antenna, constant amplitude, variable phase spatial filtering. The yellow bars indicate the lowest Doppler spread achieved through spatial filtering regardless of antenna pair.

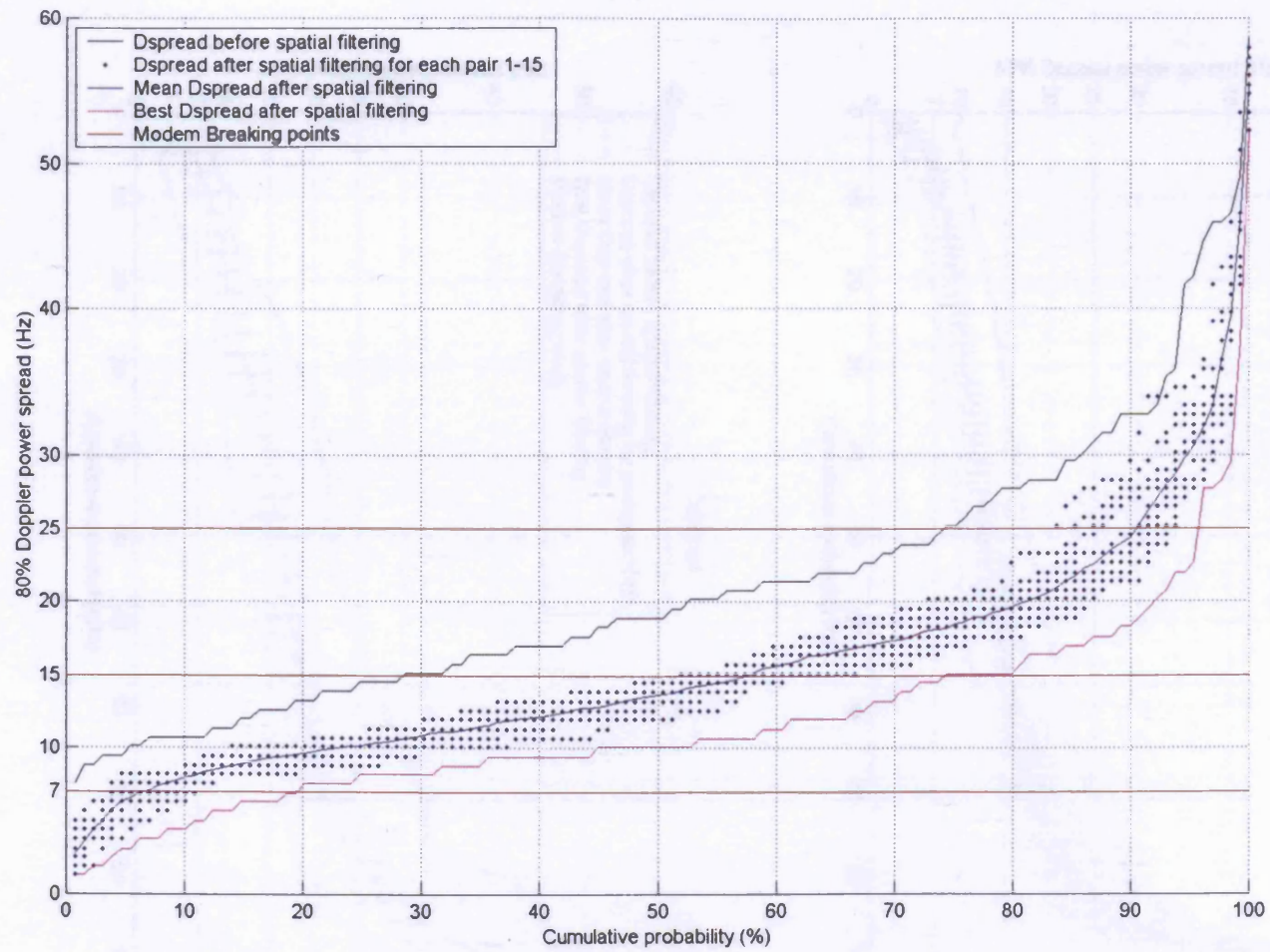


Figure 6.16 Doppler spread vs. cumulative probability (% points below the ordinate value).

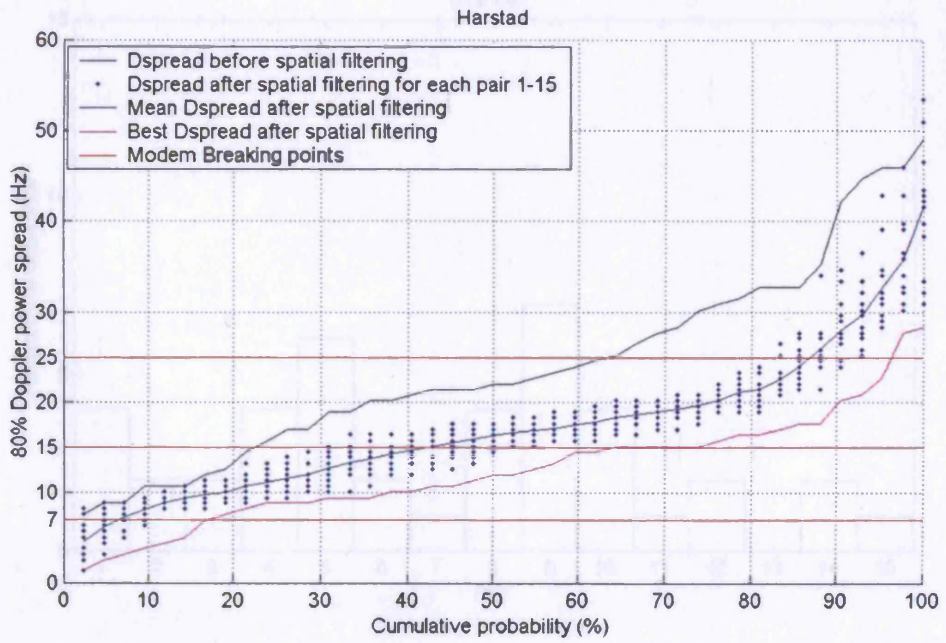
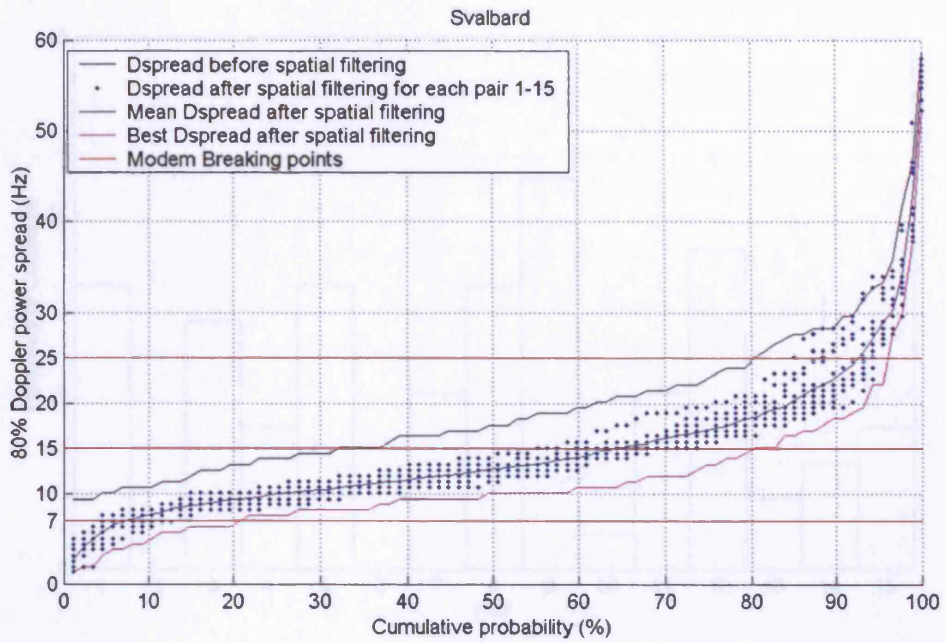


Figure 6.18 Distribution of Best Pairs

Figure 6.17 Cumulative probability distributions for each path separately.

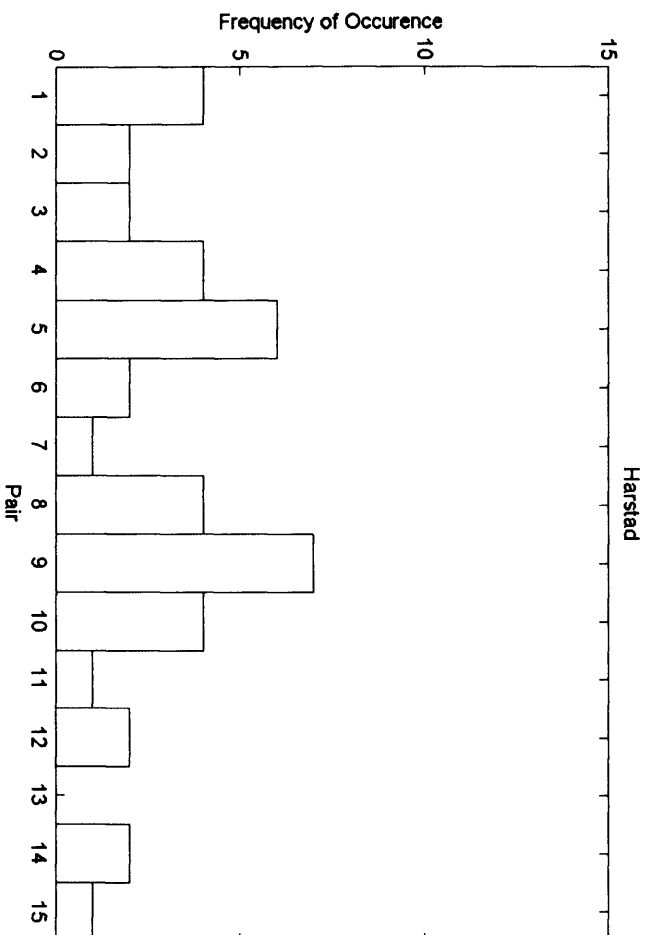
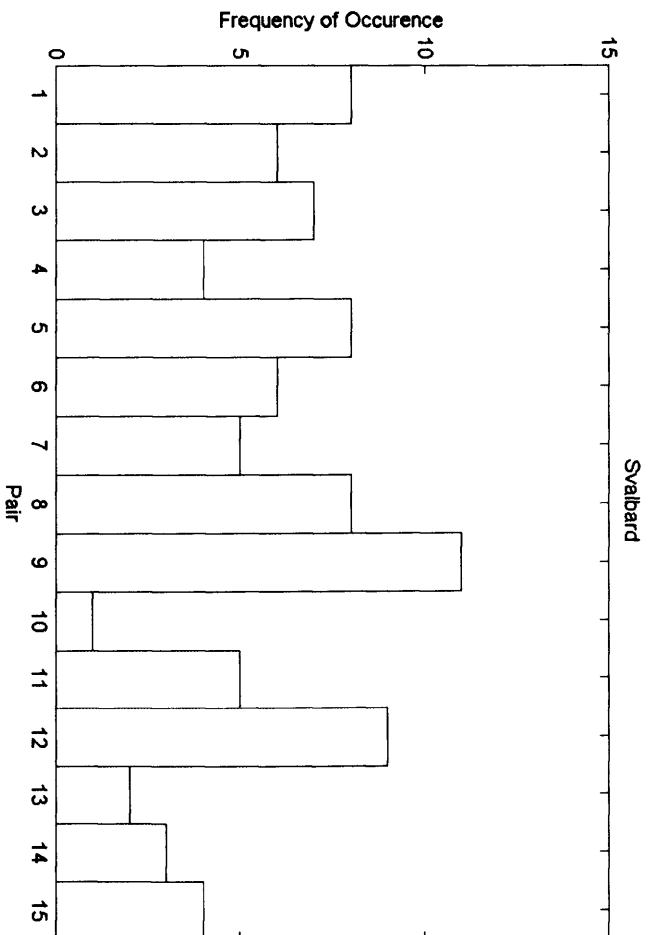


Figure 6.18 Distribution of 'Best Pairs'

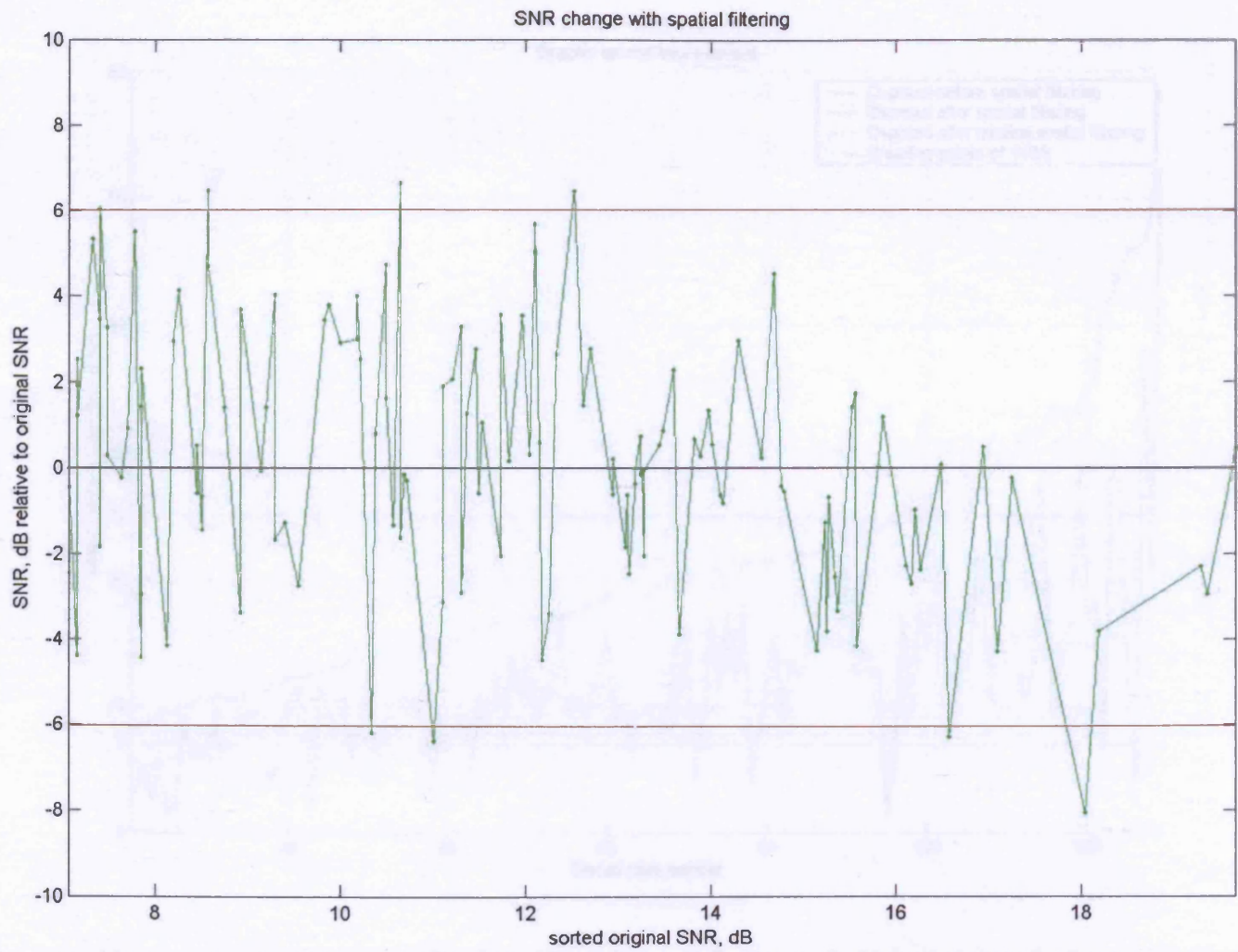


Figure 6.19 SNR change with spatial filtering, the green line represents the resulting SNR, after spatial filtering, relative to the original SNR.

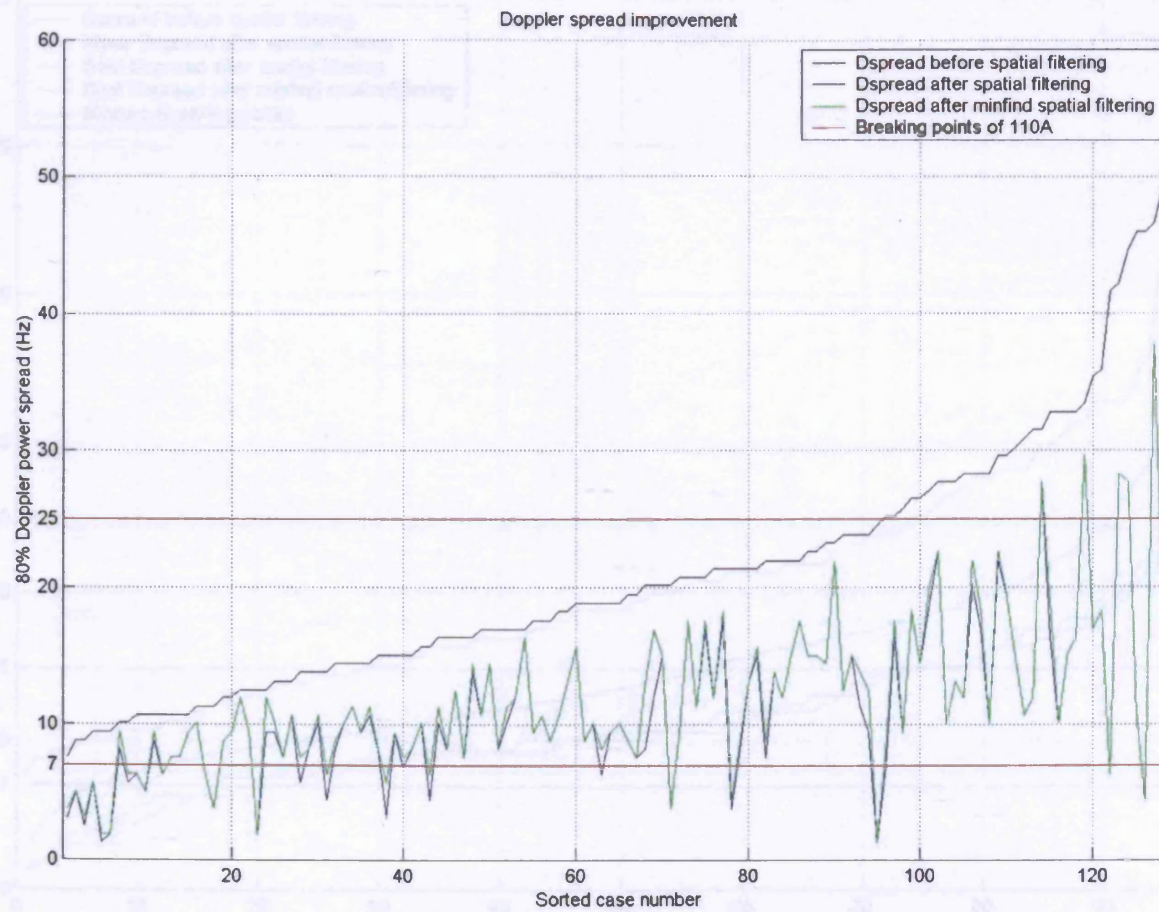


Figure 6.20 Doppler spread improvements after spatial filtering using minimum finding techniques to select the best phase angle

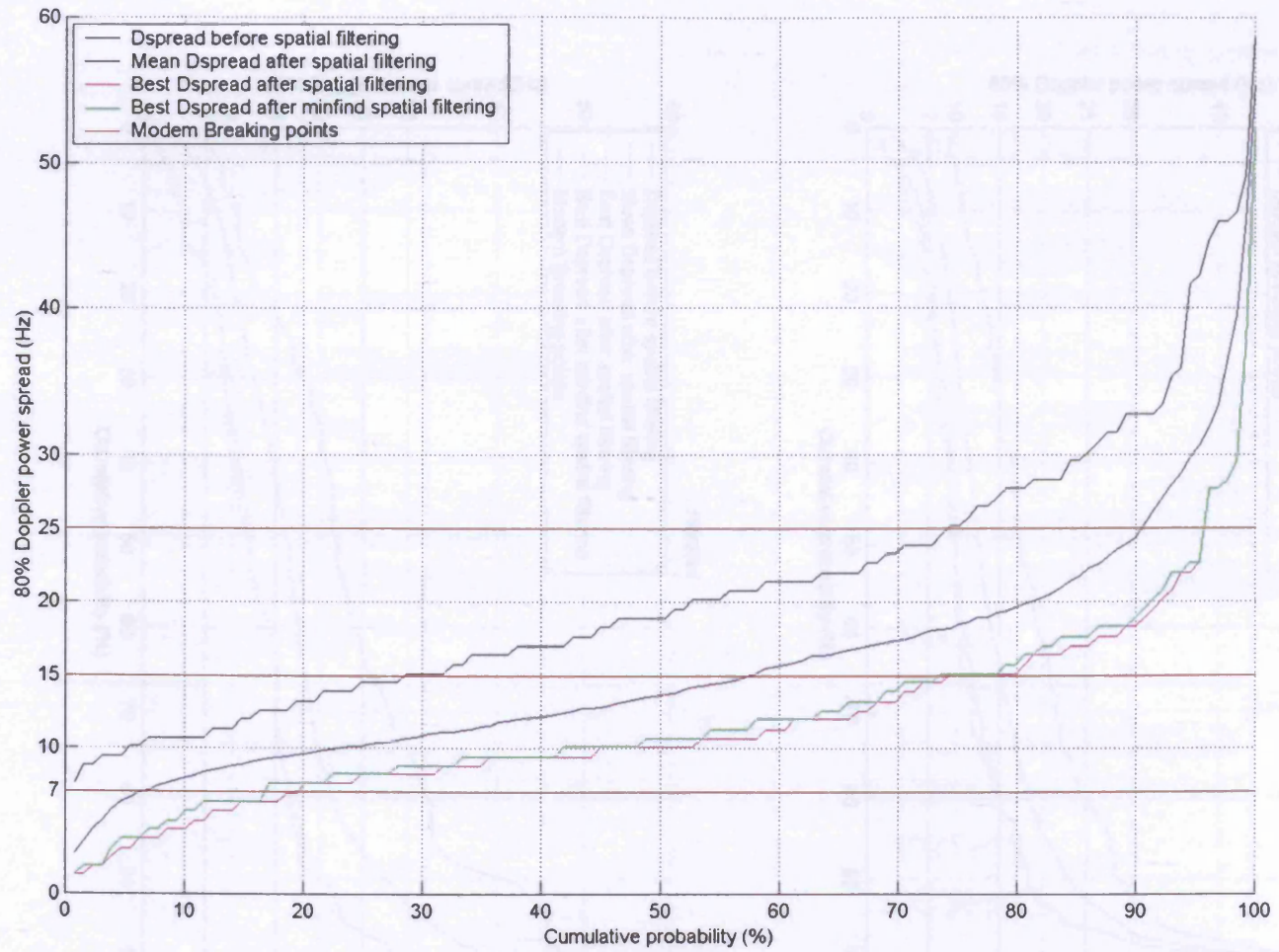


Figure 6.21 Doppler spread vs. cumulative probability (% points below the ordinate value). Including Minfind results in Green

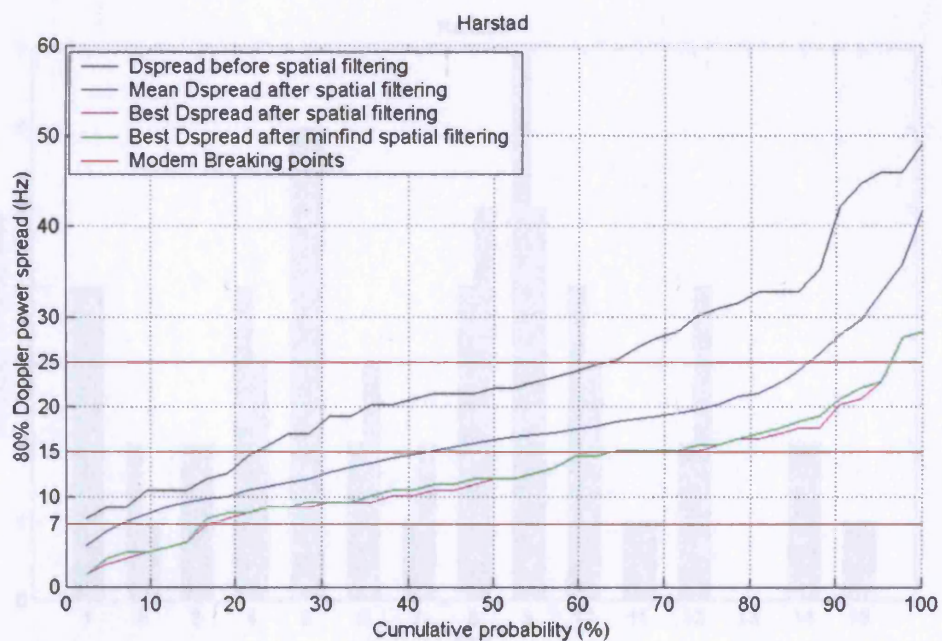
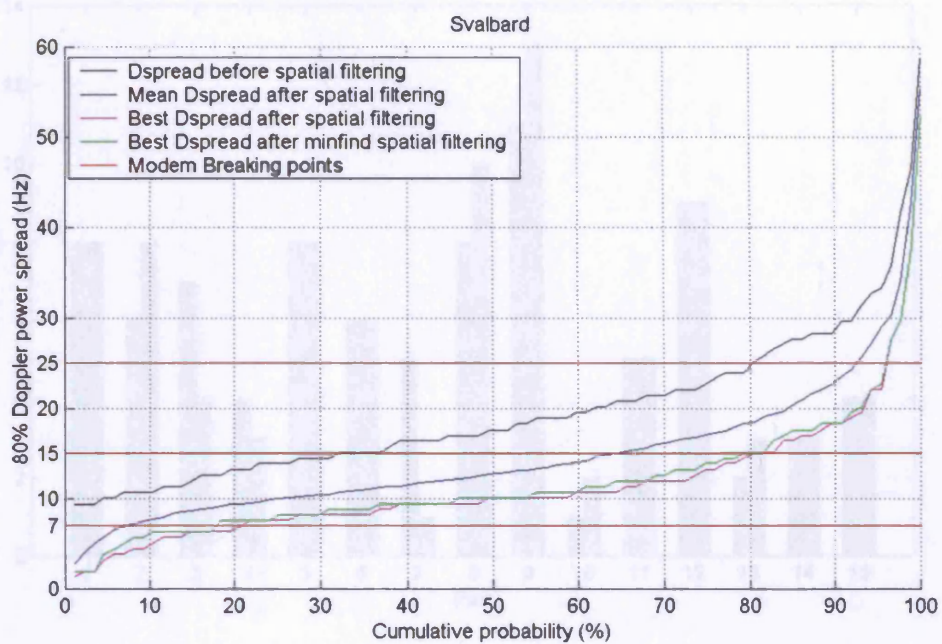


Figure 6.22 Cumulative probability distributions for each path separately

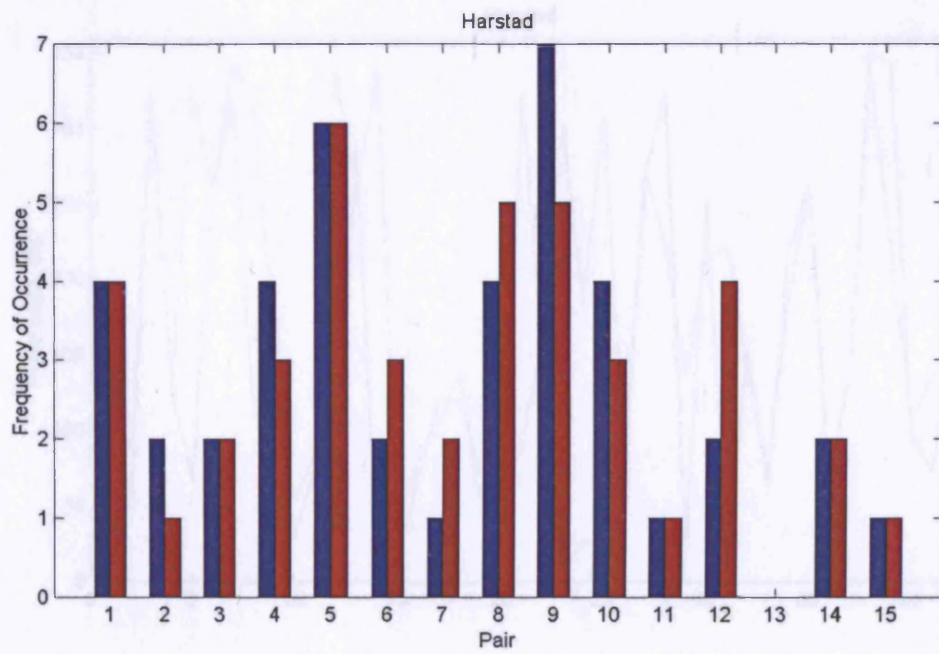
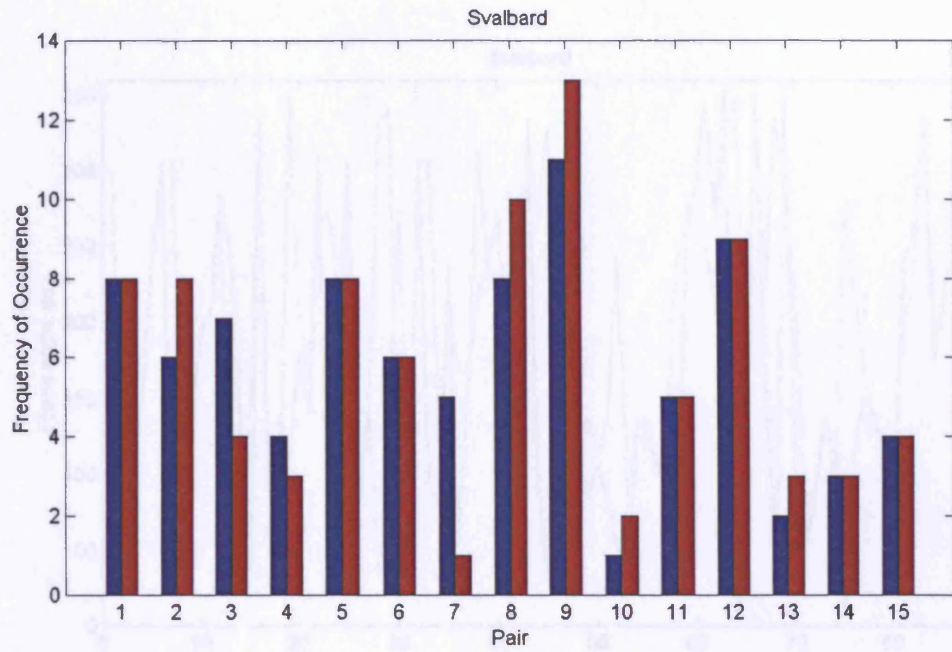


Figure 6.23 Distribution of looping and solver pairs (blue = looping, red = solver)

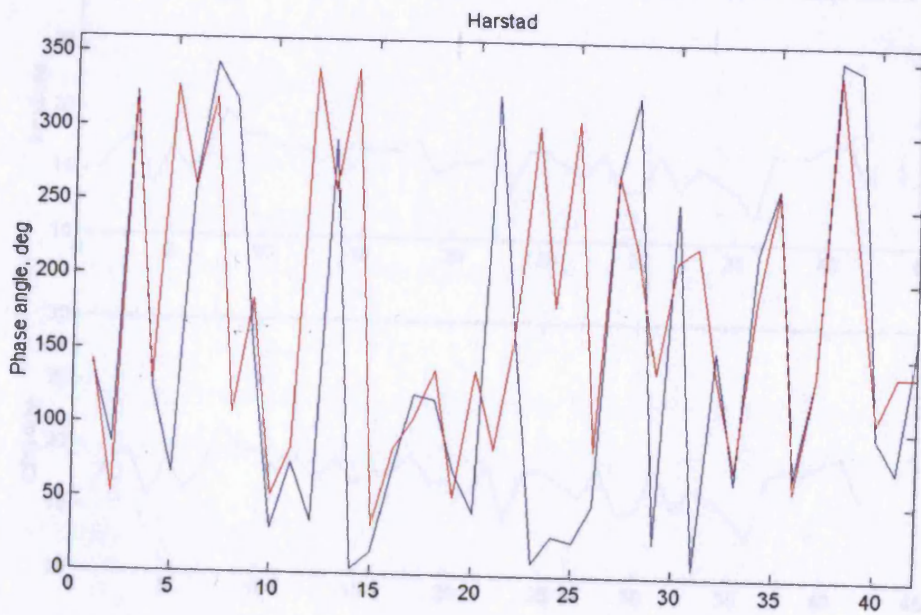
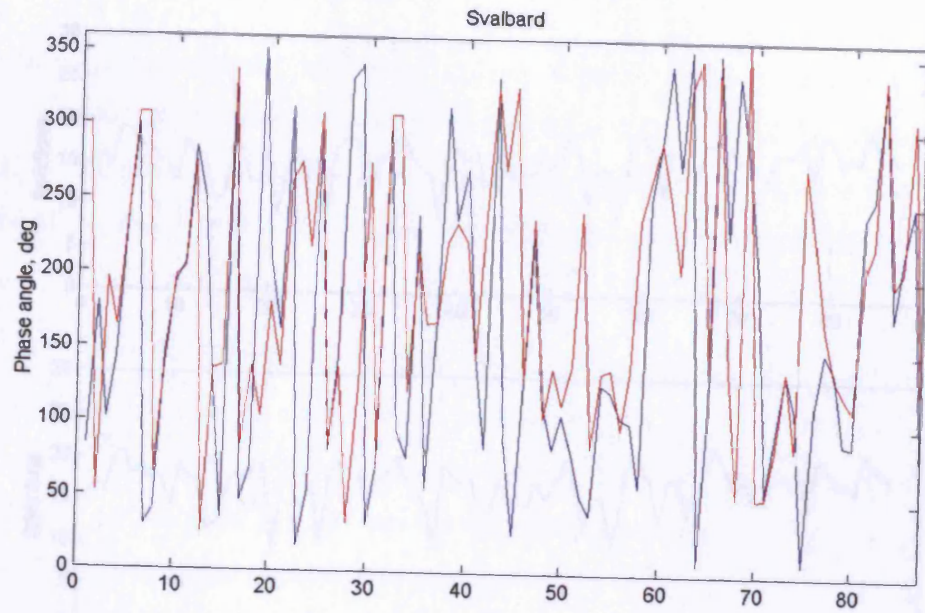


Figure 6.24 Looping and solver phase angle selections (blue = looping, red = solver), note that phase angle has been optimised using different criteria.

## 7. Conclusions and suggestions for further work

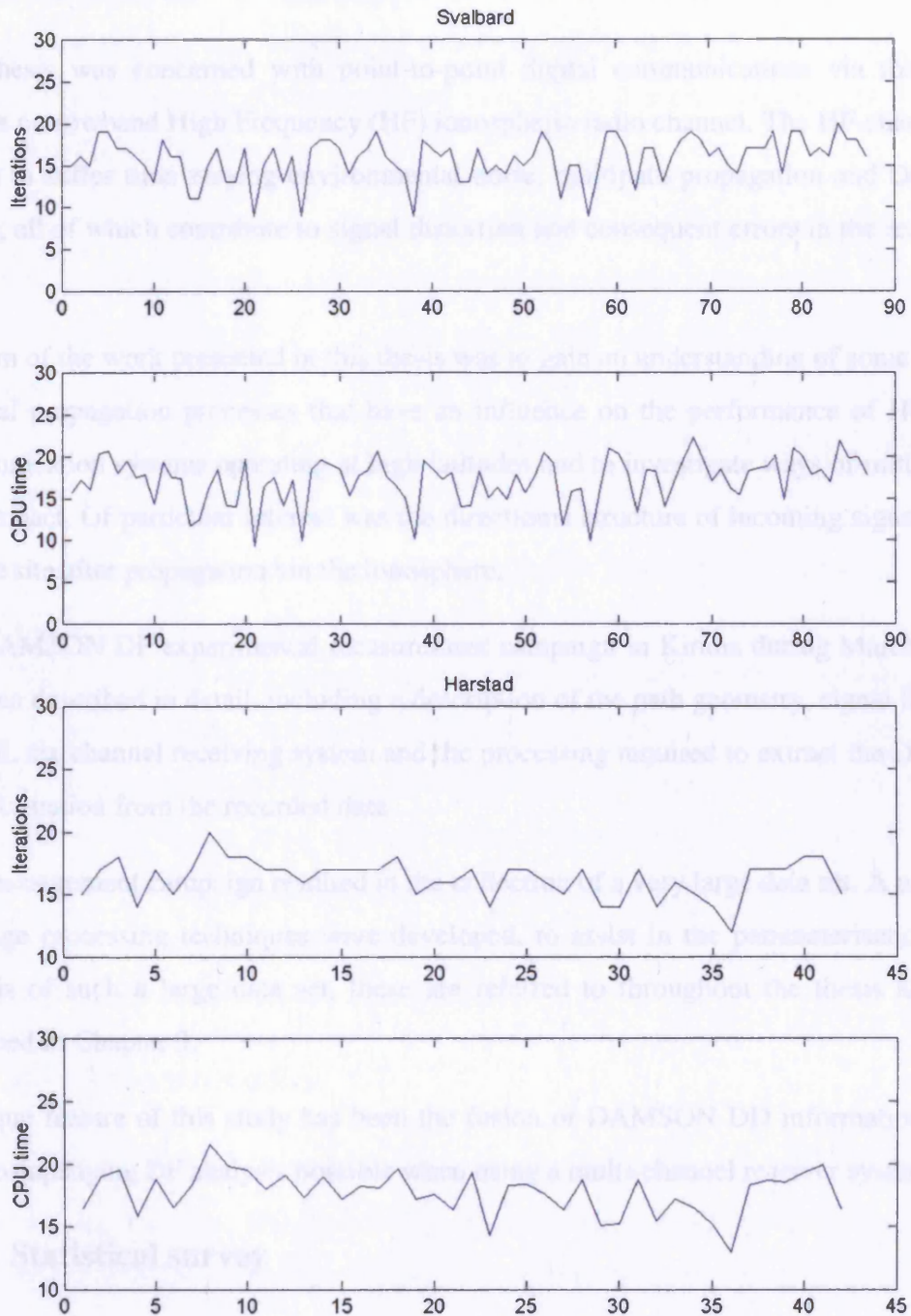


Figure 6.25 Number of iterations and CPU time required to reach a solution within tolerance

## **7. Conclusions and suggestions for further work**

This thesis was concerned with point-to-point digital communications via the high latitude narrowband High Frequency (HF) ionospheric radio channel. The HF channel is known to suffer time varying environmental noise, multipath propagation and Doppler effects, all of which contribute to signal distortion and consequent errors in the received data.

The aim of the work presented in this thesis was to gain an understanding of some of the physical propagation processes that have an influence on the performance of HF data communication systems operating at high latitudes and to investigate ways of mitigating their impact. Of particular interest was the directional structure of incoming signals at a receive site after propagation via the ionosphere.

The DAMSON DF experimental measurement campaign in Kiruna during March 1998 has been described in detail, including a description of the path geometry, signal format, the RSL six channel receiving system and the processing required to extract the DD and DF information from the recorded data.

This measurement campaign resulted in the collection of a very large data set. A number of image processing techniques were developed, to assist in the parameterisation and analysis of such a large data set, these are referred to throughout the thesis and are described in Chapter 3.

A unique feature of this study has been the fusion of DAMSON DD information with the accompanying DF analysis possible when using a multi-channel receiver system.

### **7.1 Statistical survey**

A first pass data set, based on the DAMSON DF measurements described above, has been surveyed and classified according to measured delay and Doppler spreads. It is clear that although there are a variety of propagation mechanisms occurring to cause the observed variation in the characteristics of the DD-DF plots, the majority of first pass cases have small delay spread and narrow Doppler spread. Due to the generally quiet geomagnetic conditions prevalent during the campaign, there are only a relatively small

number of cases that exhibit complex properties related to the propagation environment. Of these, however, an important observation in terms of the communication systems under consideration, is that a number of complex cases have Doppler spread exceeding the boundary of operation (7Hz) as defined in section 1.7, while none exceed the 7ms delay spread boundary.

Since signals having both narrow delay and Doppler characteristics, comprise the largest part of the first pass data set, they provide the most statistically stable sample. In general the occurrence statistics for these signals are as expected, with diurnal variation in successful propagation frequency and time of flight consistent with well understood changes in ionospheric structure during the day. Surprisingly, however, there is a significant statistical spread in the measured directions of arrival.

The statistical behaviour of the more complex delay or Doppler spread cases generally agrees with observations made previously by other authors involved with the DAMSON project. The unique DF information was used to extend the analysis and confirm that there is much more directional variation in the signal energy arriving at longer delays than for shorter delayed signal energy. For the wide Doppler spread cases, signal energy was seen to arrive from a large range of angles with a small preference for directions close to the GCP. Doppler spreading was more prevalent around midnight CGMLT, which is when the auroral oval reaches its most southern extent and thus when the propagation medium is most likely to be disturbed

## **7.2 Detailed case studies**

A number of cases were studied in detail in order to gain an understanding of the propagation environment. The analysis of sequences of cases having time delay spread confirmed the expected reduction in multi-hop propagation with increasing frequency. Over both paths, despite the quiet geomagnetic conditions at these times, there was significant off GCP propagation, particularly for the more delayed peaks. Since these cases were very narrow in Doppler, propagation was not via drifting irregularities but most likely from geographically distributed tilts in an otherwise smooth ionospheric electron density. In terms of communication system performance, although in this campaign data set delay spreading never exceeded the boundaries of operation as

discussed in section 1.7, this does not exclude the possibility that under similar propagation conditions delay spreading could exceed the boundaries.

Many cases with large Doppler spread show a trend in direction of arrival with Doppler offset, these have been attributed to scatter propagation via drifting ionospheric irregularity regions. A sequence of cases with significant Doppler spread, exhibiting such trends in direction of arrival, has been studied in detail. The ambiguity in the direction of irregularity drift, as described in *Wagner et al.* [1988 and 1995], has been resolved using DF information and the flow direction has been related to modelled convection flows in the high latitude ionosphere, which in turn are dependent on solar terrestrial magnetic conditions.

The observed movement over time of the major scattering features is consistent with the convection flows and Doppler trends. However, analysis of the crossing velocity of the irregularities, derived from both Doppler measurements and movement of the major scattering features over time, reveals that the flow velocities are actually much larger than appears from the movement calculations and that each sounding is illuminating different sets of irregularities embedded in a turbulent bulk convection flow.

It was also observed that in many Doppler spread cases, a 1-hop E-region return is visible. In general, when an E-region mode is present in a sounding, its direction of arrival is close to the GCP direction and it often has a low Doppler spread. The spectral and geographic distribution of signal energy from such a mode is much better than for the accompanying F-region Doppler/azimuth spread modes.

### **7.3 Spatial filtering**

In this campaign data set, Doppler spreading is the most critical parameter in the potential operation of high data rate communication systems. Understanding that there is often a relationship between the spectral and spatial properties of signals propagated over these high latitude paths has led to the concept of using spatial filtering to attempt to mitigate against Doppler spread in the received signals.

A selection of examples from the campaign data set was chosen on the basis of exceeding the working boundaries of the performance surfaces for the Mil-Std-188-110A 1200bps modem.

Different methods of implementing spatial filtering on this data set were applied. The phase and/or amplitude of signals, received at the elements of simple 2 or 3 element subsets of the RSL six channel array, were modified before being combined to give a single resultant output signal. The output signal was then processed to find the amount of Doppler spread. This procedure was looped through for many values of phase and/or amplitude to find the combination resulting in the least Doppler spread. Each method was found to be capable of reducing the Doppler spread of the cases in this data set, however, in light of its performance and simplicity, the constant amplitude, varying phase, two antenna approach, was determined to be the most appropriate spatial filtering method to pursue.

It is clear that this form of spatial filtering can lead to significant reductions in Doppler spread and thus improvements in the availability of modems operating over such a channel. Examination of the shape of cumulative probability of occurrence vs. Doppler spread curves for the data set indicates that there will be improved availability in the case of the Mil-Std-188-110A 300bps and 1200bps modems. However, the improvement in availability possible for a hypothetical modem, with a breaking point around 15Hz is much more significant. The cumulative probability curves around this value are relatively flat and a small change in Doppler spread leads to a large change in cumulative probability.

In terms of Mil-Std-188-110A modem performance, when the best result is chosen on a case by case basis, the difference between the percentage passing the spread criteria after spatial filtering compared to before (i.e. the % being 'fixed') is around 20% for both the 300bps and 1200bps modems. For a hypothetical modem with a breaking point around 15Hz the figure is 45%. An operational system is unlikely to have the 'luxury' of selecting the best performing pair from an array, however, on average, these results do indicate that in ~6% of cases an improvement in the mean Doppler spread after spatial filtering may 'fix' a 1200bps modem. While in ~30% of cases spatial filtering may 'fix' the hypothetical modem.

The variation of Doppler spread with phase angle,  $\psi$ , was examined and in most cases appeared to present a smooth curve with one or more minima, depending on the

propagation conditions. It is interesting to note that in many cases, all values of  $\psi$  actually led to a reduction of Doppler spread.

Having determined the effectiveness of the two antenna approach, fast solver methods were applied to the problem of optimising the selection of phase angle to give least Doppler spread. These solver methods were found to be very effective, robust and quick, with all cases in the data set converging to a good solution, comparable to the looping method solution, many times faster than the looping method. The mean convergence times are nearly short enough to be comparable with the parameter update time necessary for use in an operational spatial filtering system.

While this spatial filtering analysis has selected the best performing antenna pair from the RSL six antenna array, this would not be practical for an operational communication system. The preliminary three antenna results, however, indicate that although applying two sets of phases is too computationally intensive, it may be practical to select the best performing pair from a carefully arranged three antenna array particularly if calculation time can be reduced using fast solver methods.

## **7.4 Further Work**

Looking to the future, there are a number of areas of further work suggested by this study.

There are only relatively few complex propagation cases in the campaign data set, there is thus only very limited benefit to be gained in attempting further statistical analysis of their behaviour and occurrence. There are however still enough complex propagation cases within the data set to pursue more detailed case studies, which will shed more light on our understanding of propagation at these high latitudes.

Since the field of view of the SuperDARN HF backscatter radars (and in particular CUTLASS, which is operated by the University of Leicester) covers both DAMSON propagation paths, it may be possible to augment these case studies using measurements from both the DAMSON DF and the SuperDARN systems. The radar plot view of DAMSON DF data may be useful in this context. While detailed comparisons of measured flow directions and velocities may be possible, the different frequencies of

operation and the different aspect angles of irregularities to the systems may make comparison difficult.

Particularly interesting further work would be in the area of extending the spatial filtering analysis, initially along a number of directions.

- Using a reduced approach of selecting two antennas from a three antenna array. By ensuring that the three antenna array is a subset of the RSL six antenna array, various combinations of three antennas can be compared using the existing processed data.
- The stability in time of the selected phase angle is important, the data throughput of a communication system can be limited if it must frequently recalculate the phase angle. Papers presented by *Warrington et al.* [2000(2) and 2001] have started to address this issue. More detailed analysis, using all six of the DD-DF measurements collected at 5s intervals in each frequency time slot, will be helped by the processing speed improvements offered by the fast solver method.
- Although it performs well, the solver method has not yet been fully optimised to the spatial filtering problem. There are a number of possible ways to further improve its performance.
  - The introduction of a composite TDspr, Ttspr and SNR parameter.
  - Investigation of alternative solver algorithms.
  - Optimisation of termination tolerances.
  - Optimisation of the underlying Doppler spread calculation, since this is the most computationally intensive component of the cycle. Compilation of the MATLAB code is an option that may significantly speed up execution time.

Finally, since only a relatively small number of complex propagation cases were available in the Kiruna March 1998 campaign data set, it would be useful to re-deploy the RSL system at a more geomagnetically active time in order to collect a better selection of cases for further analysis.

## 8. References

Angling, M.J.; Cannon, P.S.; Davies, N.C.; Lundborg, B.; Jodalen, V.; Moreland, K.W., [1995], Measurements of Doppler spread on high latitude HF paths, Proceedings of AGARD Specialists Meeting on Digital Communication Systems: Propagation Effects, Technical Solutions, System Design, Athens, September 1995, pp. 17/1-7

Angling, M.J., [1995], Functional description and user guide for the DAMSON analysis software; version 5.0, Unpublished, QinetiQ, 1995

Angling, M.J.; Davies, N.C., [1997], On an ionospheric channel simulator driven by measurements of multipath and Doppler spread, Propagation Characteristics and Related System Techniques for Beyond Line-of-Sight Radio (Ref. No. 1997/390), IEE Colloquium on, 1997, pp. 4/1 -4/6

Angling, M.J.; Cannon, P.S.; Davies, N.C.; Arthur, P.C., [1997], Estimation of the availability of data modems on oblique high latitude HF paths, HF Radio Systems and Techniques, Seventh International Conference on (Conf. Publ. No. 441), 1997, pp. 159–163

Angling, M.J.; Cannon, P.S.; Davies, N.C.; Willink, T.J.; Jodalen, V.; Lundborg, B., [1998], Measurements of Doppler and multipath spread on oblique high latitude HF paths and their effects on data modems. Radio Science, 1998, Vol. 33, No. 1, pp. 97-107

Angling, M.J.; Davies, N.C., [1999], An assessment of a new ionospheric channel model driven by measurements of multipath and Doppler spread, Frequency Selection and Management Techniques for HF Communications (Ref. No. 1999/017), IEE Colloquium on, 1999, pp. 4/1 -4/6

Arthur, P.C.; Maundrell, M.J., [1997], Multi-dimensional HF Modem performance characterisation, HF Radio Systems and Techniques, Seventh International Conference on (Conf. Publ. No. 441), 1997, pp. 154–158

Basler, R.P.; Price, G.H.; Tsunoda, R.T.; Wong, T.L., [1988], Ionospheric distortion of HF signals. Radio Science, 23, (4), 1988, pp. 569-579

Benedicto, S.; Biglieri, E.; Castellani, V., [1987], Digital transmission theory, Prentice Hall Inc., 1987

Brandwood, D.H., [1994], Implementation of the IMP algorithm. IEE discussion meeting: Applications of Adaptive Signal Processing Systems, 26 January 1994

British Standard 204, [1960], Glossary of terms used in telecommunications (including radio) and electronics, 1960 and later amendments.

Broms, M.; Lundborg, B.; Jodalen, V.; Bergsvik, T., [1997], Doppler effects on high latitude HF paths during and ionospheric disturbance, HF Radio Systems and Techniques (Conf. Publ No. 411), July 1997, pp. 75 -79

Brown, D.J.; Warrington, E.M., [1999], Some approaches to real time evaluation for HF data communications, Antennas and Propagation, 1999. IEE National Conference on., 1999, pp. 353 -355

Cannon, P.S., [1989], Morphology of the high latitude ionosphere and its implications for HF communications systems, Communications, Speech and Vision, IEE Proceedings I [see also IEE Proceedings-Communications], Volume: 136 Issue: 1, Feb. 1989, pp. 1 - 10

Cannon, P.S.; Davies, N.C.; Angling, M.J.; Jodalen, V.; Moreland, K.W.; Lundborg, B., [1995], Initial results from DAMSON-a system to measure multipath, Doppler spread and Doppler shift on disturbed HF channels, Antennas and Propagation, 1995., Ninth International Conference on (Conf. Publ. No. 407) , Volume: 2, 1995, pp. 104 -108

Cannon, P.S.; Angling, M.J.; Willink, T.; Moreland, W.; Davies, N.C.; Lundborg, B.; Jodalen, V.; Broms, M., [1996], Requirements on channel probes for automatic channel selection, Frequency Selection and Management Techniques for HF Communications, IEE Colloquium on, 1996, pp. 24/1 -24/6

Cannon, P.S., [1997], Ionospheric models and measurements required by HF communication system designers and operators, Propagation Characteristics and Related System Techniques for Beyond Line-of-Sight Radio (Ref. No. 1997/390), IEE Colloquium on, 1997, pp. 1/1 -1/4

Cannon, P.S.; Angling, M.J.; Davies, N.C.; Wilink, T.; Jodalen, V.; Jacobson, B.; Lundborg, B.; Broms, M., [2000], Damson HF channel characterisation-a review, MILCOM 2000. 21st Century Military Communications Conference Proceedings, Volume: 1, 2000, pp. 59 –64

Cannon, P.S.; Angling, M.J.; Lundborg, B, [2002], Characterisation and modelling of the HF communications channel, Publ. Centre for propagation and atmospheric research, QinetiQ, Malvern, UK.

Clark, A.P., [1983], Principles of digital data transmission, second edition, Pentech press, 1983

Davies, K., [1990], Ionospheric radio, Peter Peregrinus Ltd., London, 1990

Davies, N.C.; Cannon, P.S.; Maundrell, M.J., [1992], DAMSON-a system to measure multipath dispersion, Doppler spread and Doppler shift on HF communications channels, High Latitude Ionospheric Propagation, IEE Colloquium on, 1992, pp. 2/1 - 2/4

Davies, N.C.; Cannon, P.S., [1993], DAMSON - A system to measure multipath dispersion, Doppler spread and Doppler shift on multi-mechanism communications channels, Proceedings of AGARD EPP Symposium on Multiple Mechanism Propagation Paths: Their Characterisation and Influence on System Design, Rotterdam, October 1993, pp. 36/1-6

Dhanda, B.S.; Warrington, E.M.; Jones, T.B., [1992], Some measurements of the propagation of HF radio signals over high latitude paths with special reference to FSK data transmissions, High Latitude Ionospheric Propagation, IEE Colloquium on, 1992, pp. 6/1 -6/5

Featherstone, W.; Strangeways, H.J.; Mewes, H., [1997], An improved Capon estimator for HF DF using limited sample data sets, Propagation Characteristics and Related System Techniques for Beyond Line-of-Sight Radio (Ref. No. 1997/390), IEE Colloquium on, 1997, pp. 2/1 -2/5

Featherstone, W.; Strangeways, H.J.; Darnell, M.; Mewes, H., [1997], The application of superresolution direction finding to a variety of channel conditions in the HF band, HF Radio Systems and Techniques, Seventh International Conference on (Conf. Publ. No. 441), 1997, pp. 306 –310

Featherstone, W.; Strangeways, H.J., [1998], A new real time radio frequency direction finding algorithm for Gaussian and non-Gaussian noise environments, Radio and Wireless Conference, 1998. RAWCON 98. 1998 IEEE, 1998, pp. 237 –240

Featherstone, W.; Strangeways, H.J.; Baker, P.W., [1999], Validating prediction packages using superresolution direction finding techniques and oblique ionospheric soundings, Frequency Selection and Management Techniques for HF Communications (Ref. No. 1999/017), IEE Colloquium on, 1999, pp. 16/1 -16/6

Featherstone, W.; Strangeways, H.J., [1999], Improved multipath resolution using joint space-time maximum likelihood estimation, Antennas and Propagation, 1999. IEE National Conference on, 1999, pp. 204 –208

Featherstone, W.; Strangeways, H.J., [2000], A fast, efficient approach to implementing SRDF techniques, HF Radio Systems and Techniques, 2000. Eighth International Conference on (IEE Conf. Publ. No. 474), 2000, pp. 123 –126

Feldstein, Y.I.; Starkov, G.V., [1967], Dynamics of auroral belt and polar geomagnetic disturbances, Planetary and Space Science, 1967, 15, pp. 209 –229

Gething, P.J.D., [1991], Radio Direction Finding and Superresolution, Peter Peregrinus Ltd., second edition, 1991

Gherm, V.E.; Zernov, N.N.; Strangeways, H.J.; Darnell, M., [2000], Scattering functions for wideband HF channels, HF Radio Systems and Techniques, 2000. Eighth International Conference on (IEE Conf. Publ. No. 474), pp. 341 –345

Gherm, V.E.; Zernov, N.N.; Strangeways, H.J., [2001], Scattering functions for multimoded wideband HF channels, Antennas and Propagation, 2001. Eleventh International Conference on (IEE Conf. Publ. No. 480) , Volume: 1, 2001, pp. 393 –397

Giles, T., [2001], HF modem design for extremely high simultaneous Doppler and delay spreads. Publ. of the Royal Institute of Technology, Stockholm, Sweden.  
<http://www.s3.kth.se/>

Holzworth, R.H.; Meng, C., [1975], Mathematical representation of the auroral oval, Geophysics Research Letters, 1975, Volume: 2, pp. 377 –380

Hunsucker, R.D., [1992], Auroral and polar-cap ionospheric effects on radio propagation, Mini-Review, Antennas and Propagation, IEEE Transactions on. Vol. 40, No. 7, 1992, pp. 818 -828

IEEE, [1969], Standard definitions of terms for antennas, IEEE Transactions, AP-17, 1969, pp. 264 –269

ITU-R Rec. P.533.6, [1999], HF propagation prediction method, Publ. of International Telecommunications Union, Geneva, Switzerland, <http://www.itu.org>

ITU-R Rec. P.533.6 Document 9/BL/44-E, [2002], Draft new recommendation ITU-R [9C/HF-ADAPTIVE]\* Prediction methods for adaptive HF system planning and operation, Publ. of International Telecommunications Union, Geneva, Switzerland, <http://www.itu.org>

ITU-R Rec. F.1110-2, [1997], Adaptive radio systems for frequencies below about 30 MHz, Publ. of International Telecommunications Union, Geneva, Switzerland, <http://www.itu.org>

ITU-R Rec. F.1337, [1997], Frequency management of adaptive HF radio systems and networks using FMCW oblique-incidence sounding, Publ. of International Telecommunications Union, Geneva, Switzerland, <http://www.itu.org>

ITU-R Rec. F.1487, [2000], Testing of HF modems with bandwidths of up to about 12 kHz using ionospheric channel simulators, Publ. of International Telecommunications Union, Geneva, Switzerland, <http://www.itu.org>

Jacobsen, B.; Jodalen, V.; Cannon, P.S.; Angling, M.J., [2000], HF radio propagation at high latitudes under quiet and disturbed geomagnetic conditions, HF Radio Systems and Techniques, 2000. Eighth International Conference on (IEE Conf. Publ. No. 474), pp. 187 –191

Jodalen, V.; Lundborg, B.; Jacobsen, B., [2000], Channel characteristics of HF NVIS paths in northern Scandinavia, HF Radio Systems and Techniques, 2000, (IEE Conf. Publ. No. 474), pp. 269 –273

Johnson, R.L.; Miner, G.E., [1986], Comparison of superresolution algorithms for radio direction finding, Aerospace and Electronic Systems, IEEE Transactions on. Vol. AES-22, No. 4, July 1986, pp. 432 –442

Jones, T.B., [1987], HF propagation at high latitudes, Antennas and Propagation, IEE Conference on, (Conf. Publ. No. 274) Part 2, 1987, pp. 155 -169

Jones, T.B.; Warrington, E.M., [1992], Direction of arrival measurement of HF signals propagated over high latitude paths, High Latitude Ionospheric Propagation, IEE Colloquium on, 1992, pp. 3/1 -3/8

Lockwood, M., [1993], Modelling high-latitude ionosphere for time-varying plasma convection. IEE Proceedings–H, Microwaves Antennas and Propagation, Vol.140, (2), 1993, pp. 91-100.

Mather, J.L., [1990], The incremental multi-parameter algorithm, 24<sup>th</sup> Asilomar Conference on circuits, systems and computers, Proceedings on, 1990, Volume: 1, pp. 386 –372

Mewes, H., [1997], Long term azimuth and elevation measurements in the HF band, HF Radio Systems and Techniques (Conf. Publ No. 411), July 1997, pp. 344 –348

Moyle, D.E.; Warrington, E.M., [1997], Some super-resolution DF measurements within the HF band, Antennas and Propagation, Tenth International Conference on (Conf. Publ. No. 436), Volume: 2 , 1997, pp. 71 -74

Otnes, R., [2001(1)], Factors affecting the availability of medium data rate waveforms at high latitude HF channels, 6<sup>th</sup> Nordic Shortwave Conference, HF '01, Aug 2001.

Otnes, R., [2001(2)], Guidelines for increasing the availability of low and medium data rates at high latitude HF channels, Information Systems Technology Panel Symposium on Military Communications, NATO RTO, Warsaw, Poland, October 8-10 2001.

Otnes, R.; Jodalen,V., [2001], Increasing the availability of medium data rates at high latitude HF channels, IEEE MILCOM 2001, McLean, VA, USA, Oct 2001.

Proakis, J.G., [1989], Digital communication, second edition, McGraw-Hill International, 1989

Rogers, N.C.; Warrington, E.M.; Jones, T.B., [1995], Some recent measurements of the direction of arrival of HF signals propagated over a path tangential to the mid-latitude trough, Antennas and Propagation, 1995., Ninth International Conference on (Conf. Publ. No. 407) , Volume: 2 , pp. 99 –103

Rogers, N.C., [1997], Draft Thesis, University of Leicester, 1997

Rogers, N.C.; Warrington, E.M.; Jones, T.B., [1997], Large HF bearing errors for propagation paths tangential to auroral oval, Microwaves, Antennas and Propagation, IEE Proceedings - , Volume: 144 Issue: 2 , April 1997, pp. 91 –96

Rogers, N.C.; Warrington, E.M.; Jones T.B., [2001], Oblique ionogram features associated with off-great-circle HF propagation at high latitudes, Antennas and Propagation, 2001. Eleventh International Conference on (IEE Conf. Publ. No. 480) , Volume: 1, pp. 398 –402

Schmidt, R.O., [1986], Multiple emitter location and signal parameter estimation. Trans. IEEE, AP34, 1986, pp.276-280

Smith, O.J.; Angling, M.J.; Cannon, P.S.; Jodalen, V.; Jacobsen, B.; Gronnerud, O.K., [2001], Simultaneous measurements of propagation characteristics on noncontiguous HF channels, Antennas and Propagation, 2001. Eleventh International Conference on (IEE Conf. Publ. No. 480), Volume: 1, pp. 383 –387

Stocker, A.J.; Warrington, E.M.; Jones, T.B., [2000], Directions of arrival at three frequencies on a propagation path along the mid-latitude trough: a comparison of observations with ray tracing simulations, HF Radio Systems and Techniques, 2000. Eighth International Conference on (IEE Conf. Publ. No. 474), pp. 193 –197

Strangeways, H.J.; Zatman, M.A., [1995], Experimental observations using superresolution DF and propagation path determination of additional off great circle paths due to the terminator, Antennas and Propagation, 1995, Ninth International Conference on (Conf. Publ. No. 407) , Volume: 2, pp. 69 -72

Strangeways, H.J.; Sow, S.M., [1997], HF transmitter SSL (single site location) with combined ionospheric update, Antennas and Propagation, Tenth International Conference on (Conf. Publ. No. 436) , Volume: 2, 1997, pp. 63 –66

Strangeways, H.J.; Sow, S.M., [1997], TASSEL (two angle single site emission locator), HF Radio Systems and Techniques, Seventh International Conference on (Conf. Publ. No. 441), 1997, pp. 339 –343

Tarran, C.J., [1997], Operational HF DF systems employing real time superresolution processing, HF Radio Systems and Techniques (Conf. Publ No. 411), July 1997, pp. 311 –319

Wagner, L.S.; Goldstein, J.A.; Meyers, W.D., [1988], Wideband probing of the transauroral HF channel: Solar minimum. Radio Science, Vol. 23. No. 4, 1988, pp. 555-568

Wagner, L.S.; Goldstein, J.A.; Meyers, W.D.; Bello, P.A., [1989], The HF skywave channel: Measured scattering functions for midlatitude and auroral channels and estimates for short-term wideband HF rake modem performance, IEEE Mil. Commun. Conf., 3, 1989, pp. 830 –839

Wagner, L.S.; Goldstein, J.A., [1991], Response of the high-latitude HF skywave channel to an isolated magnetic disturbance, IEE Conf. Publ. No. 339, 1991, pp. 233 – 237

Wagner, L.S.; Goldstein, J.A.; Rugar, M.A.; Kennedy, E.J., [1995], Delay, Doppler, and amplitude characteristics of HF signals received over a 1300km transauroral sky wave channel. Radio Science, Vol. 30, No. 3, 1995, pp. 659-676

Warrington, E.M., [1986], Ionospheric radiowave propagation effects observed with a large aperture antenna array. Ph.D Thesis, University of Leicester, 1986

Warrington, E.M.; Jones, T.B.; Orrell, S.M., [1989], HF propagation over a transauroral path, Antennas and Propagation, 1989. ICAP 89., Sixth International Conference on (Conf. Publ. No.301) Volume: 2, pp. 19 -22

Warrington, E.M.; Thomas, E.C.; Jones, T.B., [1990], Measurements on the wavefronts of ionospherically propagated HF radio waves made with a large aperture antenna array, *Microwaves, Antennas and Propagation* [see also *IEE Proceedings-Microwaves, Antennas and Propagation*], *IEE Proceedings H* , Volume: 137 Issue: 1 , Feb. 1990, pp. 25 –30

Warrington, E.M.; Jones, T.B., [1991], Measurements of the direction of arrival of HF sky wave signals and single site location using a seven element wide aperture (294 m) interferometer array, *Microwaves, Antennas and Propagation* [see also *IEE Proceedings-Microwaves, Antennas and Propagation*], *IEE Proceedings H* , Volume: 138 Issue: 2, April 1991, pp. 121 –130

Warrington, E.M.; Jones, T.B.; Orrell, S.M.; Dhanda, B.S., [1991], Amplitude and frequency variations of HF signals propagated over high latitude paths, *Antennas and Propagation, 1991. ICAP 91., Seventh International Conference on (IEE)*, Volume: 2, pp. 889 -892

Warrington, E.M.; Jones, T.B.; Hamadyk, P., [1992], Measurements of the direction of arrival of an oblique chirp sounder signal, *High Latitude Ionospheric Propagation, IEE Colloquium on, 1992*, pp. 4/1 -4/6

Warrington, E.M.; Jones, T.B., [1993], Observations of the direction of arrival of HF signals propagated over high latitude and mid latitude paths, *Antennas and Propagation, 1993, Eighth International Conference on, 1993*, Volume: 1, pp. 419 -422

Warrington, E.M.; Hamadyk, P.; Jones, T.B., [1993], Direction of arrival measurements of oblique chirp sounder signals at a high latitude site, *Antennas and Propagation, 1993, Eighth International Conference on, Volume: 1*, pp. 492 -495

Warrington, E.M.; Dhanda, B.S.; Jones, T.B., [1994], Observations of Doppler spreading and FSK signalling errors on HF signals propagating over a high latitude path, *HF Radio Systems and Techniques, 1994., Sixth International Conference on*, pp. 119 –123

Warrington, E.M., [1995], Measurements of direction of arrival of HF sky wave signals by means of a wide aperture antenna array and two super resolution direction finding algorithms, *Microwaves, Antennas and Propagation, IEE Proceedings -* , Volume: 142 Issue: 2 , April 1995, pp. 136 –144

Warrington, E.M., [1995], A comparison of MUSIC and an iterative null steering technique for the resolution of multi-moded ionospherically propagated HF radio signals, Antennas and Propagation, 1995., Ninth International Conference on (Conf. Publ. No. 407) , Volume: 2 , pp. 220 –224

Warrington, E.M.; Moyle, D.E., [1995], Super-resolution HF DF measurements with simultaneous chirp sounding for a path within the UK, HF Antennas and Propagation, IEE Colloquium on, 1995, pp. 4/1 -4/6

Warrington, E.M., [1996], Measurement of the angular spread of HF signals reflected from the high latitude ionosphere by means of super-resolution direction finding, Remote Sensing of the Propagation Environment (Digest No: 1996/221), IEE Colloquium on, 1996, pp. 2/1 -2/6

Warrington, E.M.; Rogers, N.C.; Jones, T.B., [1996], A comparison of predicted and measured times of propagation over high latitude paths for which direction of arrival measurements are available, Frequency Selection and Management Techniques for HF Communications, IEE Colloquium on, 1996, pp. 3/1 -3/6

Warrington, E.M.; Jones, T.B.; Dhanda, B.S., [1997], Observations of Doppler spreading on HF signals propagating over high latitude paths, Microwaves, Antennas and Propagation, IEE Proceedings -, Volume: 144 Issue: 4, Aug. 1997, pp. 215 –220

Warrington, E.M.; Rogers, N.C.; Jones, T.B., [1997], Large HF bearing errors for propagation paths contained within the polar cap, Microwaves, Antennas and Propagation, IEE Proceedings -, Volume: 144 Issue: 4, Aug. 1997, pp. 241 –249

Warrington, E.M.; Jones, T.B.; Rogers, N.C.; Rizzo, C., [1997], Directional characteristics of ionospherically propagated HF radio signals and their effect on HF DF systems, Propagation Characteristics and Related System Techniques for Beyond Line-of-Sight Radio (Ref. No. 1997/390), IEE Colloquium on, 1997, pp. 3/1 –3/10

Warrington, E.M.; Jackson, C.A., [1997], Some observations of the directions of arrival of an ionospherically reflected HF radio signal on a very high latitude path, HF Radio Systems and Techniques, Seventh International Conference on (Conf. Publ. No. 441), 1997, pp. 65 –69

Warrington, E.M. [1997], Some observations of the directions of arrival of the Doppler components of an ionospherically reflected HF radio signal from Svalbard to the UK, Antennas and Propagation, Tenth International Conference on (Conf. Publ. No. 436), Volume: 2, 1997, pp. 67 -70

Warrington, E.M.; Jones, T.B.; Rogers, N.C., [1997], Towards an ionospheric HF-DF quality factor for high latitude paths, HF Radio Systems and Techniques, Seventh International Conference on (Conf. Publ. No. 441), 1997, pp. 60 -64

Warrington, E.M., [1998], Observations of the directional characteristics of ionospherically propagated HF radio channel sounding signals over two high latitude paths, Microwaves, Antennas and Propagation, IEE Proceedings - , Volume: 145 Issue: 5, Oct. 1998, pp. 379 -385

Warrington, E.M.; Stocker, A.J.; Rizzo, C., [1999], The effect of the high latitude ionosphere on measurements of the direction of arrival of HF signals using super-resolution direction finding, Antennas and Propagation, 1999. IEE National Conference on., pp. 349 -352

Warrington, E.M.; Jackson, C.A.; Stocker, A.J.; Jones, T.B.; Lundborg, B., [2000], Observations of the directional characteristics of obliquely propagating HF radio signals and simultaneous HF radar measurements, HF Radio Systems and Techniques, 2000. Eighth International Conference on (IEE Conf. Publ. No. 474), pp. 243 -247

Warrington, E.M.; Jackson, C.A.; Lundborg, B., [2000], Directional diversity of HF signals received over high latitude paths, and the possibility of improved data throughput by means of spatial filtering, Microwaves, Antennas and Propagation, IEE Proceedings - , Volume: 147 Issue: 6 , Dec. 2000, pp. 487 -494

Warrington, E.M.; Stocker, A.J.; Rizzo, C., [2000], Behaviour of superresolution direction finding algorithms for HF signals propagating through the high latitude ionosphere, Microwaves, Antennas and Propagation, IEE Proceedings - , Volume: 147 Issue: 6 , Dec. 2000, pp. 469 -478

Warrington, E.M.; Jackson, C.A.; Lundborg, B., [2001], The directional diversity of HF signals received over high latitude paths and the possibility of improved data throughput by means of spatial filtering, *Antennas and Propagation*, 2001. Eleventh International Conference on (IEE Conf. Publ. No. 480) , Volume: 1 , pp. 378 –382

Watterson, C.C.; Juroshek, J.R.; Bensema, W.D., [1970], Experimental confirmation of an HF channel model, *Communications Technology*, IEEE Transactions on. COM-18, 1970, pp. 792 -803

Willink, T.J.; Landry, E.C., [1997], Analysis of time-varying HF propagation characteristics, *HF Radio Systems and Techniques* (Conf. Publ No. 411), July 1997, pp. 70 –73

Willink, T.J., [1997], Characteristics of ionospheric propagation at high latitudes and their impact on communications systems, *Information, Communications and Signal Processing*, IEEE International Conference on, September 1997, pp. 1709 –1713

Willink, T.J.; Davies, N.C.; Angling, M.J.; Jodalen, V.; Lundborg, B., [1999], Robust HF data communications at high latitudes, *Microwaves, Antennas and Propagation*, IEE Proceedings -, Volume: 146 Issue: 4, Aug. 1999, pp. 263 –269

Wright, J.W., [1959], Note on quiet-day vertical cross sections of the ionosphere along 75° west geographic meridian, *Journal of Geophysical Research*, 1959, Volume: 64, pp. 1631

Wright, J.W., [1962], Dependence of the ionospheric F region on the solar cycle, *Nature*, 1962, Volume: 194, pp. 461

Zatman, M.A.; Strangeways, H.J.; Warrington, E.M., [1993], Resolution of multimoded HF transmissions using the DOSE superresolution direction finding algorithm, *Antennas and Propagation*, 1993, Eighth International Conference on, pp. 415 -417

Zatman, M.A.; Strangeways, H.J., [1993], The effect of the number of noise eigenvectors used and quantisation errors on the performance of the MUSIC algorithm, *Antennas and Propagation*, 1993., Eighth International Conference on, 1993, Volume: 1, pp. 481 -484

Zatman, M.; Strangeways, H., [1994], The effect of the covariance matrix of ionospherically propagated signals on the choice of direction finding algorithm, HF Radio Systems and Techniques, 1994., Sixth International Conference on, pp. 267 –272

Zatman, M.A.; Strangeways, H.J., [1994], Bearing measurements on multi-moded signals using single snapshot data, Antennas and Propagation Society International Symposium, 1994, AP-S. Digest , Volume: 3, 1994, pp. 1934 –1937

Zatman, M.A.; Strangeways, H.J., [1994], Superresolution direction finding algorithms for the characterisation of multi-moded HF signals, AGARD, Multiple Mechanism Propagation Paths (MMPPs): Their Characterisation and Influence on System Design, July 1994

Zatman, M.A.; Strangeways, H.J., [1995], An efficient joint direction of arrival and frequency ML estimator, Antennas and Propagation Society International Symposium, 1995. AP-S. Digest , Volume: 1, pp. 431 –434

## **8.1 World Wide Web references.**

<http://cdaweb.gsfc.nasa.gov>, Coordinated Data Analysis Web (CDAWeb), NASA Goddard Space Flight Center, USA

<http://www.itu.org>, International Telecommunications Union, Geneva, Switzerland

<http://ion.le.ac.uk>, Radio and Space Plasma Physics Group, Department of Physics, University of Leicester, UK

<http://www.wdc.rl.ac.uk>, World Data Centre for Solar-Terrestrial Physics at the Rutherford Appleton Laboratory, Chilton, UK